U.S. Department of
Transportation

**Federal Railroad
Administration**

Side Impact Test and Analyses of a DOT-105 Tank Car

Office of Research,
Development
and Technology
Washington, DC 20590

REPORT DOCUMENTATION PAGE

Public reporting burden for this collection of information is estimated to average 1 hour per response, including the time for reviewing instructions, searching existing data sources, gathering and maintaining the data needed, and completing and reviewing the collection of information. Send comments regarding this burden estimate or any other aspect of this collection of information, including suggestions for reducing this burden, to Washington Headquarters Services, Directorate for Information Operations and Reports, 1215 Jefferson Davis Highway, Suite 1204, Arlington, VA 22202-4302, and to the Office of Management and Budget, Paperwork Reduction Project (0704-0188), Washington, DC 20503.

1. AGENCY USE ONLY (Leave blank)	2. REPORT DATE May 2019	3. REPORT TYPE AND DATES COVERED Technical Report – April 27, 2016

4. TITLE AND SUBTITLE Side Impact Test and Analyses of a DOT-105 Tank Car	5. FUNDING NUMBERS Contract DTFR53-11-D-00008 Task Order 008
6. AUTHOR(S) Michael Carolan[1], Przemyslaw Rakoczy[2]	

7. PERFORMING ORGANIZATION NAME(S) AND ADDRESS(ES) [1]Volpe National Transportation Systems Center [2] Transportation Technology Center, Inc. 55 Broadway 55500 DOT Road Cambridge, MA 02142 Pueblo, CO 81001	8. PERFORMING ORGANIZATION REPORT NUMBER

9. SPONSORING/MONITORING AGENCY NAME(S) AND ADDRESS(ES) U.S. Department of Transportation Federal Railroad Administration Office of Railroad Policy and Development Office of Research, Development and Technology Washington, DC 20590	10. SPONSORING/MONITORING AGENCY REPORT NUMBER DOT/FRA/ORD-19/12

11. SUPPLEMENTARY NOTES
COR: Francisco Gonzalez, III

12a. DISTRIBUTION/AVAILABILITY STATEMENT This document is available to the public through the FRA website.	12b. DISTRIBUTION CODE

13. ABSTRACT

Transportation Technology Center, Inc. (TTCI) conducted a side impact test on a Department of Transportation (DOT)-105A500W (referred to DOT-105) tank car to evaluate the performance of it under dynamic impact conditions and to provide data for the verification and refinement of a computational model. The tank car was filled with water to approximately 89.4 percent of its volume and pressurized to 100 psi. The tank car was impacted at 15.2 mph by a 297,125-pound ram car with 12- by 12-inch ram head fitted to the ram car. The ram car impacted the tank center; it punctured the tank after slowing nearly to a stop.

The John A. Volpe National Transportation Systems Center (Volpe) performed finite element (FE) modeling to estimate the overall response of the tank to the impact. The pre-test model used two different material models for the steel in the tank car shell. The pre-test model that used a lower-ductility material response was found to be in very good agreement with the test results. After the test, material coupons were cut from the car and subjected to tensile testing. The post-test FE model was updated to include the actual material behavior of the test car, and continued to give very good agreement with the test measurements.

The test data is intended to be useful to entities who wish to develop FE models of tank cars under similar puncture conditions in their modeling validation and verification efforts. By comparing model results to actual test measurements, confidence can be developed in the modeling techniques when simulating other impact conditions.

14. SUBJECT TERMS Impact test, DOT-105 tank car, tank car performance, ram head, ram car, transportation safety, toxic by inhalation, TIH, finite element analysis, FEA, finite element, FE	15. NUMBER OF PAGES 157
	16. PRICE CODE

17. SECURITY CLASSIFICATION OF REPORT Unclassified	18. SECURITY CLASSIFICATION OF THIS PAGE Unclassified	19. SECURITY CLASSIFICATION OF ABSTRACT Unclassified	20. LIMITATION OF ABSTRACT

METRIC/ENGLISH CONVERSION FACTORS

ENGLISH TO METRIC

LENGTH (APPROXIMATE)

1 inch (in)	=	2.5 centimeters (cm)
1 foot (ft)	=	30 centimeters (cm)
1 yard (yd)	=	0.9 meter (m)
1 mile (mi)	=	1.6 kilometers (km)

AREA (APPROXIMATE)

1 square inch (sq in, in^2)	=	6.5 square centimeters (cm^2)
1 square foot (sq ft, ft^2)	=	0.09 square meter (m^2)
1 square yard (sq yd, yd^2)	=	0.8 square meter (m^2)
1 square mile (sq mi, mi^2)	=	2.6 square kilometers (km^2)
1 acre = 0.4 hectare (he)	=	4,000 square meters (m^2)

MASS - WEIGHT (APPROXIMATE)

1 ounce (oz)	=	28 grams (gm)
1 pound (lb)	=	0.45 kilogram (kg)
1 short ton = 2,000 pounds (lb)	=	0.9 tonne (t)

VOLUME (APPROXIMATE)

1 teaspoon (tsp)	=	5 milliliters (ml)
1 tablespoon (tbsp)	=	15 milliliters (ml)
1 fluid ounce (fl oz)	=	30 milliliters (ml)
1 cup (c)	=	0.24 liter (l)
1 pint (pt)	=	0.47 liter (l)
1 quart (qt)	=	0.96 liter (l)
1 gallon (gal)	=	3.8 liters (l)
1 cubic foot (cu ft, ft^3)	=	0.03 cubic meter (m^3)
1 cubic yard (cu yd, yd^3)	=	0.76 cubic meter (m^3)

TEMPERATURE (EXACT)

[(x-32)(5/9)] °F = y °C

METRIC TO ENGLISH

LENGTH (APPROXIMATE)

1 millimeter (mm)	=	0.04 inch (in)
1 centimeter (cm)	=	0.4 inch (in)
1 meter (m)	=	3.3 feet (ft)
1 meter (m)	=	1.1 yards (yd)
1 kilometer (km)	=	0.6 mile (mi)

AREA (APPROXIMATE)

1 square centimeter (cm^2)	=	0.16 square inch (sq in, in^2)
1 square meter (m^2)	=	1.2 square yards (sq yd, yd^2)
1 square kilometer (km^2)	=	0.4 square mile (sq mi, mi^2)
10,000 square meters (m^2)	=	1 hectare (ha) = 2.5 acres

MASS - WEIGHT (APPROXIMATE)

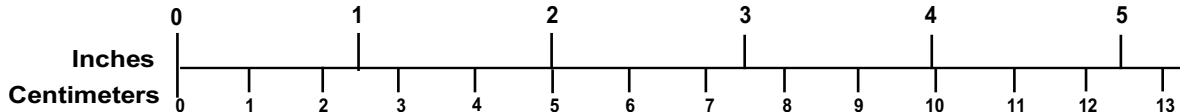|		
1 gram (gm)	=	0.036 ounce (oz)
1 kilogram (kg)	=	2.2 pounds (lb)
1 tonne (t)	=	1,000 kilograms (kg)
	=	1.1 short tons

VOLUME (APPROXIMATE)

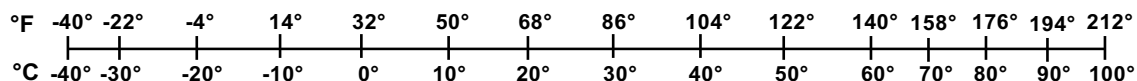|		
1 milliliter (ml)	=	0.03 fluid ounce (fl oz)
1 liter (l)	=	2.1 pints (pt)
1 liter (l)	=	1.06 quarts (qt)
1 liter (l)	=	0.26 gallon (gal)
1 cubic meter (m^3)	=	36 cubic feet (cu ft, ft^3)
1 cubic meter (m^3)	=	1.3 cubic yards (cu yd, yd^3)

TEMPERATURE (EXACT)

[(9/5) y + 32] °C = x °F

QUICK INCH - CENTIMETER LENGTH CONVERSION

Inches	0	1	2	3	4	5

Centimeters 0 1 2 3 4 5 6 7 8 9 10 11 12 13

QUICK FAHRENHEIT - CELSIUS TEMPERATURE CONVERSION

°F	-40°	-22°	-4°	14°	32°	50°	68°	86°	104°	122°	140°	158°	176°	194°	212°
°C	-40°	-30°	-20°	-10°	0°	10°	20°	30°	40°	50°	60°	70°	80°	90°	100°

For more exact and or other conversion factors, see NIST Miscellaneous Publication 286, Units of Weights and Measures. Price $2.50 SD Catalog No. C13 10286

Updated 6/17/98

ii

Acknowledgements

Contents

Illustrations

Tables

Executive Summary

The test and analyses described in this report support the overall objective of the Federal Railroad Administration's (FRA) research program to improve transportation safety for tank cars. This report documents the combined efforts sponsored by FRA of the Transportation Technology Center, Inc. (TTCI) and the U.S. Department of Transportation's (DOT) John A. Volpe National Transportation Systems Center (Volpe) to test and analyze the side impact puncture performance of a DOT-105 tank car. TTCI conducted a side impact test on the DOT-105 tank car on April 27, 2016, to evaluate its performance and to provide data for the verification and refinement of a computational model. All test requirements were met. Volpe performed both pre-test and post-test analyses of the impact response to evaluate, validate, and improve the capabilities of modeling fluid-structure interaction and puncture.

The tank car was filled with water to approximately 89.4 percent of its volume. It was then sealed and pressurized to 100 psi. The tank car was impacted by a 297,125-pound ram car traveling 15.2 mph. A 12- by 12-inch ram head fitted to the ram car impacted the tank center. The impact resulted in puncture of the tank after the ram car had slowed to less than 1 mph. This indicated that the impact occurred at a speed only slightly above the puncture/non-puncture threshold speed for these test conditions.

Pre-test finite element (FE) modeling was used to estimate the overall response of the tank to the impact, including the force-displacement response. While it was known before the test that the tank car heads and shell were made of TC128 steel, the exact material properties (i.e., yield strength, ultimate tensile strength (UTS), and ductility) were not known for this car. Therefore, the pre-test model was run using two different TC128 characteristics based on previously encountered TC128 samples. The pre-test model that used a lower-ductility TC128 material response was found to be in very good agreement with the test results, including estimation of puncture at the test speed.

After the test, material coupons were cut from the tank car shell and subjected to tensile testing. The material characterization indicated that the actual tank car material had a ductility that was below even the lower-ductility material used in the pre-test models. When the post-test model was updated to include the actual material response, the model continued to exhibit very good qualitative and quantitative agreement with the test results. The post-test model was conservative, meaning the post-test model estimated puncture at a speed lower than that measured during the test.

A second post-test model was developed to include the foam insulation between the tank and its jacket. In the pre-test model, this space was modeled as empty. This simplification resulted in a large force dropout in the model that was not seen in the test. With the inclusion of the foam insulation, the post-test model demonstrated that the force dropout could be greatly reduced by including the foam insulation within the model, giving even better agreement with the test measurements.

The results of this test, including test data and test photos, are important to the public to permit interested parties to attempt to validate and verify their own FE models simulating tank car shell impacts. By comparing model results to test measurements, confidence can be developed in the modeling techniques (e.g., modeling software, element type, fluid representation, material behaviors, etc.) used to represent the impact conditions of the test. Model validation efforts are

an essential part of any process where FE simulations are to be used to represent tank car impact conditions that have not been tested.

1. Introduction

This report documents the analyses and test results for a side impact test performed on a U.S. Department of Transportation (DOT) 105A500W (herein, referred to as DOT-105) tank car. The DOT-105 tank car is a current design pressurized car equipped with head protection and thermal protection enclosed in an exterior jacket. This report documents an impact test and describes the finite element (FE) model development and pre-test estimates, comparisons of the test and analyses, and the subsequent post-test analyses performed to address the variations between the pre-test analyses and actual test conditions.

1.1 Background

In recent years, significant research was conducted to analyze and improve the impact behavior and puncture resistance of railroad tank cars. Ultimately, the results of this research can be used by the Government regulatory agencies in the United States and Canada (i.e., the Federal Railroad Administration [FRA] and Transport Canada [TC] respectively) to establish performance-based testing requirements and to develop methods to evaluate the crashworthiness and structural integrity of different tank car designs when subjected to a standardized shell impact scenario. A performance-based requirement for tank car head impact protection has already been defined within the current regulations [1].

FRA has a continuing research program to provide the technical basis for rulemaking on enhanced and alternative performance standards for tank cars and review of new and innovative designs that are developed by the industry and other countries. In support of this ongoing research program, full-scale tests are necessary to provide the technical information to validate modeling efforts and to inform regulatory activities. These tests evaluate the crashworthiness performance of tank cars used in the transportation of hazardous materials.

Tests and associated analyses are being performed to evaluate the crashworthiness performance of tank cars. The tests and analyses have included designs that comply with current regulations as well as innovative new designs that have improved puncture resistance. FRA is currently working closely with key industry stakeholders to use the information being generated from these programs to revise and refine the construction, design, and use of tank cars.

1.2 Objectives

The objective of the test was to quantify the deformation mode, impact load-time history, and puncture resistance of an existing DOT-105 tank car in a side impact. This test was also intended to provide test data that would be made publicly available to further model validation efforts. Moreover, the impact conditions were developed so that the side impact test is: (a) safe, (b) repeatable, and (c) analyzable.

The objective of the analyses was to provide estimates of the tank car impact response both for pre-test planning and for validation of tank car impact and puncture modeling capabilities.

1.3 Scope

This report includes a discussion of developing and executing the FE models for this program, including modeling the tank car steel, modeling the water within the tank, and modeling the gas phase. This report presents the test results, discusses the execution of the test, and summarizes

the overall results of the test. Discussion of the post-test modeling adjustments are included in this report. Finally, this report presents a comparison between the test measurements and the model results.

This report does not include any results from further analyses using the DOT-105 tank car model, such as impact conditions outside of the conditions of the test. While this report refers to previously performed shell impact tests on tank cars with a different specification, no comparison of results from different tests are included within the scope of this report. Research into the puncture resistance of tank cars is ongoing, and such further simulations or comparisons may be considered in future work.

1.4 Overall Approach

Some uncertainty in a test's outcome will exist due to difficult-to-control variables of testing, such as wind speed, unknown weld qualities, and the inherent variability of material behavior even within a single plate. It is more useful to frame the discussion of test planning in terms of likelihood of puncture. In an ideal test, the target test speed would be chosen to fall somewhere in the shaded range in Figure 1 where puncture is possible, but not certain.
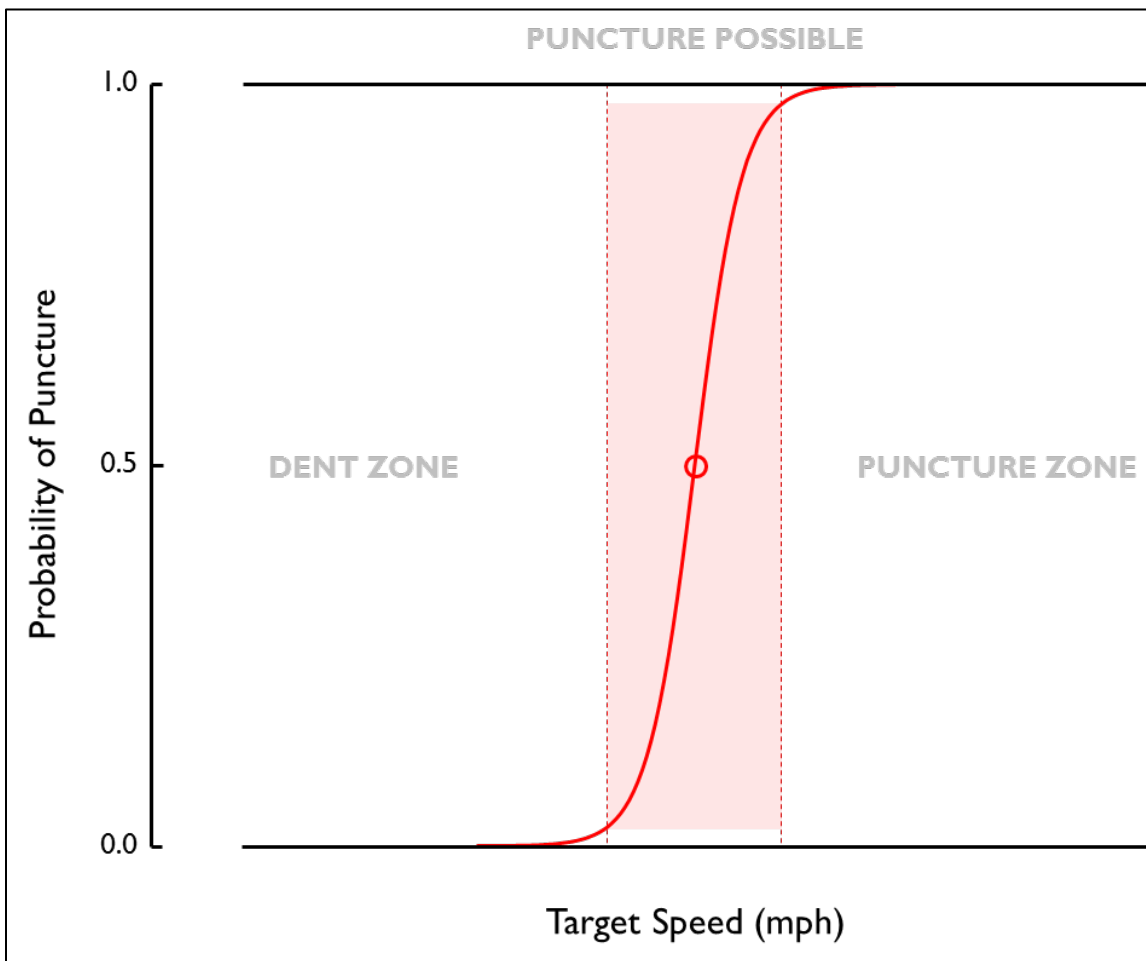
Figure 1. Schematic Illustrating Probability of Puncture versus Impact Speed

The value of a test can be increased by targeting an impact speed that is very close to the threshold speed between where the tank car punctures and where it does not puncture. If the tested impact speed is close to this threshold speed, regardless of whether or not the tank punctures, the data that is collected can be extremely valuable both for model validation and for estimating the threshold puncture speed under the given impact conditions. From a practical standpoint of test execution, the ideal range of test speeds provides a practical target to maximize the value of the test. One potential target for maximizing the value of the test data could be to run a test where the impactor is brought to a complete stop at the instant the tank punctures. Such a test would be an experimental demonstration of the threshold puncture speed, as all the ram car's initial kinetic energy was transferred into the tank car at the same instant that the tank car reaches the limit of its capacity. An incrementally slower test is a non-puncture test, and an incrementally faster test exceeds the capacity of the tank car to resist puncturing.

In the same spirit, making a blanket statement as to the superiority of a puncture test or a non-puncture test does not provide for a useful discussion without considering proximity to the theoretical threshold puncture speed. As the test speed moves further from the center of the puncture threshold range, the value of the test data decreases. Neither a test that causes catastrophic damage to the tank car structure, nor a test that scarcely creates a dent would be an effective tool for evaluating the puncture resistance of the car. These tests also would not provide much utility for model validation, evaluating the relative impact resistance offered by different tank car designs, or for evaluating new or novel methods of simulating impacts. The extremely unlikely-to-puncture case does not provide enough information to assess the model sufficiently to make a comparison, and the overwhelmingly likely-to-puncture case can result in a mode of tank failure that does not truly represent the way tank cars experience puncture near their puncture/non-puncture thresholds.

The highly nonlinear force response of an impacted tank car makes extrapolation or interpolation of test results to attempt to calculate the threshold speed between puncture and non-puncture problematic. The uncertainty of an interpolation or extrapolation increases when the test speed is either significantly higher or significantly lower than the threshold speed. Thus, if test results are obtained at speeds far away from the theoretical threshold puncture speed, the threshold puncture speed will not be known with a high degree of certainty.

A test that punctures the tank, but does not leave the impactor with an excessive amount of residual kinetic energy can be used to verify that a model captures both the overall response of the tank car and the puncture modeling techniques defined for the materials of the car. However, achieving this outcome can be extremely challenging. If a test is planned to be run at slightly above the threshold puncture speed, the threshold puncture speed is typically estimated from pre-test models. If the pre-test model predicts a higher threshold puncture speed than the tank car actually possesses, then a test that is planned to be performed at the threshold puncture speed may in fact be an excessively fast test. While the energy absorbed by the tank up to the point of puncture in the test can be used to estimate the energy necessary to cause puncture, this estimate becomes less reliable as the actual impact speed gets further from the threshold puncture speed. At the same time, if the pre-test model is overly conservative, then a test that is planned for just below the threshold puncture speed based on a conservative model may in fact result in an impact speed that is well below the threshold puncture speed.

The overall approach followed in this program of testing and analyses is presented in Figure 2. This flowchart presents a schematic view of the approach followed by John A. Volpe National

5

Transportation Systems Center (Volpe) in its model development and Transportation Technology Center, Inc. (TTCI) in developing and executing the test plans. This flowchart illustrates the collaboration between both Volpe and TTCI throughout the testing and modeling process, all of which was coordinated with FRA; for example, the instrumentation placement described in the testing plan was used to guide requests for corresponding results in the FE model. The model results could then be used to estimate the magnitude of the response (such as pressure or displacement) that the instrumentation would experience at that location. If necessary, the instrumentation in the test plan could be updated to account for the expected response from the model.

Iterative Approach to Estimating Puncture Speed

Start of Modeling

Develop and run pre-test FE model

Does model puncture at this speed?

Yes → Is result within 1 mph of a non-puncture result?
No → Reduce speed and re-run

No → Is result within 1 mph of a puncture result?
Yes →
No → Increase speed and re-run

Obtain puncture and non-puncture estimates within 1 mph range

Define tank car geometry

Define initial speed, temperature, boundary conditions, etc.

Define Pre-test material behaviors
- A1011
- Water
- Air
- Estimated TC128

Define output requests

Define geometry of test setup

Define test setup

Define instrumentation

Define test conditions

Prepare ram car

Prepare tank car

Conduct speed trials on test track

Install instrumentation

Collect and filter instrumentation data

Conduct pre/post test laser scanning

Determine target speed

Take pre/post-test photographs

Take test videos

Compare pre-test FE outputs to test measurements

Develop and run post-test FE model

Compare post-test FE outputs to test measurements

Make post-test modeling adjustments

Define post-test material behaviors
- Actual TC128
- Foam Insulation

Define actual impact speed

Cut TC128 coupons from tank and perform tensile testing

Develop test plan

Implement test plan

Conduct test and document results

Start of Test Planning

Figure 2. Flowchart Summarizing Overall Modeling and Testing Approach

Prior to the test itself, Volpe, TTCI, and FRA collaborated to determine the target test speed based on the model estimates, the desired outcome of the test, and such factors as ambient conditions (e.g., wind speed influencing actual impact speed) at the time of the test. After the test, material coupon test data from the TC128 shell of the car and the measured test speed were used to update the pre-test model to reflect the actual test conditions. Finally, the post-test model results and the test measurements were compared to one another.

1.5   Organization of the Report

Section 1 includes the introduction, a description of the objectives and scope of the report, and a description of the organization of the report.

Section 2 describes the tank car undergoing testing and analyses, and describes the shell impact test setup.

Section 3 describes the instrumentation used during the test and its placement. This description includes discussion of the cameras used to capture the impact event.

Section 4 presents the results of the test. These results include a description of the actual conditions of the impact, a description of the test itself, and a summary of the measured test data.

Section 5 describes the development of the FE models used in this program. This section describes the geometry used in the model, the different material models developed, and modeling techniques used in the pre- and post-test models.

Section 6 presents test measurements alongside the corresponding estimates from the pre-test FE models.

Section 7 presents test measurements alongside the corresponding estimates from the post-test FE models.

Section 8 includes a summary of the report, and contains concluding remarks.

Appendix A describes the positions of the cameras and targets used in the test.

Appendix B provides the full set of test data, and the material data measured during the tensile coupon tests for the TC128 steel making up the car's shell.

Appendix C includes a full set of comparisons between test measurements and FE estimates. This appendix contains comparisons for pre-test models using two different material behaviors for the post-test model using the actual TC128 behavior, and for a post-test model including insulation between the tank and jacket.

Appendix D describes the geometry and mesh on each part used in the FE models.

Appendix E contains a description of the modeling techniques that were used in both the pre- and post-test FE models.

Appendix F contains a description of how each material behavior was developed in the FE models.

2. Test Conditions

This section provides a general description of DOT-105 tank car designs, describes the details of the DOT-105 tank car used in the impact test, and describes the typical test setup used in the FRA-sponsored shell impact testing program.

2.1 Tank Car Design

The DOT-105 tank car is a pressurized tank car used in North America to carry pressurized gases. The test was performed on a DOT-105 tank car equipped with head protection and foam insulation enclosed in the exterior jacket. According to the certificate of construction, this car was constructed between 1979 and 1980. The nominally 0.775-inch thick tank car shell is constructed with TC128 Grade B steel. The tank was made of a cylindrical shell with an inside diameter of 100.45 inches. The tank itself was covered with a 4-inch layer of foam insulation having a density of 2 pounds per cubic foot, which is enclosed within an 11-gauge steel jacket. The jacket had an inside diameter of 110 inches.

The drawings for an example DOT-105 tank car general arrangement are shown in Figure 3 [2].
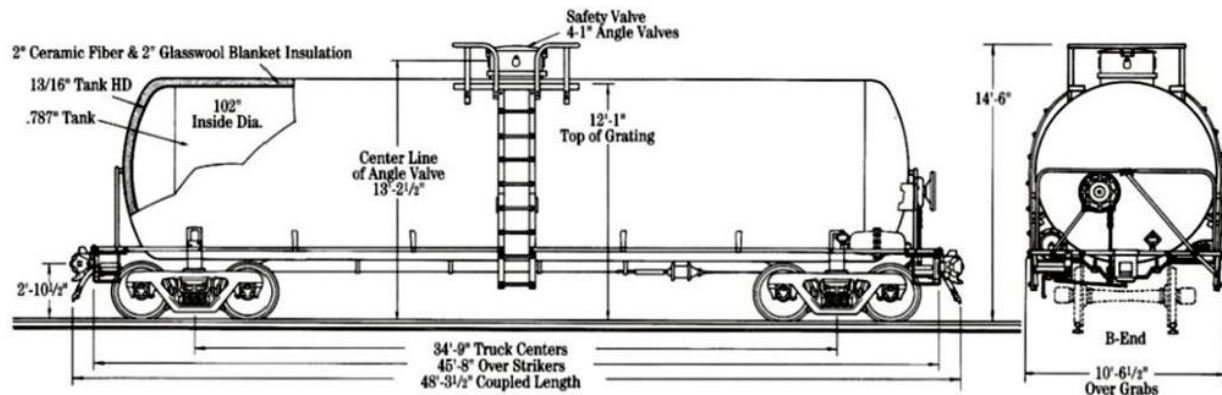
Figure 3. Example DOT-105 Tank Car Design Specification

The certificate of construction for the group of tank cars including the tested DOT-105 listed its full water capacity as 17,360 gallons. The car was designed to carry a commodity having a density of approximately 11.74 pounds per gallon at 68 °F. Since the test used water within the tank, the tank car in the test would be somewhat lighter than a car filled to the same level with the design commodity. The outage for the test conditions was obtained using the loading procedure described in Section 2.2.

2.2 Test Setup

The side impact test was performed on April 27, 2016, at the Transportation Technology Center (TTC) in Pueblo, CO. The test was performed by sending a ram car into the side of a tank car that was mounted on skids and backed by a rigid impact barrier, as Figure 4 shows.

Figure 4. Target Tank Mounted on Support Skids

The tank car structure and all interior welds were visually inspected before the test for any damage or evidence of repair.

Figure 5(a) shows the two skids oriented parallel to the track with one side against the impact barrier that the tank car was placed on. Four sections of I-beams were welded to the tank car and skids for the attachment, as Figure 5(b) shows. The tank car with skids attached was placed on 1-inch steel plates. This test configuration was designed to minimize the test car rollback and allow the tank car on the skids to slide on the steel plates during the impact.

(a) Support skids   **(b) Welded I-beam connection**

Figure 5. Tank Support Skid System

The tank car jacket and shell were not modified in any way. The tank car's ladder would have interfered with the impactor; therefore, it was removed before the test. Water was used as the lading for this test, in lieu of any commodity that would be carried in this type of car. The tank car was filled with water until it was shell full. This capacity was measured as 17,028 gallons. Based on a desired outage of 10.6 percent, 1,805 gallons of water were then pumped out of the tank. The height from the top of the water to the top of the tank was measured to be approximately 16.5 inches. The manhole lid was sealed, and the car was pressurized to 100 psi just before the test.

The indenter was positioned to align with the mid length and mid height of the target tank car as closely as possible. Figure 6 shows the ram car. For this test, a 12- by 12-inch indenter with 1.0-inch radii on the edges and corners was used. The same indenter was used in the impact test of a DOT-111 tank car [3] and a DOT-112 tank car [4], permitting comparison of the results to one another. Additionally, this large indenter was expected to result in a considerable amount of fluid motion (i.e., "sloshing") during the test, requiring careful modeling of the lading to be able to capture this motion.

Figure 6. Ram Car and Head (from previous test)

Figure 7 and Figure 8 shows the 12- by 12-inch indenter attached to the ram car aligned with the tank car. The ram car was weighed before the test to confirm the actual weight. The measured weight was 297,125 pounds.

Figure 7. Ram Arm with 12- by 12-inch Indenter (from previous test)

**Figure 8. Overall Test Setup (left) and Ram Arm with 12- by 12-inch Indenter
Aligned with Center of the Tank Car (right)**

3. Test Instrumentation

The instrumentation installed on the ram car and the tank car included accelerometers, speed sensors, pressure transducers, and string potentiometers. Additionally, conventional-speed and high-speed video cameras captured the impact test from multiple angles. The instrumentation, its placement, and the data acquisition system used in the impact test are described in this section.

3.1 Overview

The test configuration and instrumentation were all consistent with the specifications of the test implementation plan [5]. Table 1 is a list of all instrumentation used for this test. Additional descriptions of the various types of instrumentation are provided in the following subsections.

Table 1. Instrumentation Summary

Type of Instrumentation	Channel Count
Accelerometers	11
Speed Sensors	2
Pressure Transducers	11
String Potentiometers	10
Total Data Channels	**34**
Digital Video	5 Cameras (plus 2 HD for redundancy if time allows)

3.2 Ram Car Accelerometers and Speed Sensors

The local acceleration coordinate systems are defined relative to the ram car. Positive x, y, and z directions are forward, left, and up relative to the lead end of the ram car.

Three triaxial accelerometers were mounted on the longitudinal centerline of the ram car at the front, rear, and near the middle of the car. Two uniaxial accelerometers were mounted on the left and right sides of the car to supplement recording of longitudinal acceleration. The positions of these accelerometers are illustrated in Figure 9. A summary of the ram car accelerometer types and positions are provided in Table 2.
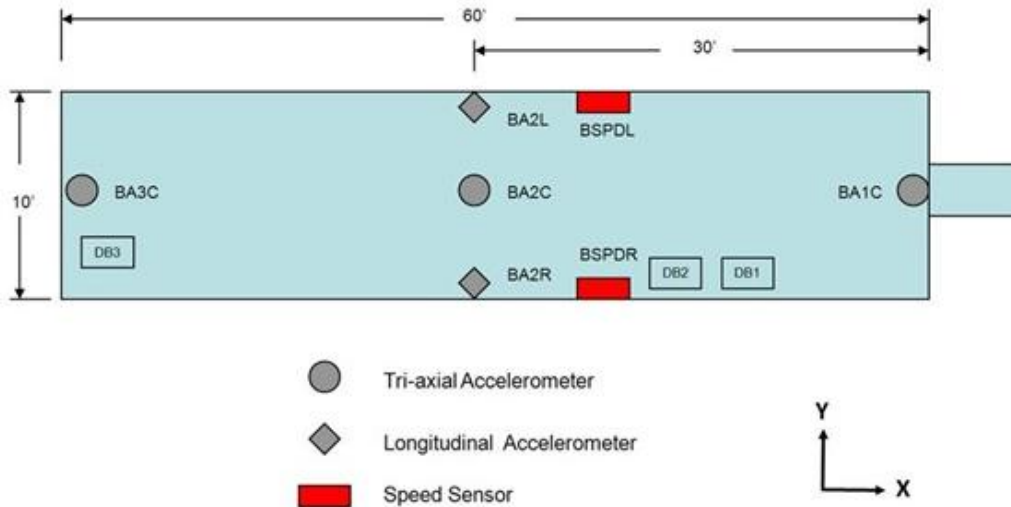
Figure 9. Ram Car Instrumentation

Table 2. Ram Car Accelerometers

Channel Name	Sensor Description	Range
BA1CX	Leading end, Centerline, X Accel	200 g
BA1CY	Leading end, Centerline, Y Accel	100 g
BA1CZ	Leading, Centerline, Z Accel	200 g
BA2LX	Middle, Left Side X Accel	100 g
BA2CX	Middle, Centerline, X Accel	50 g
BA2CY	Middle, Centerline, Y Accel	50 g
BA2CZ	Middle, Centerline, Z Accel	50 g
BA2RX	Middle, Right Side X Accel	100 g
BA3CX	Trailing end, Centerline, X Accel	200 g
BA3CY	Trailing end, Centerline, Y Accel	100 g
BA3CZ	Trailing end, Centerline, Z Accel	200 g

Speed sensors were mounted on both sides of the ram car to provide accurate measurement of the car's speed within 2 feet of the impact point. The speed sensors were reflector-based light sensors, which used ground reflectors separated by a known distance in conjunction with light sensors mounted on the car that triggered as the car passed over the reflector. The last reflector was positioned to align with the sensor when the ram head was within a few inches of the impact point. The time interval between passing the reflectors was recorded, and speed was calculated from distance and time. A handheld radar gun was also used to take supplemental speed measurements.
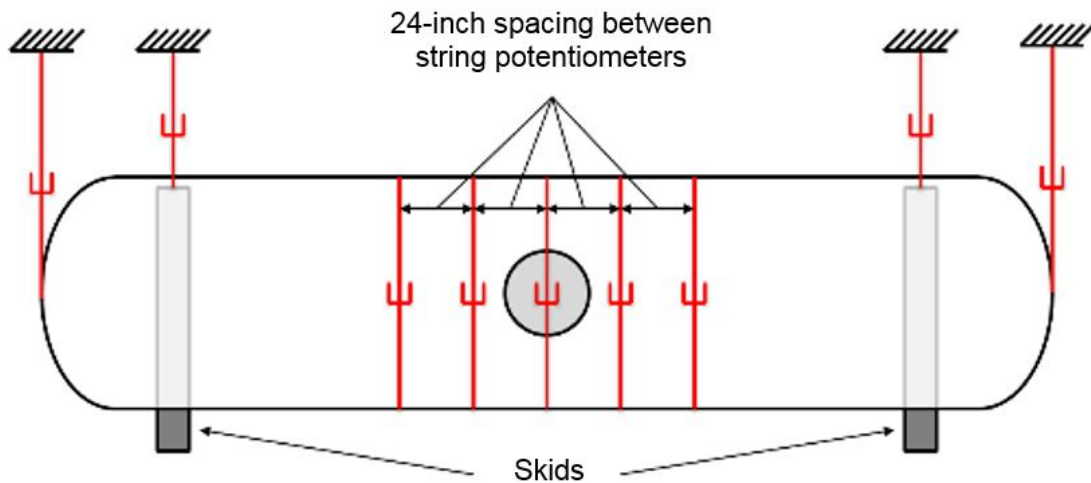
3.3   Tank Car String Potentiometers and Pressure Transducers

The local displacement coordinate systems (except for the tank head) are defined relative to the tank car. Positive x, y, and z directions are forward, left (away from the wall), and up relative to the B-end of the tank car. Tank head displacements are positive toward the impact wall.
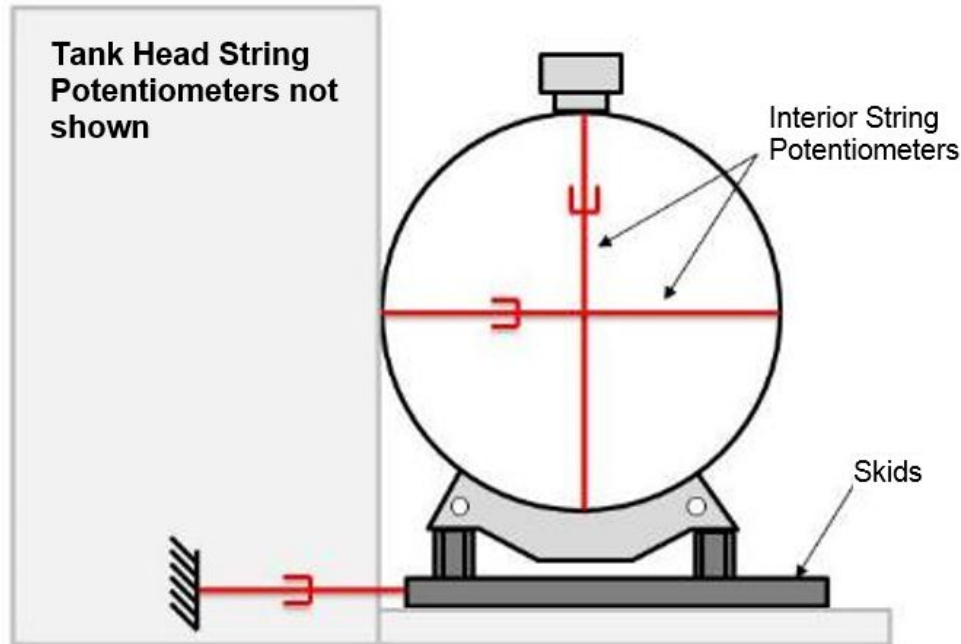
Six string potentiometers were used to measure the tank crush displacements around the immediate impact zone during the test. Five string potentiometers measured the dent formation of the tank at the tank center and at locations 24 inches and 48 inches to either side of the impact point. The sixth string potentiometer measured the vertical deformations of the tank at the center (aligned with the impact point). Four additional string potentiometers were used to measure the tank motions. The string potentiometers were attached to each of the tank skids and to the center of the tank heads at either end of the car. Fixed anchor positions were established so that these measurements are for the longitudinal motions of the tank head and skid movements. Table 3 provides a list of all string potentiometers inside and outside the tank car. Figure 10 and Figure 11 show their placement.

Table 3. Tank Car String Potentiometers

Area	Location	Axis	Channel Name	Range (inches)
Impact Area	A-End – 48-inch offset	Y	TD1Y	40
Impact Area	A-End – 24-inch offset	Y	TD2Y	50
Impact Area	Center	Y	TD3Y	50
Impact Area	Center	Z	TD3Z	40
Impact Area	B-End – 24-inch offset	Y	TD4Y	50
Impact Area	B-End – 48-inch offset	Y	TD5Y	40
Tank Head	A-End	Y	TDAend	50
Tank Head	B-End	Y	TDBend	50
Skid	A-End	Y	TDAskid	50
Skid	B-End	Y	TDBskid	50

**Figure 10. Tank Car String Potentiometers (top)**

**Figure 11. Tank Car String Potentiometers (side)**

Two pressure transducers were mounted on the manhole, one on the pressure relief valve and one to measure pressure in the outage during the impact. In addition, an array of 11 pressure transducers were setup within the tank to record the pressure pulse through the lading. These were mounted in an array along the walls, bottom and top of the tank. The positions of the pressure transducers are shown in Figure 12, Figure 13, and summarized in Table 4.

Table 4. Tank Car Pressure Transducers

Location	Channel Name	Sensor Description	Range (psi)
PR Valve	TPRV	Pressure Relief Valve	500
A Top	TP1000	A-End Top Pressure	300
A Back wall	TP1090	A-End Back Wall Pressure	300
A Front wall	TP1270	A-End Front Wall Pressure	300
A Floor	TP1180	A-End Floor Pressure	300
M Top	TP2000	Mid-length Top Pressure	300
M Back wall	TP2090	Mid-length Back Wall Pressure	300
M Front wall	TP2270	Mid-length Front Wall Pressure	300
M Floor	TP2180	Mid-length Floor Pressure	300
C Back wall	TP3090	Center Back Wall Pressure	300
C Floor	TP3180	Center Floor Wall Pressure	300
C Front wall	TP3270	Center Front Wall Pressure	300
Manhole lid	TPMH	Outage Pressure	500
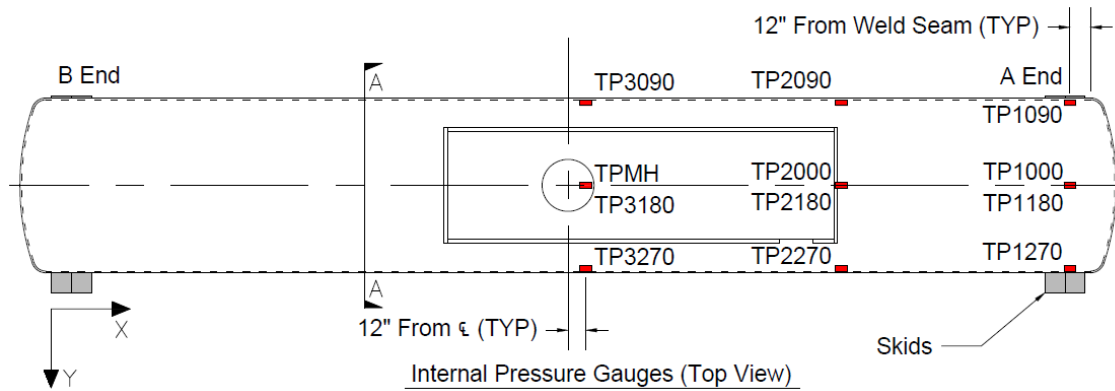
Figure 12. Tank Car Pressure Transducers (top)

Section A-A (Typical Cross Section At Pressure Gauges)
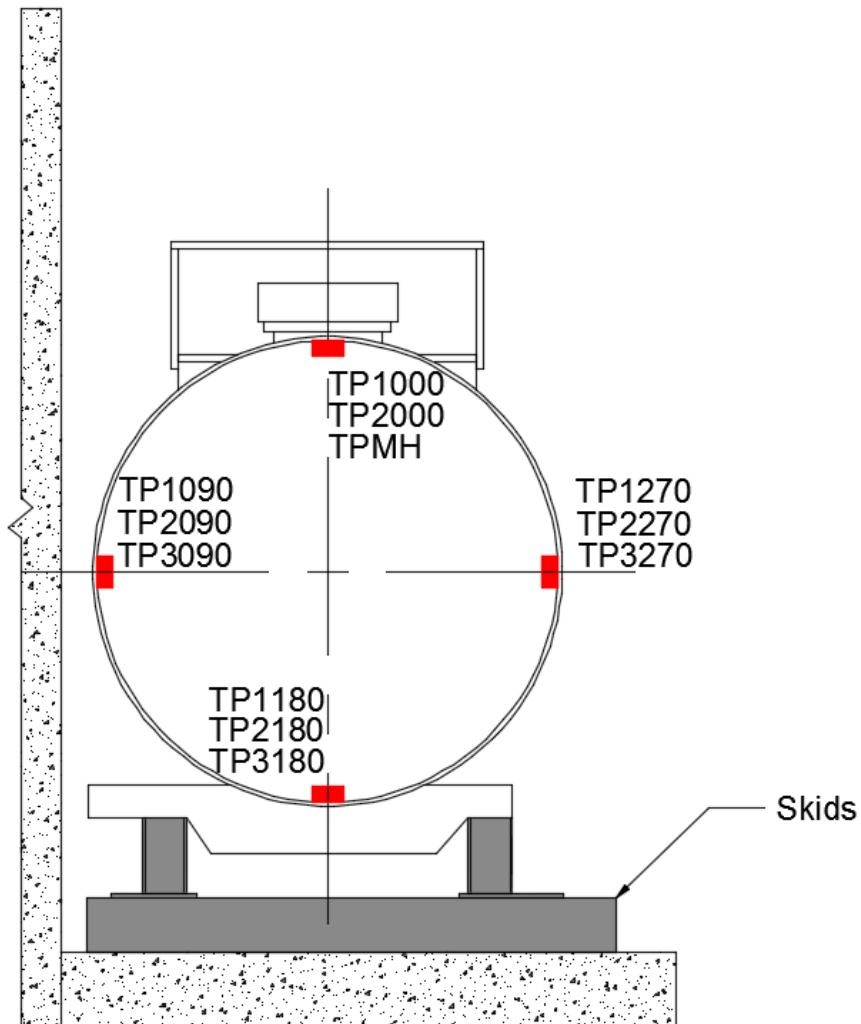
Figure 13. Tank Car Pressure Transducers (side)

3.4 Real Time and High Speed Photography

Three high-speed and two real time high definition video cameras were used to document the impact event. Appendix A contains a schematic of the locations of the cameras and positions of the targets.

3.5 Data Acquisition

A set of 8-channel battery-powered onboard data acquisition systems recorded the data from instrumentation mounted on the ram car. These systems provided excitation to the instrumentation, analog anti-aliasing filtering of the signals, analog-to-digital conversion, and recording of each data stream. A similar set of ground-based data acquisition systems was used to record data from the pressure transducers on the tank car.

The data acquisition systems were GMH Engineering Data BRICK Model III units. Data acquisition complied with the appropriate sections of SAE J211 [6]. Data from each channel was anti-alias filtered at 1,735 Hz then sampled and recorded at 12,800 Hz. Data recorded on the data bricks was synchronized to time zero at initial impact. The time reference came from closure of the tape switches on the front of the test vehicle. Each data brick is ruggedized for shock loading up to at least 100 g. Onboard battery power was provided by GMH Engineering 1.7 Amp-hour 14.4 Volt NiCad Packs. Tape Switches, Inc.'s model 1201-131-A tape switches provided event initial contact.

Software in the data bricks was used to determine zero levels and calibration factors rather than relying on set gains and expecting no zero drift. The data bricks were set to record 1 second of data before initial impact and 4 seconds of data after initial impact.

4. Results

As described in Sections 2.1 and 2.2, this was a side impact test on a DOT-105 tank car, performed on April 27, 2016. As a result of this impact, the tank shell punctured, and a portion of the tank shell was ejected outward. This section describes the results of the test, including the test conditions, the observed impact sequence, a description of the mode of failure of the tank car shell, and the post-test geometry of the tank car. This section also contains a summary of the test measurements, discussion of the post-processing of the raw data, and discussion of the behaviors observable in the test measurements.

4.1 Test Conditions

This test involved a 15.2 mph side impact by a structurally rigid 297,125-pound ram car with a 12-inch square impactor head into the side of the DOT-105 tank car, backed by a rigid impact barrier. The actual impact speed was very close to the target test speed of 15 mph. The test tank car was filled to approximately 89.4 percent capacity with water to simulate standard commodity loading volume of a DOT-105 tank car and pressurized to 100 psi. At the time of the test, the ambient conditions included a wind speed of 3 mph from the southwest, and an air temperature of 50 °F. Prior to the test, the water within the tank had a measured temperature of ~55 °F.

4.2 Details of Test

Pre-test simulations estimated a failure speed range of 14.5 to 17 mph. The most significant influence on this estimated puncture speed range was the assumed material properties of the TC128 making up the tank shell. Since the actual properties of TC128 making up the car shell were not known prior to the test, this range is larger than the range of estimated puncture speeds expected for a known TC128 material behavior. Discussion of how the target test speed was chosen based on pre-test simulations is contained in Section 6.

The tank shell failed in a manner that had not been seen in previous side impact tests [3] [4] [7] [8]. In previous side impact tests where the tank shell did not puncture, the ram car was brought to a stop and rebounded from the tank car, moving away from the tank car until its brakes brought it to a stop. In previous tests where the tank punctured, the ram car continued moving forward due to its excess kinetic energy after the tank lost its ability to resist the impact, resulting in the ram head being embedded within the punctured tank. In this test, elements of both behaviors were observed. The tank ruptured, with a portion of the tank shell being ejected outward. A review of high-speed videos and test data revealed that the ram car was brought to a stop shortly after puncture, and rebounded away from the tank after the impact until its brakes brought it to a stop. Figure 14 shows the impact at an instant just before puncture.

19

Figure 14. Deformed Tank Just Prior to Puncture

Figure 15 shows the damage to the tank car after impact. The jacket is visibly torn, and a portion of the shell was ejected from the car, leaving a large hole in the center of the tank car shell.


Figure 15. Tank Car—Post Impact (impact side)

The tank car recovered a significant portion of energy post-rupture, resulting in a rebound. This behavior was observed in previous non-puncture tests, while previous puncture tests where the ram car did not rebound did not feature a rebound by the struck tank car. Figure 16 shows the post-test position of the tank car relative to the supporting wall.


Figure 16. Tank Car—Post Impact (wall side)

The ejected portion of the tank car shell came to rest on the right side (relative to the ram car's direction of travel) support skid. Figure 17 shows the portion of tank car shell that ejected from the car during the impact, with annotations indicating its approximate dimensions. The portion of the ejected shell facing upwards in this photograph was the internal surface of the tank. Two instrumentation brackets from the internal string potentiometers are visible in this portion of the ejected shell. A lighter area surrounded by a dashed line corresponds to the area of contact between the impactor and the outside surface of the tank car. From this photograph, it is apparent that the path of the fracture included the area of the tank shell under the left-side edge of the impactor.
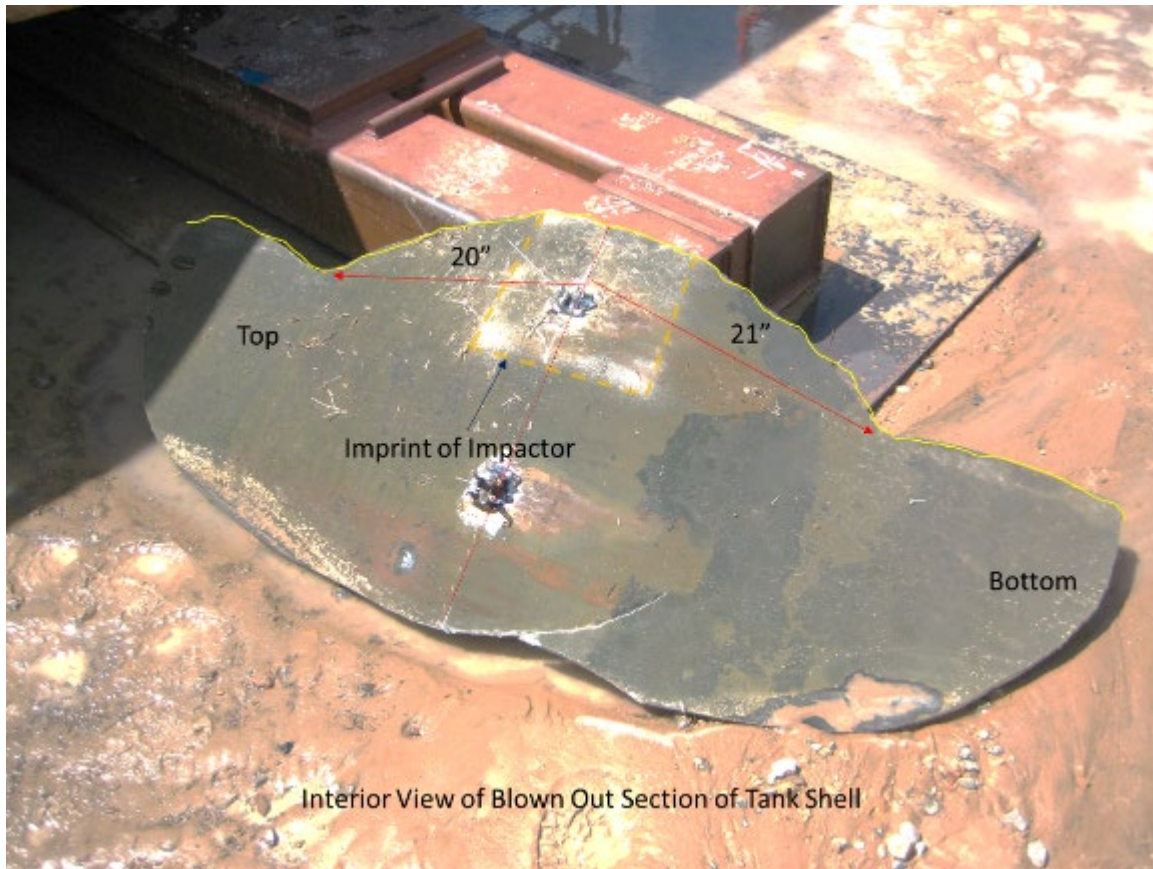
Figure 17. Tank Car Shell Segment Ejected from Tank Car

Figure 18 shows three images of the tank shell after the test. The left-side image shows the hole in the tank immediately after the test, the center image shows the hole in the tank after the jacket and insulation have been removed, and the right-side image shows the geometry of the ejected portion of the shell, taken from the three-dimensional laser scan data.
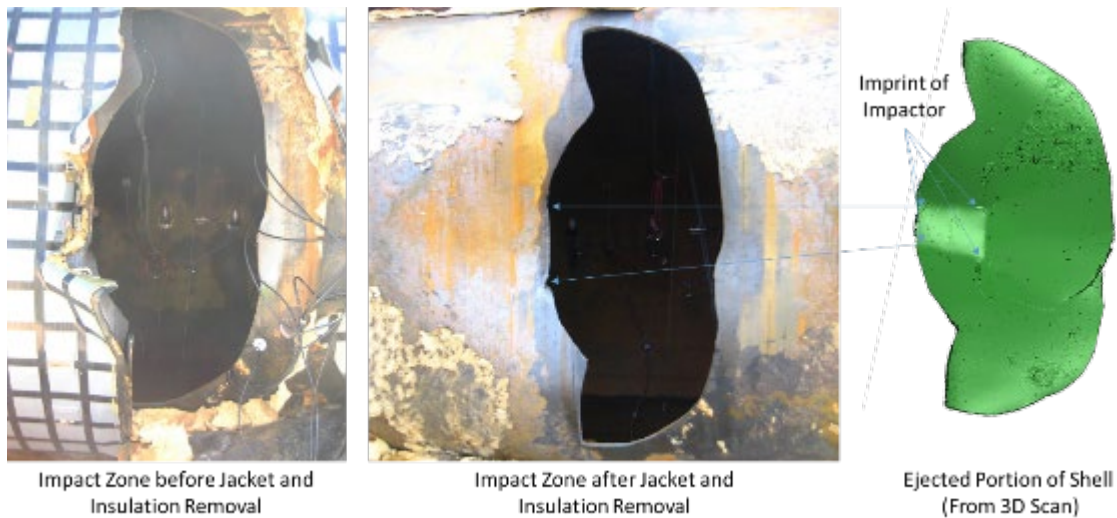
Figure 18. Post-test Photographs of Impact Zone (left), Impact Zone After Jacket and Insulation Removal (center), and Three-dimensional Scan of Ejected Portion of Shell (right)

While the ejected portion of the shell was found outside of the car after the test, this region was first pushed inward during the impact. Post-test examination indicated occurrence of two different modes of shell failure during this test. The initial process of failure is a failure of the tank shell under a corner of the impactor on the left-side edge of the impactor. This is consistent with failure modes observed in previous puncture tests, as well as previous puncture simulations. Figure 19 shows a series of images documenting the fracture surface beneath the left-side edge of the impactor. The left-side images in this figure depict the fracture surface on the intact portion of the tank shell, with inset images providing a detailed view of the areas of highly deformed steel under the corners of the impactor. Close examination of the lower of these two regions revealed a fleck of red paint, apparently from the red-painted tip of the impactor. The right-side images in this figure depict the fracture surface on the corresponding edge of the ejected portion of the shell, with insets showing the approximate locations of the impactor corners. Arrows were drawn on this image to indicate where the impactor corners on the ejected shell portion aligned with the intact portion of the tank shell.

23
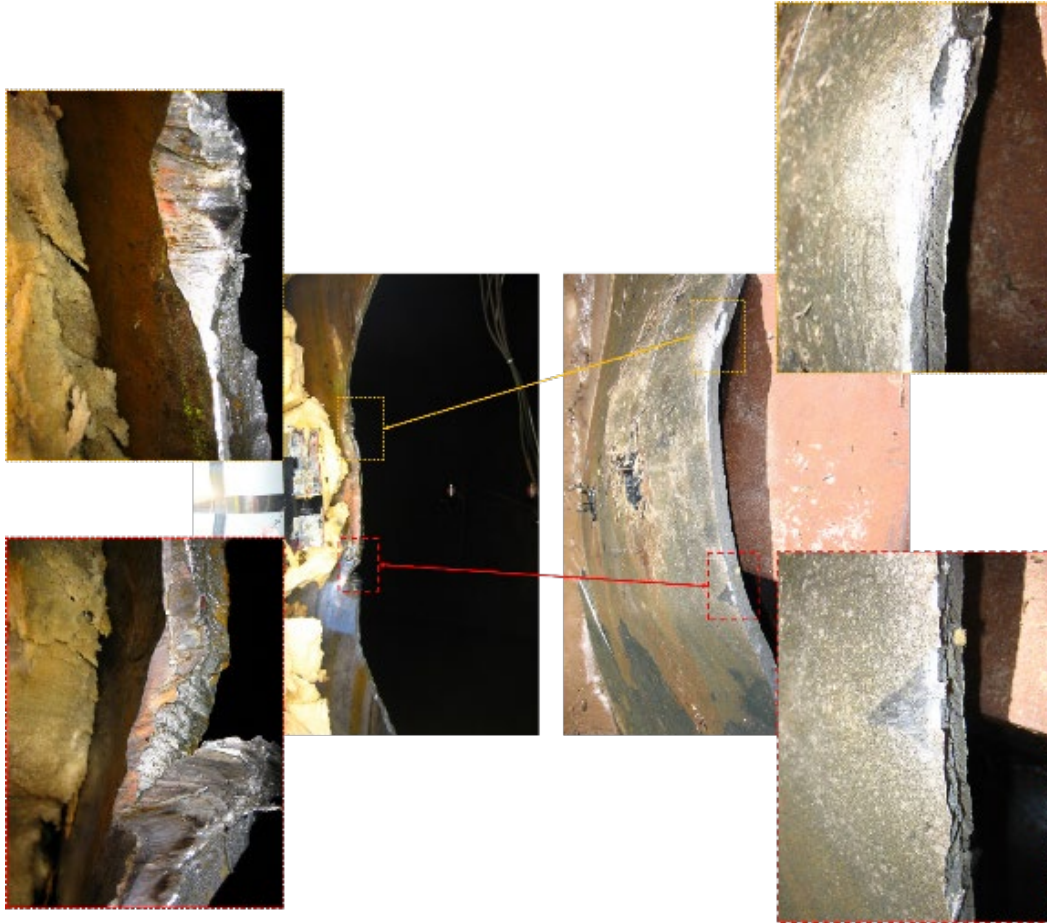
Figure 19. Images of Fracture Surface beneath Impactor Edge on Intact Tank Shell (left) and Ejected Portion of Tank Shell (right)

Following the initial failure, the internal pressure of the tank pushed back on a now-compromised vessel. Since the impactor had so little excess kinetic energy in this test, the ram car did not continue to push the tank shell back within itself. Rather, the internal pressure continued to push outward on the compromised shell, causing the fracture to expand. In turn, the compromised shell pushed outward against the ram car. The internal pressure of the tank caused the shell failure to spread outward from the initial puncture under the corners of the impactor. Since the ram car was brought to a stop shortly after puncture initiated, the internal pressure of the car was able to force the failed portion of the shell to eject outward, rather than being pushed into the tank by the ram car's excess momentum.

A series of photographs were taken of the fracture surfaces on the tank car shell itself. Figure 20 shows the hole in the side of the tank car after the test, with three inset images featuring details of the fracture surface in three areas. On both the left and right sides of the hole, a series of photographs were assembled into composite images to show the scope of the fracture surface at different heights. This composite image was assembled to help explain how the observed damage around the hole in the tank shell provides evidence for the sequence of fracture propagation. The sequence of fracture propagation was determined from careful examination of the fracture surface on the tank shell. This composite image provides documentation of what was observed at the fracture surface on the remaining portion of the tank shell.
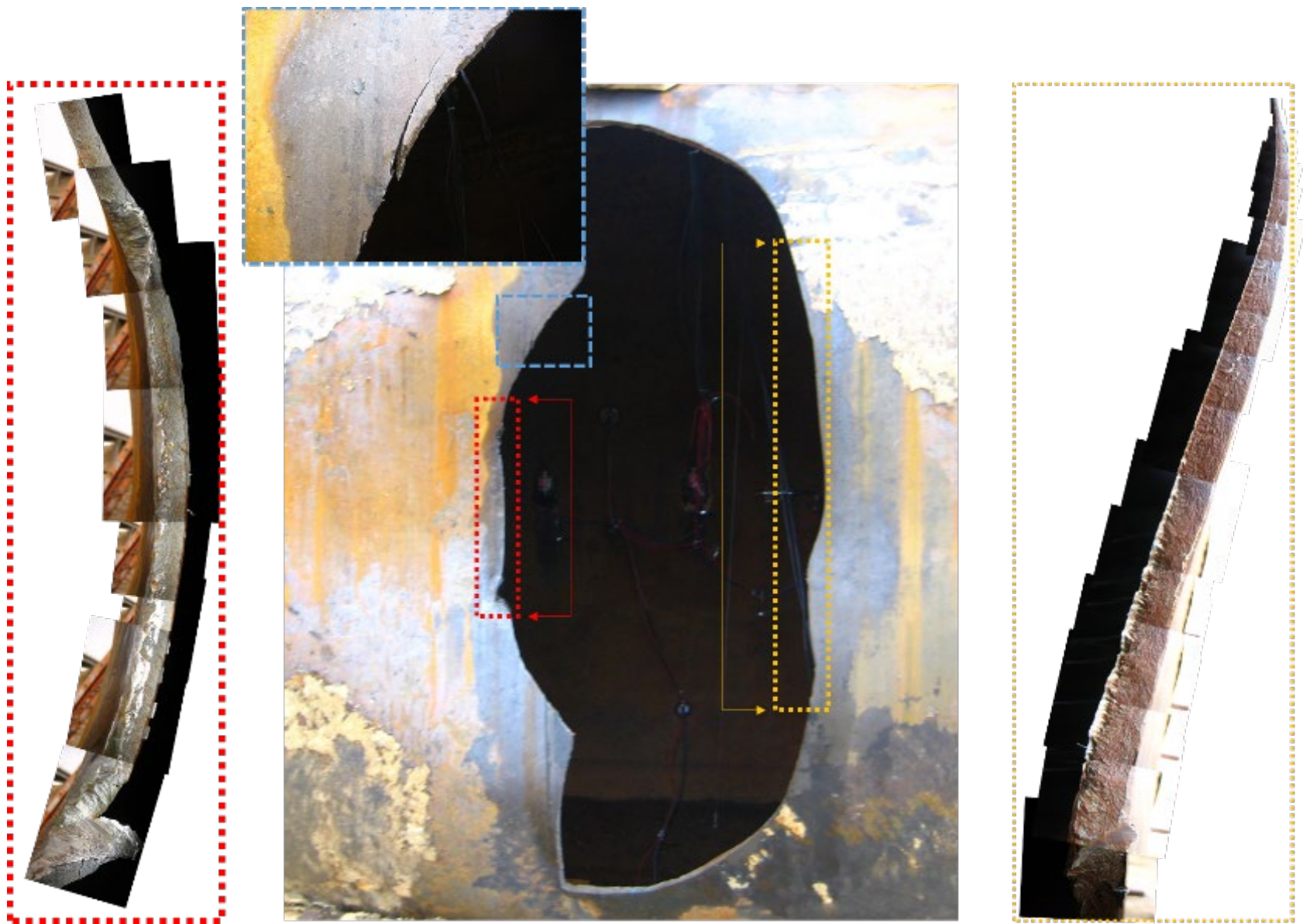
Figure 20. Composite Images Showing Fracture Surfaces on Tank

In the smaller of the two composite images (left side, red frame) two regions of highly deformed material are apparent. These two regions correspond to the top and bottom corners of the left-side of the impactor. Outside of this region, the tank shell exhibits very little evidence of through-thickness deformation in the fractured areas.

On the right side of the tank (yellow frame), the puncture does not correspond to a region in contact with the impactor. This region also exhibits relatively little through-thickness deformation on the fractured surface remaining on the tank car. This side of the fractured portion of the shell failed due to internal pressure on the compromised shell after the puncture had initiated under the impactor. Thus, the second failure may be thought of as the tank rupturing (breaching due to internal pressure) rather than puncturing (breaching due to external impact).

Finally, there was a third area of fracture observed above the left-side impact zone where the fracture appeared to begin to branch into the tank shell, but the failure did not propagate fully in this direction.

TTCI performed additional steel microstructure analysis. Three samples were taken from the ring of puncture for the analysis. Several photographs with different magnification were taken from each of the samples. Inspection of the photographs found no abnormal steel grain microstructure. Figure 21 shows example photographs of steel microstructure from one of the samples. Photographs from all samples are in Appendix B5.
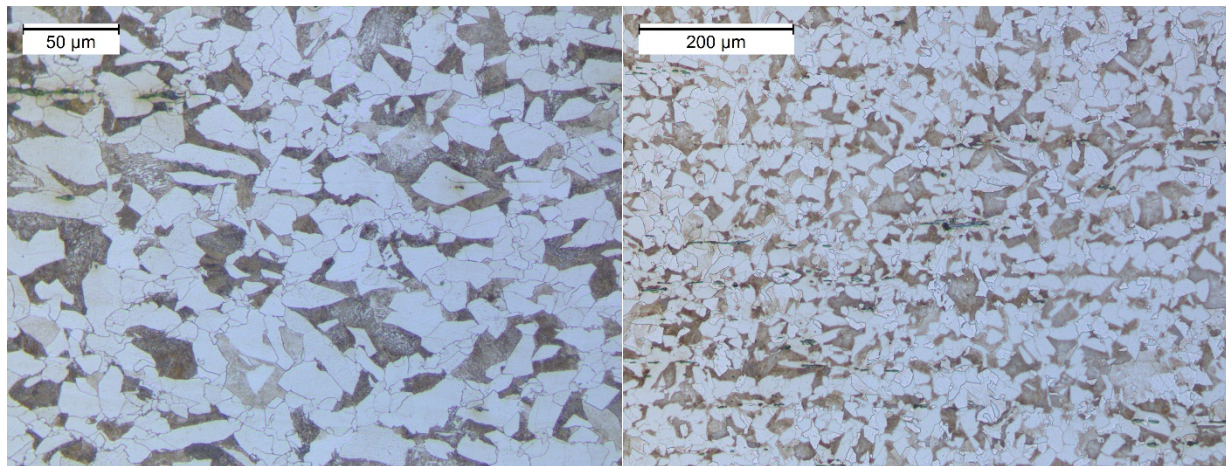

Figure 21. Steel Microstructure

4.3   Measured Data

The data collected in the test was processed (offset corrections, filtering, etc.) initially by TTCI and provided to Volpe for comparison to analyses. The offset adjustment procedure ensures that the data that is plotted and analyzed contains only impact-related accelerations and strains and excludes electronic offsets or steady biases in the data. To determine the necessary offset, the data collected before impact was averaged. This offset was then subtracted from the entire data set for each channel. This post-test offset adjustment is independent of, and in addition to, the pre-test offset adjustment made by the data acquisition system.

The post-test filtering of the data was accomplished with a phaseless four-pole digital filter algorithm consistent with the requirements of SAE J211 [6]. A 60 Hz channel frequency class (CFC) filtering was applied for the filtered acceleration data shown in this report. A summary of the measured data is provided in this section. Appendix B contains the plots of filtered data from all transducers.

The longitudinal acceleration of the ram car was one of the primary measurements in the test, and multiple accelerometers were used on the ram car to capture this data. The ram car acceleration was used to derive the impact energy, deceleration of the ram car, and contact forces between the ram car and target tank car. The ram car average longitudinal acceleration history from all the ram car accelerometers shown in Figure 22.
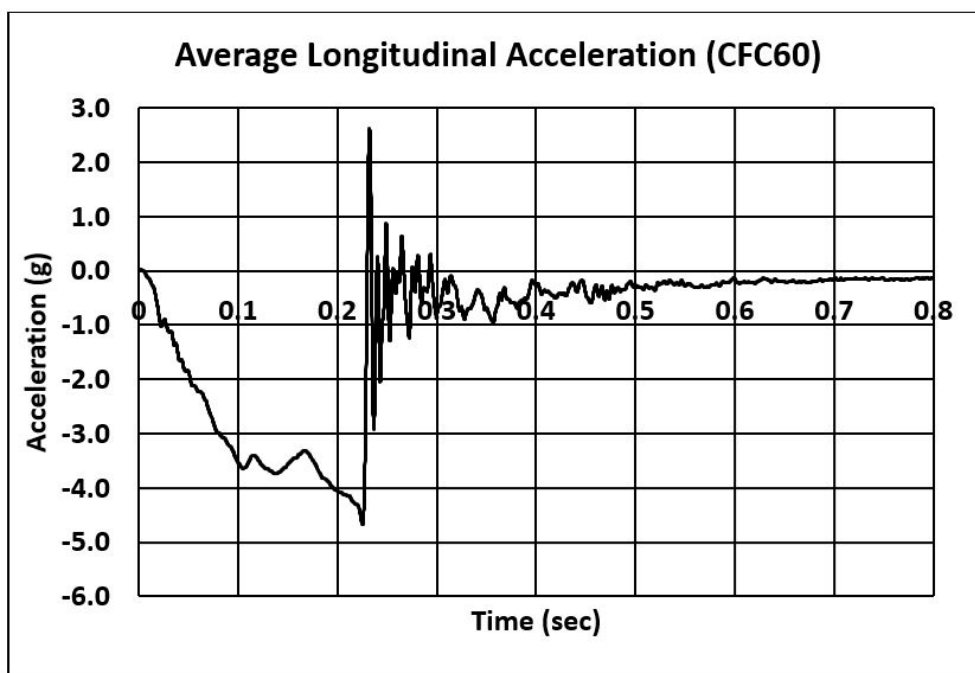
Figure 22. Longitudinal Acceleration Data (Averaged)

The maximum measured deceleration was approximately 4.7 g. Deceleration drops to 0 at approximately 0.23 of a second after the initial impact.

The ram car velocity history in the test can be calculated by integrating the average longitudinal acceleration of the ram car and using the impact speed measurement as an initial condition. Contact forces between the ram head and target tank car can be calculated as a product of the average acceleration and mass of the ram car. Figure 23 shows both the force-time and velocity-time histories, where negative velocity is the speed of rebounded ram car. This data shows that the ram car was traveling at less than 1 mph at the time of the force drop that corresponds to puncture.
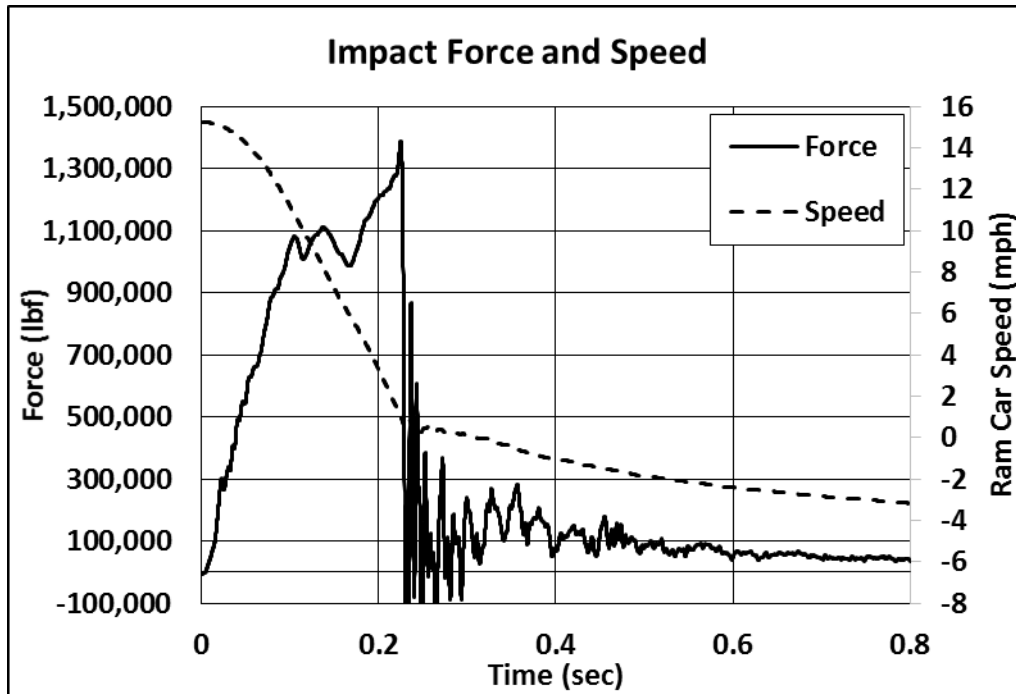
Figure 23. Impact Force and Ram Car Speed

Similarly, a kinetic energy was calculated for the ram car from the speed-time history and weight. Figure 24 shows the kinetic energy time history of the ram car and energy absorbed by the tank car. The absorbed energy by the tank car is capped at the time of the maximum force when the puncture occurred, at approximately 0.225 of a second.
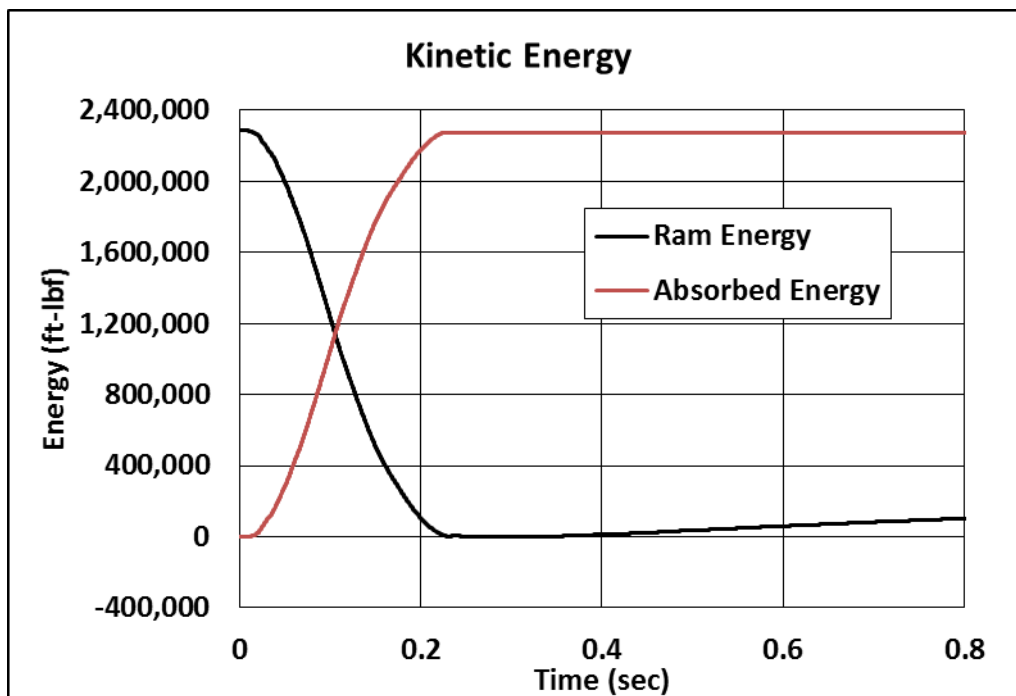

Figure 24. Kinetic Energy

The total kinetic energy of the ram car was approximately 2,287,000 ft-lbf and the energy absorbed by the tank car before puncture 2,274,000 ft-lbf. The difference between the initial kinetic energy and the energy absorbed by the tank before puncture was only 13,000 ft-lbf of excessive energy, or only 0.6 percent of the total kinetic energy.

Another significant impact response measured in the test is the effects of the internal pressure as the tank indentation forms and reduces the volume of the tank. The tank is initially pressurized at 100 psi relative to atmospheric pressure. Additionally, the tank was filled to an approximately 10.6 percent outage volume with water, which can be approximated as incompressible for the impact behavior. As a result, the gas volume in the outage was compressed as the dent formation reduced the tank volume and the internal pressure increased. As described in Section 3.3, pressure transducers were mounted at several locations in the tank within the water and at the pressure release valve within the air.

Figure 25 shows pressure data from the center of the tank car (i.e., transducers TP3090, TP3180, TP3270, and TPMH). The comparison of pressure data shows that the pressure was dominated by the average hydrostatic pressure developed from the denting and volume change. However, there were additional dynamic pressures caused by the sloshing motions of the water in the tank that added local pressure variations that can be up to approximately 110 psi different from the average value. The impact increased the hydrostatic pressure by approximately 40 psi, with the maximum pressure occurring at the time of puncture. After the puncture, the TP3090 was pulled together with the cable by the ejected portion of the tank shell, causing significant reading noise on most of the gages. The only pressure gage that had a steady reading throughout the test was the TPMH measuring the outage pressure at the center. This is because this transducer was attached to outside of the of the manway lid and was unaffected by the puncture.
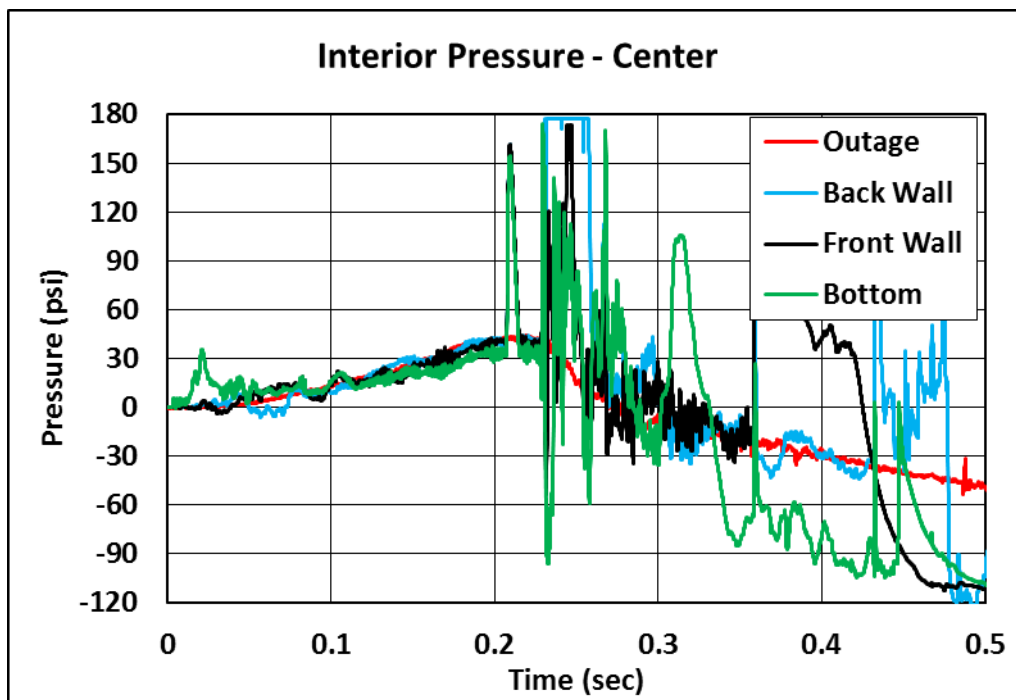

Figure 25. Pressure Data Measured at the Center of the Tank Car

29

The remaining quantitative measurements made of the tank impact behavior were displacement histories recorded with string potentiometers. These included both internal tank deformations and external tank movements at both ends of the tank. Layout of the string potentiometers is described in Section 3.3.

The measured displacements for the tank internal string potentiometers (TD1Y through TD5Y) are shown in Figure 26. Overall, the data shows consistent measurements of the tank deflections with the largest deflection at the impact and reduced displacements at distances further from the center of the impact indentation. In general, there is good agreement between the transducers at the same distance from the impact center on different sides of the impact. The gage TD1Y appeared to have experienced a malfunction, as the sharp spikes in the data are not consistent with a physical behavior. Figure 27 shows vertical displacement of the shell inside the tank car at the mid-length cross-section. The spike in displacement after 0.2 second is believed to be caused by a water flow after the puncture or cables that were pulled with the sensors on the ejected section of the shell.
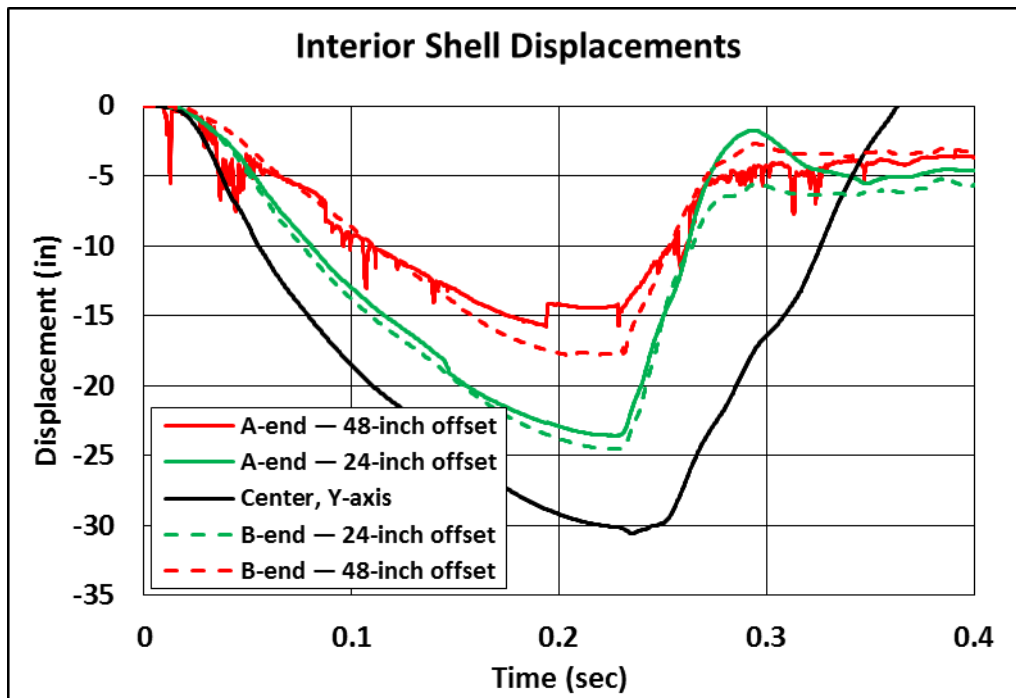
Figure 26. Internal Horizontal Displacements
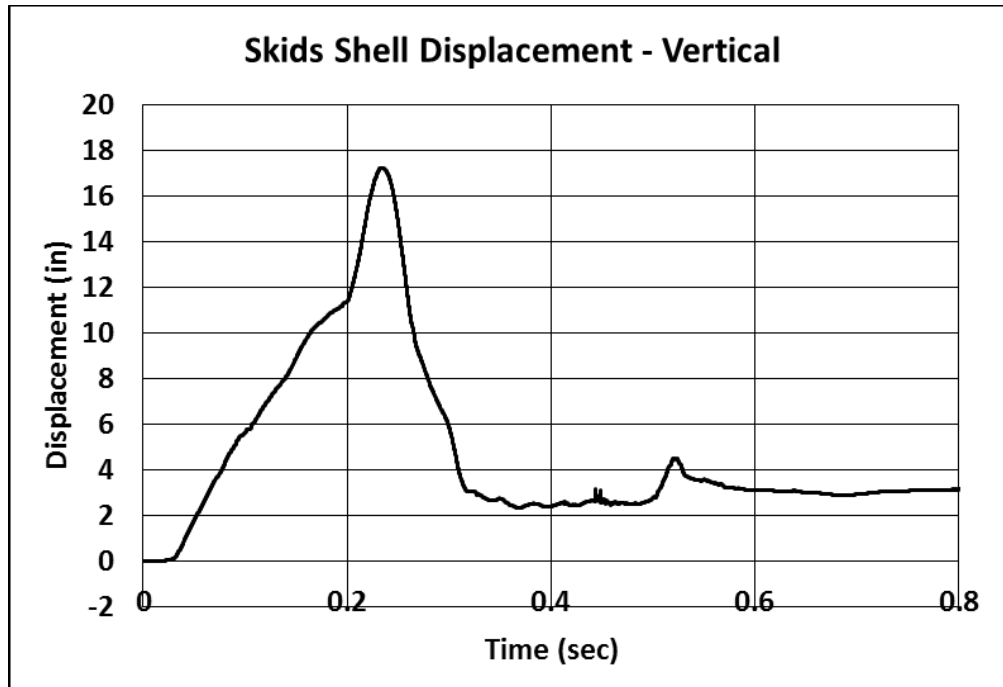
Figure 27. Internal Vertical Displacement

The measured displacements for the tank end external string potentiometers are shown in Figure 28 and Figure 29. The displacements of the car ends were delayed from the motions in the impact zone, and little displacement is seen for the first 50 milliseconds of the response. Note that the measurements of the car end head displacements and the skid displacements are nearly identical and the response is very symmetric between the A-end and B-end of the tank until rebound occurred approximately 0.3 second after impact. For both the head and skid measurements, the A-end experienced a slightly larger displacement than the B-end.

31
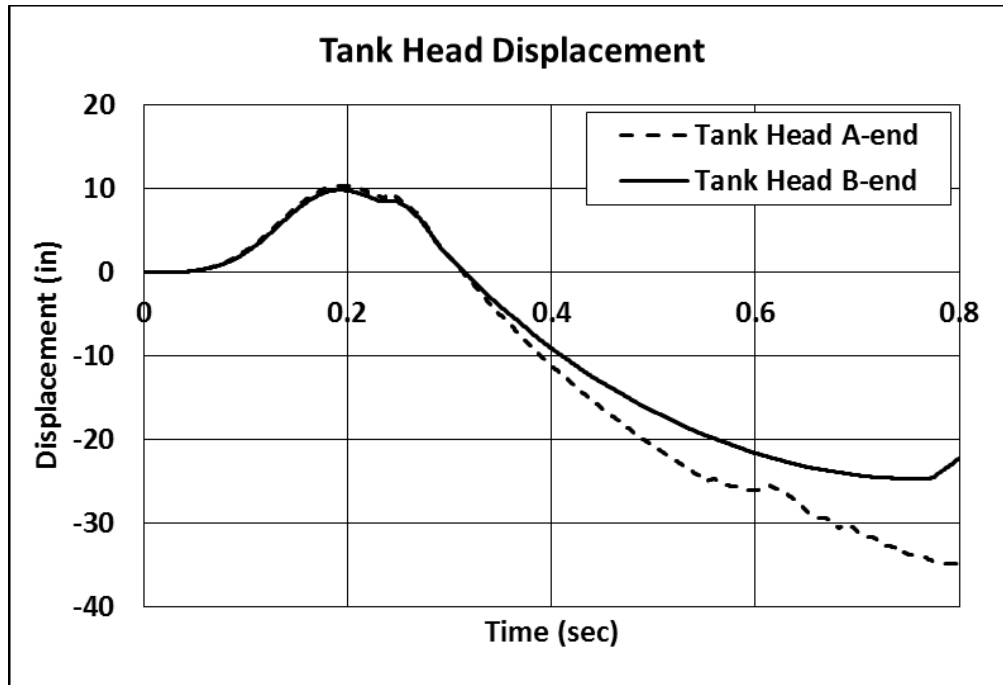
Figure 28. External Displacements—Tank Car Heads
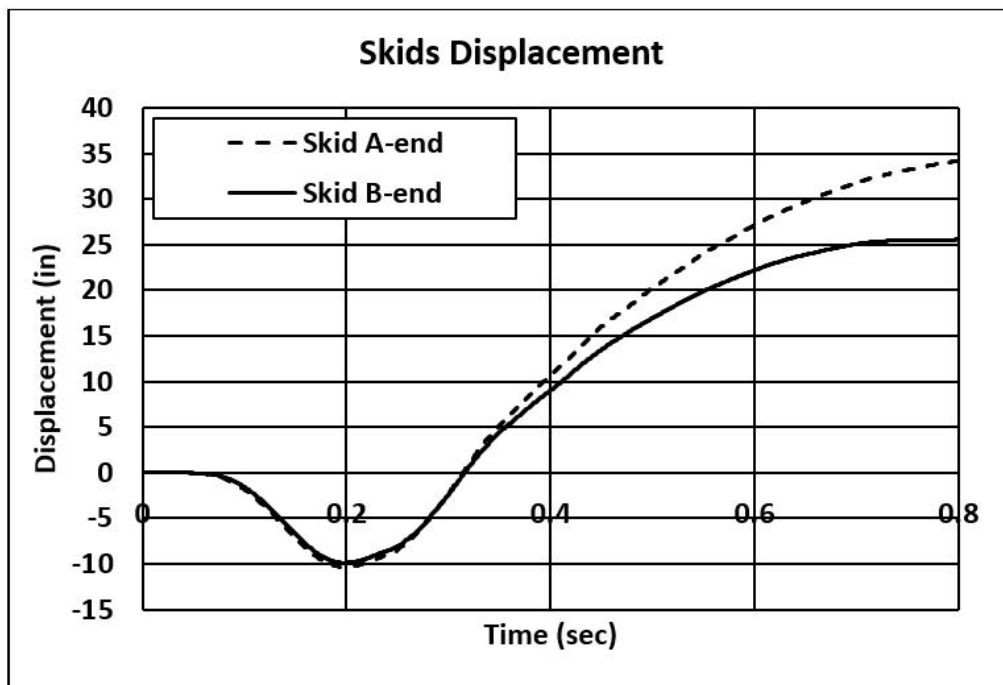
Figure 29. External Displacements—Skids

After the test, TTCI used a Light Detection and Ranging-based measurement system to scan the geometry of the tank car to capture the three-dimensional geometry of the deformation pattern. Additionally, TTCI used a separate scanning system with a higher resolution to capture the

32

geometry of the ejected portion of the tank car shell. The scanned geometry of the tank car itself is shown in Figure 30, and the geometry of the ejected portion of the shell is shown in Figure 31.
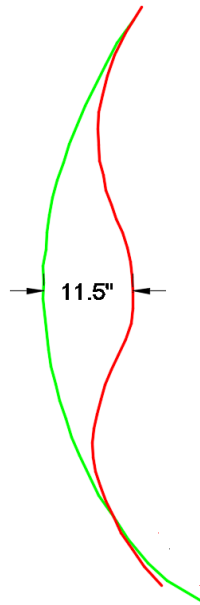
Figure 30. Scanned Geometry of Tank Car—Center Cross-section

Figure 31. Scanned Geometry of Ejected Panel Segment

5. FE Model Development

FE models of the DOT-105 tank car were used before the test to help plan the instrumentation placement and estimate the desired impact speed. Volpe developed the FE models, which incorporated and expanded upon several modeling techniques that were used during simulations of previous tank car impact tests [7] [9] [10] [11]. The DOT-105 tank car models required definition of the tank car geometry, geometry of the impact setup (e.g., impact wall, impactor, etc.), definition of boundary conditions, constraints, and initial conditions, and development of several material models. Additionally, modeling techniques such as element types, mesh sizes, and fluid/structure interactions were selected.

Following the test, two changes were introduced to the pre-test models to improve their agreement with the test results. The first change was to replace the pre-test TC128 behavior with a material response developed using post-test material coupon test results. The second change was to include the foam insulation between the tank and jacket into the post-test model. Those changes are discussed in Section 7. The purpose of the post-test model was to more closely approximate the actual conditions of the test, and to achieve improved agreement between the test and FEA results. The post-test models were also run at the measured test speed of 15.16 mph.

5.1 Overview of Models

The pre-test and post-test FE models are made up of geometry representing the different components in the test setup, material parameters describing the behavior of the materials making up the car and its lading, and numerous constraints, boundary conditions, and loads describing the conditions of the test. As a part of both the pre- and post-test modeling studies, non-puncture models were developed along with puncture-capable models. Non-puncture models featured a simplified material behavior, where the tank and jacket featured only elastic-plastic material responses, not ductile failure behaviors. Since the material definitions in the non-puncture models were not capable of simulating puncture, coarser meshes were used in the impact zones of these models in the interest of reducing model runtime. The non-puncture models were useful for investigating several parameters, including insulation behavior, before implementing any new behavior in the more complex puncture models.

In addition to featuring more complex material definitions capable of simulating element degradation and removal, the puncture-capable models featured refined meshes on the tank and jacket in the areas of contact with the impactor. For the tank, this refined area was meshed using solid elements, while the much thinner jacket featured a refined shell mesh. All FE results presented in this report were obtained using puncture-capable models.

All models (pre-test, post-test, puncture, and non-puncture) used a half-symmetric condition, with a vertical-longitudinal symmetry plane at the centerline of the tank car to reduce the size of the model. The tank geometry was simplified, with structures such as the bolster omitted. These simplifications have a relatively minor effect on the impact response of the tank under the test conditions. The pre-test model is shown in Figure 32.
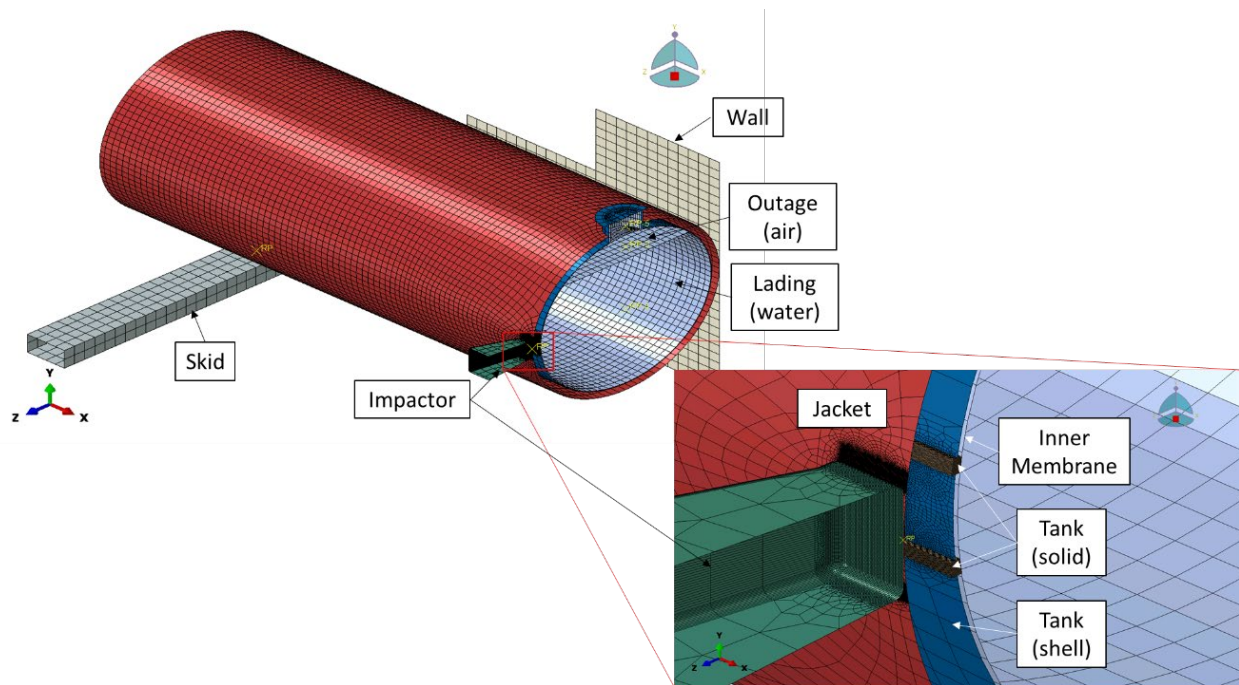
Figure 32. Annotated Pre-test FE Model

The models were developed using the Abaqus/CAE preprocessor and executed in Abaqus/Explicit [12]. Abaqus/Explicit is a commercially available, general purpose nonlinear FE solver capable of simulating dynamic impacts involving complex material behaviors such as plasticity and puncture. The Abaqus software also includes several modeling techniques to represent the water and air phases of the lading, permitting these two parts to be modeled explicitly. The simulation techniques used in the DOT-105 tank car models included modeling an elastic-plastic material response for the tank and jacket, ductile failure implementation of the Bao-Wierzbicki (B-W) triaxiality-based damage initiation model, and modeling of the water and air phases within the tank. Following the test, the model underwent several adjustments to obtain better agreement between the test results and the FE results based on the conditions of the test. The FE models were run for sufficient time to capture the impact event from first contact through puncture of the tank, or until the impactor rebounded in case of a non-puncture result.

The impact conditions for the test, and therefore the FE model, were chosen specifically to permit comparison between this test and the 2013 test of a DOT-111 tank car [3] and the 2014 test of a DOT-112 tank car [4]. As previously described, the 12-inch by 12-inch impactor was used in this DOT-105 tank car impact test and in the DOT-111 and DOT-112 tests. Previous shell impact tests on DOT-105 tank cars have used a 6-inch by 6-inch impactor [7] [10], or used a 12-inch by 12-inch impactor in conjunction with a protective panel installed on the tank car [8]. Therefore, this test was the first shell impact test of an unmodified DOT-105 tank car to use the 12-inch by 12-inch impactor.

The air and water phases of the lading were each modeled using a fluid cavity modeling approach. Previously, a smoothed particle hydrodynamics (SPH) modeling approach was used to model the air phase of the DOT-112 test, with Lagrangian formulation for the water phase [4]. For this DOT-105 tank car test, a hydraulic cavity was defined for the water phase, with a pneumatic cavity defined for the pressurized air phase. The cavity approach is a simplified

36

modeling technique that represents the fluid species (either gas or liquid) using an average pressure over the entire volume. This average pressure will change over the course of the impact simulation, as the volume enclosing the pneumatic cavity is reduced through tank deformation. This dual-cavity approach to fluid modeling gave satisfactory representation of the fluid response seen in this test, while offering considerable computational efficiency over an explicit representation of the liquid phase.

5.2 Summary of the Assembly

The parts making up the model can generally be divided into three categories: rigid bodies, deformable bodies made of steel, and deformable bodies made of other materials. Since the model was half-symmetric, the part weights in the FE model generally correspond to half of the weight of the actual tested geometry. The exception to this is the skid, as the skid exists entirely to one side of the symmetry plane. Therefore, the full weight of the skid is included in the model. Table 5 contains a summary of the parts making up the FE model used in puncture-capable simulations. This table contains the weight of the part in the model, as well as the weight of the full part (2x model weight) for applicable parts. A full description of each part can be found in Appendix D.

Table 5. Summary of Parts in FE Models

		Number of Elements	Part Weight (in model)	Part Weight (Full)
		-	lbf	lbf
Rigid Bodies	Impactor	7,354	148,562.5	297,125
	Rigid Wall	442	N/A	N/A
	Skid	361	3,500	3,500
Deformable, Steel	Jacket	36,520	3,323	6,646
	Tank (Shell Elements)	8,668	19,420.5	38,841
	Tank (Solid Elements)	47,538	7.6	15.26
Deformable, Non-steel	Internal Membrane	9,560	66,650.1	133,300.2
	Foam Insulation (post-test model only)	44,498	419.6	839.2

5.3 Material Behaviors in FE Models

Four material definitions were used in both the pre-test and post-test FE models without adjustment: A1011 steel, an internal membrane, water, and air. A fifth material, TC128 steel, was modeled using different properties in the pre-test and post-test models. The material properties input to the FE models are summarized in this section. Complete descriptions of the

development of the A1011 and TC128 characterizations are given in Appendix F. A post-test model including a material characterization of the foam insulation between the tank shell and jacket was also developed. The development of the foam insulation model is also described in Appendix F.

5.3.1 Membrane

As described in Appendix D7, an artificial surface was modeled within the tank to define the limits of the hydraulic and pneumatic cavities. Since this surface does not correspond to any physical structure within the tank, modeling techniques were chosen to minimize the increase in either mass or stiffness introduced into the model by the membrane. Additionally, the membrane material was modeled as having the same mass density of steel to avoid the minimum time increment becoming dominated by the artificial material in the membrane. The material properties of the membrane are summarized in Table 6.

Table 6. Material Properties Defined for Membrane Material

Parameter	Value
Density	0.00073499 lbf * s^2/inch
Modulus of Elasticity	30,000 psi

Additionally, a nonstructural mass was added to the membrane part to account for the mass of the water within the tank. This nonstructural mass is described further in Appendix D7.

5.3.2 A1011

The outer jacket was presumed to be made of A1011 for the tested DOT-105 tank car. The material properties defined for the A1011 material were derived from behaviors described in "Detailed Puncture Analyses of Various Tank Car Designs: Final Report – Revision 1" [7]. A full description of the development of the material parameters is provided in Appendix F3. These parameters are summarized in Table 7.

Table 7. Summary of Material Parameters for A1011

Parameter	Value
Modulus of Elasticity	3 x 10^7 psi
Plasticity	Piecewise nonlinear (see Appendix F3)
Poisson's Ratio	0.3
Mass Density	7.35 x 10^{-4} lbf-s^2/inch
Damage Initiation	B-W Envelope (see Appendix F3)
Damage Progression	Linear, 1,500 in-lbf/in^2
Mesh Implementation	0.04 inch Fully integrated shell (S4) Elements

5.3.3 Water

The liquid phase of the lading was modeled as water at approximately 55 °F. Within Abaqus, a hydraulic cavity model was used to describe the behavior of the liquid water. The key material properties that must be input to the model are the material's density and its bulk modulus. Values for density and speed of sound were obtained by interpolating published tabular values to

the anticipated test temperature of 55 °F. Initial conditions are discussed further in Appendix E7.
The bulk modulus of a fluid can be determined from speed of sound and density according to
Equation 1.

Equation 1. Calculation of Bulk Modulus

$$K = c_0^2 \rho \text{ [13]}$$

The properties used in the DOT-105 tank car model are shown in Table 8. This table includes
both nominal units and the specific units used in the unit system of the FE model.

Table 8. Properties of Water Used in FE Models

Property	Value (nominal units)	Value (input to Abaqus)
Density (ρ)	999.28 [14] $\frac{kg}{m^3}$	$9.41 \times 10^{-5} \frac{lbf \cdot \frac{s^2}{in}}{in^3}$
Speed of Sound (c_0)	1456.44 [15] $\frac{m}{sec}$	$57,340.3 \frac{inch}{sec}$
Bulk Modulus (K)	-	$309,500 \frac{lbf}{in^2}$

While density is among the parameters defined for the water in the hydraulic cavity, this value of
density is only used by the solver to calculate the bulk modulus of the liquid in the hydraulic
cavity. Thus, an additional nonstructural mass was added to the membrane part to account for
the mass of the water within the tank. This nonstructural mass is described further in Appendix
D7.

5.3.4 Air

The gas phase of the lading was modeled as air at a gauge pressure of 100 psi, as this was the
desired internal pressure for the tank car during the test. Within Abaqus, a pneumatic cavity
material model was defined to allow the pressure within the air to change in response to changes
in outage volume as the tank deformed and the water moved through the outage. Note that in
addition to the material properties defined for the cavity, ambient pressure, initial pressure, and
initial temperature values needed to be defined for the cavity. Initial conditions are discussed
further in Appendix E7. The pneumatic cavity approach used in the model required definition of
the universal gas constant, the molecular weight of the air, and the molar specific heat capacity.
The universal gas constant and molecular weight properties are given in nominal units as well as
the specific units required for the FE model of the DOT-105 tank car in Table 9.

Table 9. Properties for Air

Property	Value (nominal units)	Value (input to Abaqus)
Universal Gas Constant (R)	$8.3144\,[16]\,\frac{J}{mol \cdot K}$	$73.583\,\frac{in \cdot lbf}{mol \cdot K}$
Molecular Weight (MW)	$28.97\,[17]\,\frac{kg}{kmol}$	$1.654 \times 10^{-4}\,\frac{\frac{lbf \cdot s^2}{in}}{mol}$

The molar specific heat for air was calculated according to Equation 2.

Equation 2. Calculation of Molar Specific Heat

$$C_{pmolar} = C_p \times MW$$

Values for the specific heat capacity of air (C_p) were obtained from published values [18]. Table 10 shows the calculated values for molar specific heat at different temperatures that were defined as inputs to the FE models in the unit system used in the FE models.

Table 10. Molar Specific Heat for Air

Temperature (K)	C_{pmolar} $\dfrac{in \cdot lbf}{mol \cdot K}$
250	257.2
300	257.7
350	258.5
400	259.7

5.3.5 TC128

One purpose of this test was to subject the tank car to a moderately high speed impact that was close to the threshold speed between a puncture and a non-puncture test. While it was known from the certificate of construction that the tank was manufactured from TC128 Grade B steel between 1979 and 1980, the actual stress-strain response of the steel making up the car's shell was not known. The minimum mechanical properties of TC128 that were required at the time of the car's construction are shown below in Table 11 [19].

Table 11. Minimum Properties for TC128B

Property	Value
Yield Strength	50,000 psi
Ultimate Tensile Strength	81,000 psi
Elongation at Failure	22% (2-inch gauge)
Elongation at Failure	16% (8-inch gauge)

One purpose of the pre-test models was to provide an estimate of the speed range where puncture could be expected to occur. Based on a review of the mechanical properties of TC128 from tank

cars of a similar vintage [20] and previous material characterizations of TC128 samples [7], two TC128 material response characteristics were developed for pre-test modeling. These characteristics were intended to represent a material that slightly exceeded the minimum ductility requirement for TC128 (i.e., New Normalized TC128), and to represent a TC128 sample that greatly exceeded the ductility requirement (i.e., Test 2 TC128). It was expected that by modeling the most and least-ductile TC128 materials for which data were available, the pre-test model would bound the expected range of impact speeds necessary to puncture the tank.

Detailed descriptions of how these two materials were selected as candidates for pre-test material responses, the process for creating the necessary material parameters in Abaqus, and the simulation of coupon tests of these materials are all contained in Appendix F4. The material models developed for the two varieties of TC128 used in the pre-test models are summarized in Table 12.

Table 12. Summary of Material Parameters for Pre-test TC128

Parameter	Value
Modulus of Elasticity	3×10^7 psi
Plasticity	Piecewise nonlinear (see Appendix F4)
Poisson's Ratio	0.3
Mass Density	7.35×10^{-4} lbf-s^2/inch
Damage Initiation	B-W Envelopes (see Appendix F4)
Damage Progression	Exponential, 700 in-lbf/in^2
Mesh Implementation	0.085 inch Fully Integrated Brick (C3D8) Elements

The results of tensile coupon simulations modeled using the Test 2 TC128 and New Normalized TC128 material models are shown in Figure 33.
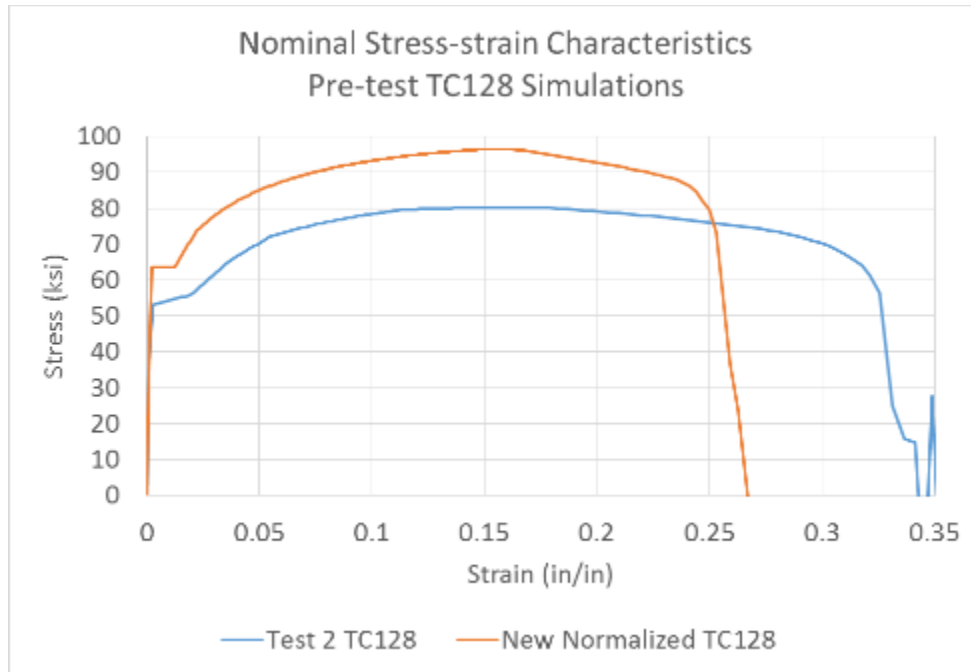
Figure 33. Nominal Stress-strain Characteristics from FE Simulations of Test 2 TC128 and New Normalized TC128 Varieties

The ductile failure initiation envelopes used for each material in the pre-test models are shown in Figure 34.
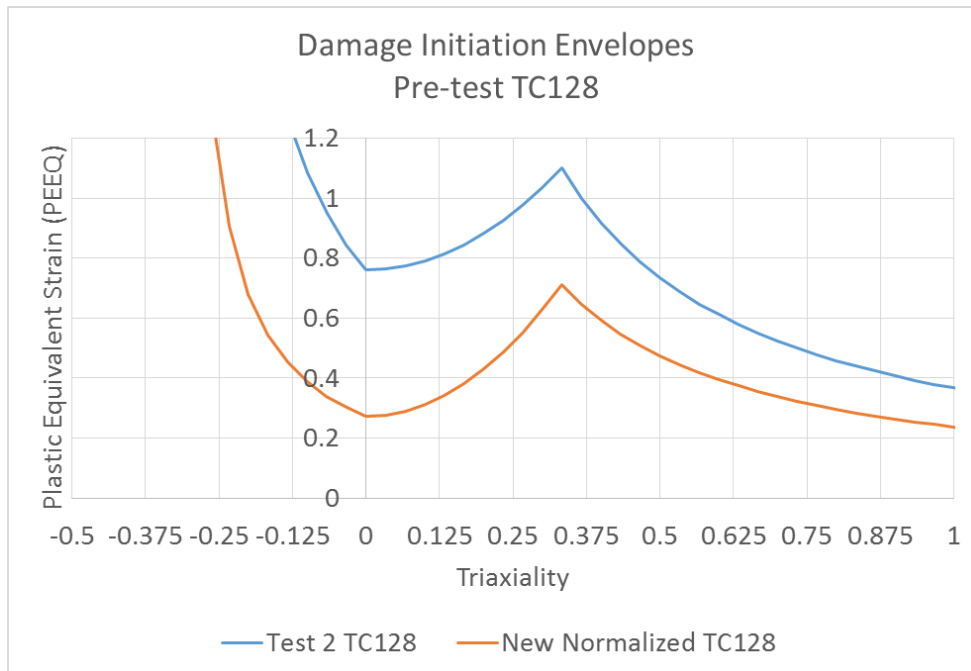
Figure 34. Damage Initiation Envelopes for Test 2 TC128 and New Normalized TC128 Varieties

5.4 Modeling Techniques Common to Pre-test and Post-test Models

In addition to the geometry making up the models, a series of constraints, loads, initial conditions, and boundary conditions were applied to each model to approximate the loading and support conditions in the test. These techniques were generally common to both the pre-test and post-test FE models. Appendix E contains a detailed discussion of these techniques.

5.5 Modeling Techniques Adjusted Between Pre-test and Post-test Models

Several modeling techniques were adjusted in the post-test model, based on the outcome of the test. These modeling techniques and their adjustments are described in this section.

5.5.1 Material Behavior

Following the test, coupons were cut from the shell and subjected to tensile testing. The results of the coupon tests were used to develop the post-test TC128 material response, referred to as actual TC128. The process of developing the plastic stress-strain response in the format required by Abaqus, and the process of developing the ductile failure initiation and progression parameters are discussed in Appendix F4.

Figure 35 contains a plot of the nominal stress-strain response obtained from FE simulation of the actual TC128 steel alongside the two pre-test TC128 steel responses. This figure shows that the actual TC128 featured the highest yield strength, but the lowest ductility of the three modeled materials.
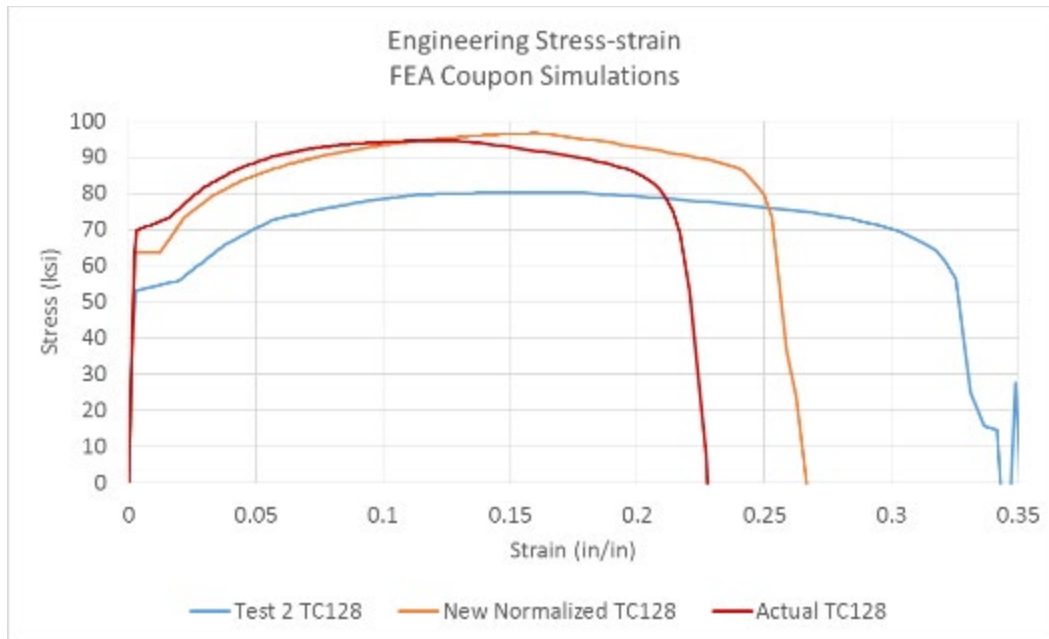
Figure 35. Nominal Stress-strain Characteristics from FE Simulations of All TC128 Steel Varieties

Figure 36 contains a plot of the damage initiation envelopes of the actual TC128 material alongside the two pre-test TC128 steel responses. The actual test material was found to have a damage initiation envelope that is much closer to the New Normalized TC128 envelope than to the Test 2 TC128 envelope. As is discussed in Appendix F4, the damage initiation envelope

developed for the actual TC128 material has its cusp at a calculated value, while the two pre-test material models have cusps that are forced to occur at a triaxiality of 1/3.
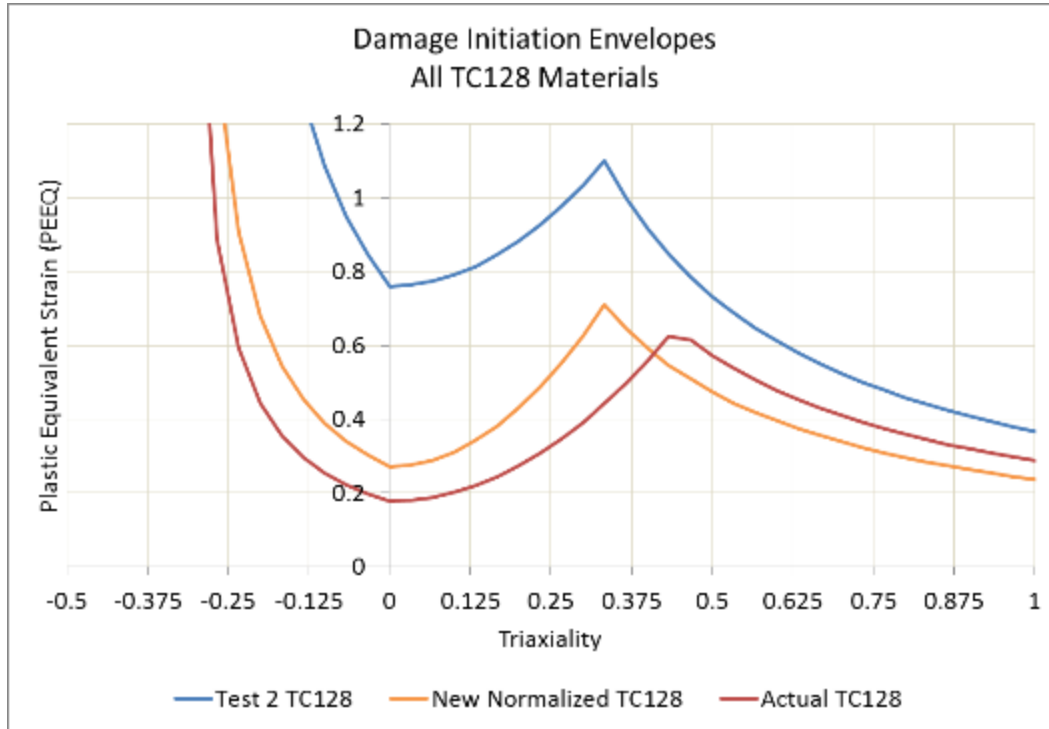
Figure 36. Damage Initiation Envelopes for All TC128 Materials

5.5.2 Foam Insulation

While the pre-test models exhibited very good agreement for the overall shape of the force-displacement response (qualitative agreement), for the measurements (quantitative agreement) and for the puncture outcome based on the New Normalized TC128 characterization, the pre- and post-test FEA each featured a dropout in force that was not measured during the test. One potential source of this dropout was hypothesized to be the modeling simplification of a 4-inch gap between the outside of the tank and the inside of the jacket. In the tested tank, this gap is filled with foam insulation. It was thought that by modeling this gap as empty space, the tank was not actually being constrained by the impact wall until it had traveled through this 4-inch gap, allowing the tank to build up speed as it was pushed back and creating more fluid sloshing than occurred in the actual test.

To test this hypothesis, the post-test model was run using the gap simplification from the pre-test model, and it was also run with a simplified foam material filling the gap. The foam material's properties were developed as described in Appendix F6.

44

6. Comparison of Test Response to Pre-test Analysis

Pre-test FE modeling was used to estimate the overall response of the tank to the impact, including the force-displacement response, as well as to estimate the expected range of puncture speeds based on different TC128 steel properties. For each TC128 material used in the pre-test model, the simulated impact speed was varied in an iterative manner to attempt to estimate a puncture speed range within a 1-mph band. If a given combination of impact speed and material behavior resulted in puncture, then the model's speed was reduced and the model re-run. If the model did not puncture, then the impact speed was increased and the model re-run. This process was then repeated for the other pre-test TC128 steel characterization.

The results of the pre-test modeling are summarized in Table 13, and more completely described in appendices C1 and C2. This table contains four results: the highest speed for which the model estimated a non-puncture outcome and the lowest speed for which the model estimated a puncture outcome for each of the two pre-test material behaviors. Based on these results, and assuming that the two selected materials do bound the limits of material responses likely to be encountered during the test, these results indicate that for an impact speed below 14.5 mph, the tank would not be expected to puncture, regardless of the actual material response. Beginning at 14.5 mph, the likelihood of puncture increases with increasing speed. For speeds beyond 17 mph, puncture would be a very likely outcome.

Table 13. Summary of Pre-test FE Model Results

Material	Highest Speed Without Puncture (mph)	Lowest Speed with Puncture (mph)
Test 2 TC128	16.5	17
New Normalized TC128	14.5	15

The target test speed of 15 mph was chosen to be within the range where puncture was a likely outcome, but not a certain outcome. Based on previous tank car tests, the expected test speed was within a +/-0.5 mph band around the target test speed. Thus, the anticipated range of impact speeds was 14.5 to 15.5 mph. The actual test speed, as determined from speed traps, was 15.16 mph.

6.1 Comparison of Force-versus-displacement Results

Pre-test models using both the Test 2 TC128 and New Normalized TC128 steel were run at the target test speed of 15 mph. The force-versus-displacement results from those models are compared to the test results in Figure 37. In the test, the mass of the impactor is multiplied by the average deceleration from the onboard accelerometers to obtain impact force. In the FE models, the acceleration is calculated at a single point on the impactor, since the impactor is modeled as a rigid body. Therefore, the impact forces in the FE models are simply the product of impactor mass and acceleration. A CFC60 filter has been applied to the test and FE results shown.
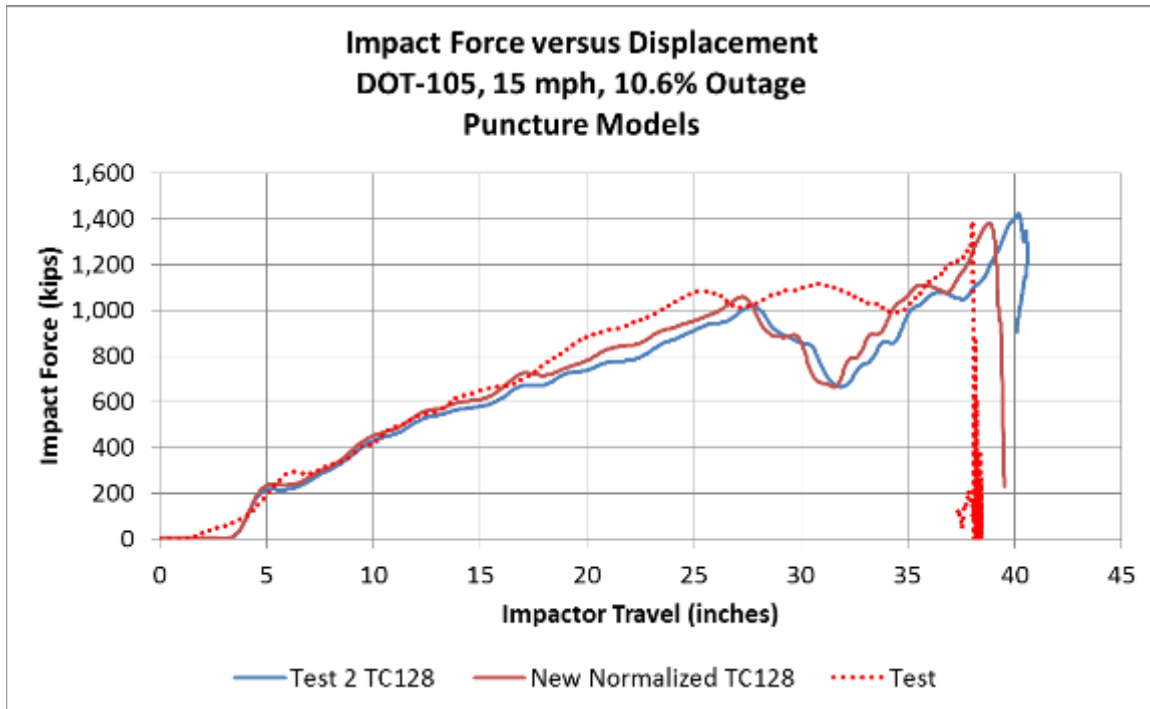
Figure 37. Force-displacement Responses from Pre-test FEA Using Test 2 TC128 and New Normalized TC128 Materials

Both the pre-test models show a similar shape as the test measurements. The models do a good job of capturing the overall response of the test, including the changes-in-slope to the response as the impactor deforms the tank car and pushes it back against the wall. The pre-test model using the Test 2 TC128 did not experience a puncture, and thus the impactor can be seen to rebound in this figure. The pre-test model using New Normalized TC128 estimated a puncture; thus, the impactor continued to travel in the same direction after the peak force drops. Both pre-test FE models experience a larger drop in force at approximately 32 inches of impactor travel than was measured during the test. Finally, both pre-test FE models were in very good agreement with both the maximum force and the maximum indentation measured during the test.

6.2 Comparison of Air Pressure Results

Figure 38 shows a comparison plot of the average air pressure in the pre-test analyses compared to the test data. For each FE result, the average pressure in the outage is reported. For the test data, the air pressure measured by the gauge in the manway is plotted. Both pre-test FE models captured the shape of the pressure-time response measured in the test, though the models both underestimate the maximum pressure measured in the test. This underestimate is likely due to the pneumatic cavity only representing the average air pressure over the full outage volume, while in the actual tank the pressure can vary with both time and location within the tank.
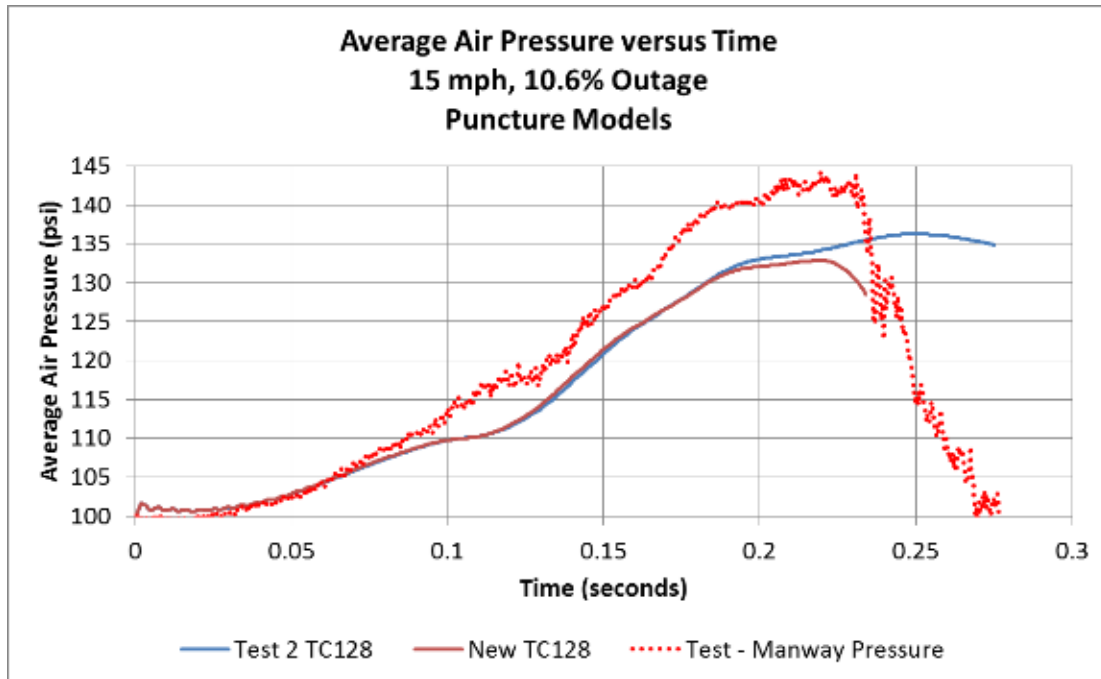
Figure 38. Air Pressure-time Responses from Pre-test FEA Compared to Test Results

6.3   Comparison of String Potentiometer Results

Figure 39 contains a plot comparing the internal string potentiometer measurement at the center of the car against the pre-test FE model results. In both pre-test FE models, the model captured the general shape of the test response quite well.
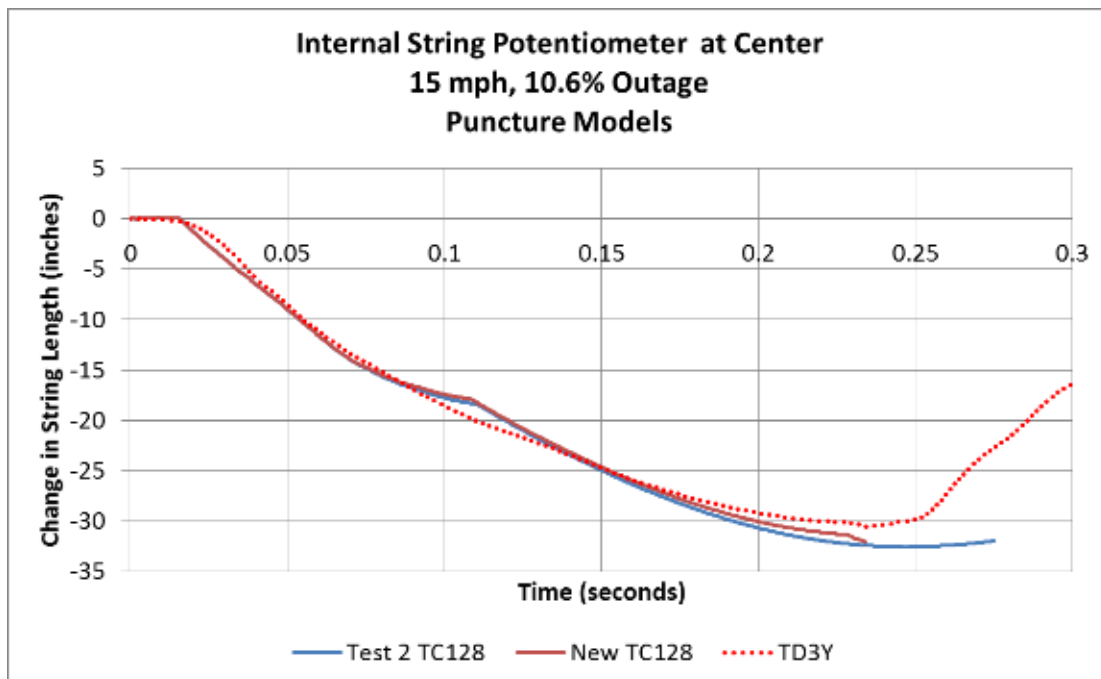
Figure 39. Change in Center String Potentiometer Length for Pre-test FEA Compared to Test Results

47

Figure 40 contains a plot comparing the vertically oriented internal string potentiometer measurements at the center of the car against the pre-test FE model results. Both pre-test models exhibit good agreement with the test results in terms of the overall shapes of the curves, and the general magnitudes of the responses up to 0.2 second. The test measurements indicated a larger change-in-length than either model. After this time, the internal string potentiometer in the test exhibits a large increase in length that is not captured by either model. This increase in string potentiometer length in the test measurement may be due to fluid motion within the tank causing more string to pull out of the potentiometer than would be pulled out by ovalization of the tank.
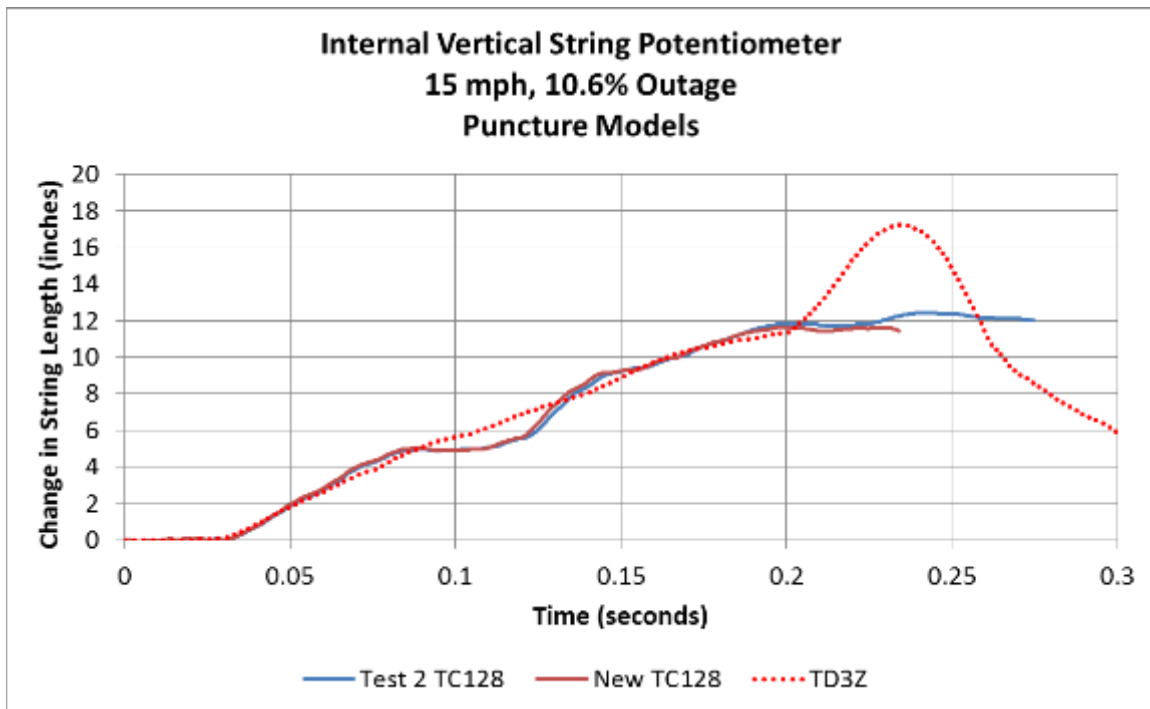
Figure 40. Change in Vertical String Potentiometer Length for Pre-test FEA Compared to Test Results

6.4 Summary of Peak Test Measurements and FE Results for Pre-test Model Using New Normalized TC128 Behavior

Since the pre-test model run using New Normalized TC128 steel at 15 mph estimated a puncture, and the test punctured at a speed only slightly above this, the results from this pre-test model are more closely compared with the test results. Table 14 presents a summary of the level of agreement between the peak measurements from the pre-test FEA and the test.

**Table 14. Comparison of Peak Results from New Normalized TC128
Pre-test Model (15 mph) and Test Results (15.16 mph)**

Result	Unit	Pre-test FEA	Test	% Difference
Longitudinal Acceleration	G's	4.6	4.7	-0.7%
Impact Force	kips	1,381.3	1,390.8	-0.7%
Displacement at Peak Force	inches	38.8	38.0	2.1%
Energy Absorbed at Peak Force	1×10^6 ft-lbf	2.2	3	-5.4%
48" Offset String	inches	-18.0	-15.8	13.9%
Potentiometer			-18.2	-1.3%
24" Offset String	inches	-24.8	-23.6	5.2%
Potentiometer			-24.5	1.2%
Center String Potentiometer	inches	-32.0	-30.6	4.8%
Vertical String Potentiometer	inches	11.6	17.2	-32.5%
Skid String	inches	-11.2	-10.4	8.6%
Potentiometer			-9.9	13.7%
Head String	inches	-11.2	-10.3	9.0%
Potentiometer			-9.8	15%
Outage Pressure	psi	132.9	144.3	-7.9%

7. Comparison of Test Response to Post-test Analysis

Following the test, the pre-test FE model was updated to include the actual material properties to better reflect the support provided by the rigid wall and ground, and to be run at the measured impact speed of 15.16 mph. The post-test modeling results for this impact speed are compared to the test results in this section. Two different post-test models are discussed in this section. The first featured a gap between the outside of the tank and the inside of the jacket, and the second included a simplified representation of foam insulation between the tank and jacket.

7.1 Post-test Model Without Insulation

In general, there was good agreement between the post-test FEA results and the measurements made during the test, as Figure 41 shows. The complete set of comparisons between post-test FEA and test results can be found in Appendix C.
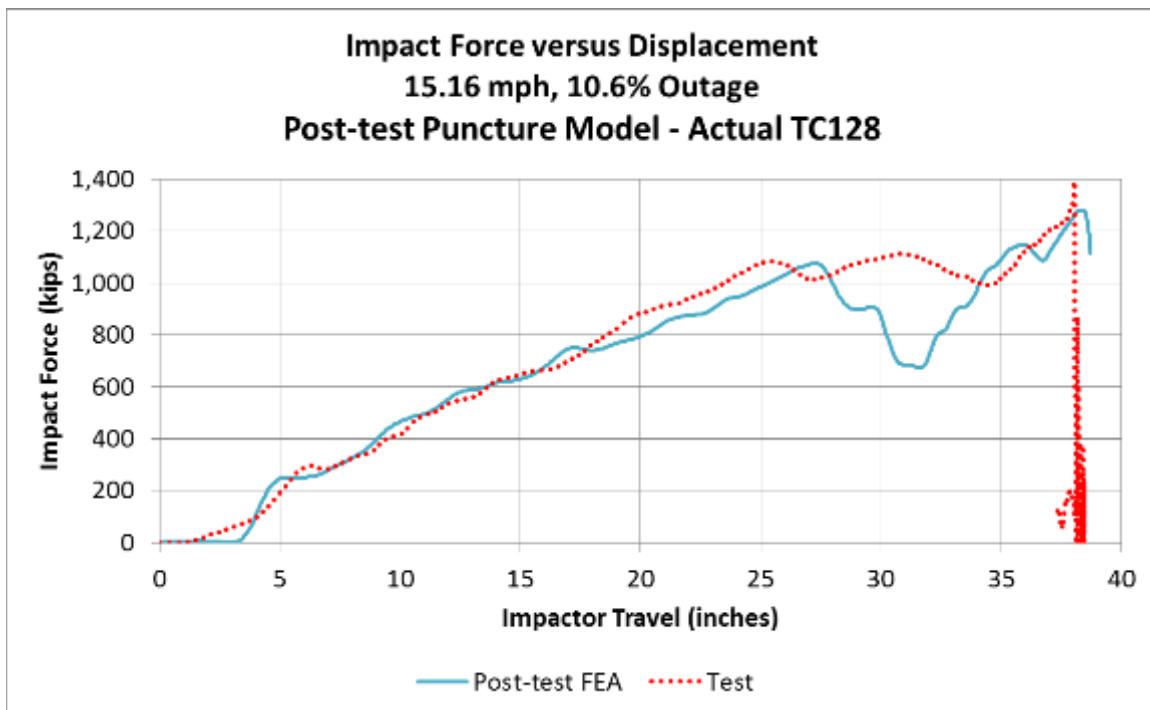
Figure 41. Post-test FEA and Test Force-displacement Results

Figure 42 displays a series of frames from the post-test FE model. These images show relatively little reduction in volume of the outage. The analysis terminated at approximately 0.22 seconds due to puncture of the tank.
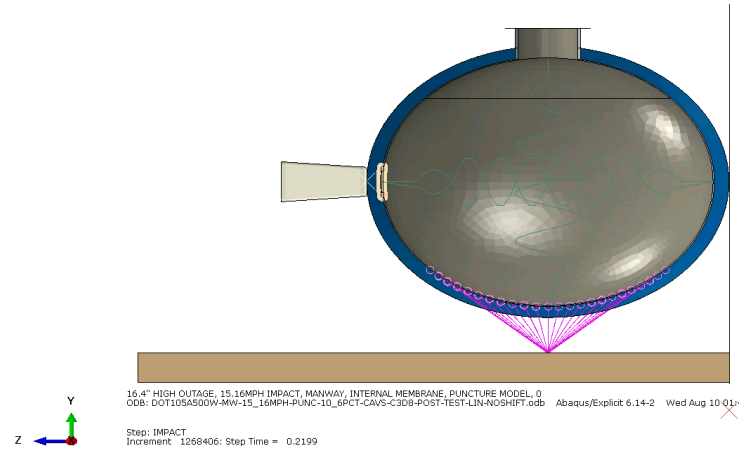
t=0.0s

Initial Position of Model
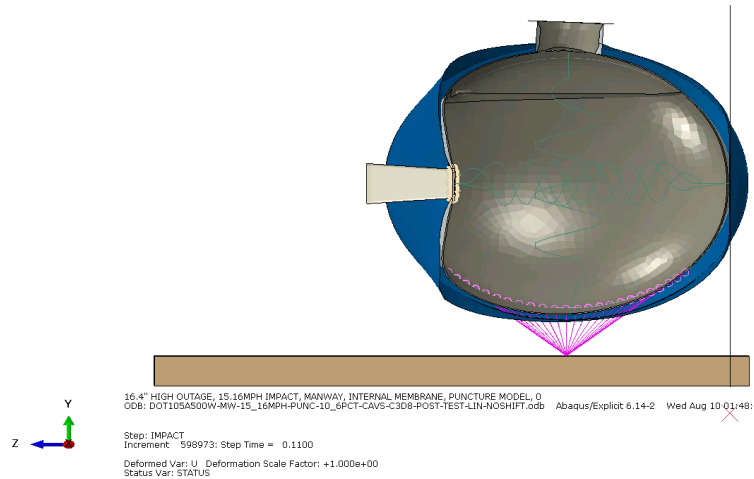
t=0.11s

Midway through Impact
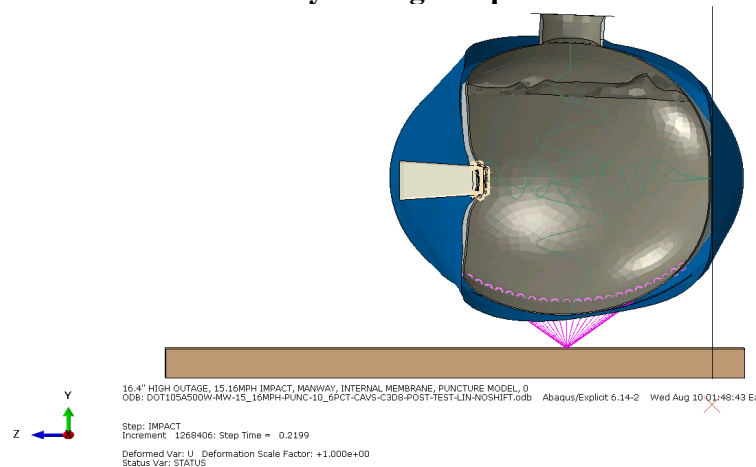
t=0.22s

Frame After Puncture

Figure 42. Impact Progression, Post-test FE Model

Overall, the FE model does a good job of capturing the response of the fluid during the test. The model exhibits somewhat lower pressures compared to the test, particularly as the fluid displacement increases toward the end of the impact event. Figure 43 shows side and front section views of the tank at two times. The top row corresponds to t=0, the initial position of the model. The bottom row corresponds to t=0.22 seconds, after the tank has punctured in the simulation. In both views, translucency is activated in the model to better view parts blocked by other parts.
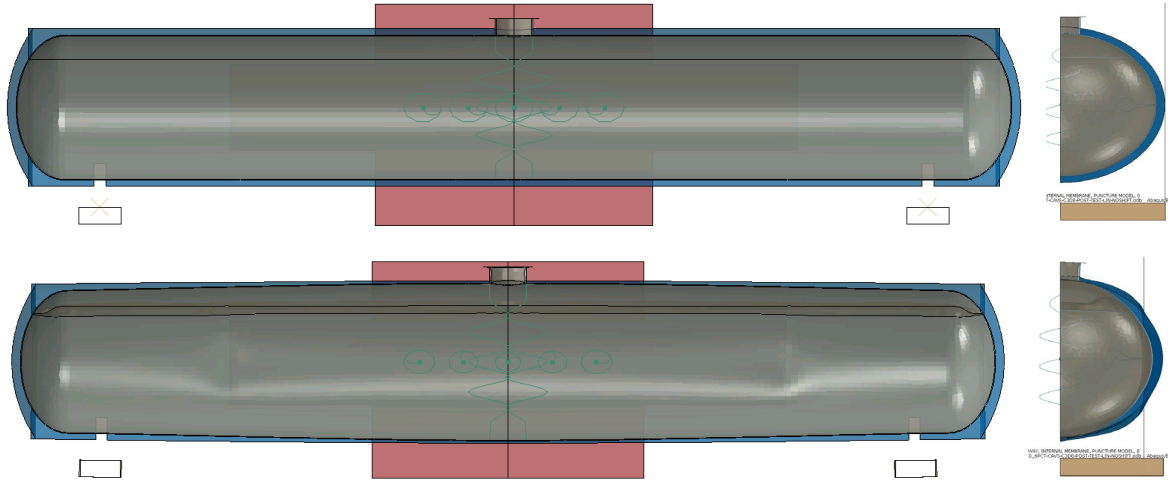
Figure 43. Cross-section View at 0 Seconds (top) and 0.22 Seconds (bottom)

As an overall comparison, the average pressure-time history from the transducer in the manway within the air phase in the test and average air pressure within the outage in the FE model are plotted in Figure 44. The general response exhibits good correlation between the test and the post-test model, but the model does exhibit lower pressures than those measured in the test for much of the response.
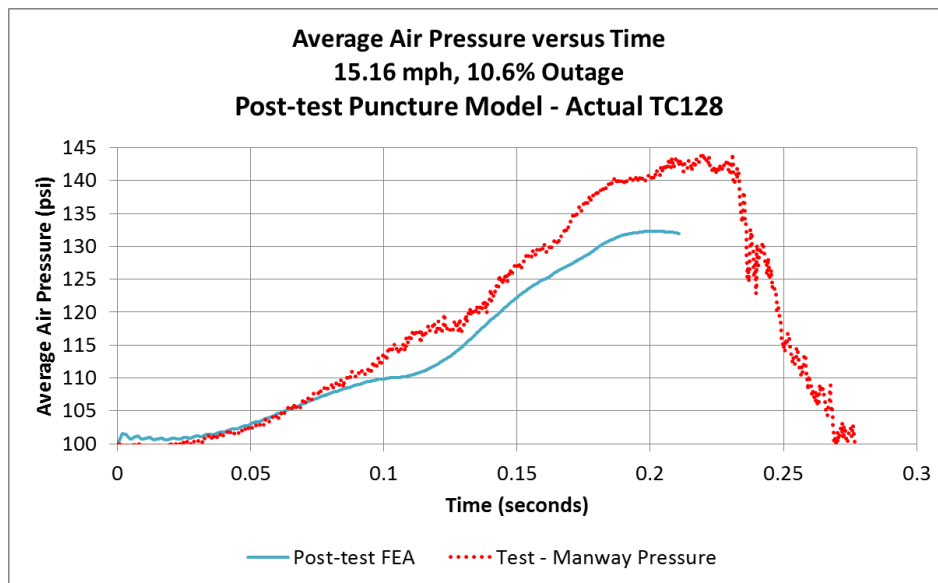
Figure 44. Average Water Pressure in Post-test FEA and Test

52

Figure 45 contains a plot of the A-end (TDASKID) and B-end (TDBSKID) skid displacements measured during the test and the skid displacement calculated in the post-test FE model. The overall shapes of the three responses are similar, and the FE model captured the maximum displacement well. There is a difference in timing between the test measurements and the model results.
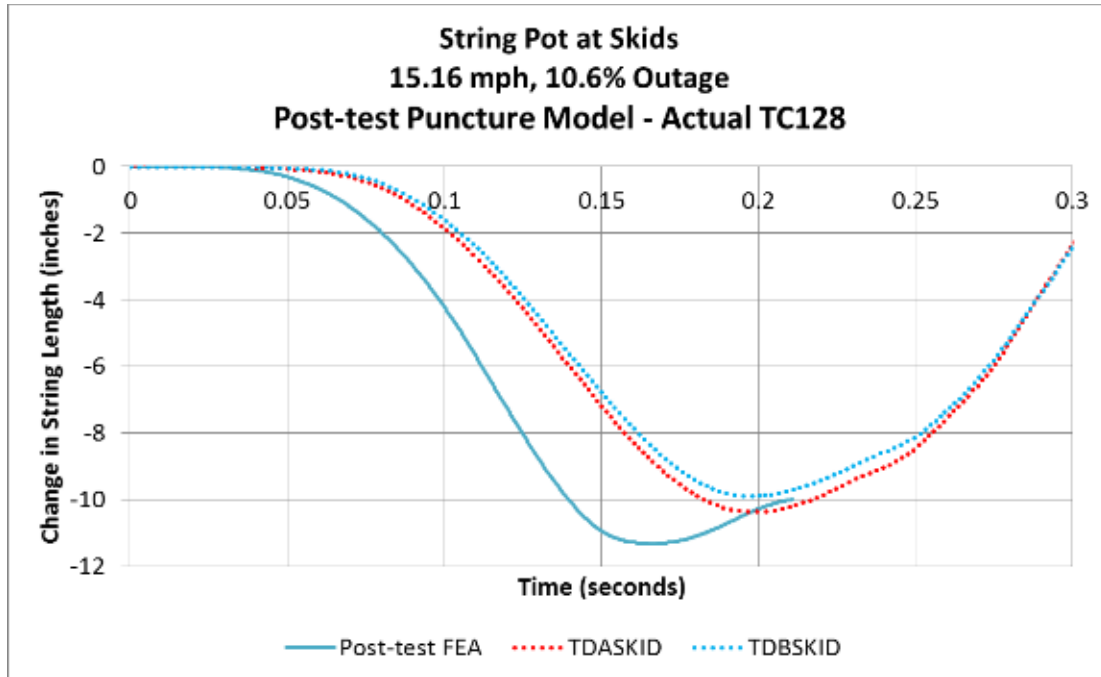
Figure 45. Skid Displacement in Post-test FEA and Test

The indentation of the tank at the center of the tank was measured in the test by string potentiometers and calculated in the FE model using soft springs. The two results for the center of the car are plotted in Figure 46. The model and the test are in good agreement over the range captured by the model. Since the FE model punctured at approximately 0.22 seconds, the FE results are limited to that range. After puncture in the test, the string potentiometer began to measure a decrease in indentation as the tank recovered its elastic energy, prior to the shell segment being ejected from the tank.
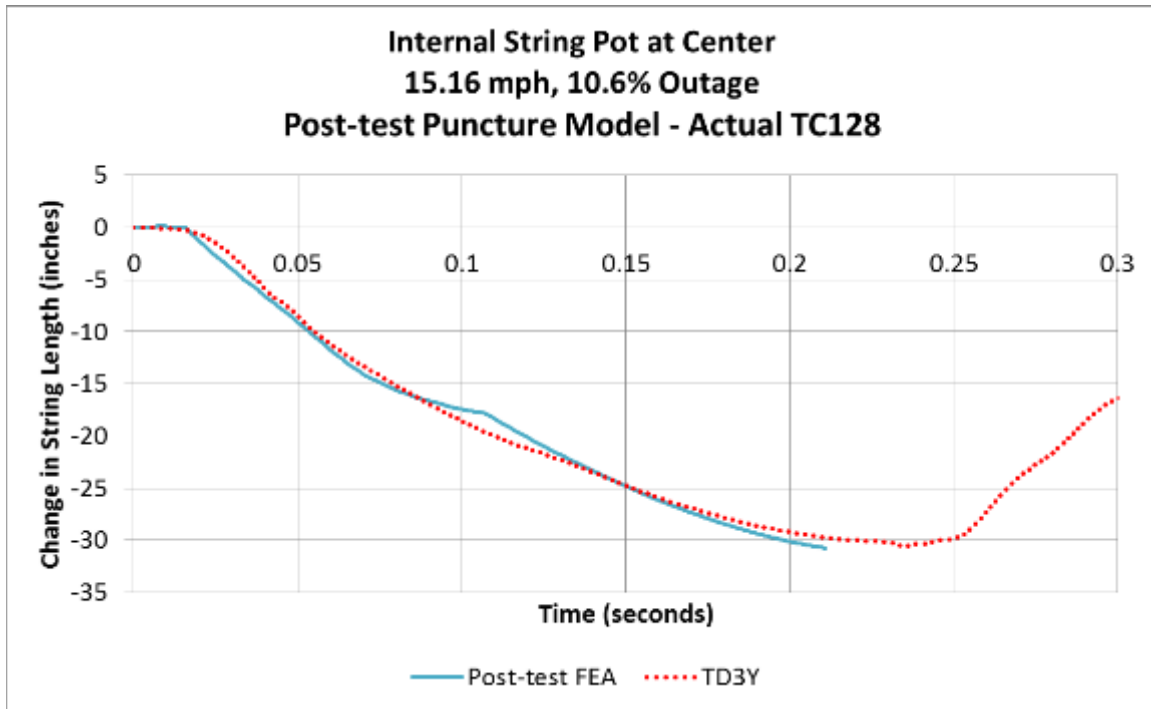
Figure 46. Internal String Potentiometer Measurement at Center of Tank in Post-test FEA and Test

The complete set of test and post-test FEA results are compared in Appendix C. Table 15 contains a comparison between the peak measurements from the test and the corresponding peak value calculated for each output in the post-test FE model. This table also includes a column indicating the difference between the test measurement and FE calculations. The post-test model exhibited agreement that is consistent with the agreement obtained between the pre-test FEA and the test measurements.

54

Table 15. Comparison of Peak Results from Actual TC128 Post-test Model (15.16 mph) and Test Results (15.16 mph)

Result	Unit	Post-test FEA	Test	% Difference
Longitudinal Acceleration	G's	4.3	4.7	-7.8%
Impact Force	kips	1,282.0	1,390.8	-7.8%
Displacement at Peak Force	inches	38.4	38.0	0.9%
Energy Absorbed at Peak Force	1×10^6 foot-pounds	2.2	2.3	-5.2%
48" Offset String Potentiometer	inches	-17.8	-15.8	13.1%
			-18.2	-1.9%
24" Offset String Potentiometer	inches	-24.4	-23.6	3.2%
			-24.5	-0.6%
Center String Potentiometer	inches	-30.7	-30.6	0.5%
Vertical String Potentiometer	inches	11.7	17.2	-32.1%
Skid String Potentiometer	inches	-11.3	-10.4	9.2%
			-9.9	14.4%
Head String Potentiometer	inches	-11.3	-10.3	9.8%
			-9.8	15.7%
Outage Pressure	psi	132.3	144.3	8%

Overall, the post-test FE results are within 10 percent of the test measurements for nearly every measurement. There are four test-FE result comparisons that fall outside of this range: one of the 48-inch offset strings potentiometers within the tank, the vertical string potentiometer within the tank, one of the skid string potentiometers, and one of the head string potentiometers. It is notable that for the 48-inch offset string potentiometer within the tank, and the skid and head string potentiometers outside the tank, the FE results were within 10 percent of the measurement made on the second such measurement location. As previously discussed in Section 6, the vertical string potentiometer measurement during the test included a sudden change in string length at a late stage in the test. The source of this sudden change in string length was not apparent from review of the test documentation.

In general, the post-test FE model exhibited equal or better agreement with the test results compared to the pre-test model using New Normalized TC128 steel (shown in Table 14). One area where the pre-test model exhibited closer agreement was in the longitudinal acceleration, which is used to calculate the maximum impact force. In this measurement, the post-test model exhibits conservatism compared to the test result. In this context, conservatism means that the model estimates puncture will occur at a lower absorbed energy than was measured during the test. One possible reason for this conservatism in the post-test model is in the variety of material responses found by performing tensile testing of several coupons of TC128 steel making up the tested car. The post-test material modeling matched a characteristic in the middle of the range of characteristics found for this car. However, if the area of puncture from the test featured material having a slightly superior puncture resistance than what was modeled, then the model would tend to underestimate the threshold puncture speed. The material modeling of the post-test behavior is described in Appendix F4.

55

7.2   Post-test Model with Insulation

Additionally, a post-test model was created to investigate the effects of foam insulation. This model used the actual test speed and the actual TC128 material properties in the car's shell. The purpose of including insulation was to investigate a dropout in force experienced by the pre- and post-test models that was not measured during the test. One hypothesis as to the source of this dropout involved the simplification made in the previous models where the space between the jacket and tank was modeled as dead space, while the tested car contained foam insulation in this location. Since the jacket was always modeled as being flush against the impact wall, the cases without insulation would have allowed the internal tank to move unconstrained through the 4-inch gap between tank and jacket. This could allow the tank to develop an unrealistic momentum, and create a second impact when the tank suddenly encountered the jacket pressed against the rigid wall. By including insulation, the tank would be prevented from developing this unconstrained motion.

A simplified foam insulation material was developed by modifying a foam insulation material model from the Abaqus example problem library [21] using parametric relationships for foam insulation [22]. Foam material characterization for the actual material in the DOT-105 tank car was not performed as a part of this study, as the intent of modeling insulation was simply to assess whether the lack of insulation could be an explanation for the force dropout in the models. The full set of post-test FE results using foam insulation can be found in Appendix C4, and a description of developing the foam material model can be found in Appendix F6.

The force versus displacement response of the post-test FE model with insulation is compared with the test measurements in Figure 47. The force dropout seen in previous models at an impactor displacement of approximately 32 inches has been eliminated in this result. The simplification of modeling an empty space between tank and jacket in previous models may be responsible for the appearance of this force dropout.
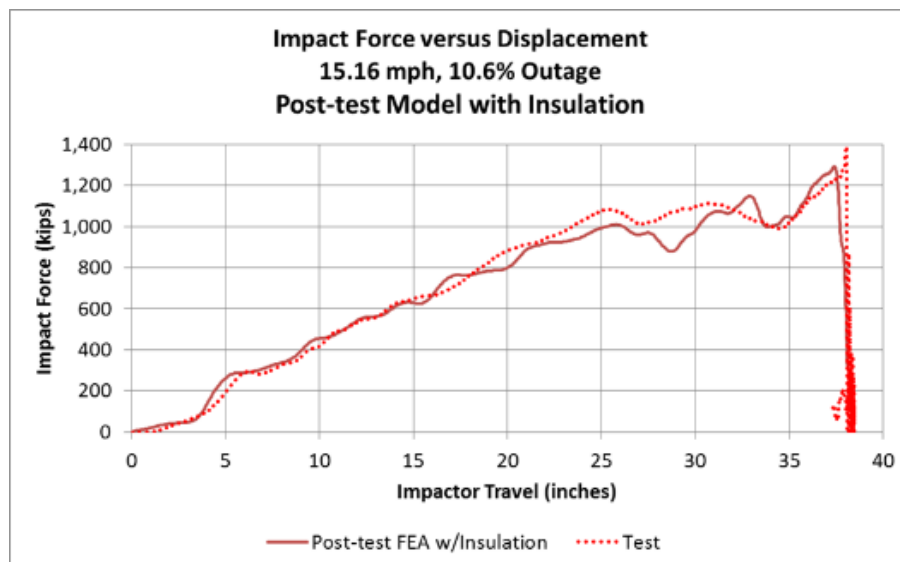
Figure 47.   Post-test FEA with Insulation and Test Force-displacement Results

Table 16 shows a table comparing the results from the post-test FE model with insulation to the test measurements. In general, there continues to be very good agreement between the test measurements and the FE estimates.

Table 16. Comparison of Peak Results from Actual TC128 Post-test Model with Insulation (15.16 mph) and Test Results (15.16 mph)

Result	Unit	Post-test FEA (insulated)	Test	% Difference
Longitudinal Acceleration	G's	4.3	4.7	-7.1%
Impact Force	kips	1,292.3	1,390.8	-7.1%
Displacement at Peak Force	inches	37.4	38.0	-1.6%
Energy Absorbed at Peak Force	Million foot-pounds	2.2	2.3	-4.6%
48" Offset String Potentiometer	inches	-17.4	-15.8	10.4%
			-18.2	-4.3%
24" Offset String Potentiometer	inches	-23.8	-23.6	0.9%
			-24.5	-2.8%
Center String Potentiometer	inches	-31.0	-30.6	1.2%
Vertical String Potentiometer	inches	11.5	17.2	-33.0%
Skid String Potentiometer	inches	-10.2	-10.4	-2.0%
			-9.9	2.7%
Head String Potentiometer	inches	-9.8	-10.3	-5.2%
			-9.8	0.0%
Outage Pressure	psi	133.0	144.3	8%

8. Conclusion

This report documents the combined efforts of TTCI and Volpe to test and analyze the side impact puncture performance of a DOT-105 tank car. This research supports FRA's tank car research program to provide the technical basis for rule-making on enhanced and alternative performance standards for tank cars.

The tank car was filled with water to approximately 89.4 percent of its volume. It was then sealed and pressurized to 100 psi. The test was intended to strike the car at a speed high enough to result in significant damage to the tank and possibly puncture the tank's shell. The tank car was impacted by a 297,125-pound ram car traveling 15.2 mph. A 12- by 12-inch ram head fitted to the ram car impacted the tank center. The impact punctured the tank shell after slowing the impact car to less than 1 mph.

The internal pressure of the tank caused the shell failure to spread outward from the initial puncture under the corners of the impactor. Since the ram car was brought to a stop shortly after puncture initiated, the internal pressure of the car could force the failed portion of the shell to eject outward, rather than being pushed into the tank by the ram car's excess momentum. This ejected section of the shell pulled a pressure transducer and a string potentiometer out with it, causing multiple disruptions in data after the puncture.

Pre-test FE modeling was used to estimate the overall response of the tank to the impact, including the force-displacement response. Due to uncertain parameters in the test conditions (e.g., material properties and actual test speed), the pre-test models were intended to bound the range of likely puncture speeds. The model estimated that the tank could puncture after an impact of between 14.5 and 17 mph, depending on the ductility of the TC128 in the car's shell. Thus, the test outcome of puncture after nearly stopping the car from a 15.2 mph impact agreed with the pre-test modeling. The pre-test models exhibited good agreement with the measured force-displacement result from the test. Additionally, the internal pressure-time response and the displacements of the tank measured by string potentiometers were all in good agreement with the pre-test model estimates.

Following the test, material coupons were cut from undamaged regions of the tested car. These coupons were used to generate a new material response, which was implemented in the post-test FE model. Additionally, the post-test model was run at the actual impact speed as measured during the test. One additional change made in the post-test modeling was to include a representation of the insulation between the tank car shell and jacket. The post-test model further improved the agreement with the test measurements. When run at the test speed, the post-test model estimates puncture of the tank car based on the actual material responses. The post-test model is conservative, as evidenced by the residual speed in the impactor at the time of puncture. In the post-test model without insulation, the impactor slowed to approximately 3 mph, while the test measurements indicate that the impactor slowed to 0.5 mph at the time of puncture. In the post-test model with insulation, the impactor slowed to approximately 2.4 mph. These results indicate that the test speed only slightly exceeded the puncture/non-puncture threshold speed. Thus, the model would estimate puncture at a slightly lower impact speed than would be expected to puncture the car if a future test were to be run at exactly the puncture/non-puncture threshold speed.

Post-test model results indicated that including the foam insulation in the model improves agreement between the model and the test measurements. Importance of modeling the insulation will depend on the thickness and stiffness of the insulation material.

The FE modeling performed in this effort used simplified hydraulic and pneumatic cavity modeling techniques to simulate the water and air responses, respectively. These modeling simplifications resulted in a puncture-capable model with an improved runtime compared to previously used explicit lading representations. The test measurements confirmed that these modeling simplifications provided a reasonable representation of the fluid behaviors in the tank car. However, it should be noted that this test featured a relatively small tank car having a relatively large outage at an initially elevated pressure. Further work is necessary to ascertain whether the cavity simplifications are appropriate for larger capacity tank cars, small outage volumes, and outages that are initially at a lower pressure.

One intent of this test was to produce test data that could be used by other entities wishing to model tank car impacts during their model validation activities. Currently, FRA does not have agreed-upon model validation criteria or procedures for models used to simulate tank car impacts. However, establishing that a complex computational model has a sound basis in physics, is a fundamental part of any modeling or simulation activity. Developing a set of criteria and procedures for validating tank car impact and puncture response models should be considered as a future activity if new or innovative tank cars are to be developed in the future that may be evaluated using modeling.

9. References

1. Pipeline and Hazardous Materials Safety Administration (PHMSA), DOT. Tank-head puncture-resistance systems. Title 49 Code of Federal Regulations § 179.16.

2. Elkins, A. *Field Guide to Tank Cars*. American Association of Railroads. 2017

3. Kirkpatrick, S. W., Rakoczy, P., and MacNeill, R. A. "Side Impact Test and Analyses of a DOT-111 Tank Car." U.S. Department of Transportation: Federal Railroad Administration, Technical Report, DOT/FRA/ORD/15/30, October 2015.

4. Rakoczy, P., and Carolan, M. "Side Impact Test and Analysis of a DOT-112 Tank Car." U.S. Department of Transportation: Federal Railroad Administration, Technical Report, DOT/FRA/ORD-16/38, December 2016.

5. Transportation Technology Center, Inc. "Test Implementation Plan for FRA Tank Car Side Impact, Revision 1," April 14, 2016.

6. SAE J211/1 Standard. 1995. "Instrumentation for Impact Test – Part 1: Electronic Instrumentation." SAE International, Warrendale, PA, 2007.

7. Kirkpatrick, S. W. "Detailed Puncture Analyses of Various Tank Car Designs: Final Report – Revision 1." Applied Research Associates, January, 2010.

8. Carolan, M., Jeong, D. Y., Perlman, B., Murty, Y. V., Namboodri, S., Elzey, R. K., Anankitpaiboon, S., Tunna, L., and Fries, R. "Application of Welded Steel Sandwich Panels for Tank Car Shell Impact Protection." U.S. Department of Transportation: Federal Railroad Administration, DOT/FRA/ORD-13/19, April, 2013.

9. Yu, H., Jeong, D. Y., Gordon, J. E., and Tang, Y. H. "Analysis of Impact Energy to Fracture Unnotched Charpy Specimens Made from Railroad Tank Car Steel," Proceedings of the 2007 ASME Rail Transportation Division Fall Technical Conference, RTDF2007-46038, September 2007.

10. Tang, Y. H., Yu, H., Gordon, J. E., Jeong, D. Y., and Perlman, A. B. "Analysis of Railroad Tank Car Shell Impacts Using Finite Element Method," Proceedings of the 2008 IEEE/ASME Joint Rail Conference, JRC2008-63014, April 2008.

11. Yu, H., Tang, Y. H., Gordon, J. E., Jeong, D. Y. "Modeling the Effect of Fluid-Structure Interaction on the Impact Dynamics of Pressurized Tank Cars," Proceedings of the 2009 ASME International Mechanical Engineering Congress and Exposition, IMECE2009-11926, Lake Buena Vista, FL, November 2009.

12. Abaqus 6.14-2. Dassault Systemes Simulia Corp, Providence, RI, 2014.

13. Smits, A. J. *A Physical Introduction to Fluid Mechanics*. John Wiley & Sons, Inc. New York, 2000.

14. The Engineering Toolbox. "Water – Density, Specific Weight, and Thermal Expansion Coefficient." 2003.

15. The Engineering Toolbox. "Speed of Sound in Water." 2004.

16. The Engineering Toolbox. "Universal and Individual Gas Constant." 2004.

17. The Engineering Toolbox. "Air – Molecular Weight and Composition." 2004.

18. Urieli, I. "Specific Heat Capacities of Air." *Engineering Thermodynamics*, 2008.

19. Association of American Railroads. *AAR Specifications for Tank Cars, Appendix M*. M-1002. 1978.

20. McKeighan, P. "Mechanical Properties of Tank Car Steels Retired from the Fleet." Southwest Research Institute Report to the Volpe Center, 2008.

21. Abaqus Example Problems Manual. "Example Problem 2.1.12 – Cask Drop with Foam Impact Limiter." Dassault Systemes Simulia Corp, Providence, RI, 2014.

22. Goods, S. H., Neuschwanger, C. L., and Whinnery, L. L.. Mechanical properties of a structural polyurethane foam and the effect of particulate loading. United States: N. p., 1998. DOI:10.2172/650182.

23. The Engineering Toolbox. "Air – Altitude, Density and Specific Volume." 2003.

24. USGS Geographic Names Information System (GNIS). *GNIS Detail – Pueblo Memorial Airport*. United States Geologic Survey.

25. U.S. Climate Data. Climate Pueblo – Colorado and Weather Averages Pueblo. Daily Normals, Pueblo, CO, April.

26. Lee, Y. W., and Wierzbicki, T. "Quick Fracture Calibration for Industrial Use," Impact & Crashworthiness Laboratory Report No. 115, August 2004.
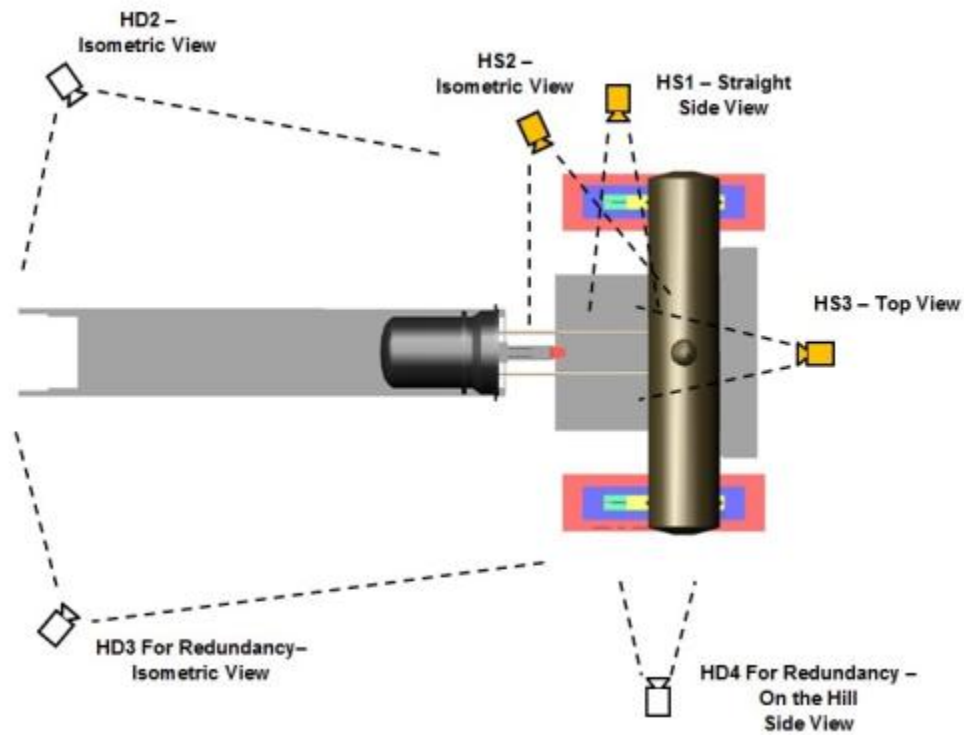
Figure A1. Camera Positions (top)—High Speed (HS), High Definition (HD)
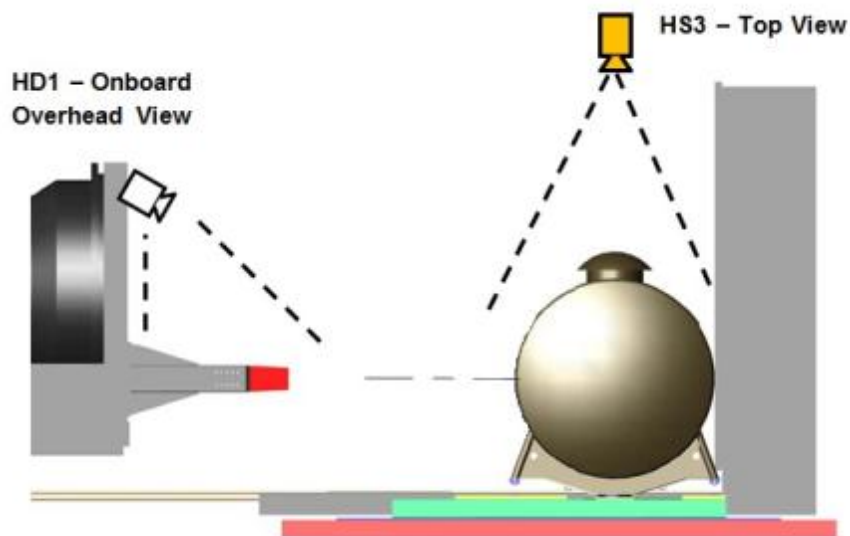
Figure A2. Camera Positions (side)—High Speed (HS), High Definition (HD)
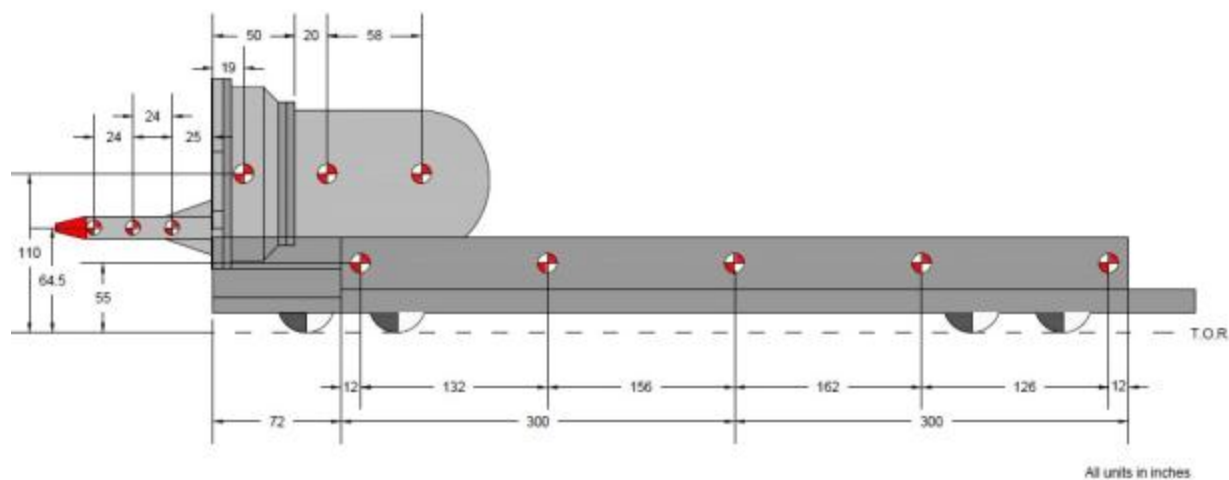
Figure A3. Ram Car Target Positions
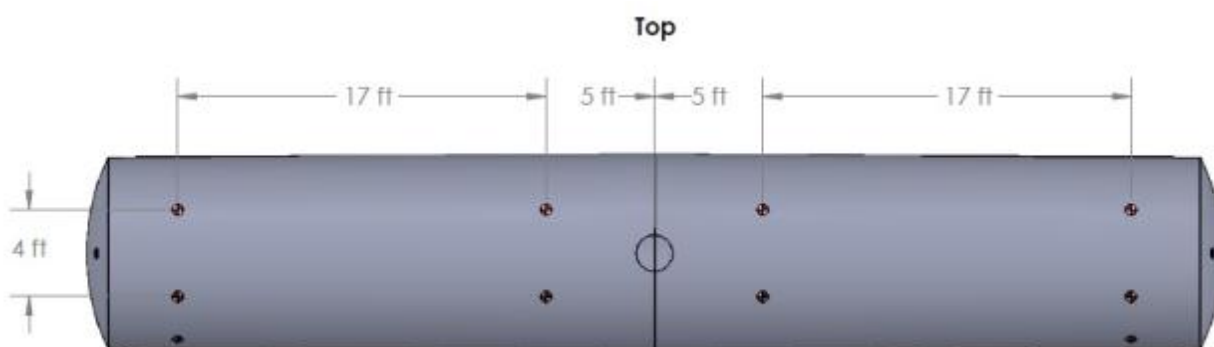
Figure A4. Tank Car Target Positions (top)
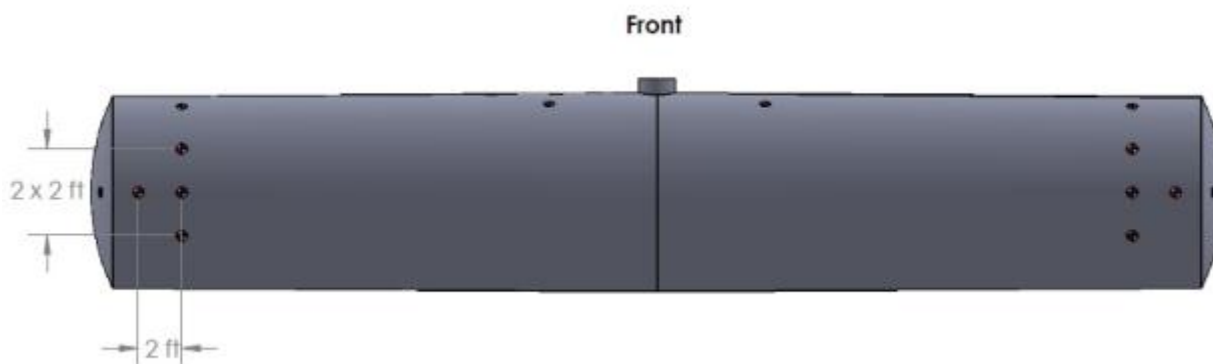
Figure A5. Tank Car Target Positions (front)

63
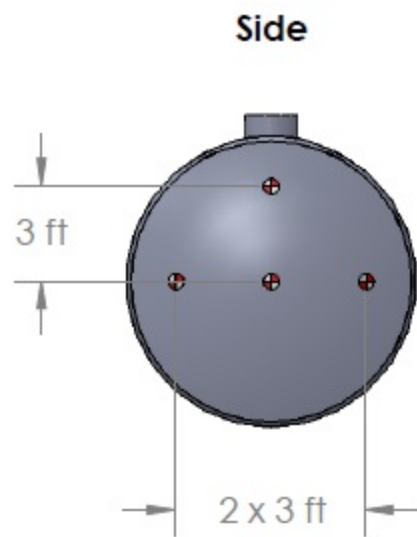
Figure A6. Tank Car Target Positions (side)

Appendix B.
Test Data

This appendix contains raw and filtered test data. The raw accelerations and internal pressures measured on different locations on the ram car were processed as described in this paragraph. The test data from -1 second to -0.1 seconds on each channel were averaged, and this value was subtracted from the test measurements in order to remove any initial offsets in the data. Each channel was then filtered to channel frequency class (CFC) 60, using the procedures given in SAE J211 [6]. Displacement data did not require any filtration.

B1 – Accelerations
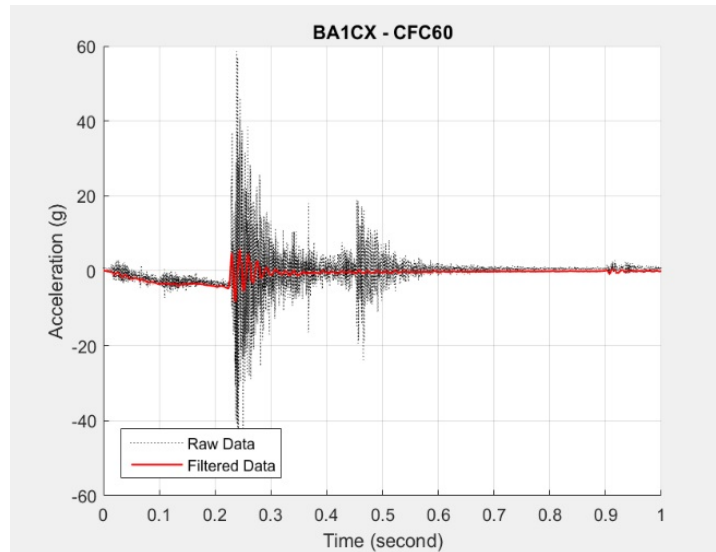
Figure B1. Raw and CFC60 Filtered Acceleration-time Data from BA1CX
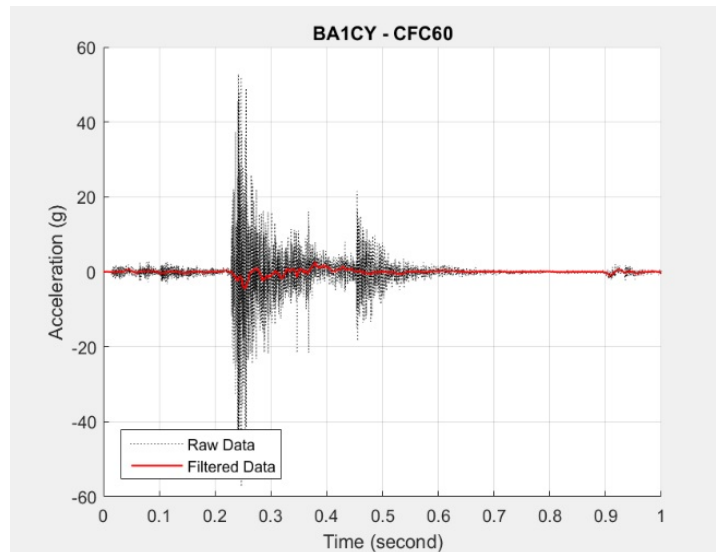
Figure B2. Raw and CFC60 Filtered Acceleration-time Data from BA1CY
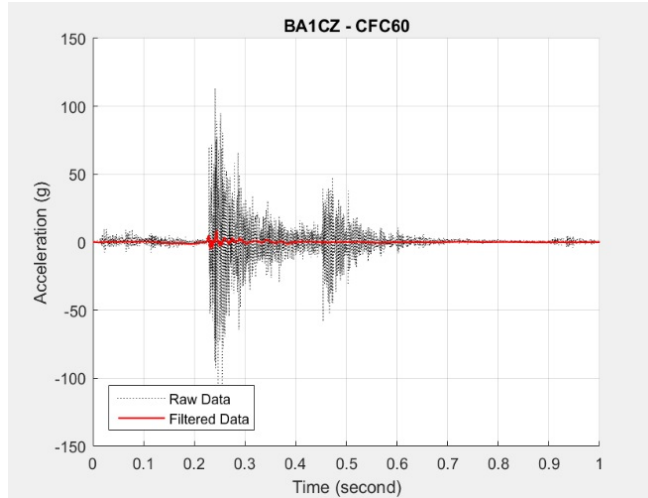
Figure B3. Raw and CFC60 Filtered Acceleration-time Data from BA1CZ
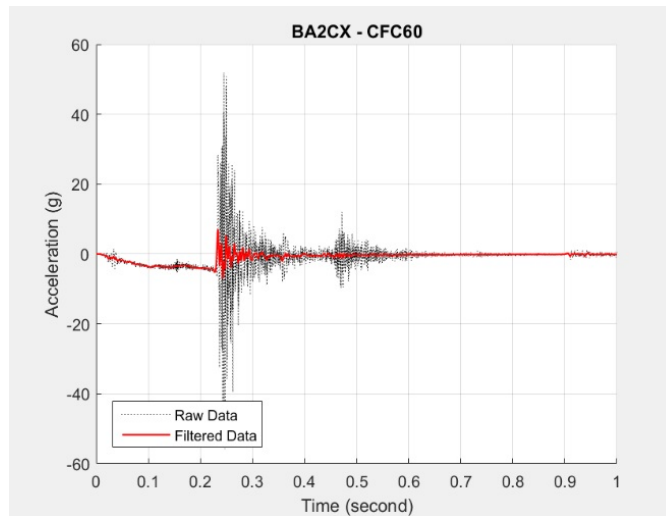
Figure B4. Raw and CFC60 Filtered Acceleration-time Data from BA2CX
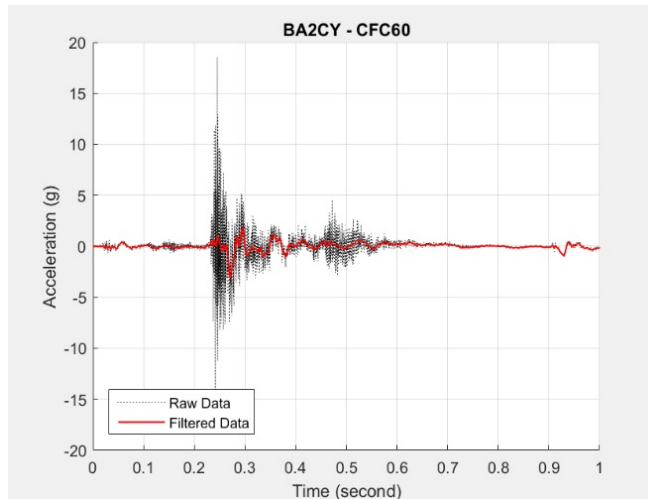
Figure B5. Raw and CFC60 Filtered Acceleration-time Data from BA2CY
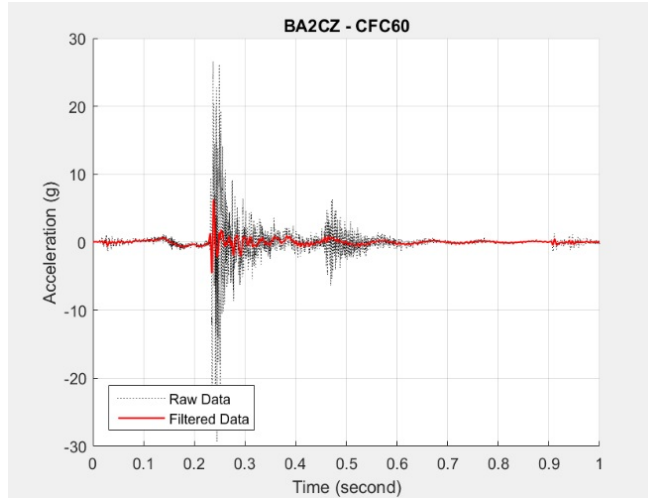
Figure B6. Raw and CFC60 Filtered Acceleration-time Data from BA2CZ
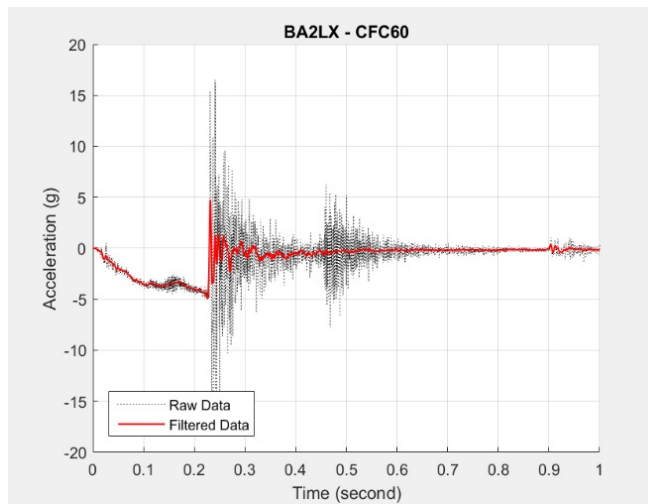
Figure B7. Raw and CFC60 Filtered Acceleration-time Data from BA2LX
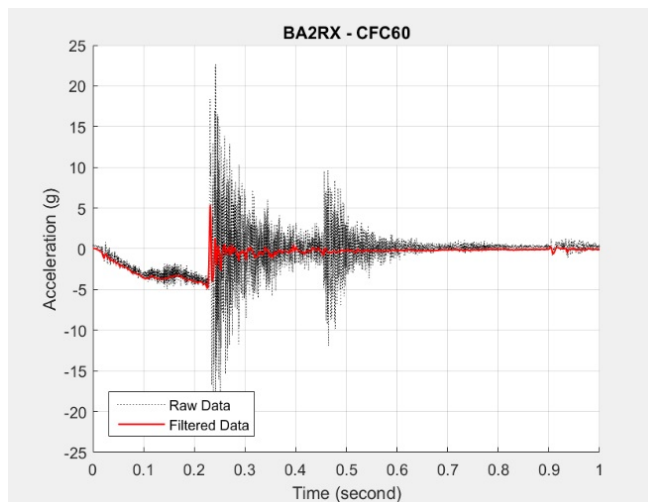
Figure B8. Raw and CFC60 Filtered Acceleration-time Data from BA2RX
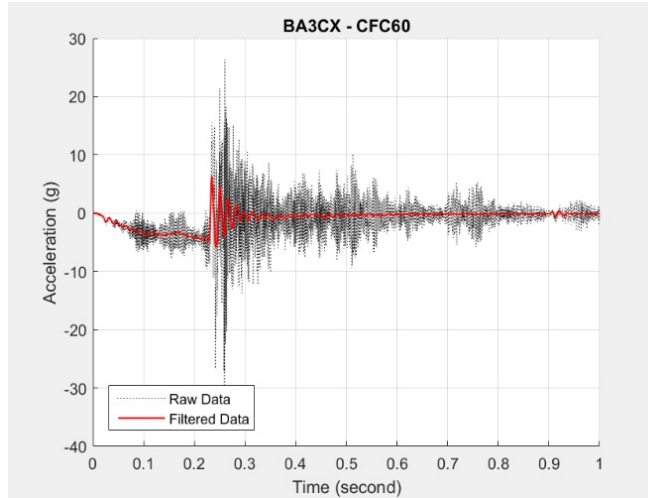
Figure B9. Raw and CFC60 Filtered Acceleration-time Data from BA3CX
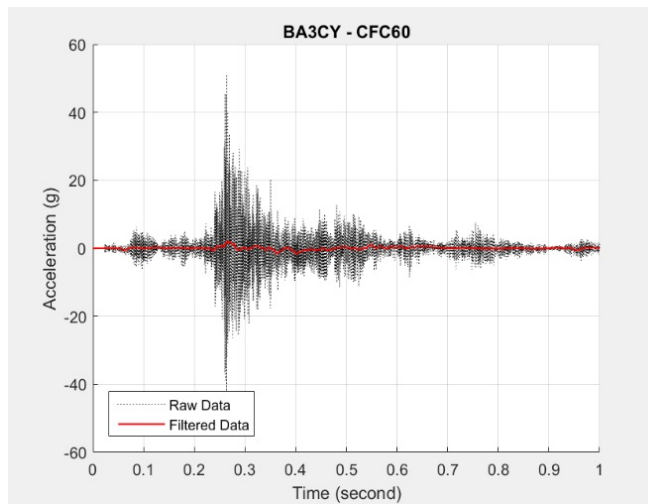
Figure B10. Raw and CFC60 Filtered Acceleration-time Data from BA3CY
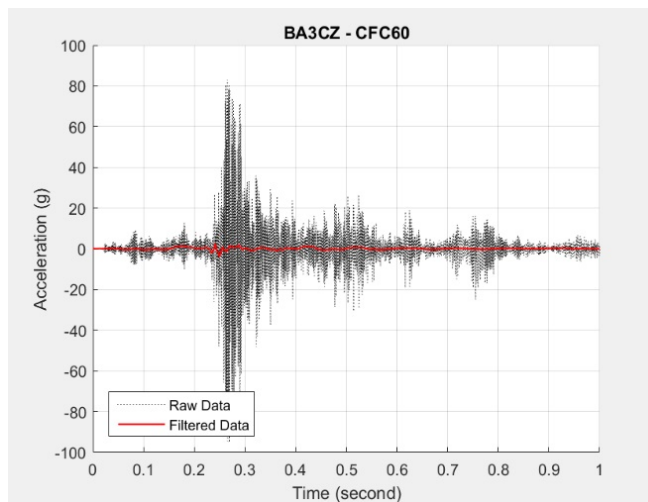
Figure B11. Raw and CFC60 Filtered Acceleration-time Data from BA3CZ

B2 – Pressures
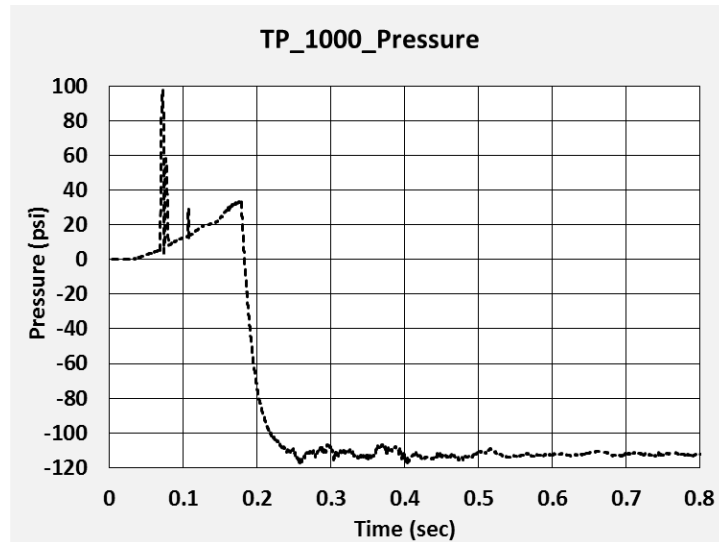
Figure B12. Raw Pressure-time Data from TP1000
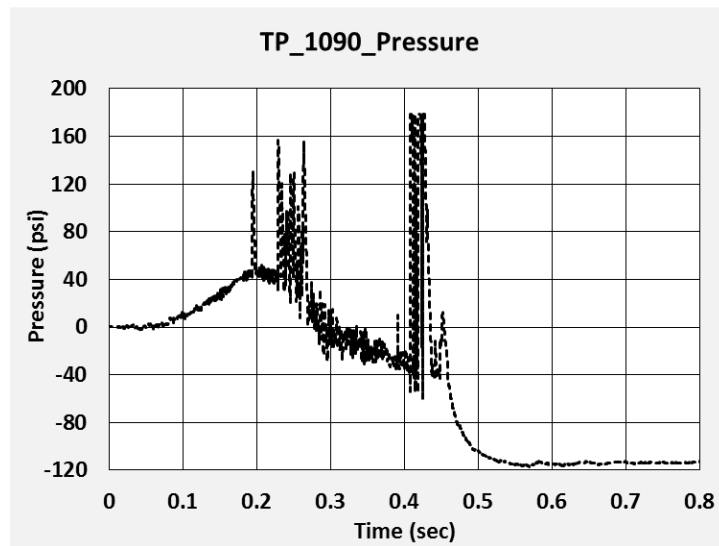
Figure B13. Raw Pressure-time Data from TP1090
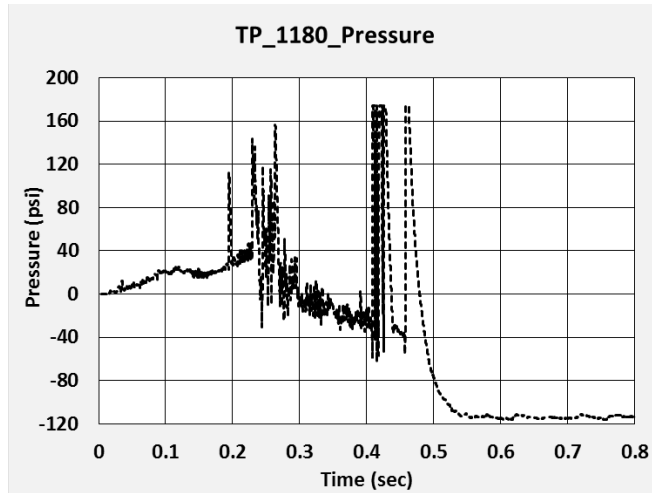
Figure B14. Raw Pressure-time Data from TP1180
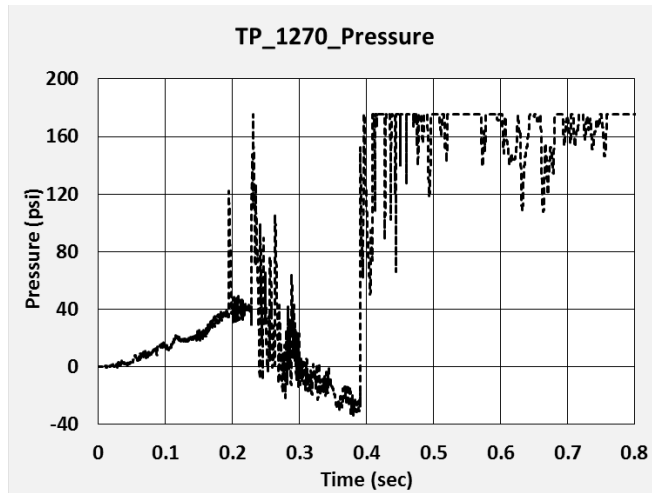
Figure B15. Raw Pressure-time Data from TP1270
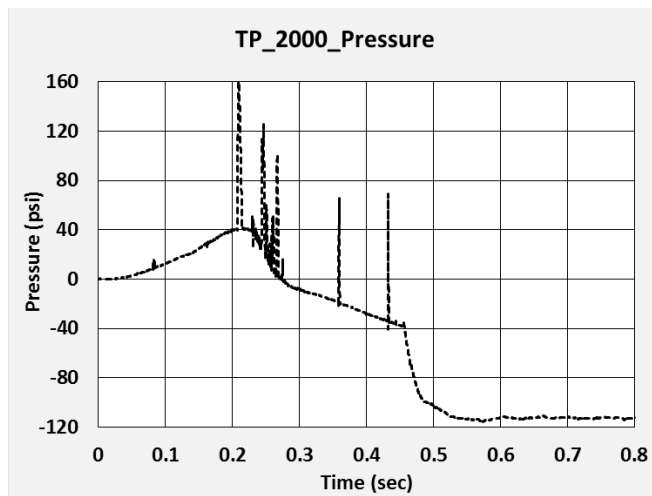
Figure B16. Raw Pressure-time Data from TP2000

70
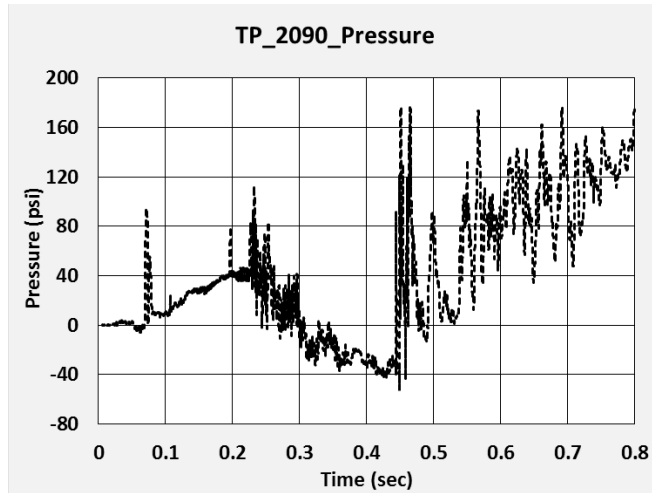
Figure B17. Raw Pressure-time Data from TP2090
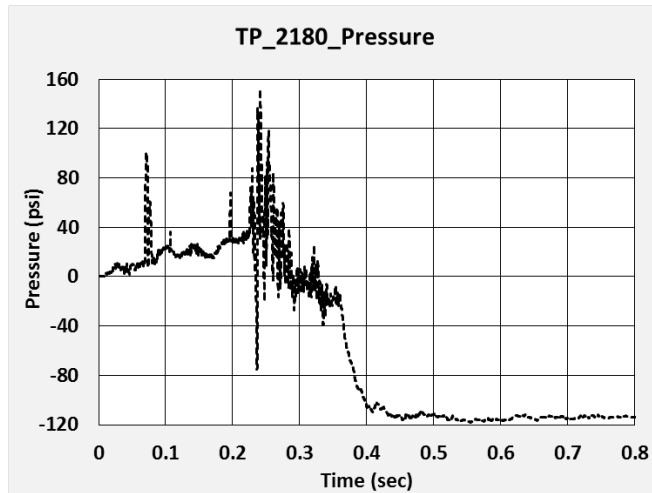
Figure B18. Raw Pressure-time Data from TP2180
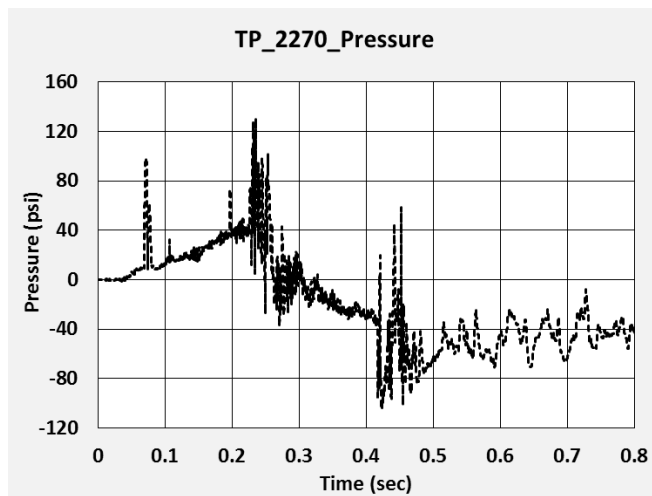
Figure B19. Raw Pressure-time Data from TP2270

71
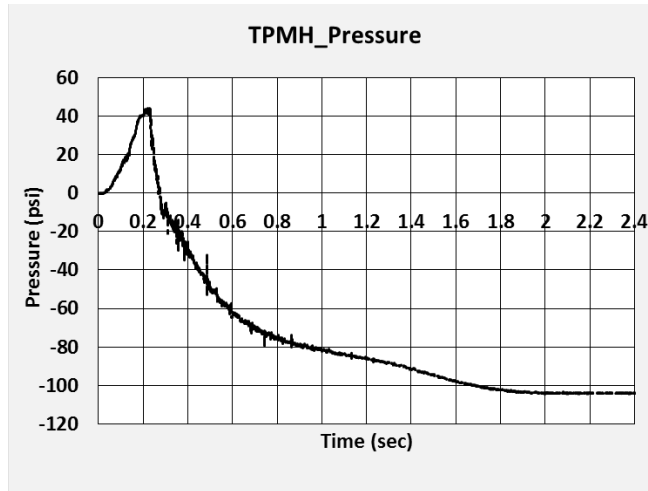
Figure B20. Raw Pressure-time Data from TPMH
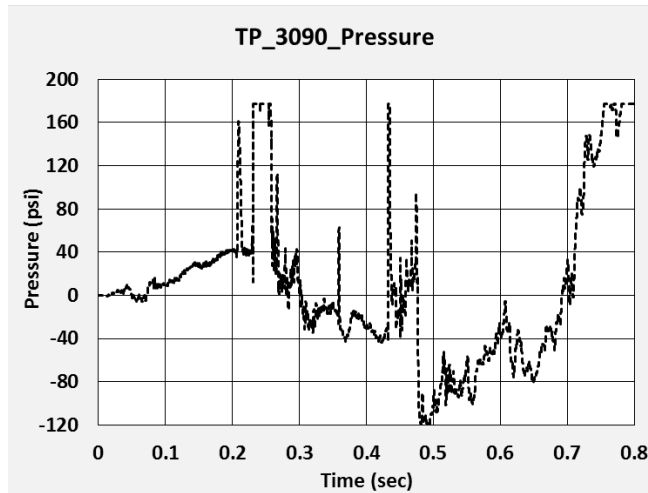
Figure B21. Raw Pressure-time Data from TP3090
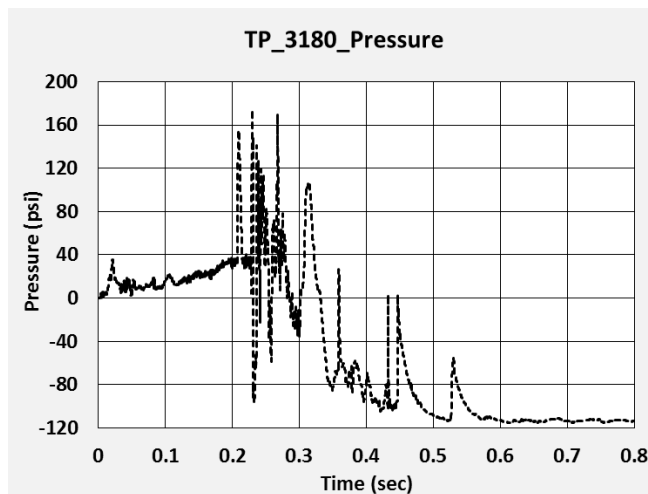
Figure B22. Raw Pressure-time Data from TP3180
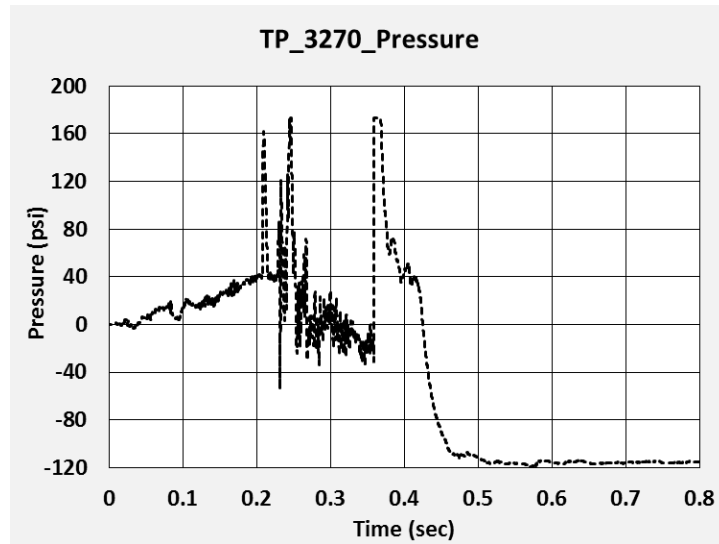
Figure B23. Raw Pressure-time Data from TP3270

B3 – Displacements
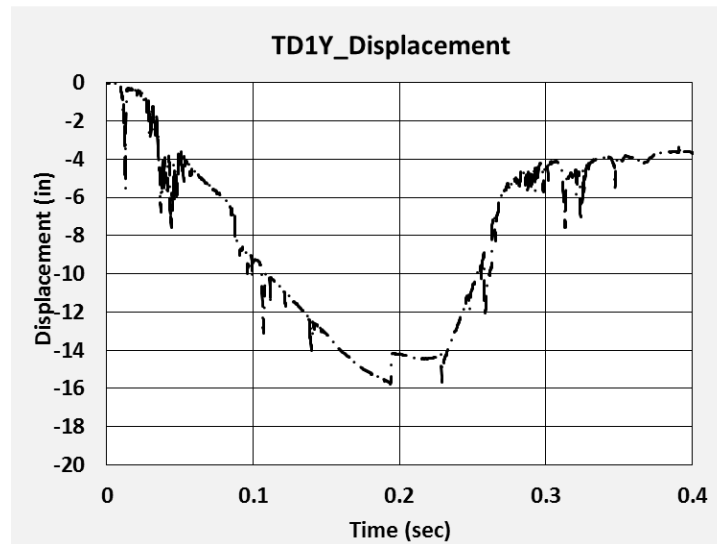
Figure B24. Raw Displacement-time Data from TD1Y
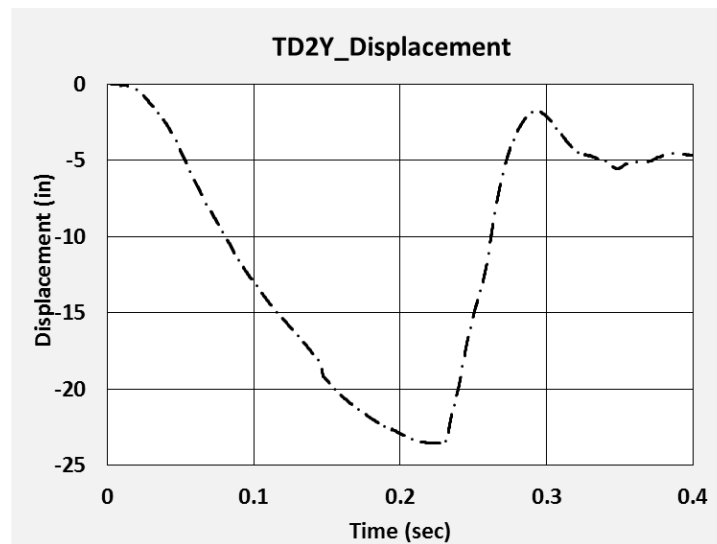
Figure B25. Raw Displacement-time Data from TD2Y
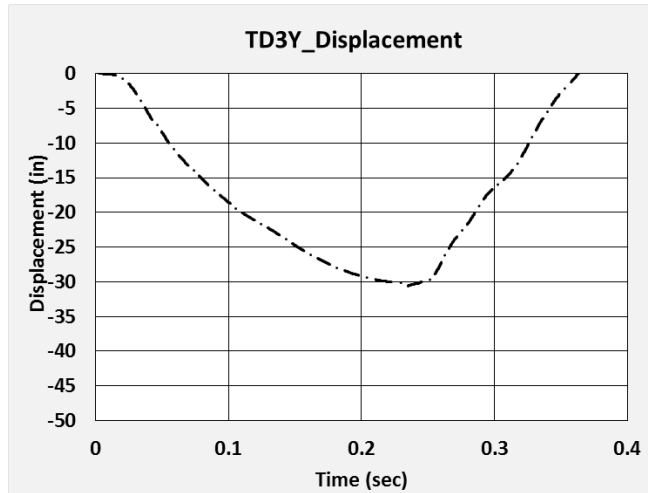
Figure B26. Raw Displacement-time Data from TD3Y
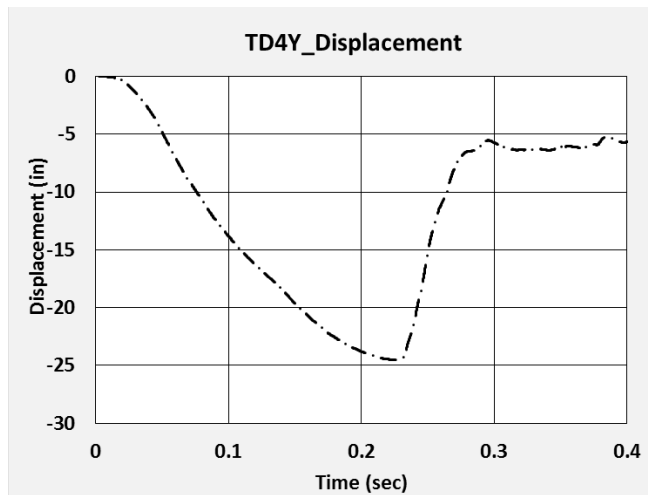
Figure B27. Raw Displacement-time Data from TD4Y
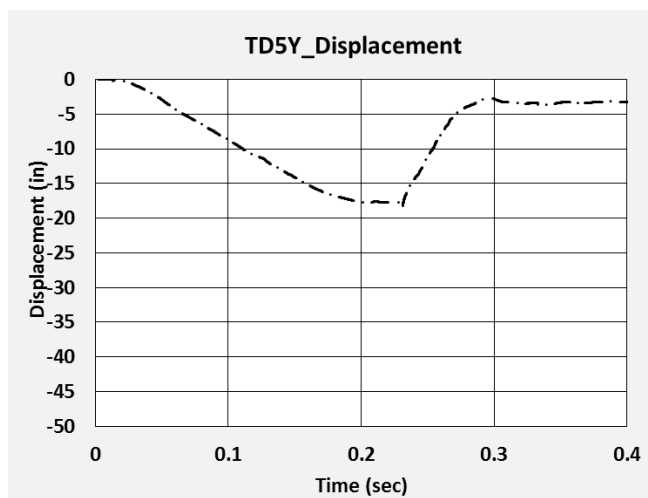
Figure B28. Raw Displacement-time Data from TD5Y
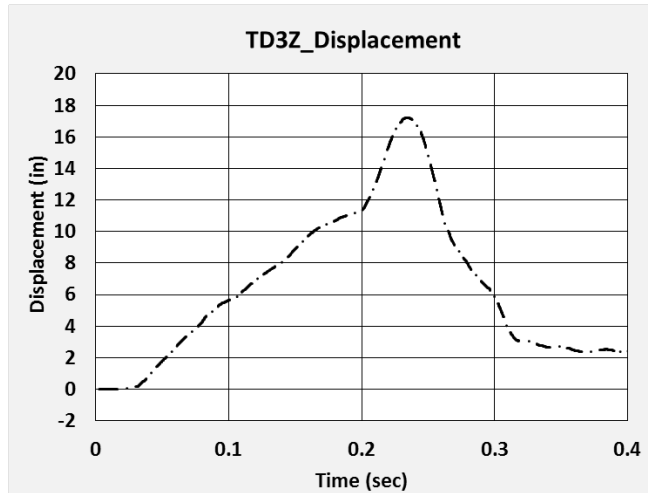
Figure B29. Raw Displacement-time Data from TD3Z
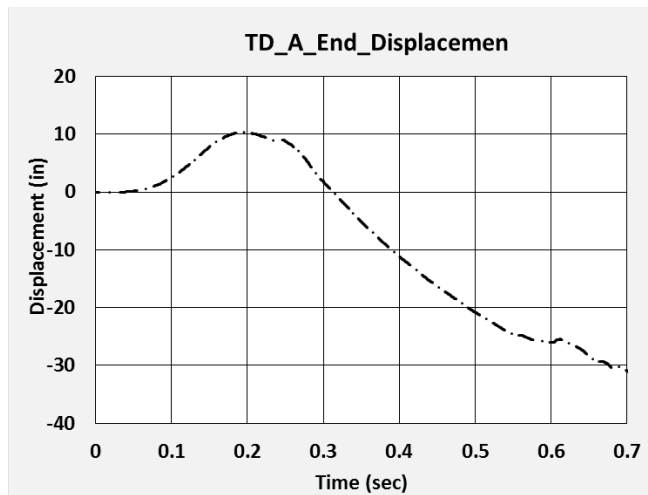
Figure B30. Raw Displacement-time Data from Displacement Transducer on A-End Head
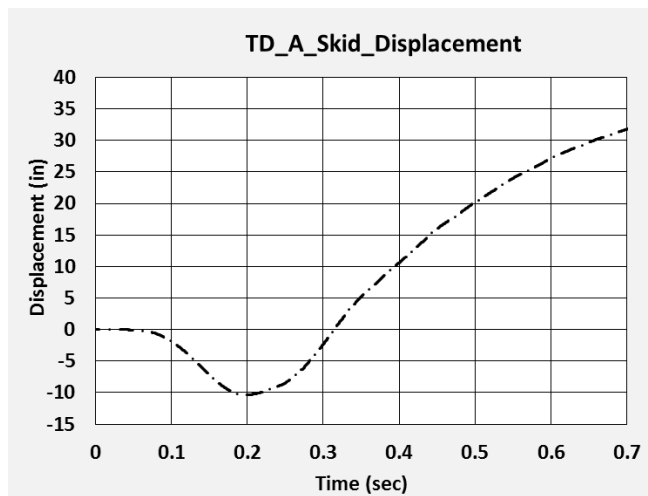
Figure B31. Raw Displacement-time Data from Displacement Transducer on A-End Skid

76
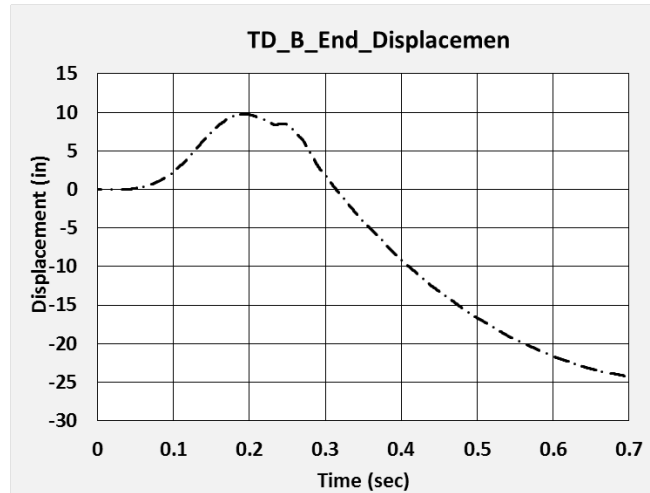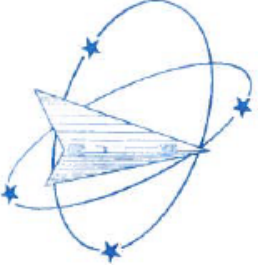
Figure B32. Raw Displacement-time Data from Displacement Transducer on B-End Head
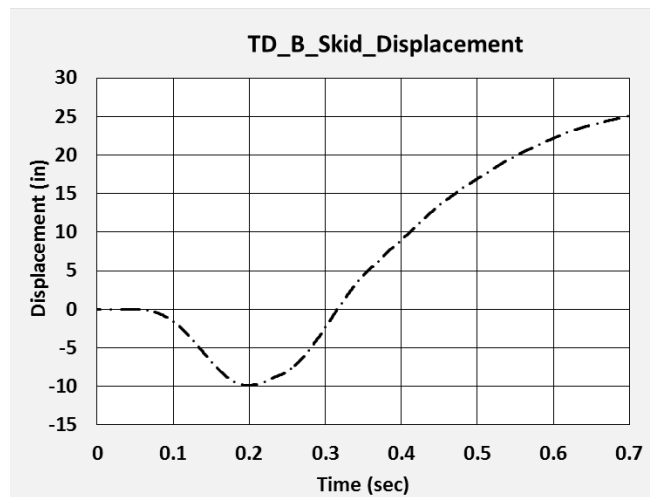
Figure B33. Raw Displacement-time Data from Displacement Transducer on B-End Skid

77

B4 – Material Characterization Results

Westmoreland Mechanical Testing & Research, Inc.
P.O.Box 388; 221 Westmoreland Drive
Youngstown, PA 15696-0388 U.S.A.
Telephone: 724-537-3131   Fax: 724-537-3151
Website: www.wmtr.com   E-Mail: admin@wmtr.com
WMT&R is a technical leader in the material testing industry.

TESTING CERT 621-01 & 621-02

CERTIFICATION

Section 1 of 1

June 6, 2016
Transportation Technology Center Inc.
55500 DOT Road
P.O. Box 11130
Pueblo, CO 81001

WMT&R Report No. 6-62761
P.O. No. 31686
WMT&R Quote No. QN162086 Rev.1

Attention: Przemyslaw Rakoczy

Subject: All processes, performed upon the material as received, were conducted at WMT&R, Inc. in accordance with the WMT&R Quality Assurance Manual, Rev. 11, dated 12/03/2008.
The following tests were performed on this order: TENSILE

TENSILE RESULTS: ASTM E8-15a
SPEED OF TESTING: 0.005 in./in./min.
MATERIAL: Carbon Steel

DISPOSITION: Report

Sample	TestLog Number	Temp.	UTS ksi	0.2% YS ksi	Elong %	RA %	Modulus Msi	Ult. Load lbf	0.2% YLD. lbf	Orig. Dia. (in.)	Final Dia. (in.)	4D Orig GL (in.)	4D Final GL (in.)	Orig. Area (sq. in.)	Machine Number	A\U\R
R1-S1	Z02006	Room	94.4	69.5	21	48	31.4	18574	13685	0.5006	0.3599	2.00	2.42	0.19682106	M10	R
R1-S2	Z02007	Room	94.7	69.7	22	49	30.1	18623	13715	0.5004	0.3589	2.00	2.43	0.19666383	M10	R
R1-S3	Z02008	Room	94.5	70.6	22	49	31.5	18603	13902	0.5007	0.3578	2.00	2.44	0.19689970	M10	R
R2-S1	Z02009	Room	94.0	70.2	22	52	31.9	18528	13832	0.5009	0.3487	2.00	2.44	0.19705704	M10	R
R2-S2	Z02010	Room	93.9	70.8	21	41	34.0	18520	13957	0.5010	0.3836	2.00	2.41	0.19713572	M10	R
R2-S3	Z02011	Room	94.1	70.6	21	47	32.6	18575	13930	0.5012	0.3657	2.00	2.42	0.19729315	M10	R

A\U\R: A=ACCEPTABLE, U=UNACCEPTABLE, R=REPORT

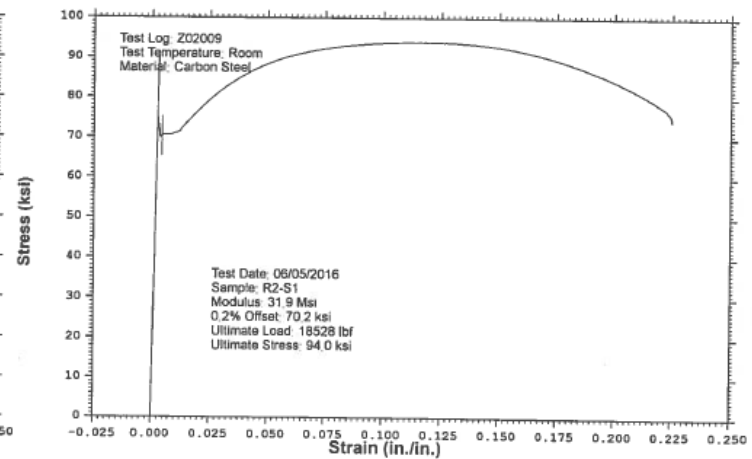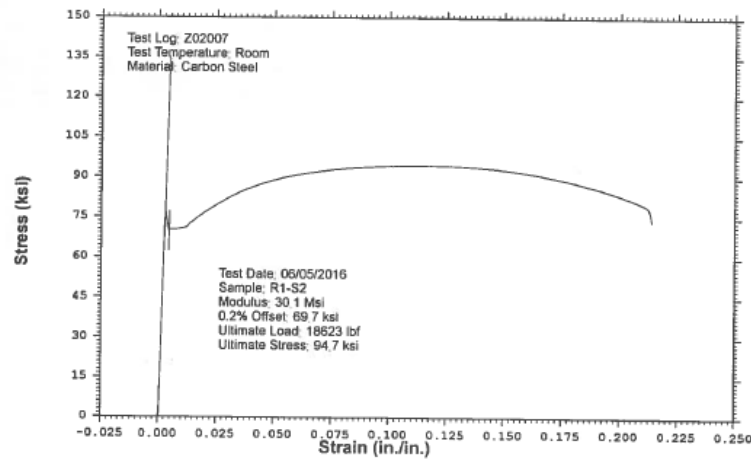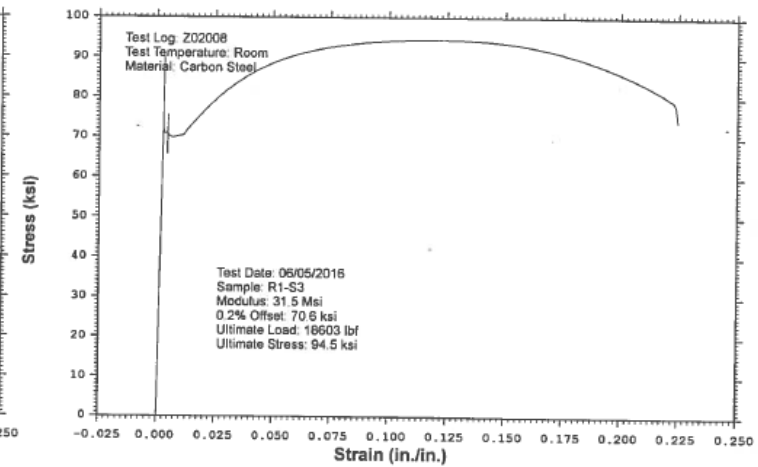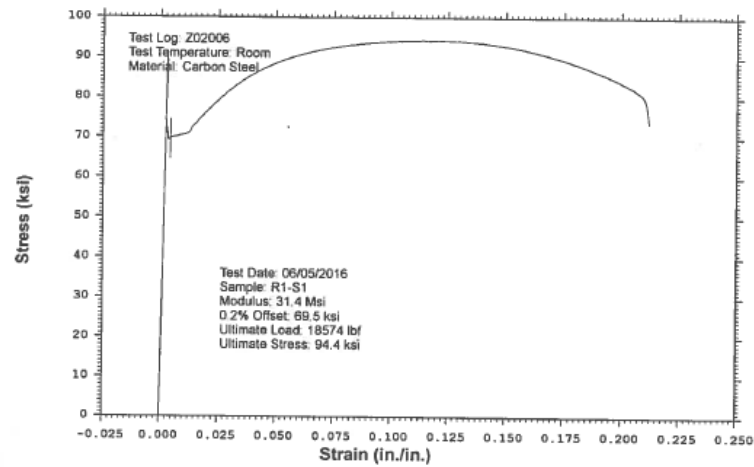**Figure B34. Page 1 of Material Tensile Test Report**

Figure B35. Page 2 of Tensile Test Report Showing Stress-strain Responses
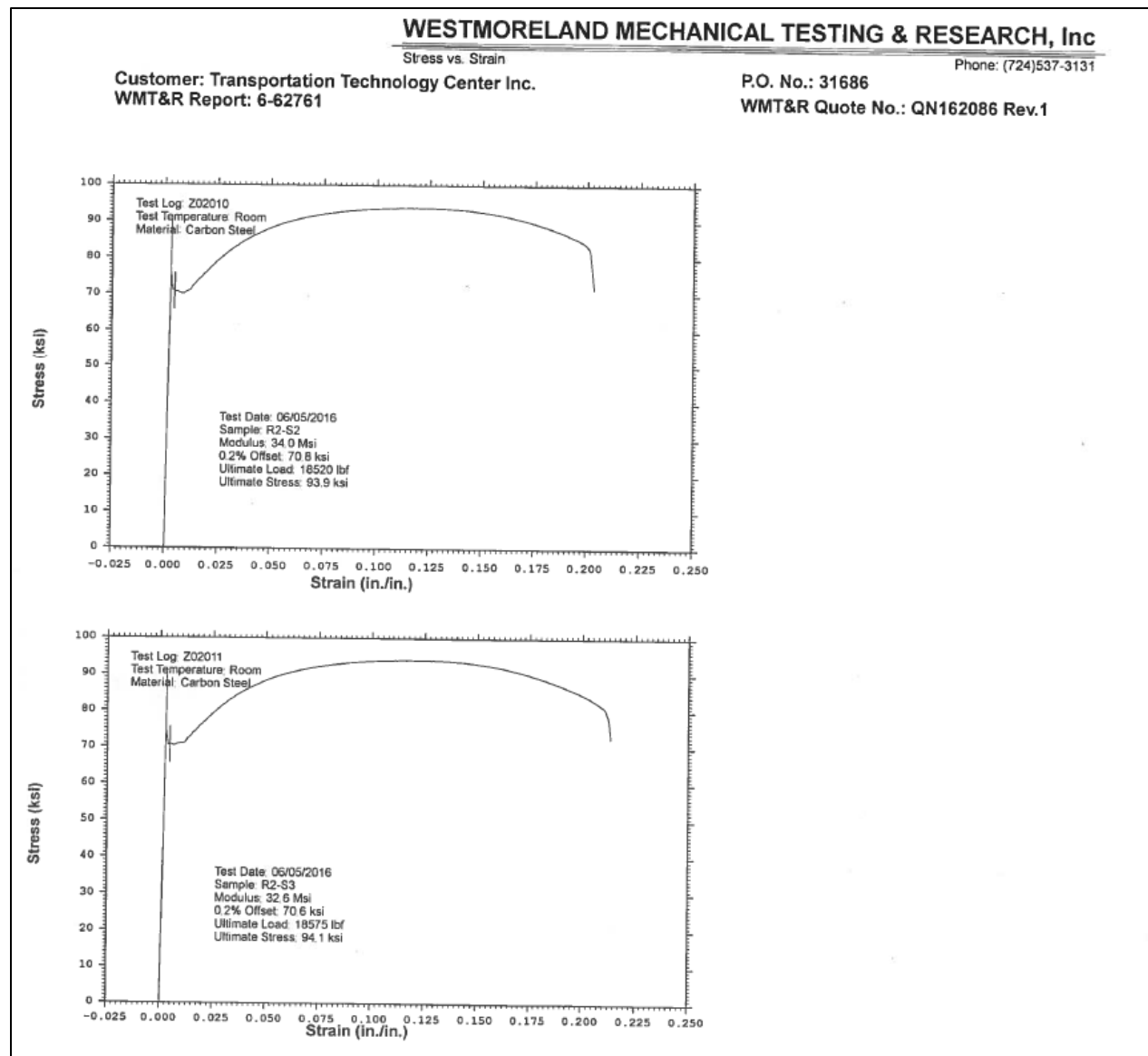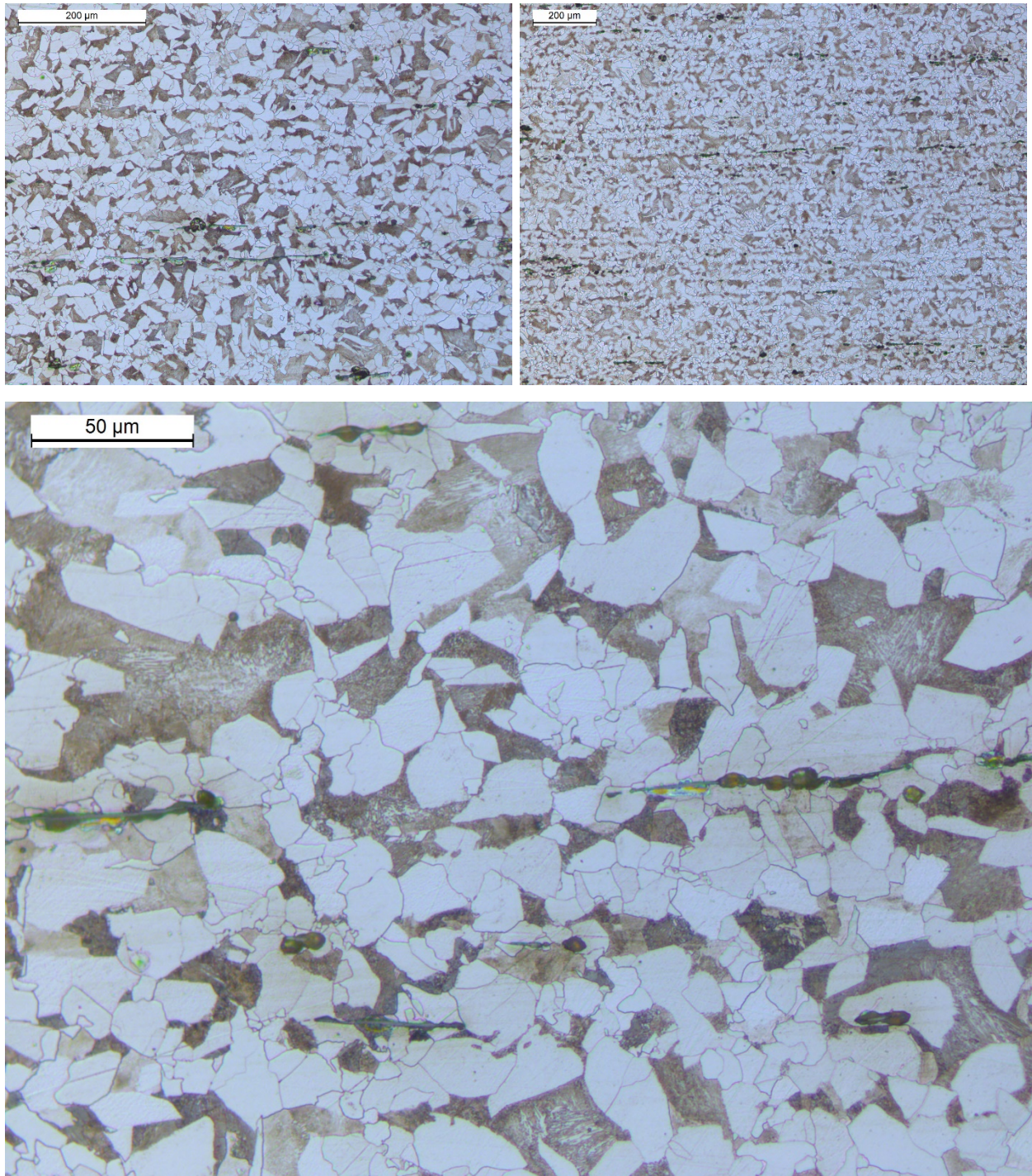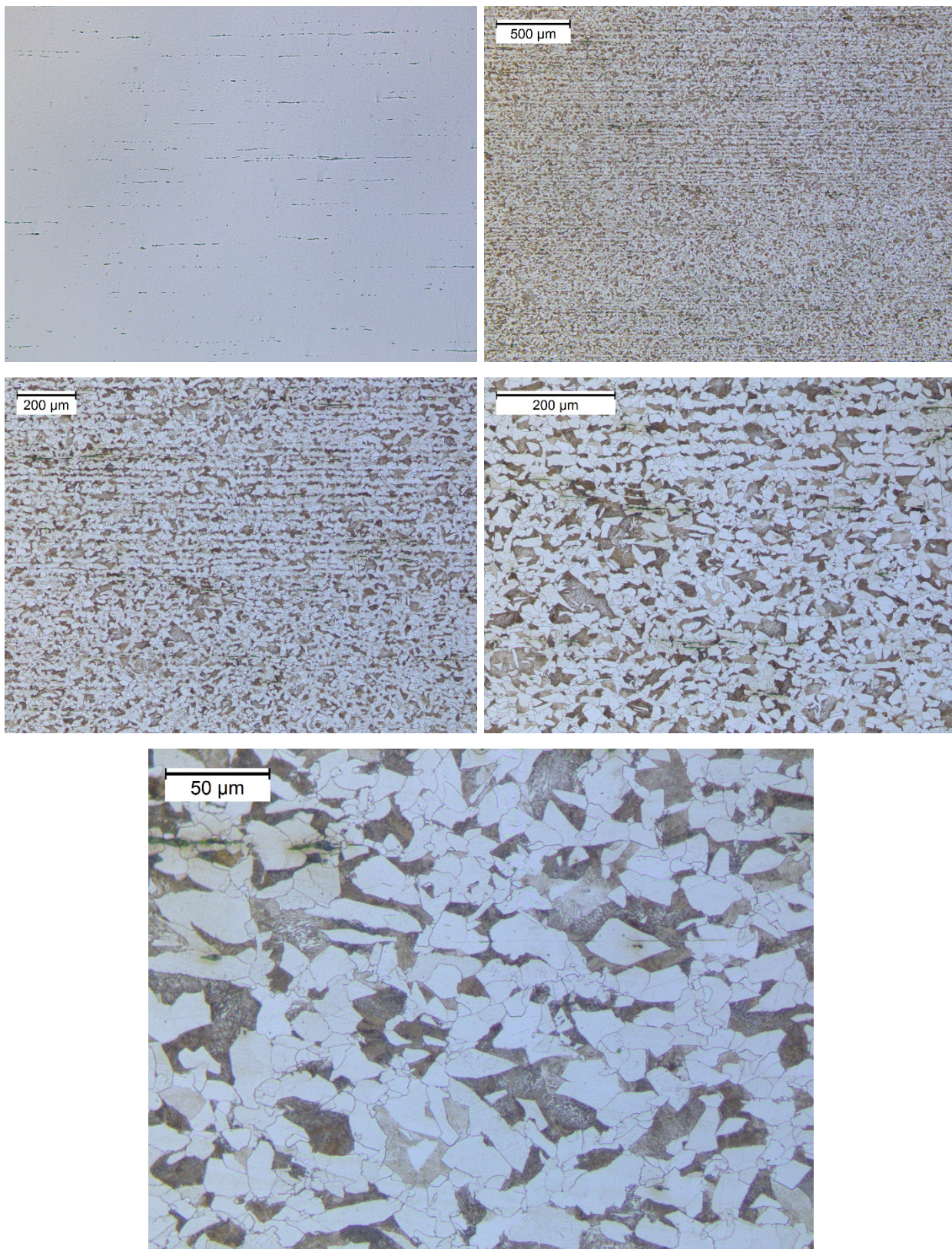
Figure B36. Page 3 of Tensile Test Report Showing Stress-strain Responses
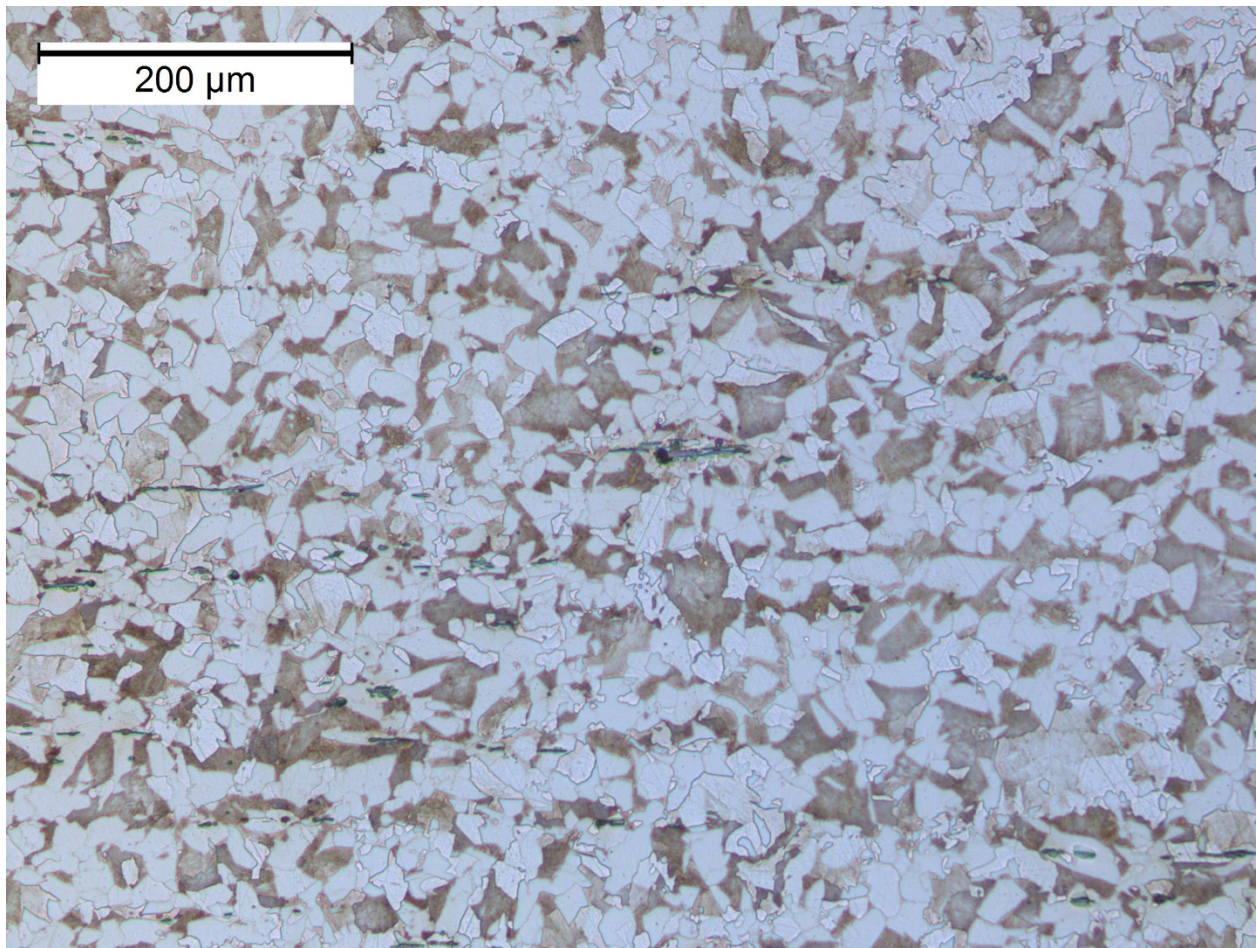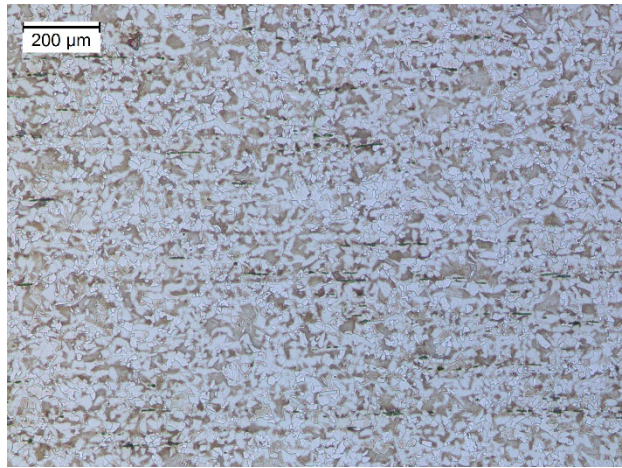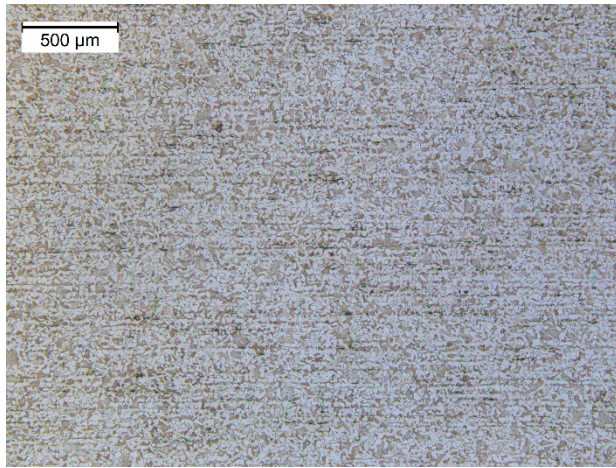
B5 – Microstructure Analysis

Figure B37. Sample 1

Figure B38. Sample 2

Figure B39. Sample 3

Appendix C.
Finite Element Analysis and Test Results

## C1 – Pre-test FEA and Test Results—New Normalized TC128 Steel

The pre-test model run at 15 mph with New Normalized TC128 steel experienced puncture. Thus, the pre-test FE model results presented in the following series of plots (Figure C1 through Figure C11) end at approximately 0.23 second of simulated impact, as that is when the model punctured.
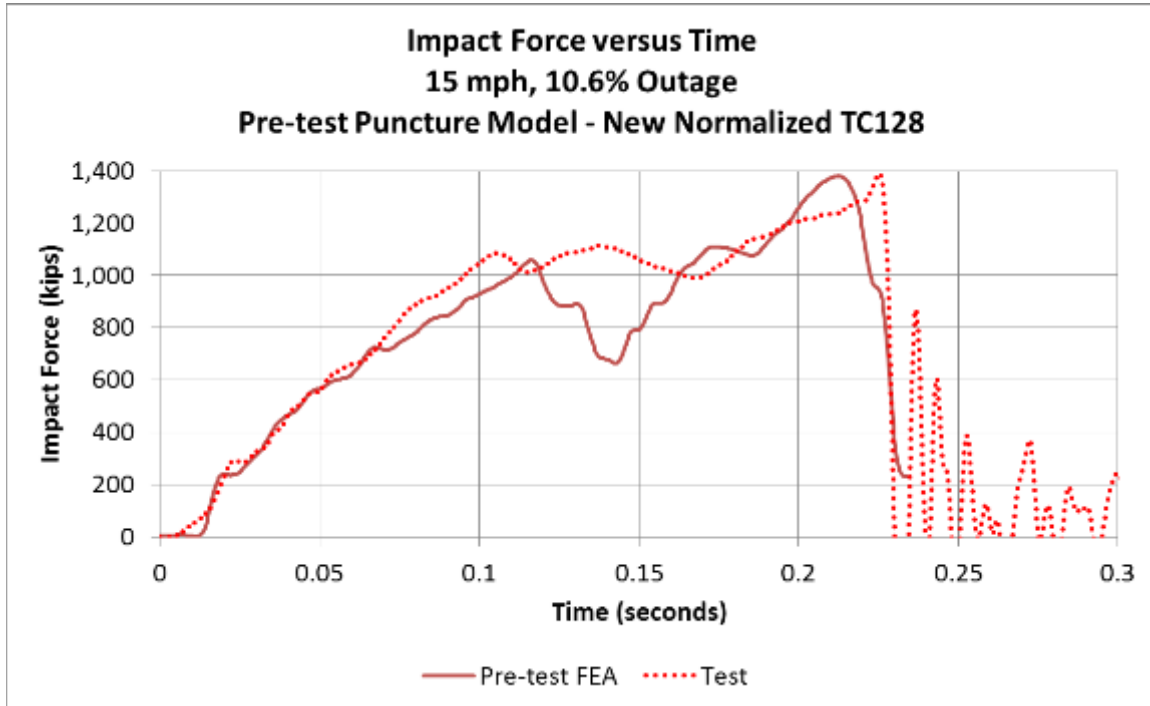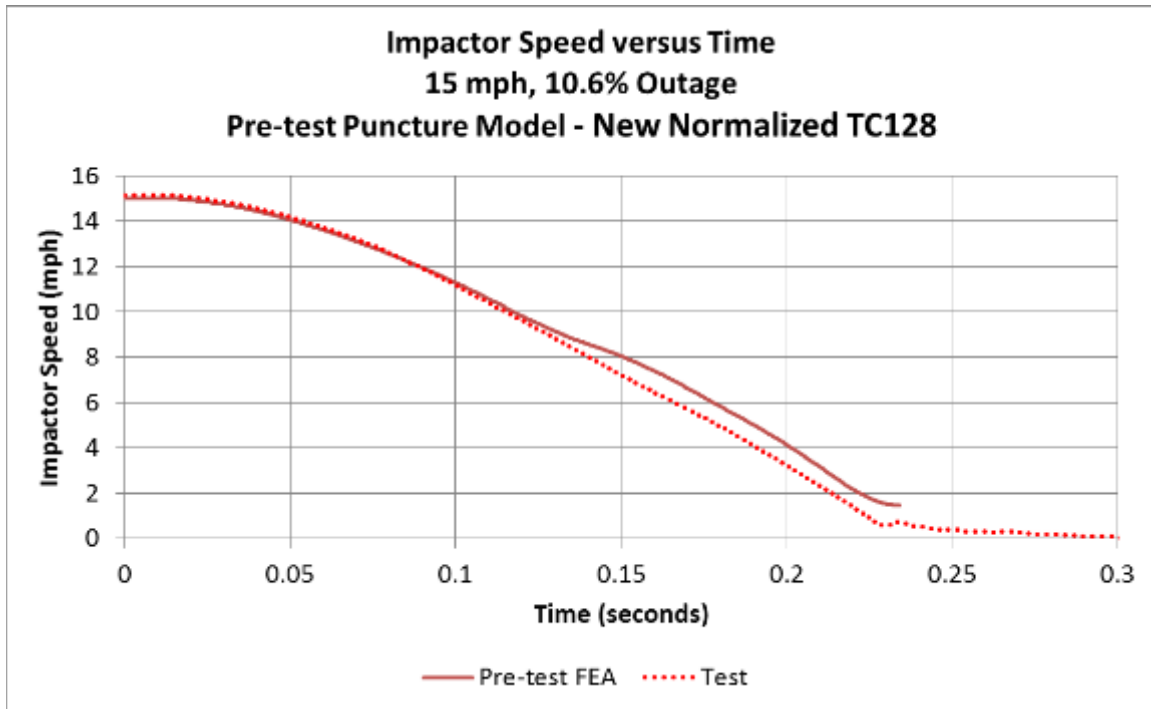

Figure C1. Impact Force versus Time, 15 mph Pre-test FEA with New Normalized TC128 and Test Data
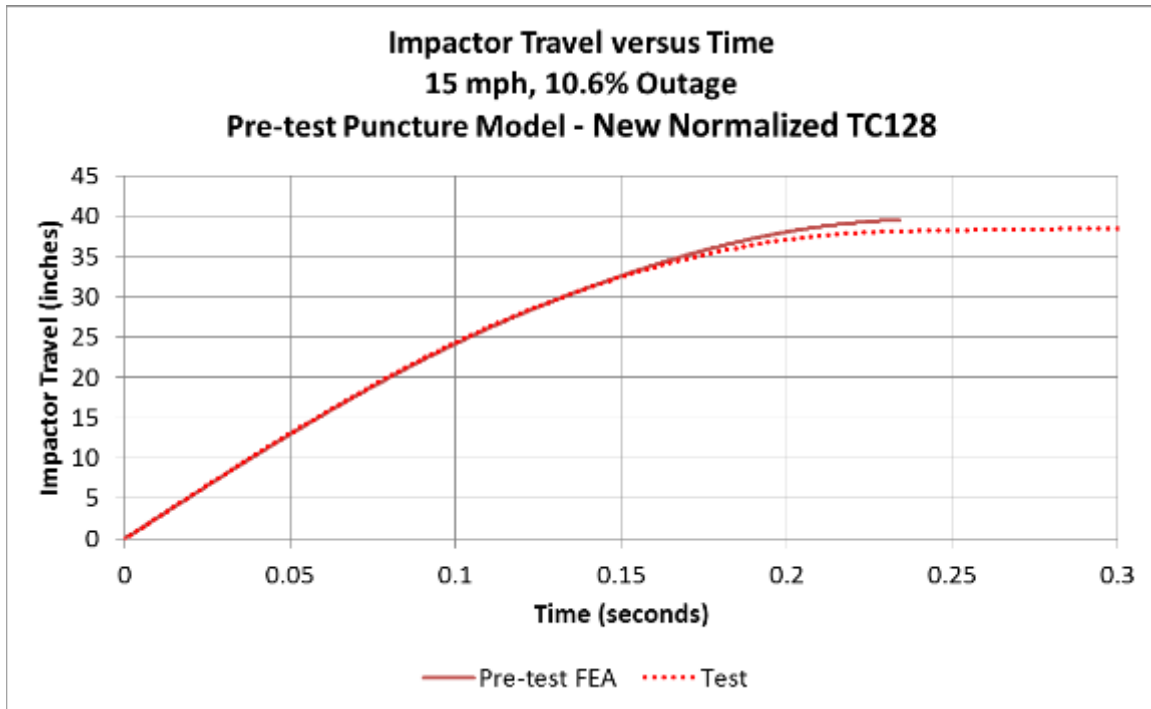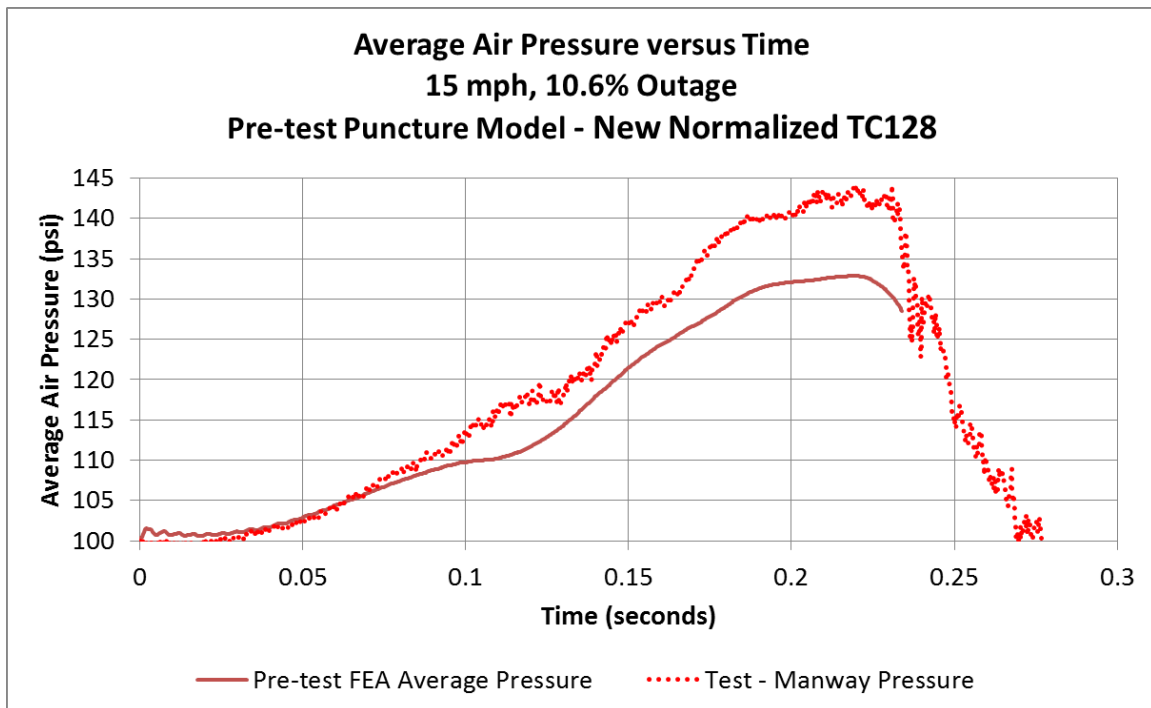
**Figure C2. Impactor Travel versus Time, 15 mph Pre-test FEA with
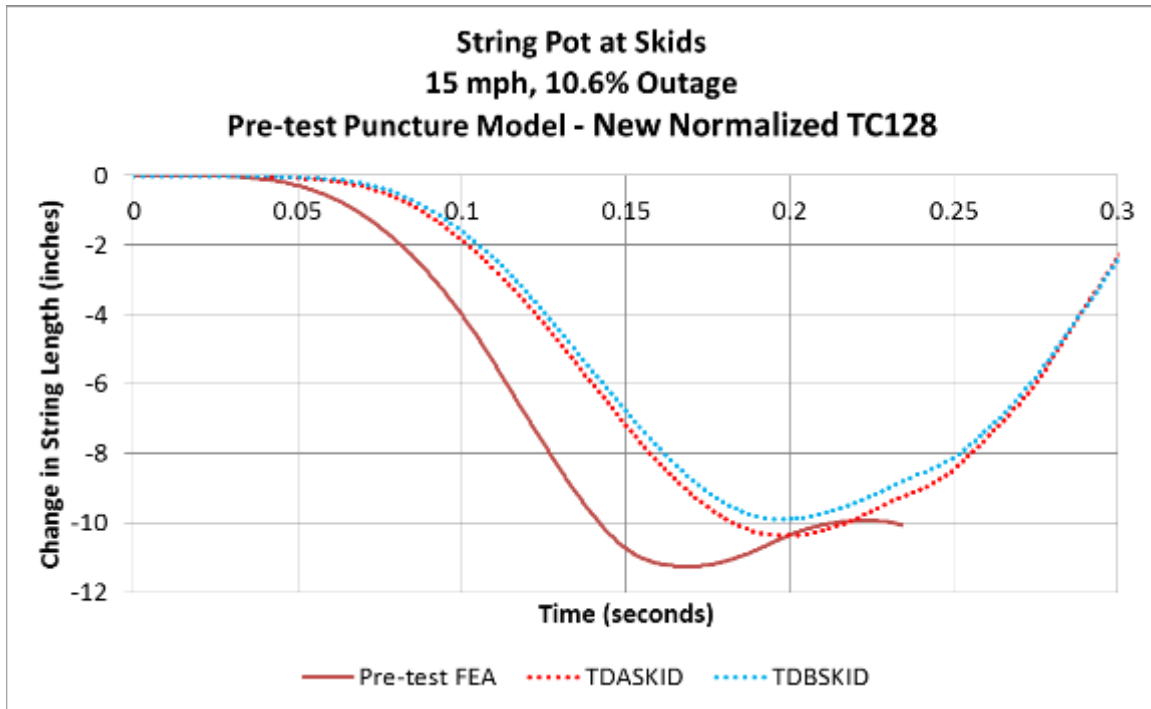New Normalized TC128 and Test Data**
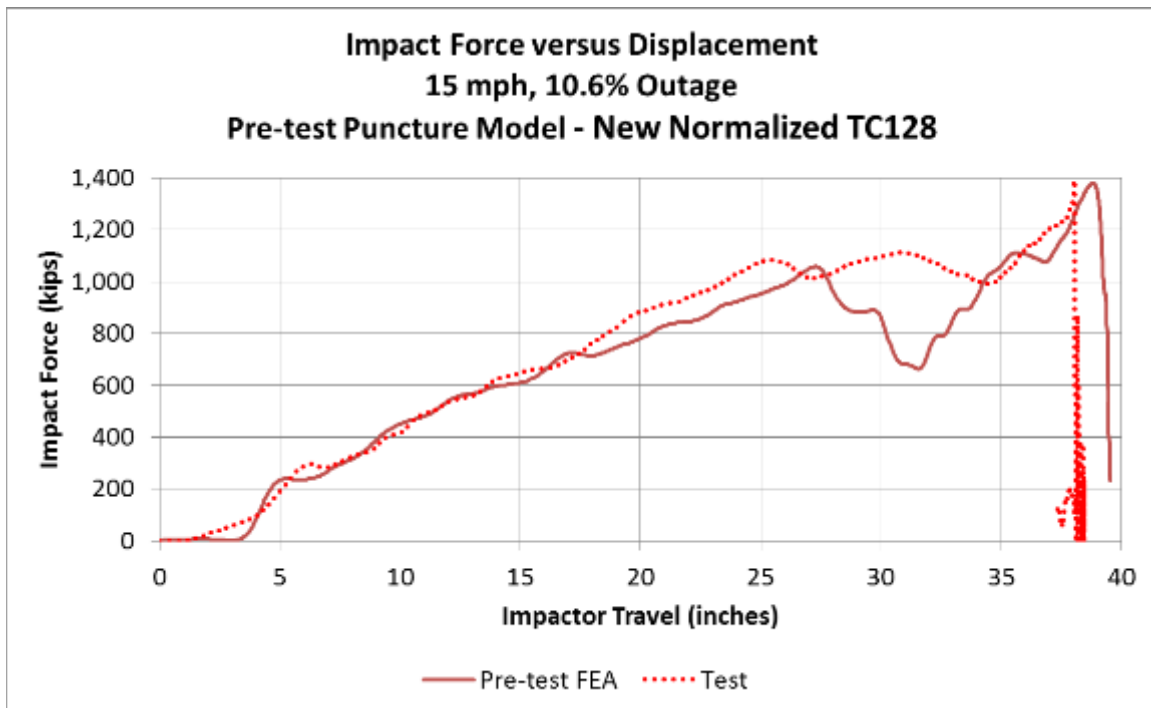
**Figure C3. Impact Force versus Impactor Travel, 15 mph Pre-test FEA with
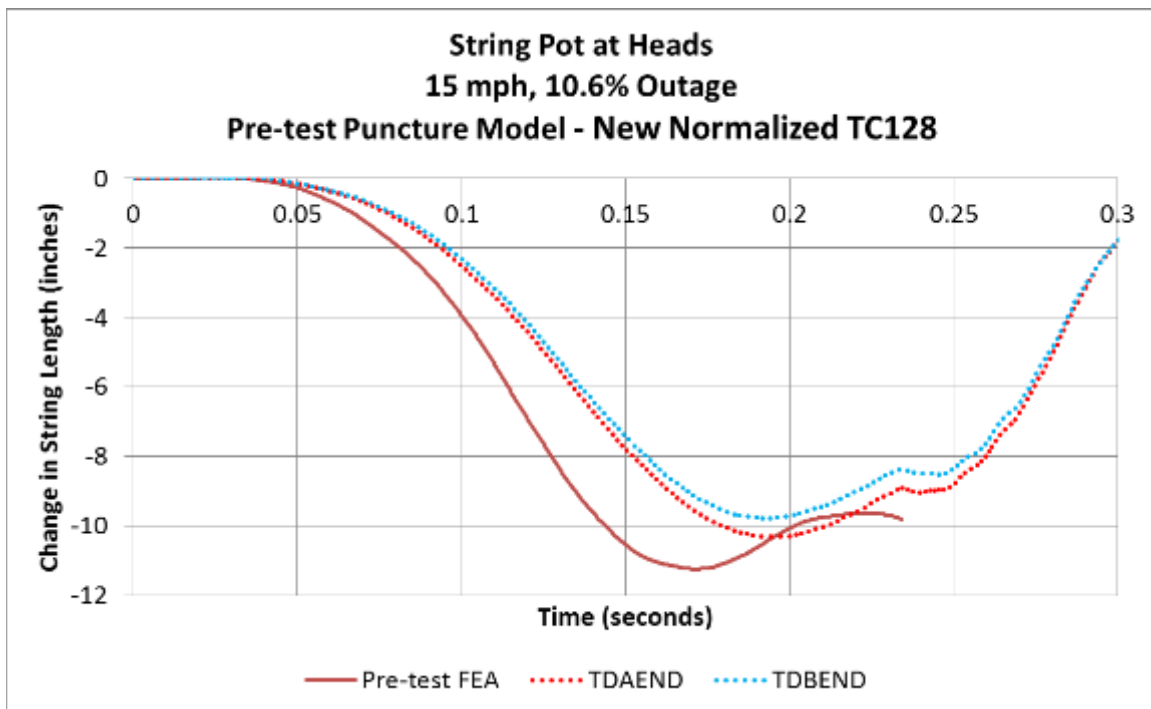New Normalized TC128 and Test Data**

Figure C4. Impactor Speed versus Time, 15 mph Pre-test FEA with New Normalized TC128 and Test Data
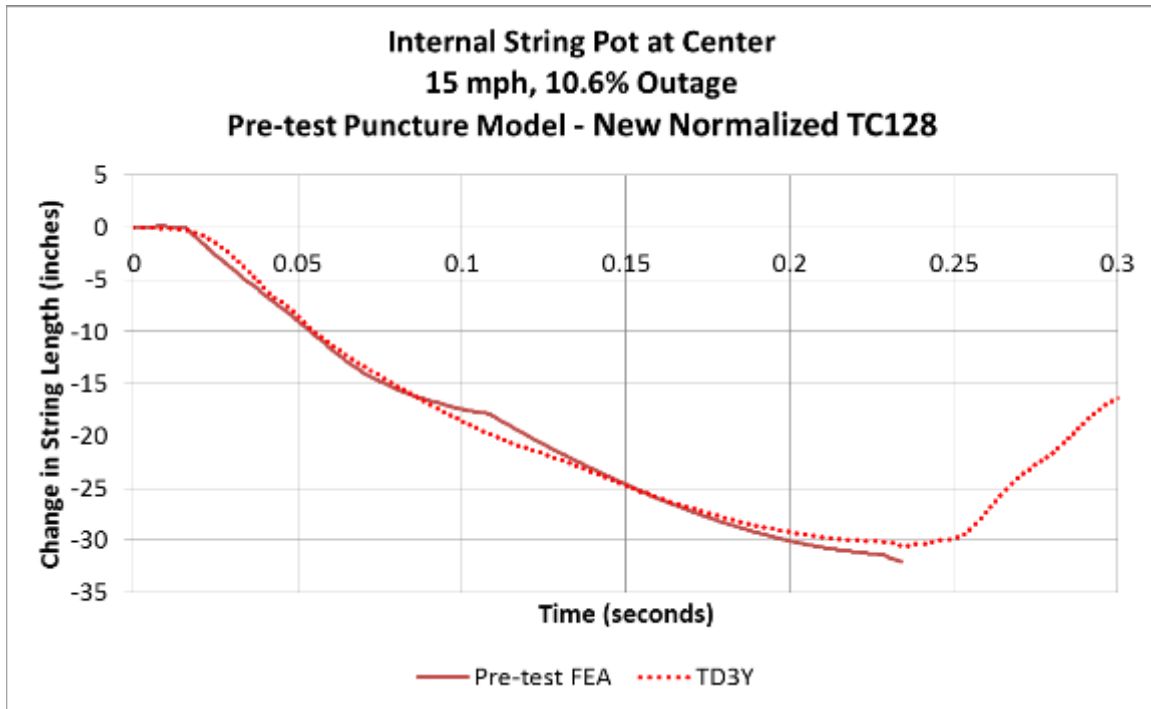

Figure C5. **Average Air Pressure versus Time, 15 mph Pre-test FEA with New Normalized TC128 and Test Data**

Figure C6. String Potentiometers at Skids, 15 mph Pre-test FEA with New Normalized TC128 and Test Data
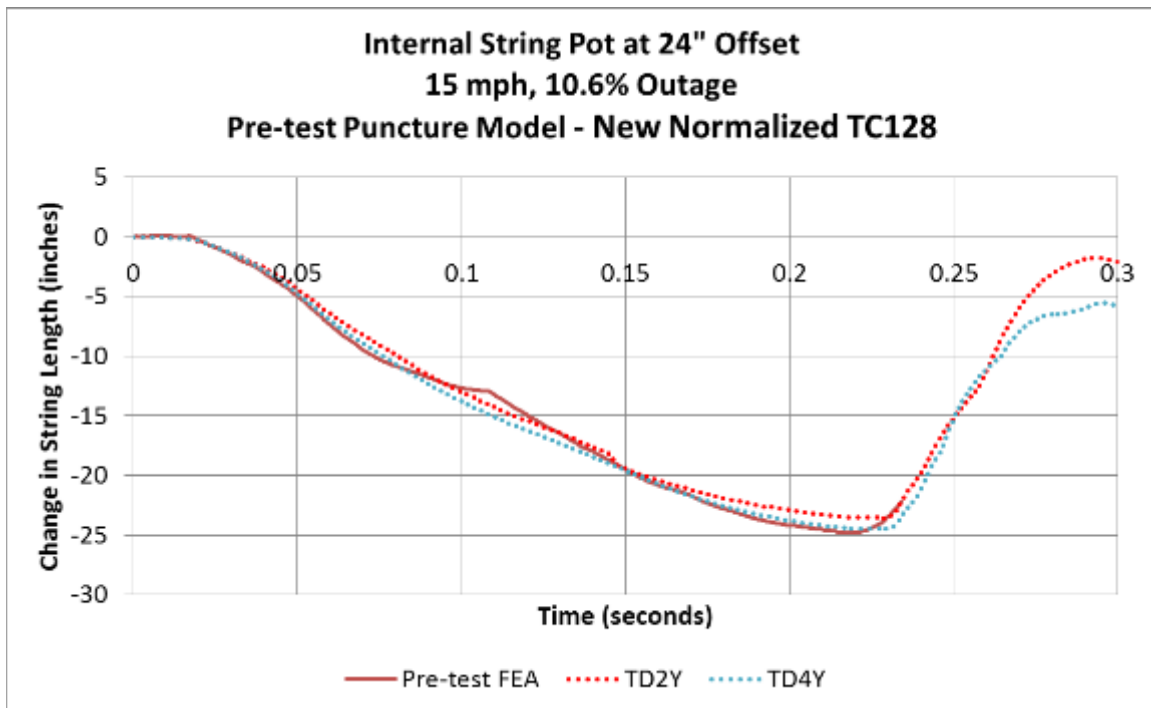

Figure C7. String Potentiometers at Heads, 15 mph Pre-test FEA with New Normalized TC128 and Test Data

**Figure C8. Internal String Potentiometer at Center of Tank, 15 mph
Pre-test FEA with New Normalized TC128 and Test Data**
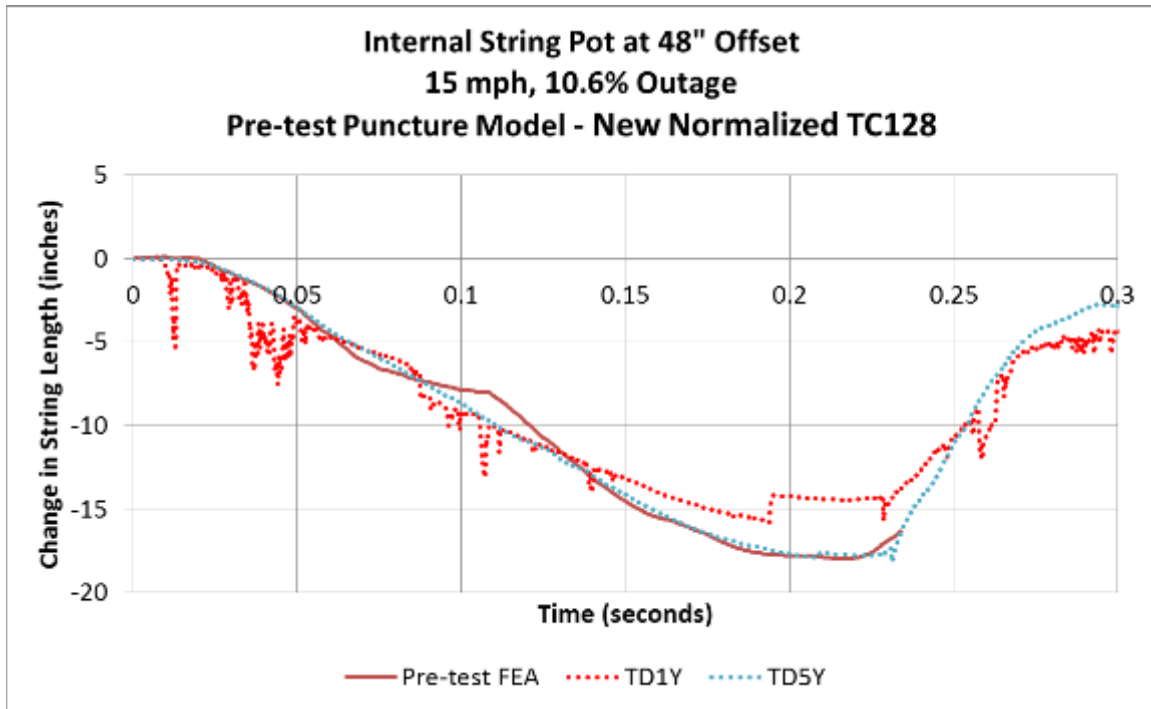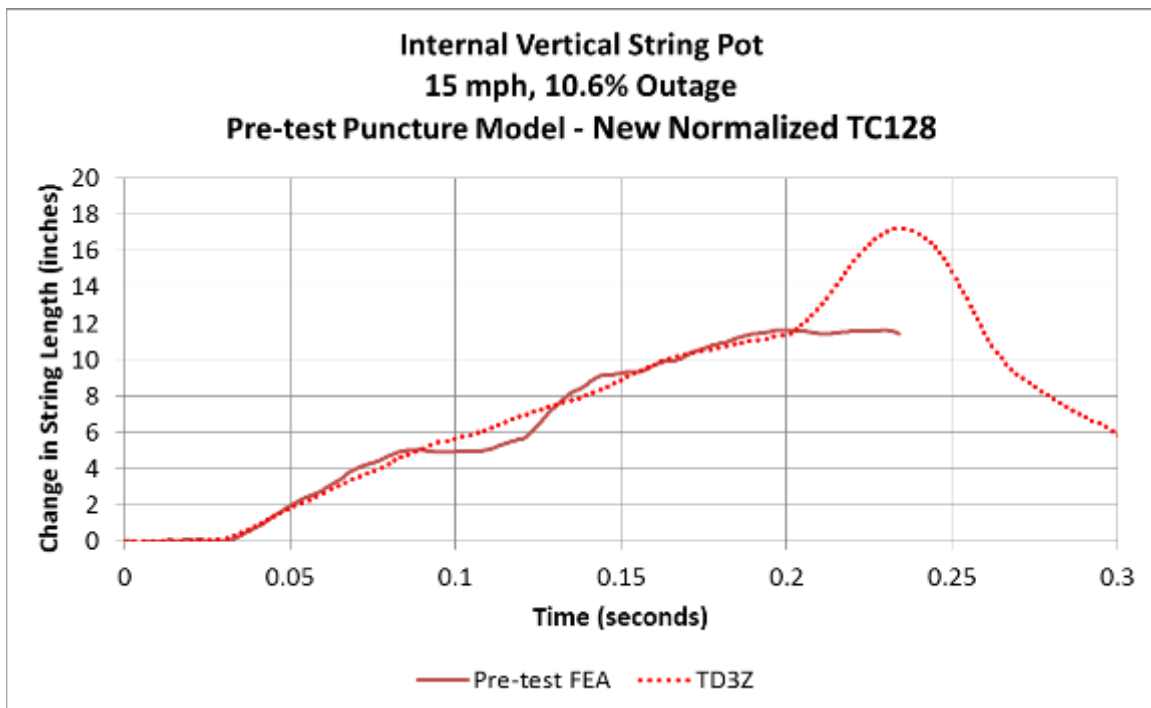

**Figure C9. Internal String Potentiometers 24 inches from Impact, 15 mph
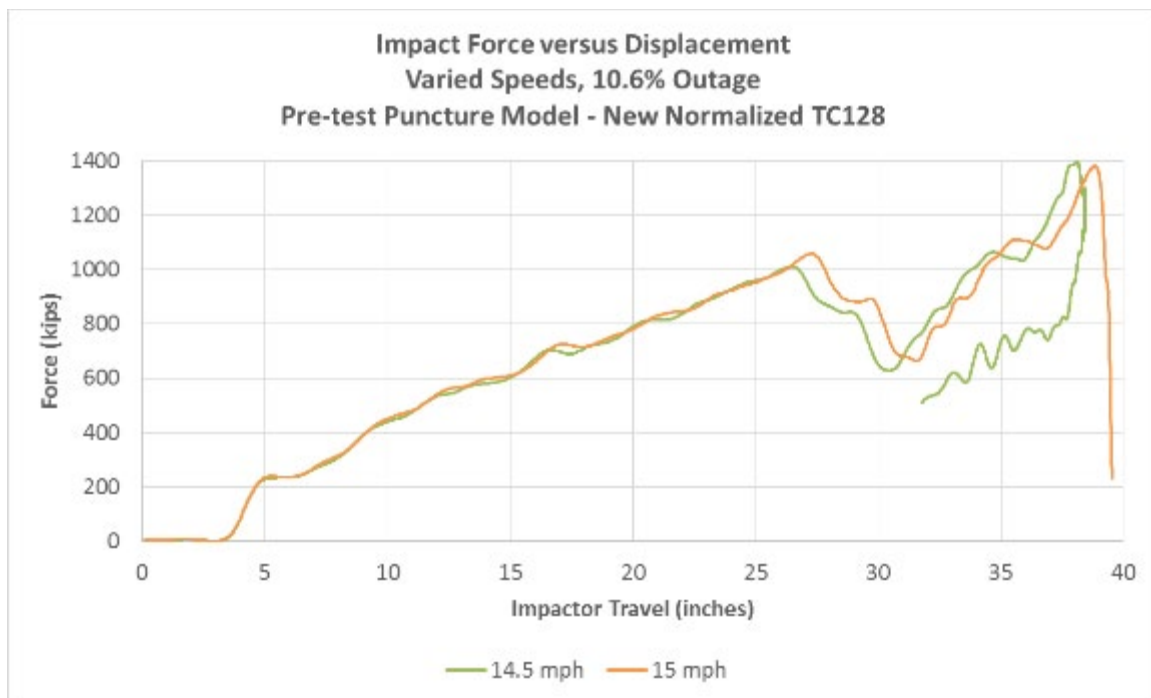Pre-test FEA with New Normalized TC128 and Test Data**

Figure C10. Internal String Potentiometers 48 inches from Impact, 15 mph Pre-test FEA with New Normalized TC128 and Test Data

Figure C11. Internal Vertical String Potentiometer, 15 mph Pre-test FEA with New Normalized TC128 and Test Data

In addition to running the pre-test model with New Normalized TC128 steel at 15 mph, a series of iterative simulations was used to estimate the range of speeds that would define the threshold between a puncture simulation and a non-puncture simulation. The model was found to puncture at an impact speed of 15 mph, but did not fully puncture at a 14.5 mph impact. The force versus displacement responses from these two pre-test FE simulations are shown in Figure C12. In this figure, the non-puncture nature of the 14.5 mph simulation is apparent, as the impactor rebound can be observed after the peak force is reached. In the 15-mph simulation, the impactor continues moving in its initial direction after the tank has punctured. Thus, the model estimates that the threshold speed between a puncture and a non-puncture outcome is somewhere between 14.5 and 15 mph for the New Normalized TC 128 material model.

**Figure C12. Impact Force versus Impactor Travel, 14.5 and 15 mph
Pre-test FEA with New Normalized TC128**

C2 – Pre-test FEA and Test Results—Test 2 TC128 Steel

The pre-test model run at 15 mph with Test 2 TC128 did not experience puncture. The pre-test models were run for approximately 0.275 second, which was long enough to allow the impactor to rebound from the tank car. The pre-test FE model results presented in the following series of plots (Figure C13 through Figure C23) end at approximately 0.275 seconds of simulated impact.
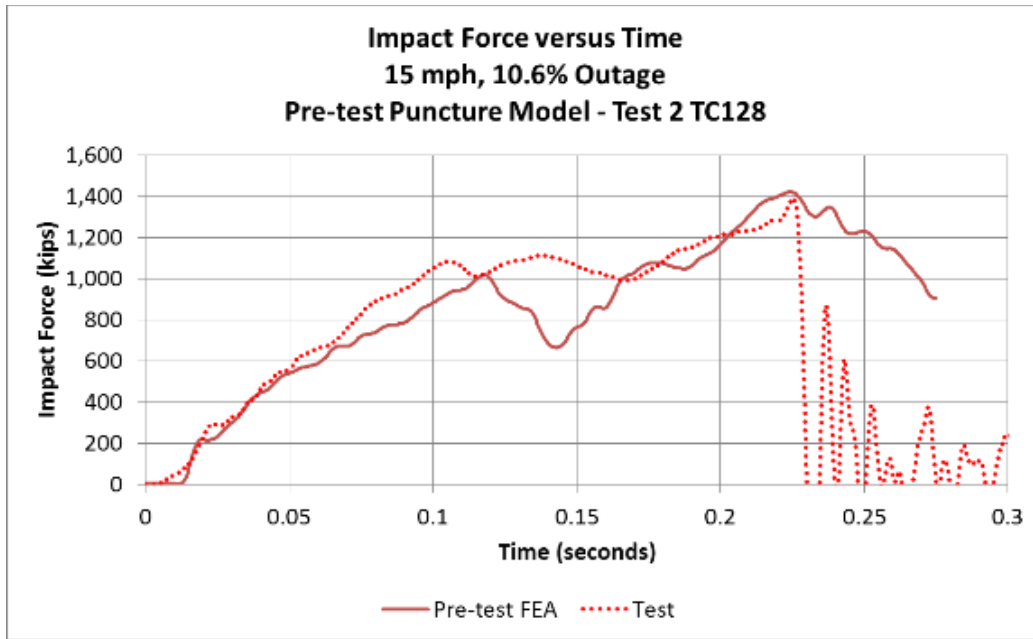
Figure C13. Impact Force versus Time, 15 mph Pre-test FEA with Test 2 TC128 and Test Data
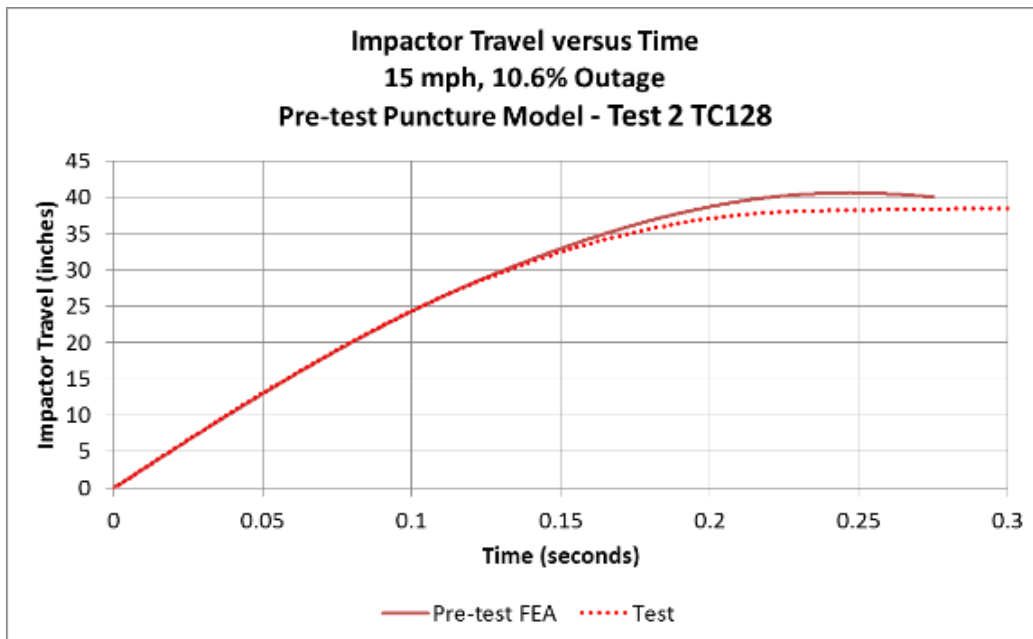
Figure C14. Impactor Travel versus Time, 15 mph Pre-test FEA with Test 2 TC128 and Test Data

91
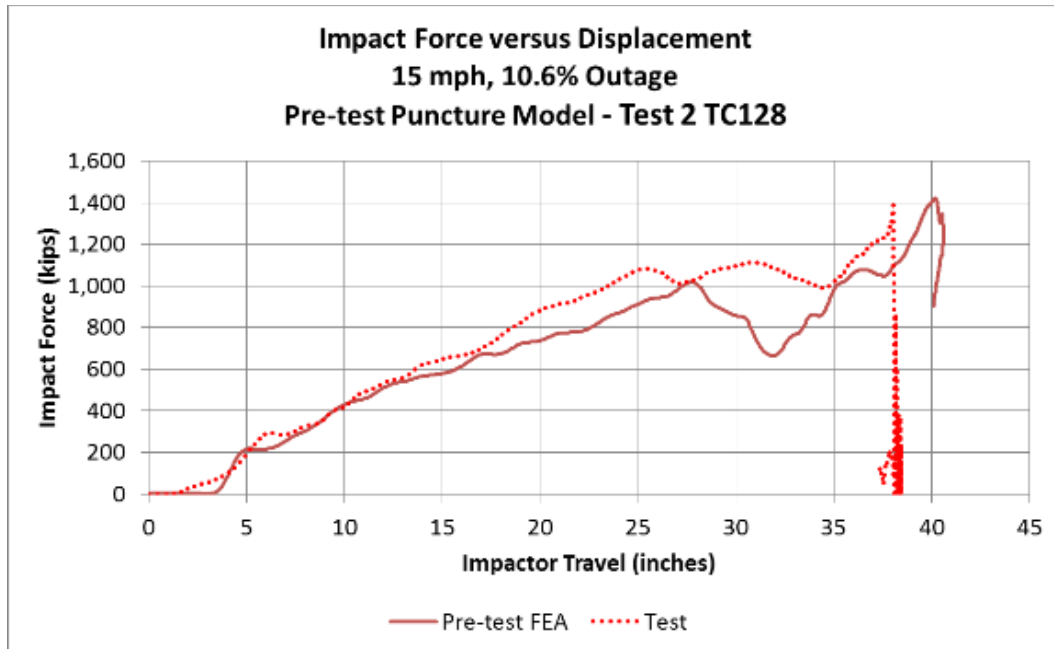
Figure C15. Impact Force versus Impactor Travel, 15 mph Pre-test FEA with Test 2 TC128 and Test Data
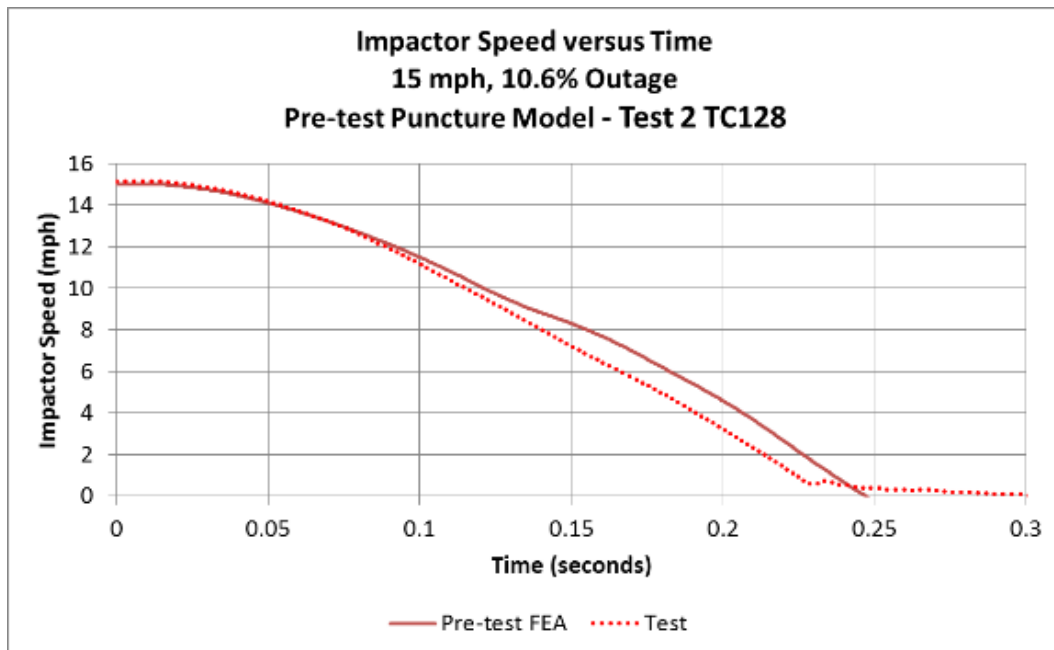
Figure C16. Impactor Speed versus Time, 15 mph Pre-test FEA with Test 2 TC128 and Test Data
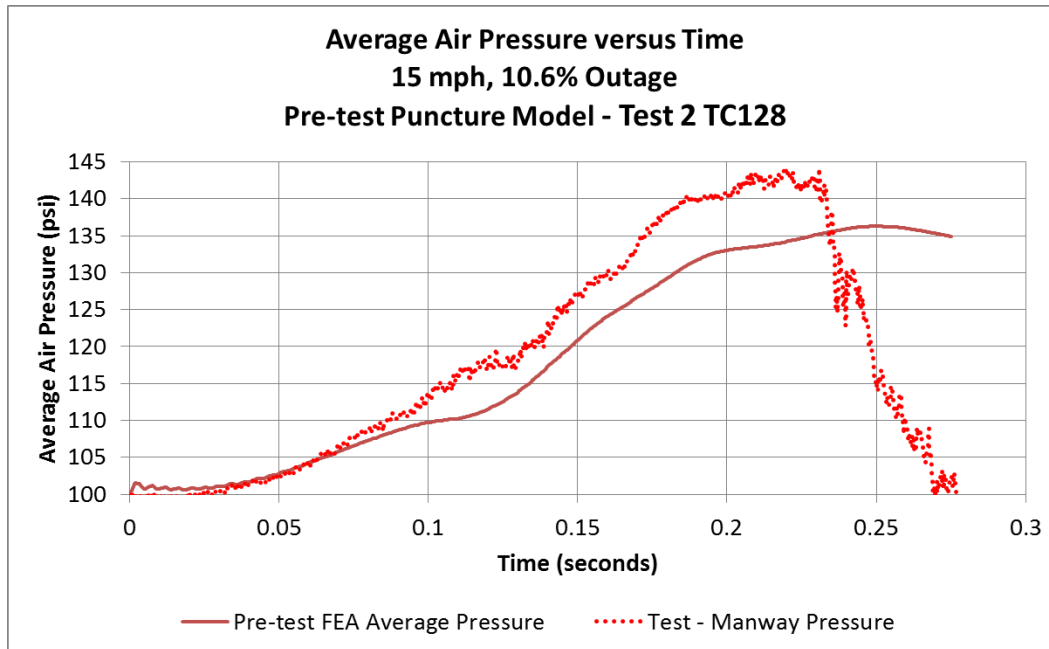
Figure C17. Average Air Pressure versus time, 15 mph Pre-test FEA with Test 2 TC128 and Test Data
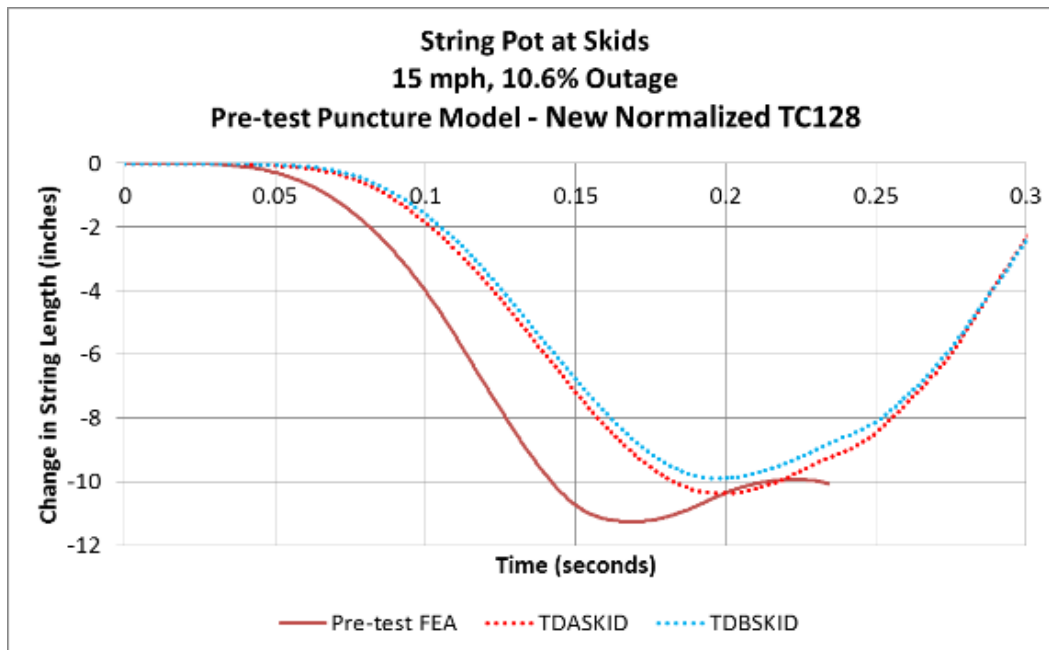
Figure C18. String Potentiometers at Skids, 15 mph Pre-test FEA with Test 2 TC128 and Test Data

93
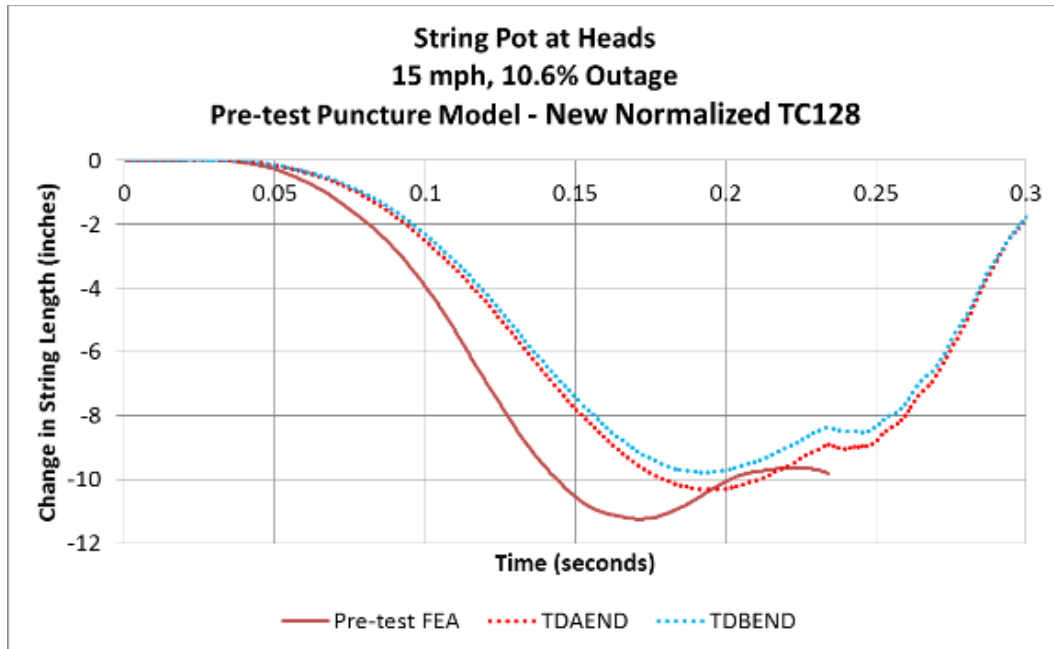
Figure C19. String Potentiometers at Heads, 15 mph Pre-test FEA with Test 2 TC128 and Test Data
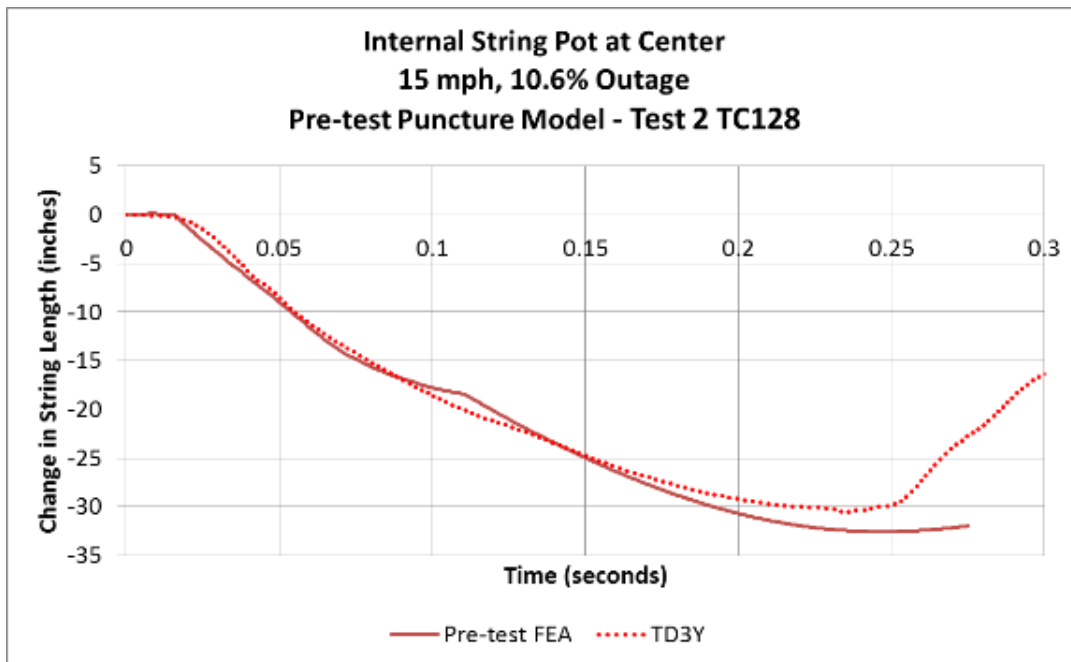
Figure C20. Internal String Potentiometer at Center of Tank, 15 mph Pre-test FEA with Test 2 TC128 and Test Data
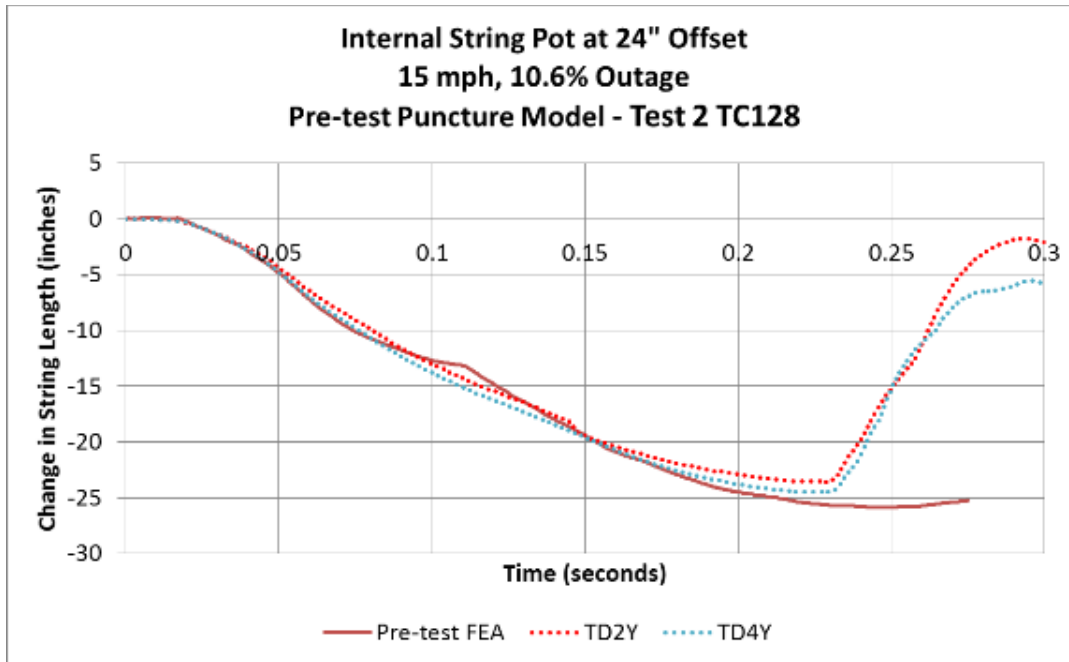
Figure C21. Internal String Potentiometers 24 inches from Impact, 15 mph Pre-test FEA with Test 2 TC128 and Test Data
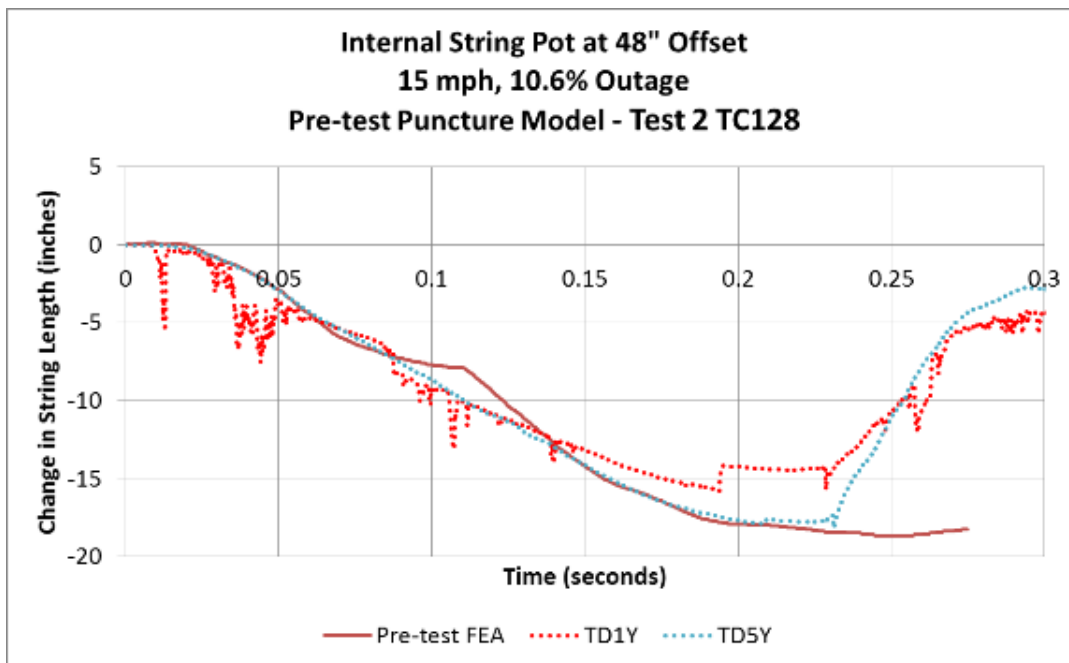
Figure C22. Internal String Potentiometers 48 inches from Impact, 15 mph Pre-test FEA with Test 2 TC128 and Test Data
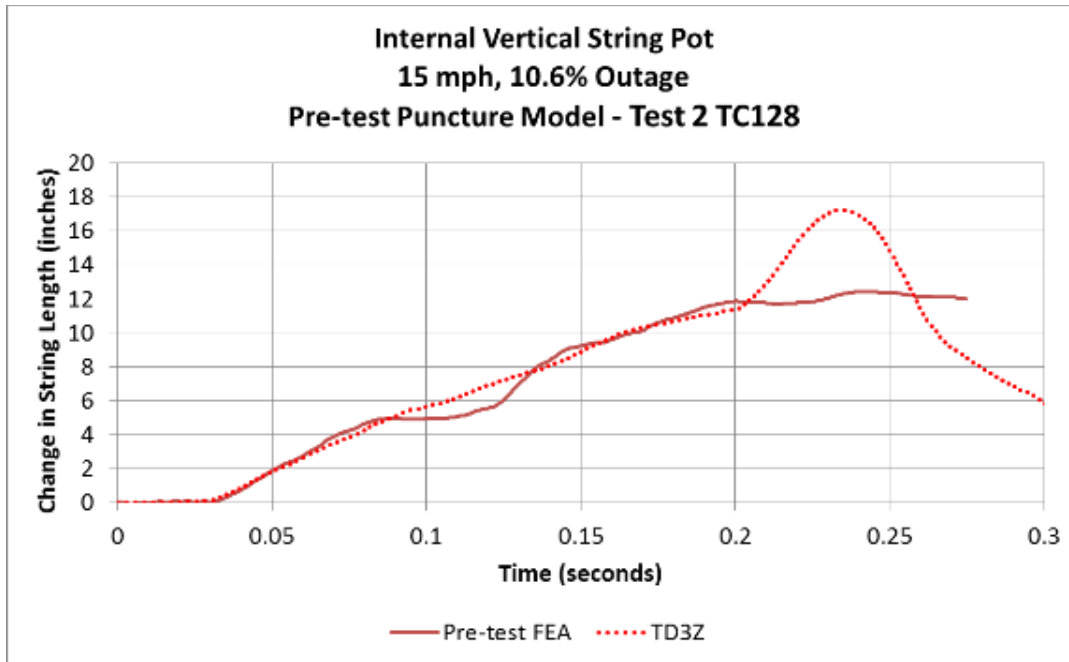
**Figure C23. Internal Vertical String Potentiometer, 15 mph Pre-test FEA
with Test 2 TC128 and Test Data**

In addition to running the pre-test model with New Normalized TC128 steel at 15 mph, a series of iterative simulations was used to estimate the range of speeds that would define the threshold between a puncture simulation and a non-puncture simulation. The pre-test FE model was found to puncture from an initial impact at 17 mph, but did not fully puncture from a 16.5 mph impact. These two force versus displacement responses are plotted in Figure C24. Thus, the model estimates that the threshold speed between a puncture and a non-puncture outcome is somewhere between 16.5 and 17 mph for the Test 2 TC128 material model.
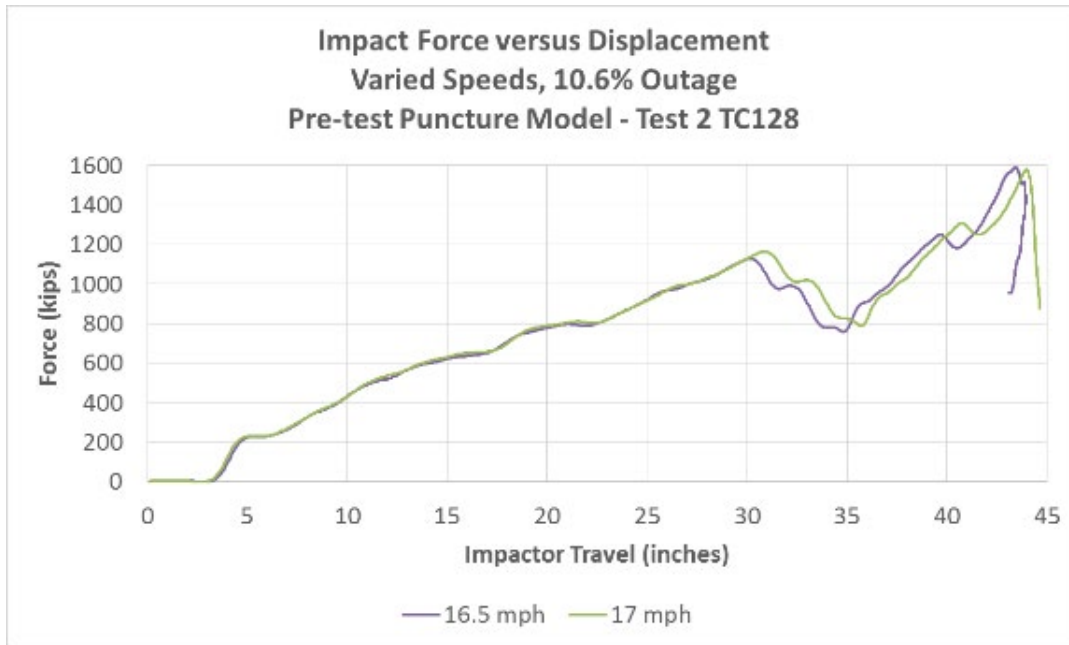
Figure C24. Impact Force versus Impactor Travel, 16.5 and 17 mph Pre-test FEA with Test 2 TC128

C3 – Post-test FEA and Test Results—Actual TC128 Steel, 15.16 mph

The post-test FEA results are compared to the test measurements in Figure C25 through Figure C35. Results derived from accelerometers or pressure transducers have been filtered using a CFC60 filter. The post-test FE model was run at the measured test speed of 15.16 mph. The changes implemented in the post-test model compared to the pre-test model are described in Section 5.5.
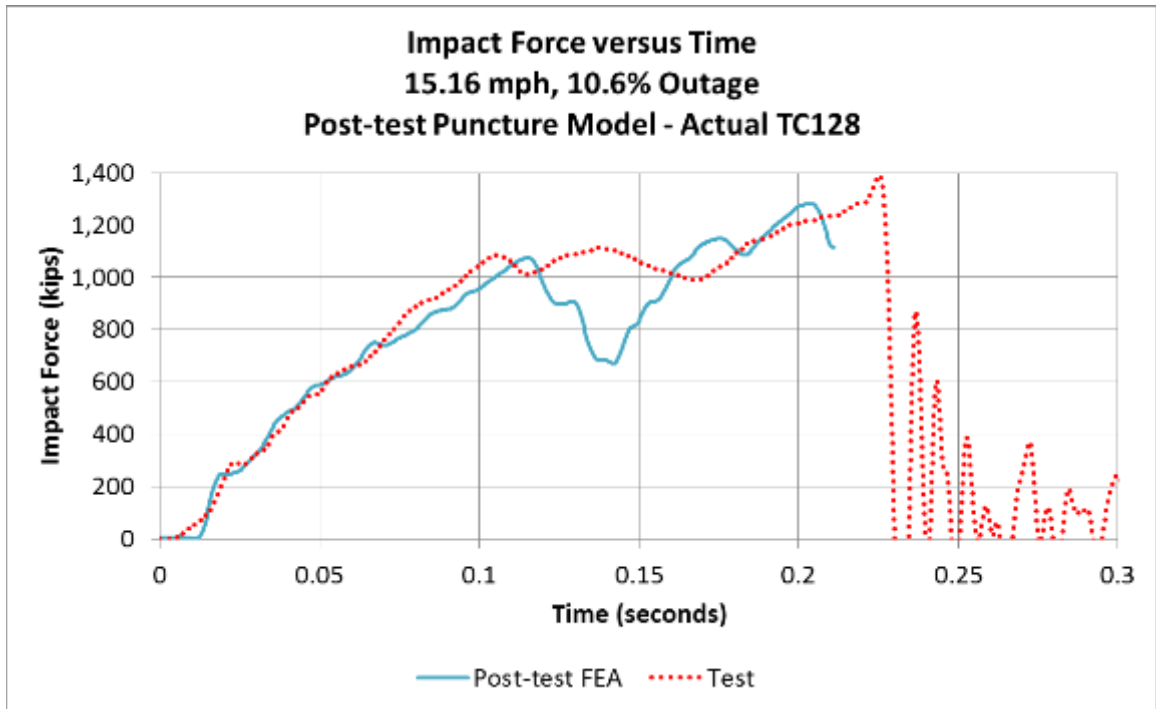
Figure C25. Impact Force versus Time, Post-test FEA and Test Data
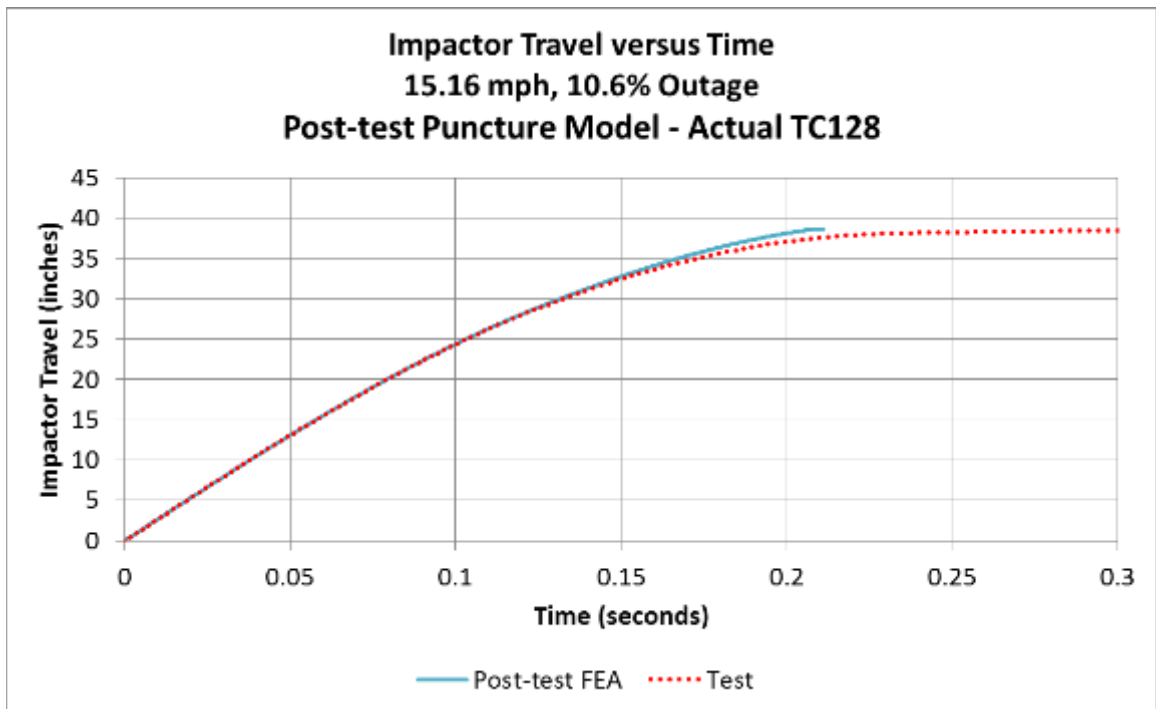
Figure C26. Impactor Travel versus Time, Post-test FEA and Test Data
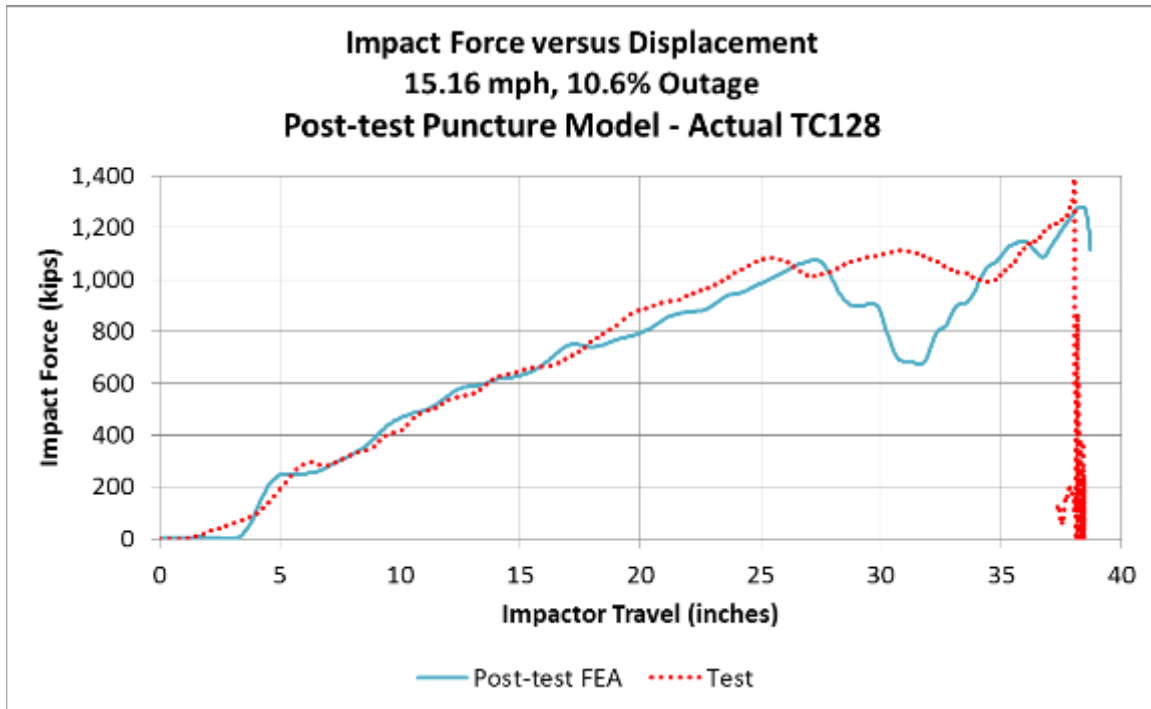
Figure C27. Impact Force versus Impactor Travel, Post-test FEA and Test Data
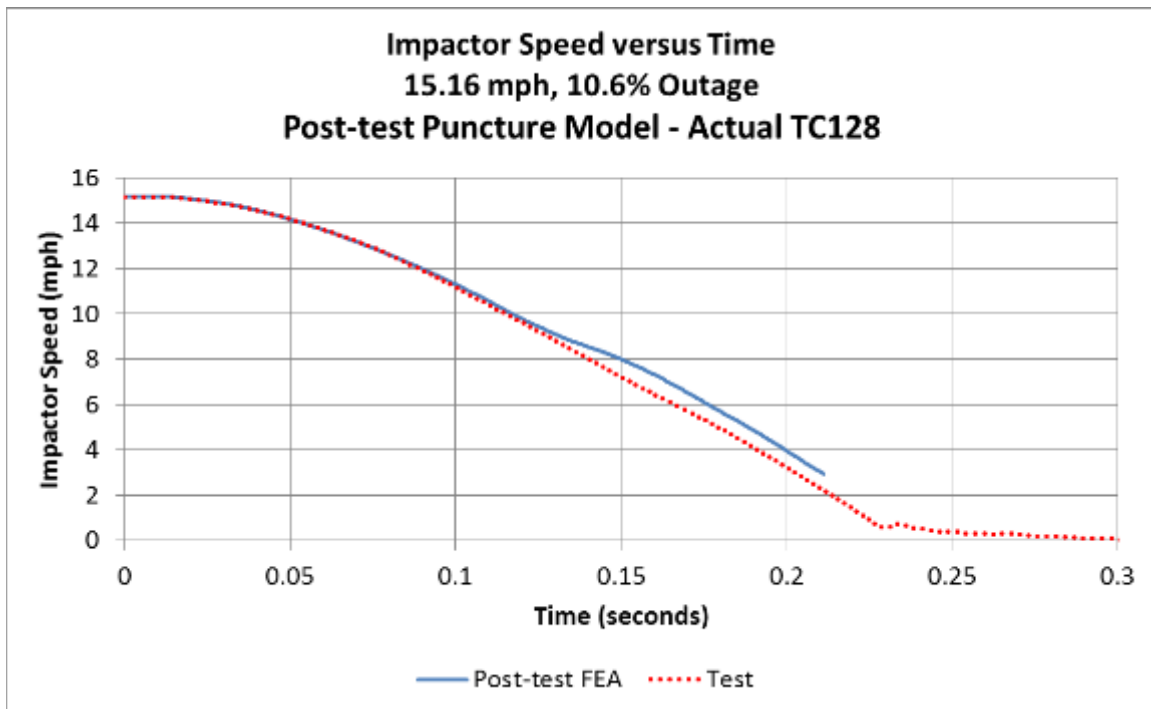
Figure C28. Impactor Speed versus Time, Post-test FEA and Test Data
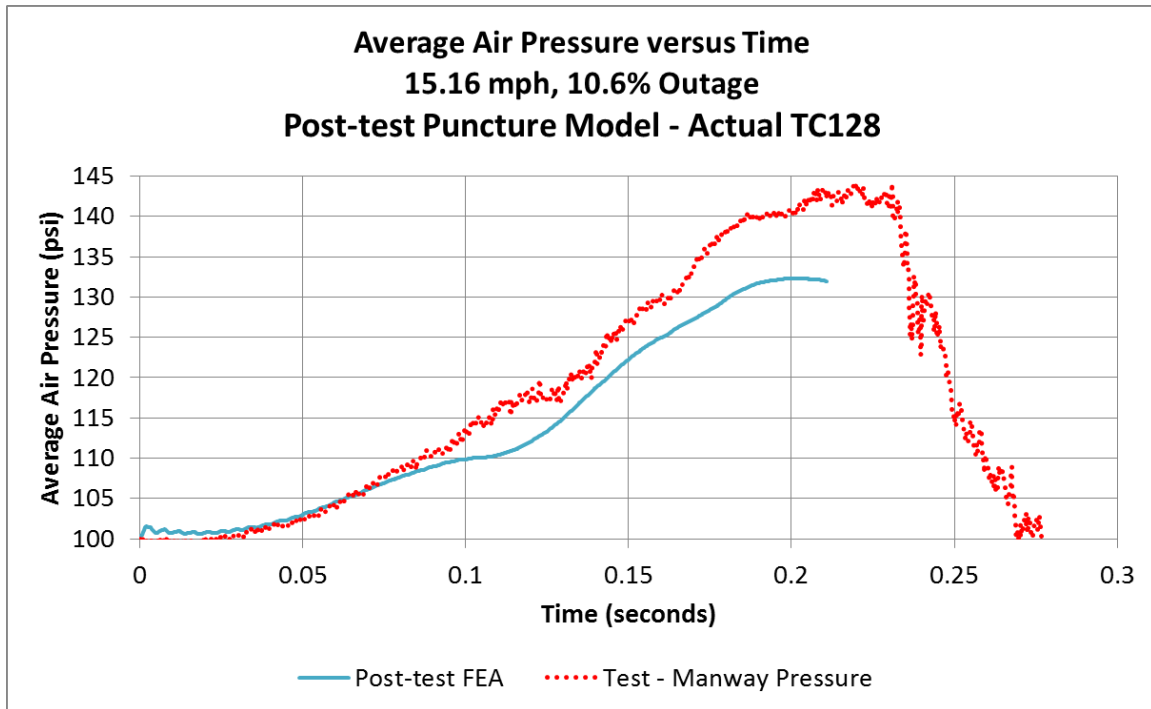
Figure C29. Average Air Pressure versus Time, Post-test FEA and Test Data
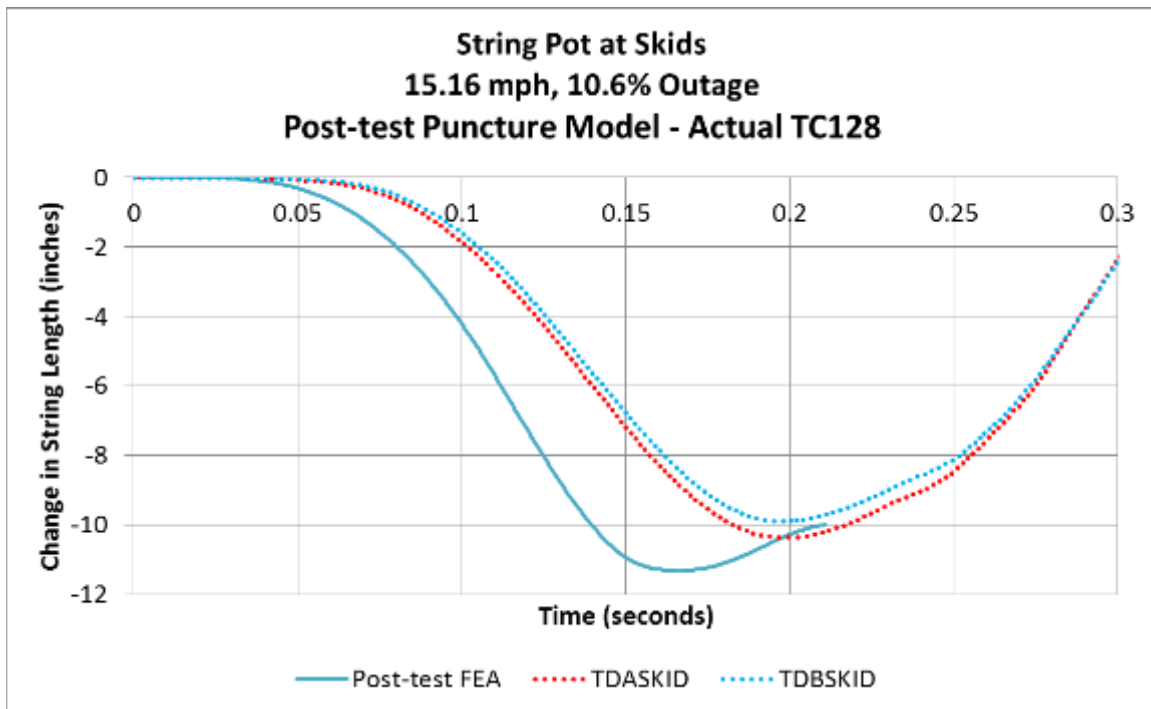
Figure C30. String Potentiometers at Skids, Post-test FEA and Test Data

100
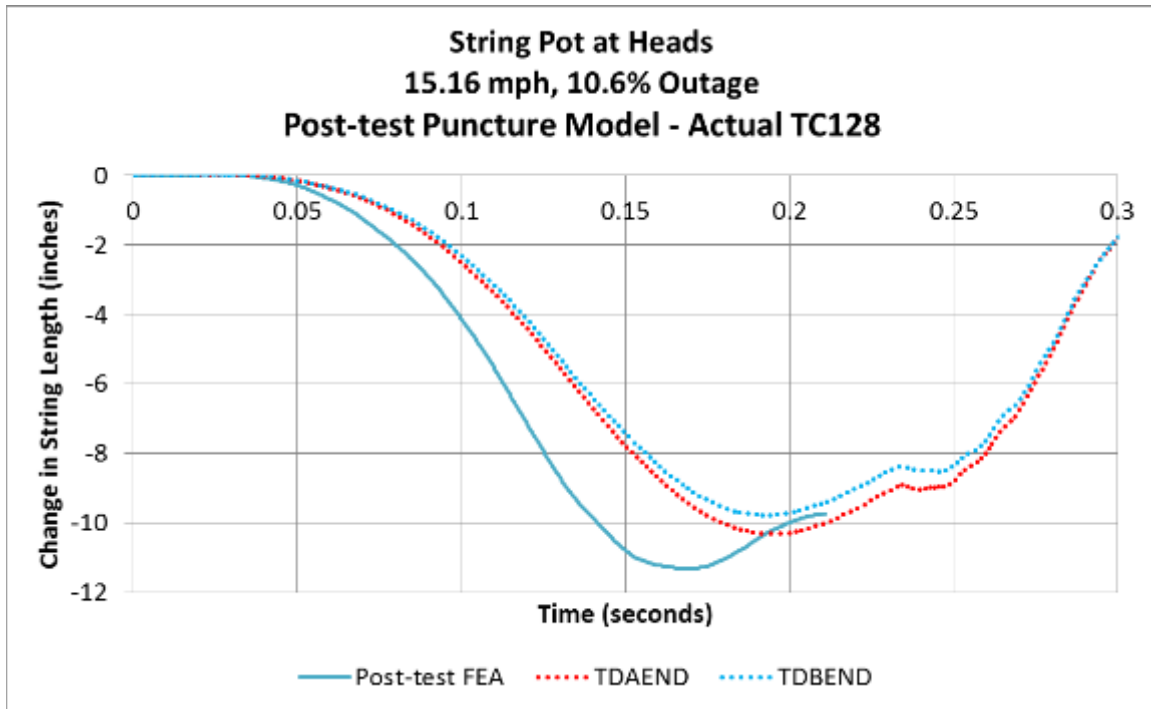
Figure C31. String Potentiometers at Heads, Post-test FEA and Test Data
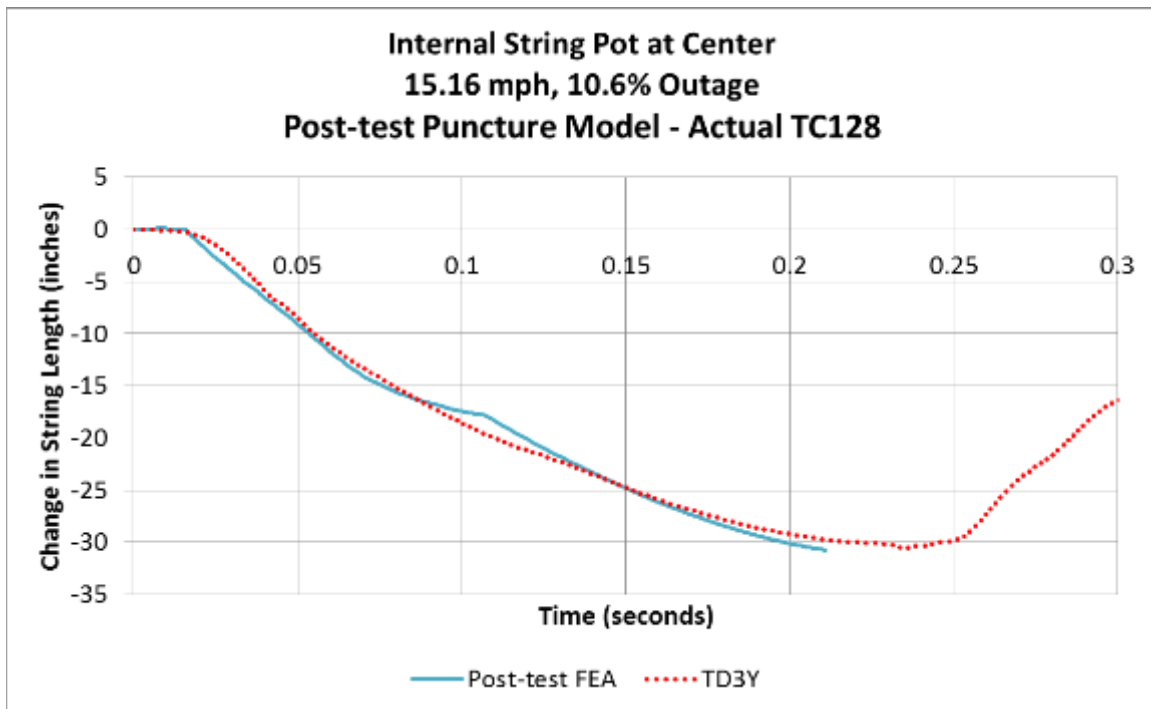
Figure C32. Internal String Potentiometer at Center of Tank, Post-test FEA and Test Data
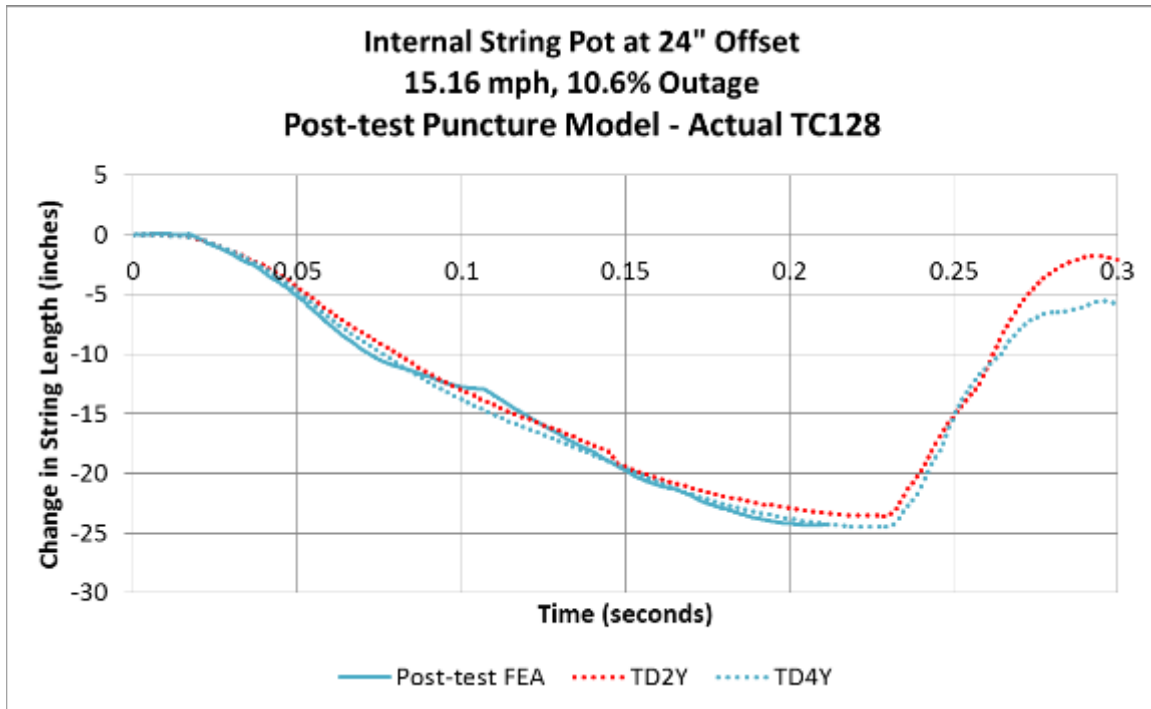
**Figure C33. Internal String Potentiometers 24 inches from Impact, Post-test FEA and Test Data**
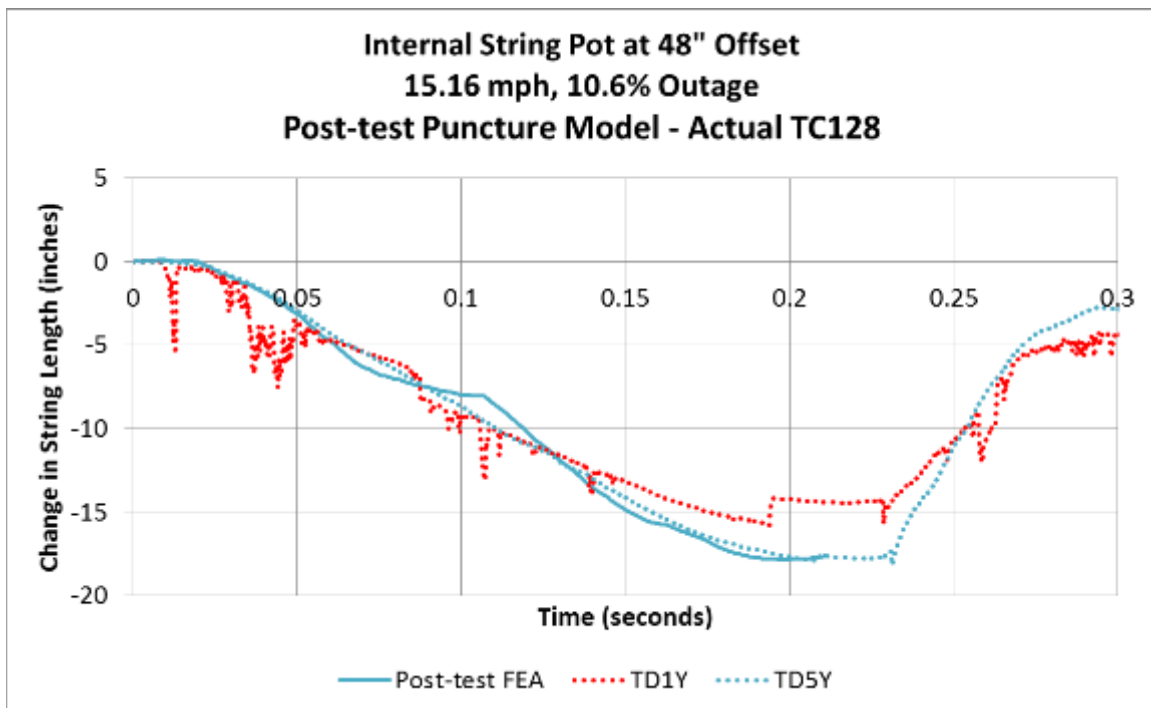
Figure C34. Internal String Potentiometers 48 inches from Impact, Post-test FEA and Test Data
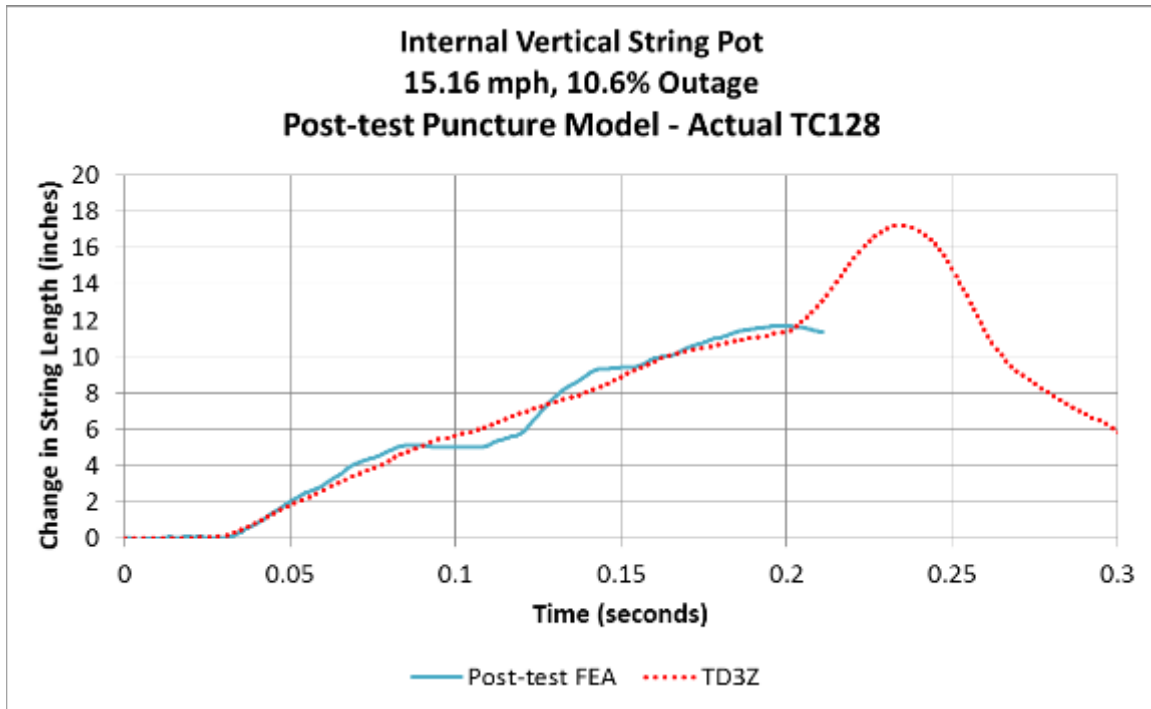
Figure C35. Internal Vertical String Potentiometer, Post-test FEA and Test Data

C4 – Post-test FE Model with Insulation

Finally, a post-test FE model incorporating a simplified insulation material between the jacket and tank was run to assess the influence of the insulation on the overall impact response. This model was run at the test speed of 15.16 mph, with the tank shell modeled using actual TC128 steel. The results in this section (shown in Figure C36 through Figure C46), specifically the force-time and force-displacement results, show that the force drop seen in the pre-test models can be greatly reduced by including insulation within the model. No further modeling was performed to attempt to characterize the insulation behavior, as the intent of this modeling effort was to determine whether including the insulation in the model would improve the agreement between the measured test forces and those estimated by the model.
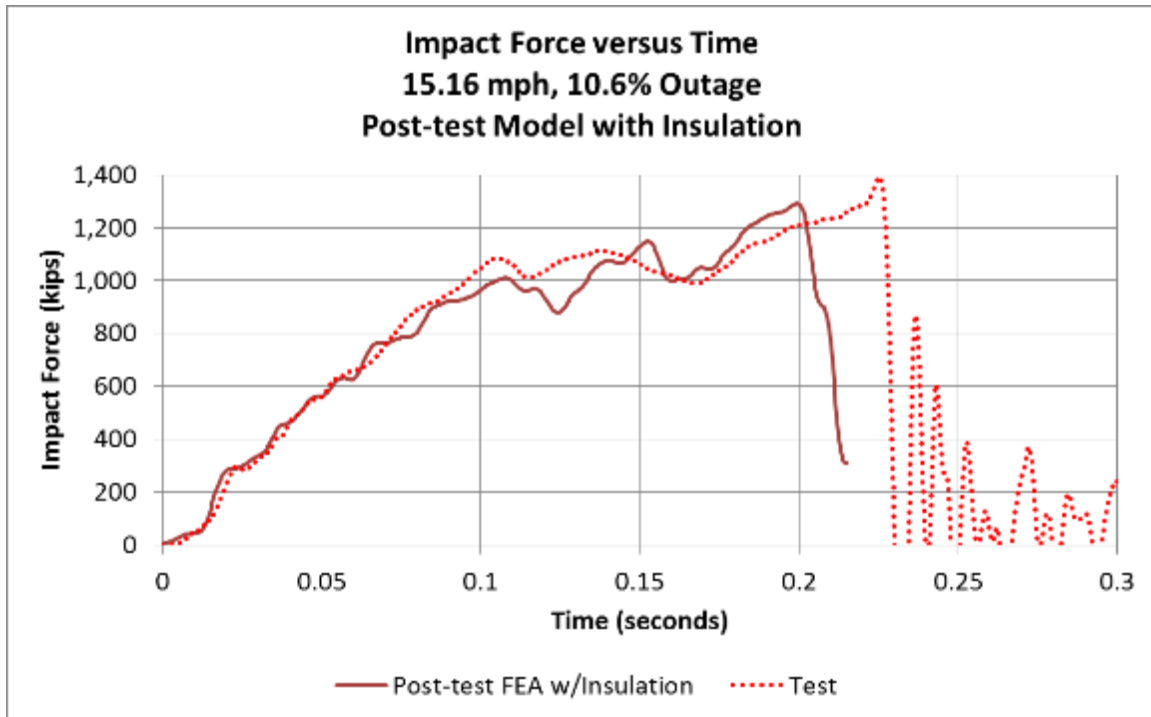
Figure C36. Impact Force versus Time, Post-test FEA with Insulation and Test Data
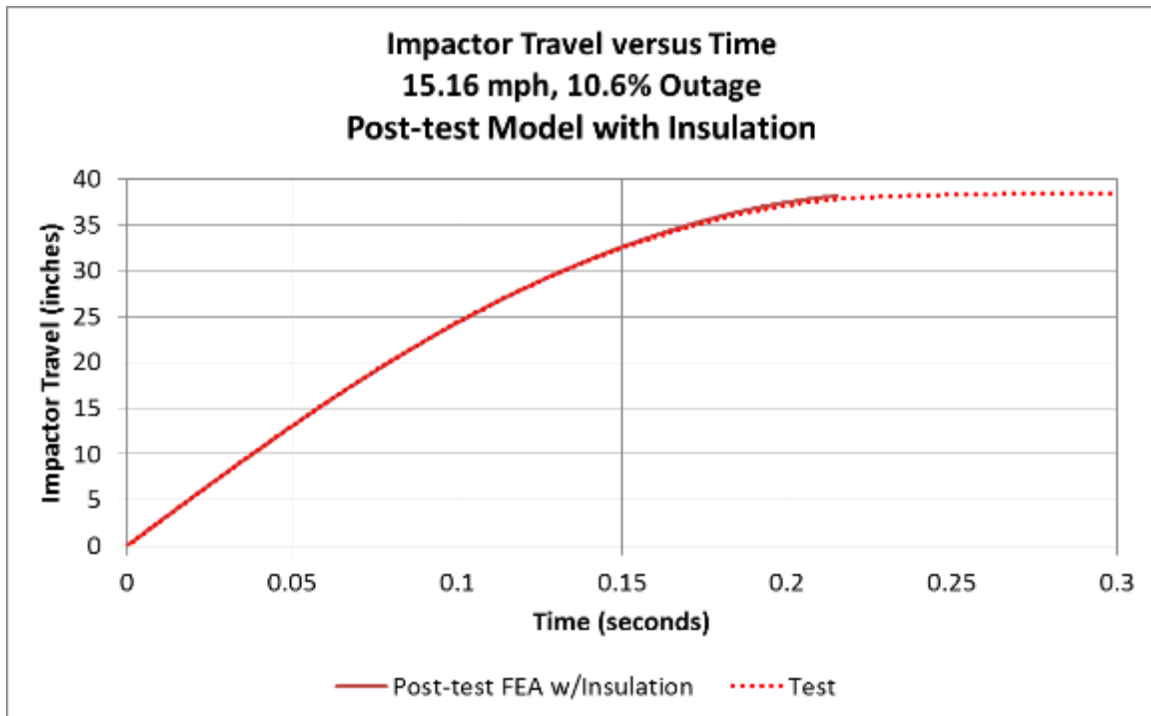
Figure C37. Impactor Travel versus Time, Post-test FEA with Insulation and Test Data

104
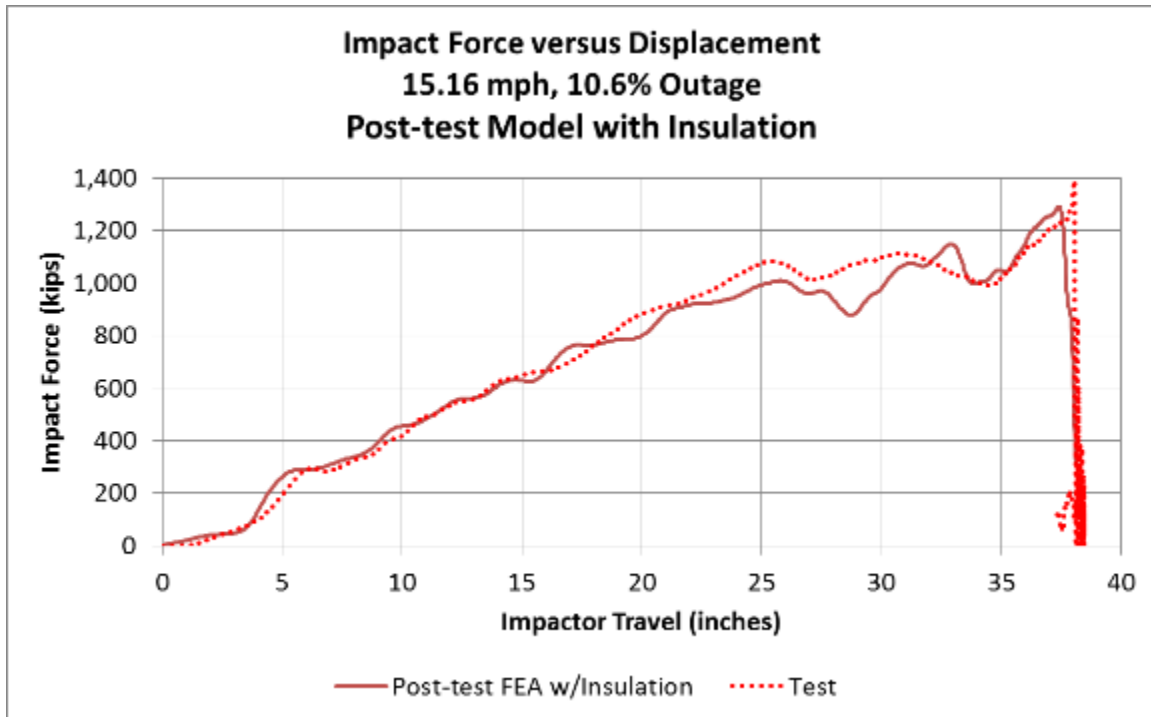
Figure C38. Impact Force versus Impactor Travel, Post-test FEA with Insulation and Test Data
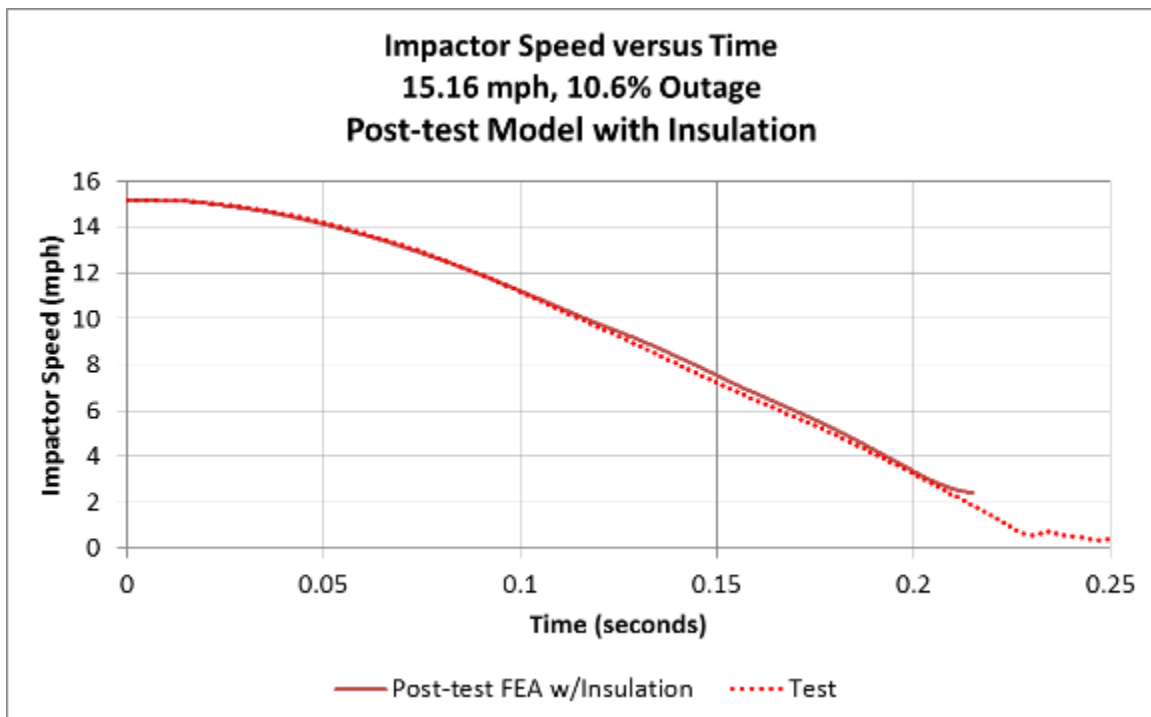

Figure C39. Impactor Speed versus Time, Post-test FEA with Insulation and Test Data
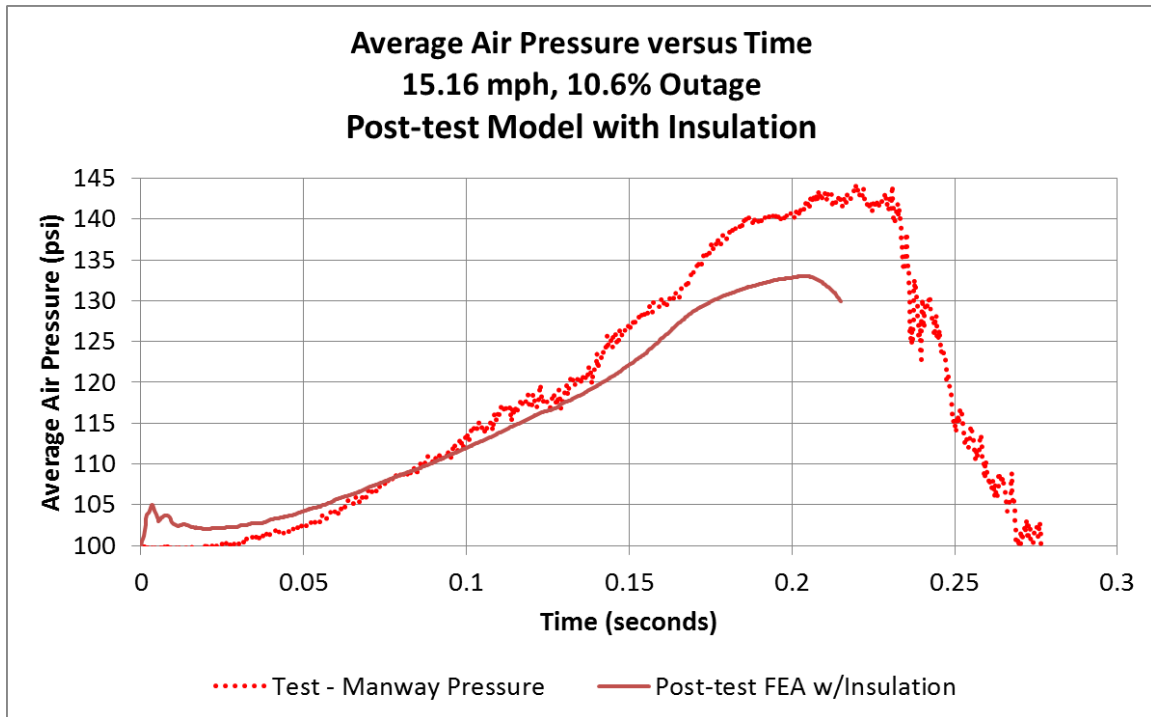
**Figure C40. Average Air Pressure versus Time, Post-test FEA with Insulation and Test Data**
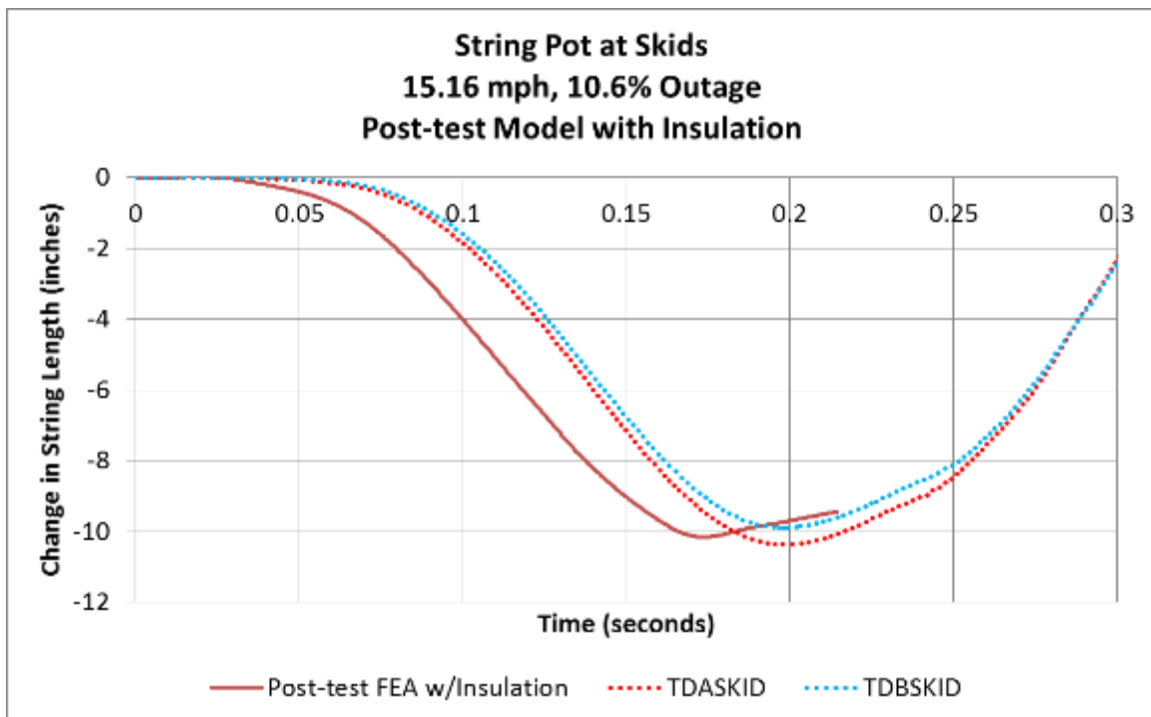
Figure C41. String Potentiometers at Skids, Post-test FEA with Insulation and Test Data
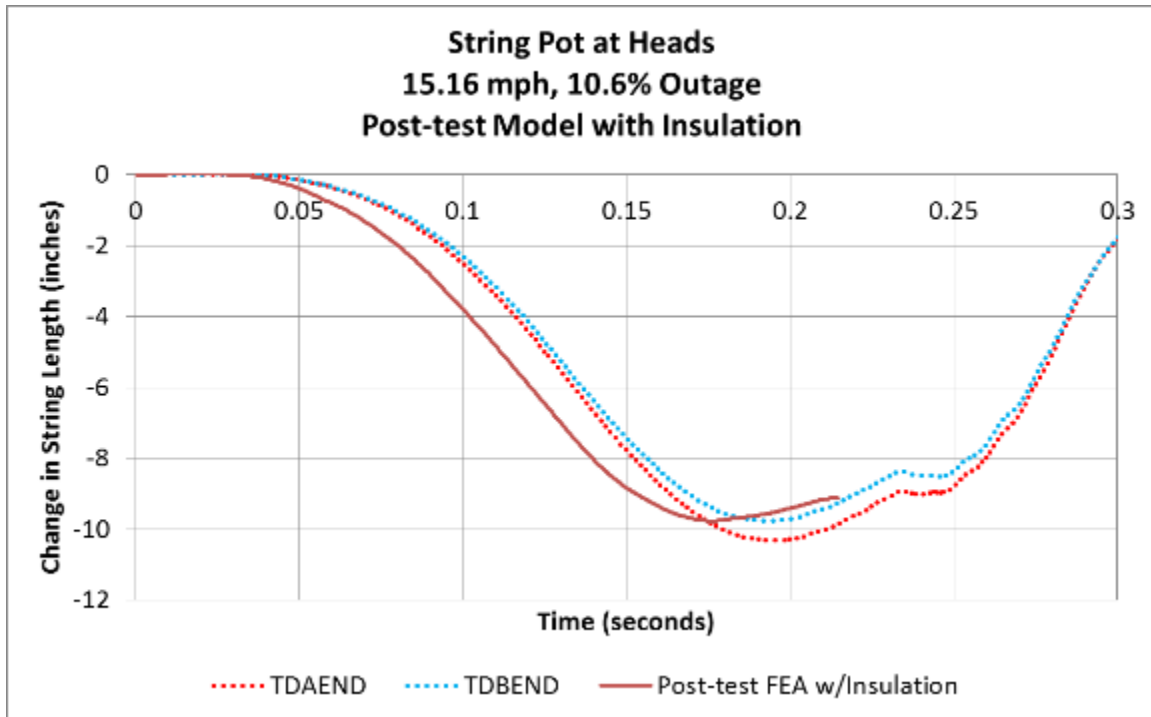
Figure C42. String Potentiometers at Heads, Post-test FEA with Insulation and Test Data
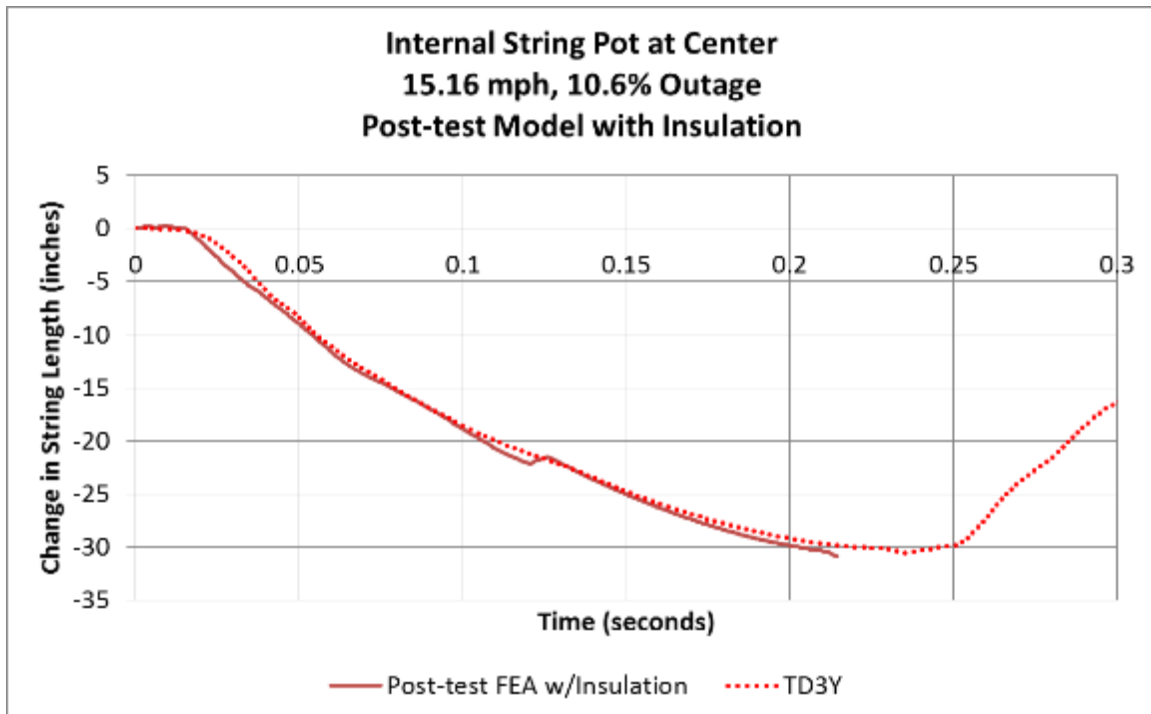
Figure C43. Internal String Potentiometer at Center of Tank, Post-test FEA with Insulation and Test Data

107
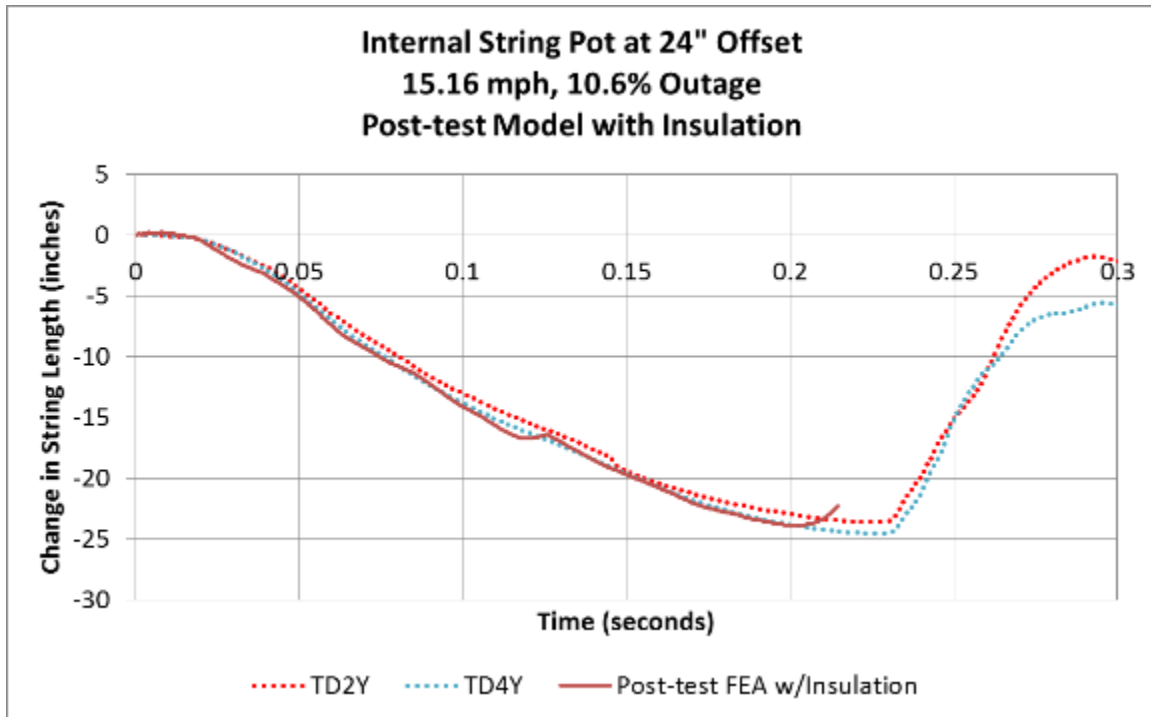
Figure C44. Internal String Potentiometers 24 inches from Impact, Post-test FEA with Insulation and Test Data
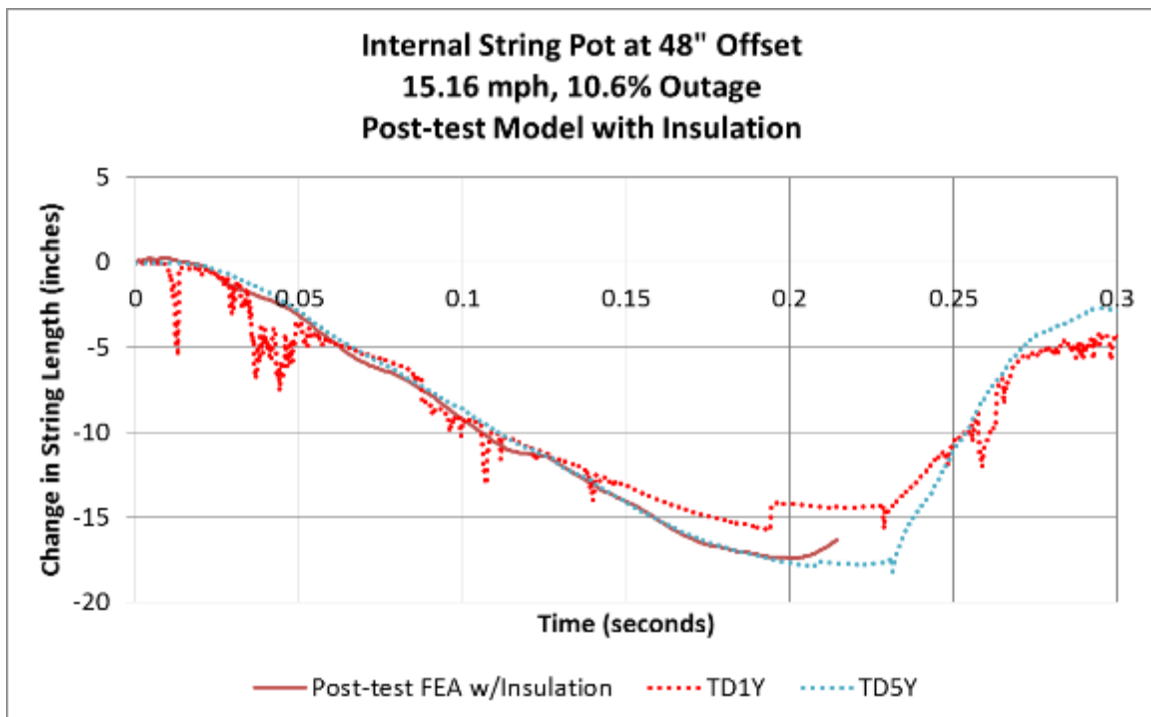
Figure C45. Internal String Potentiometers 48 inches from Impact, Post-test FEA with Insulation and Test Data
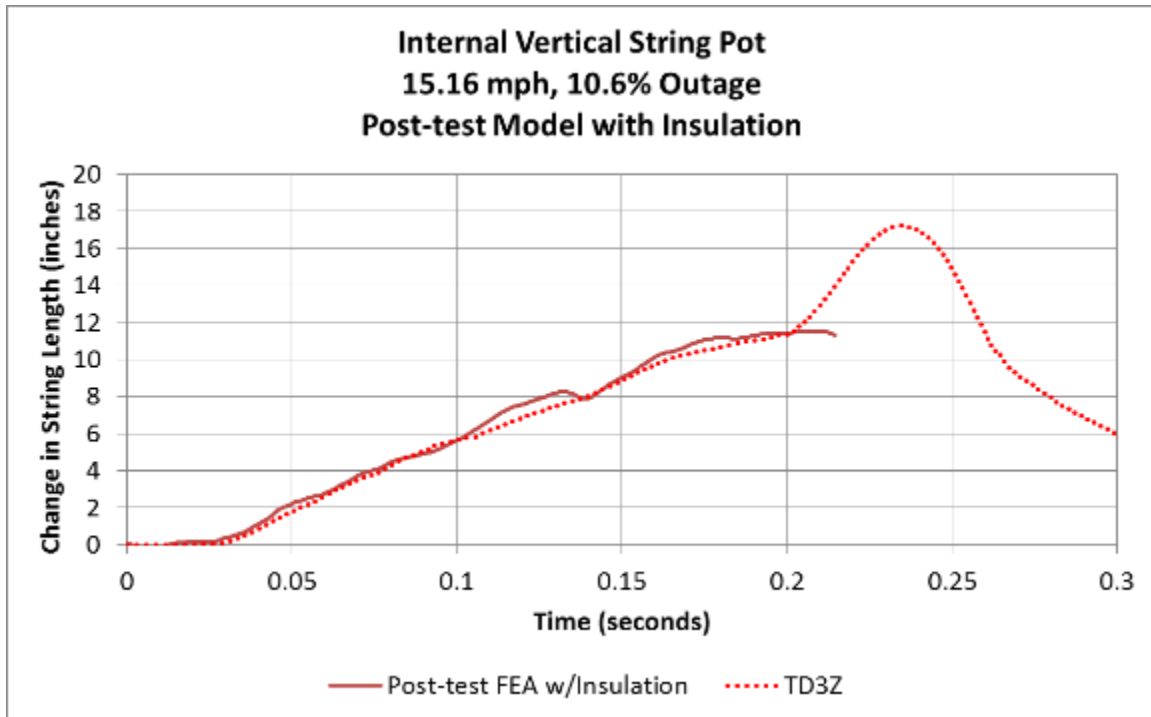
**Figure C46. Internal Vertical String Potentiometer, Post-test FEA with Insulation and Test Data**

Appendix D.
Geometry in Pre-test and Post-test
Finite Element Models

A discussion of each of the parts making up the model is contained in the following paragraphs. Note that for parts that are bisected by the symmetry plane, the values reported in the following tables for mass and number of elements correspond to what was included in the FE model (i.e., half the mass of the physical body during the test).

Rigid parts were used when it was important to include a part for its inertia or for its interaction through contact, but where the deformation of the part could be neglected in the calculations. Four parts were modeled as rigid bodies.

D1 – Rigid Impactor

The impactor was modeled as a rigid body in the DOT-105 tank car FE models. The simulations used a 12- by 12-inch square impactor with 1-inch radii edges around the impact face. The geometry included the impact face and the tapered cone back to the portion of the impactor where the impactor attached to the ram car. Since only the impactor itself was modeled and this model used one-half symmetry, half of the mass of the entire ram car was assigned to the reference node on the impactor. The impactor, both with and without mesh, is shown in Figure D1. Table D1 is a summary of the properties of the impactor used in the FE model.
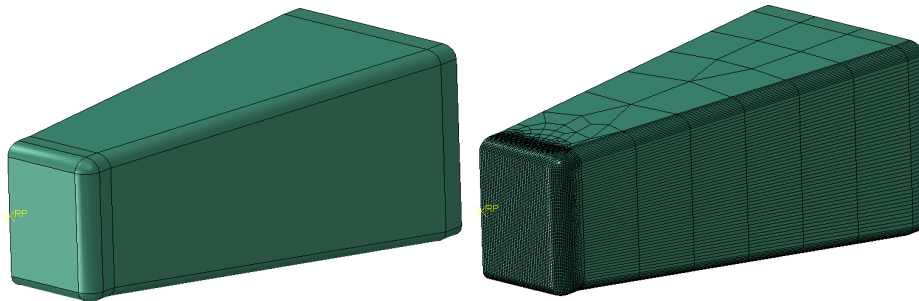
Figure D1. Impactor Geometry (left) and Mesh (right)

Table D1. Properties of Impactor in FE Model

Type of Part	Rigid
Number of Elements	R3D4: 7303
	R3D3: 50
	MASS: 1
Part Weight	148,562.5 lbf

D2 – Rigid Wall

The rigid wall was modeled as a rigid body in the DOT-105 tank car FE model. Since the wall was constrained against motion in any direction, no mass needed to be defined for this part. The wall's geometry and mesh are shown in Figure D2. Table D2 is a summary of the properties of the rigid wall used in the FE model.
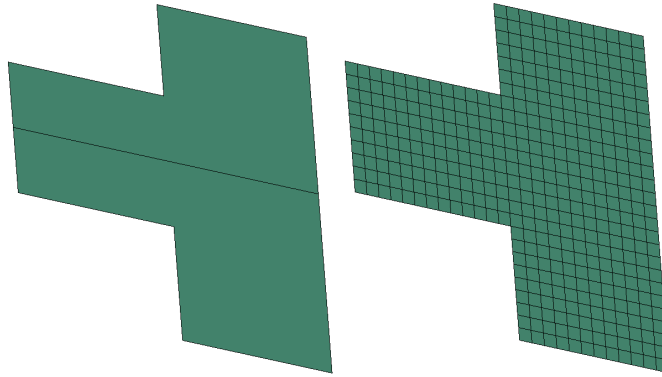
Figure D2. Rigid Wall Geometry (left) and Mesh (right)

Table D2. Properties of Rigid Wall in FE Model

Type of Part	Rigid
Number of Elements	R3D4: 442

D3 – Skid

The trucks of the tank car were removed prior to the test. The bolster of the car rested directly upon a set of skids, which themselves rested upon steel plates (see Figure 5). The skids were designed to inhibit rigid-body roll of the tank car following rebound from the rigid wall during a test. The skid geometry and mesh are shown in Figure D3. Note that since this part exists entirely to one side of the symmetry plane, the mass and geometric properties correspond to the actual mass and geometry of one full skid. Table D3 is a summary of the properties of the skid used in the FE model.
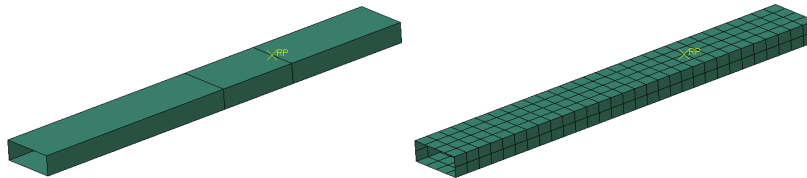
Figure D3. Skid Geometry (left) and Mesh (right)

Table D3. Properties of Skid in FE Model

Type of Part	Rigid
Number of Elements	R3D4: 360
	MASS: 1
Part Weight	3,500 lbf

D4 – Jacket

The jacket was modeled entirely with deformable shell elements. The diameter of the jacket part was 110.1196 inches, representing the mid-plane of the actual jacket. The jacket featured a semicircular cutout at its 12 o'clock position to allow the manway to pass through. Most of the jacket was meshed with quadrilateral, reduced integration (S4R) elements with a 3.5-inch mesh seed. A small number of triangular, reduced elements (S3R) were used to mesh the head. In the

area of the jacket that would be contacted by the impactor, the mesh was made up of quadrilateral, full integration (S4) elements with a 0.04-inch mesh seed. The region of refined mesh was C-shaped in the FE model, as the jacket puncture was assumed to initiate around the perimeter of the impactor. Thus, the fine mesh intended to capture puncture only needed to extend around the region that would make contact with the perimeter of the impactor. A transition zone between the fine mesh and the coarse mesh also used full integration elements. Since only half the jacket is included in the FE model due to symmetry, the mass of the jacket in the FE model corresponds to half the mass of the physical jacket. Figure D4 shows the geometry and mesh of the jacket.
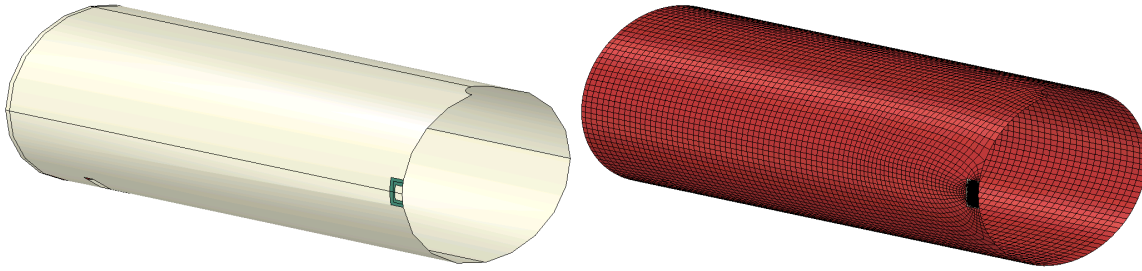
Figure D4. Jacket Geometry (left) and Mesh (right)

The transition between 3-inch S4R mesh and 0.04-inch S4 mesh in the impact zone is shown in Figure D5. Table D4 is a summary of the properties of the jacket used in the FE model.
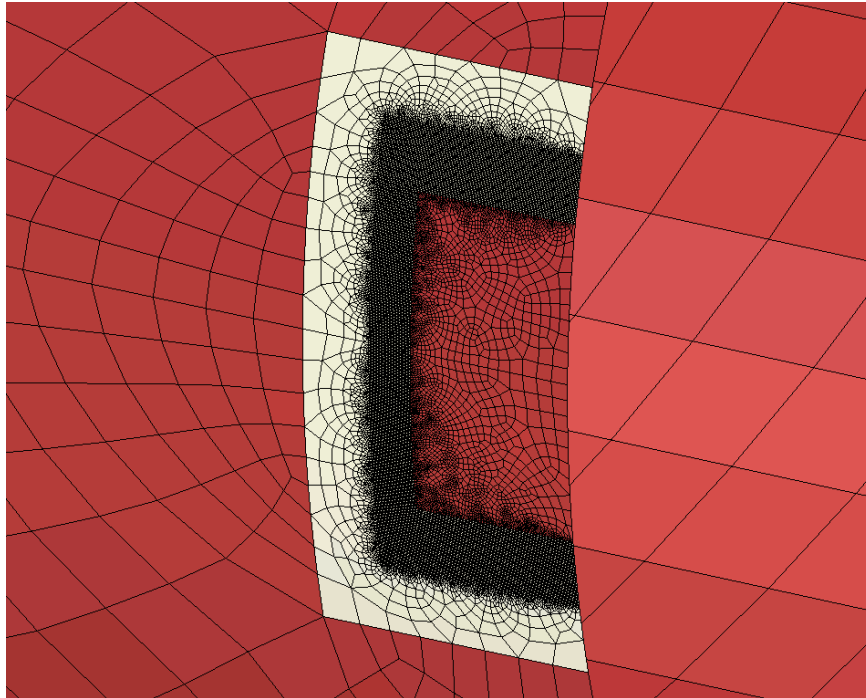
Figure D5. Jacket Mesh in Impact Zone

Table D4. Properties of Jacket in FE Model

Type of Part	Deformable, Shell
Number of Elements	S4R: 12,276
	S4: 24,226
	S3R: 18
Shell Thickness	0.1196 inches (11 gauge)
Head Thickness	0.1196 inches (11 gauge)
Material(s)	A1011
Part Weight	3,323 lbf

D5 – Tank—Shell Elements

The commodity tank was modeled using two different techniques. In the impact zone, the tank was modeled using solid "brick" elements. This part is discussed in Section D6. Away from the impact zone, the tank was modeled using shell elements. The shell portion of the tank is described in this section. Since only half the tank is included in the FE model due to symmetry, the mass of the tank in the FE model corresponds to half the mass of the physical tank.

Figure D6 shows the shell portion of the tank. This part was globally meshed using quadrilateral reduced integration (S4R) elements with a 3.5-inch mesh seed. At the edges of the impact zone, the mesh was seeded such that each shell element edge would span exactly two solid elements on the impacted patch (Figure D7). The mesh in the region of attachment to the solid plate was meshed using quadrilateral fully integrated (S4) elements. A technique referred to as shell-to-solid coupling was used to attach the solid patch to the edges of the shell mesh on the tank. The shell part of the tank represents the mid-plane surface of the tank. The shell part has a mid-plane diameter of 101.225 inches in the model. The models include a small number of S3R elements in the head. Table D5 is a summary of the properties of the tank (shell mesh) used in the FE model.
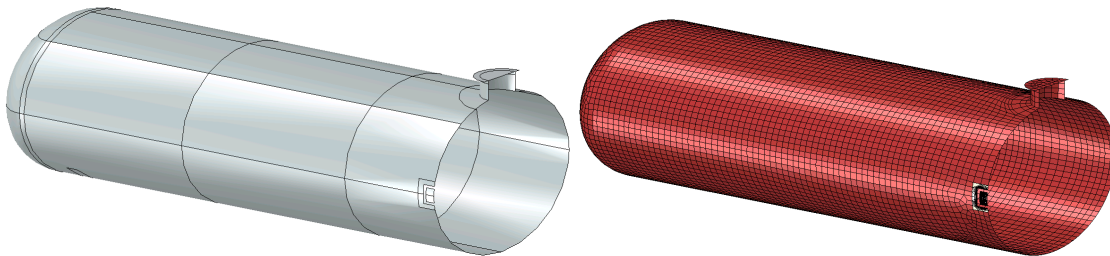
Figure D6. Shell Tank Geometry (left) and Mesh (right)
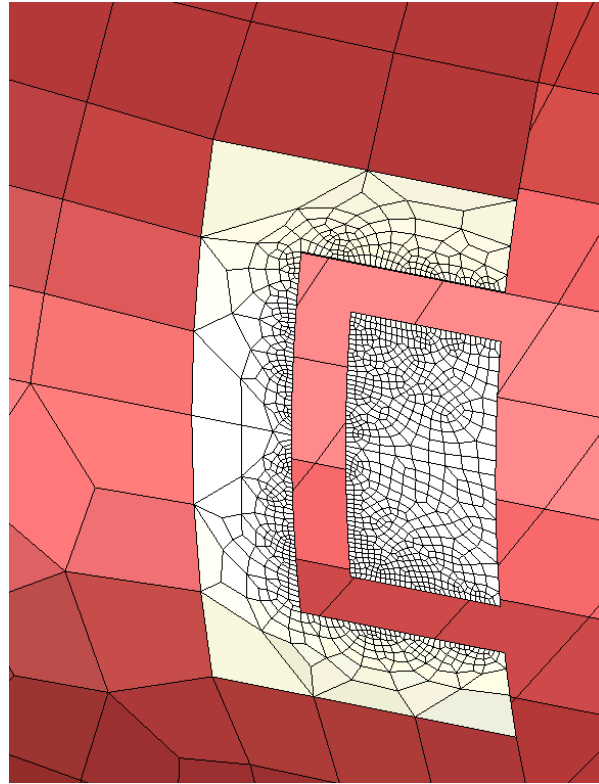
Figure D7. Shell Tank Mesh in Impact Zone

Table D5. Properties of Tank (shell mesh)

Parameter	Pre-test Model	Post-test Model
Type of Part	Deformable, Shell	Deformable, Shell
Shell Thickness	0.775 inches	0.775 inches
Head Thickness	13/16 inches (0.8125 inches)	13/16 inches (0.8125 inches)
Number of Elements	S4R: 7,426	S4R: 7,426
	S4: 1,225	S4: 1,225
	S3R: 17	S3R: 17
Material(s)	Test 2 TC128, or;	Actual TC128
	New Normalized TC128	
Part Weight	19,420.5 lbf	19,420.5 lbf

D6 – Tank—Solid Elements

The commodity tank was modeled using two different techniques. Away from the impact zone, the tank was modeled using shell elements. This part is discussed in Section D.5. In the impact zone, the tank was modeled using solid brick elements. The solid portion of the tank is described in this section. Since only half the tank is included in the FE model due to symmetry, the mass of the solid portion of the tank in the FE model corresponds to half the mass of the corresponding portion of the physical tank.

Figure D8 shows the solid portion of the tank. The outer height of the part measures approximately 12.25 inches high by 6.125 inches wide. The inner cutout measures approximately 9 inches high by approximately 4.5 inches wide. The part was meshed using a 0.085-inch mesh seed, resulting in nine elements through the thickness of the tank shell. The solid portion of the tank was meshed using eight-node hexahedral "brick" (C3D8) elements. The solid tank mesh was attached to the shell tank mesh along the outer and inner edges using shell-to-solid coupling. Table D6 is a summary of the properties of the tank (solid mesh) used in the FE model.
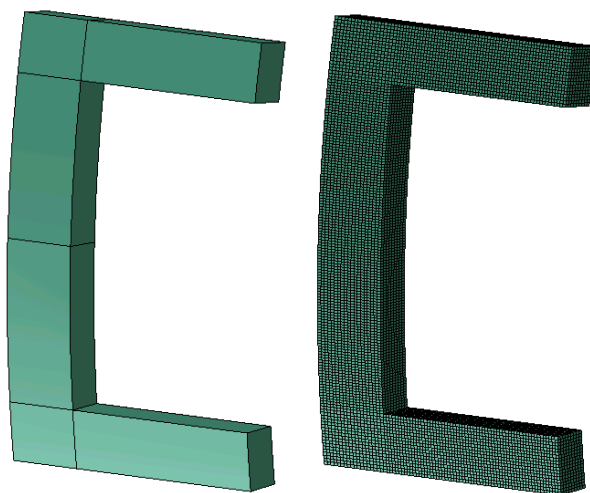
Figure D8. Solid Tank Geometry (left) and Mesh (right)

Table D6. Properties of Tank (Solid Mesh)

Parameter	Pre-test Model	Post-test Model
Type of Part	Deformable, Solid	Deformable, Solid
Number of Elements	C3D8: 47,538	C3D8: 47,538
Shell Thickness	0.775 inches	0.775 inches
Material(s)	Test 2 TC128, or;	Actual TC128
	New Normalized TC128	
Part Weight	7.6 lbf	7.6 lbf

D7 – Membrane

The FE model of the DOT-105 tank car included a deformable membrane part that represented the extents of the lading. The liquid and gas phases of the contents of the tank were modeled within the tank using a hydraulic and a pneumatic cavity, respectively. The material properties used to describe the behavior of the air are described in Section 5.3.4, and the material properties used to describe the water are described in Section 5.3.3. In the model, the outage volume was filled with air.

Hydraulic and pneumatic cavity modeling techniques are simplified approaches to capturing the inertial and pressure effects of the liquid lading and the pressure response of the air in the outage. For either cavity, geometry within the model that encloses the limits of the fluid is used to define the volume of the cavity. For the hydraulic cavity, the water in the tank is bounded by the shell

of the tank itself and by its free surface in contact with the outage. For the pneumatic cavity, the outage is bounded by the interior of the tank and the free surface of the water. Thus, the membrane part's geometry represents the interior of the tank, with a horizontal plane to represent the boundary between the air and the water.

For each cavity defined within the membrane, the solver calculates the average pressure and temperature in each time increment during the impact. As the tank deforms from the impact, the hydraulic cavity changes shape. Since the water is highly incompressible, the indentation of the tank can only reduce the volume of the air in the outage. The pneumatic cavity models the air as an ideal gas with user-defined initial pressure and temperature, and a universal gas constant. Thus, as the volume of the tank is reduced, the volume of the outage decreases and thus, the pressure within the pneumatic cavity increases.

Since the pneumatic and hydraulic cavities only calculate the average pressures and temperatures within the cavity, and not the fluid pressure or temperature at each point throughout the lading, this technique reduces the simulation runtime compared to techniques that represent the fluid explicitly as a mesh or collection of particles. However, the average-behavior simplification may not be well suited to all conditions, such as an impact that featured an extremely large tank, or a significant variation in pressure over the volume of either the air or liquid.

Both the hydraulic and pneumatic cavity models require a geometric surface to be defined within the model that defines the boundary of each cavity. Each cavity is also required to have a reference point defined within the volume of the cavity. This reference point is used to define the interior of the cavity, and is also the point to which initial temperatures and pressures are defined for each cavity. Since the tank car model is a half-symmetric model, the cavity is not entirely enclosed within the membrane. In the case of a cavity bisected by a symmetry plane, it is necessary to place the cavity's internal reference point on the symmetry plane.

As discussed in Appendix D5, the shell geometry of the tank represents the mid-plane geometry of the tank. If this geometry was used to define the outer surfaces of the pneumatic or hydraulic cavities, the cavity volumes would be too large, since the volume enclosed was based on the mid-plane surface and not the inner surface of the tank. The membrane part was defined to correspond to the inner surface of the tank's geometry. Since the membrane represents geometry that is not physically present within the tank, the membrane was chosen to be as thin and flexible as practical within the model, without causing the model to terminate due to excessively distorted membrane elements. The membrane typically had a thickness of 0.05 inch.

The membrane includes a horizontal plane at the transition between the gas phase of the outage and the liquid phase of the lading. In this way, the horizontal plane is used to define both the surface enclosing the water and the surface enclosing the air. The height of this horizontal plane (measured from the 12 o'clock position of the membrane within the membrane, as shown in Figure D9) was adjusted to give the desired outage for this tank.
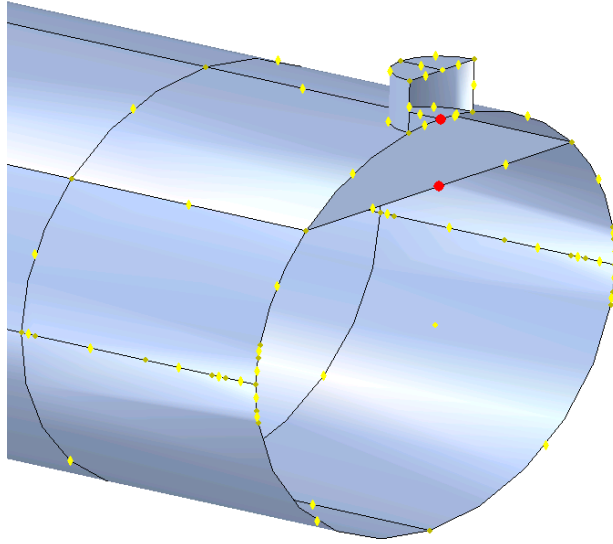
Figure D9. Reference Points for Outage Height within Membrane Part

The relationship between outage height and outage volume for this model is shown in Figure D10. This figure also includes a quadratic regression equation for the volume versus height relationship. For the desired outage of 10.6 percent, the model used an outage height of approximately 16.5 inches below the top of the membrane.

In the chart:

DOT105A500W
Outage Table

$y = 0.016648x^2 + 0.402675x - 0.673365$
$R^2 = 0.999975$

Y-axis: Outage (%)
X-axis: Air Phase Height (inches)

Legend: ◆ Outage %   ☐ Desired Outage   —— Poly. (Outage %)
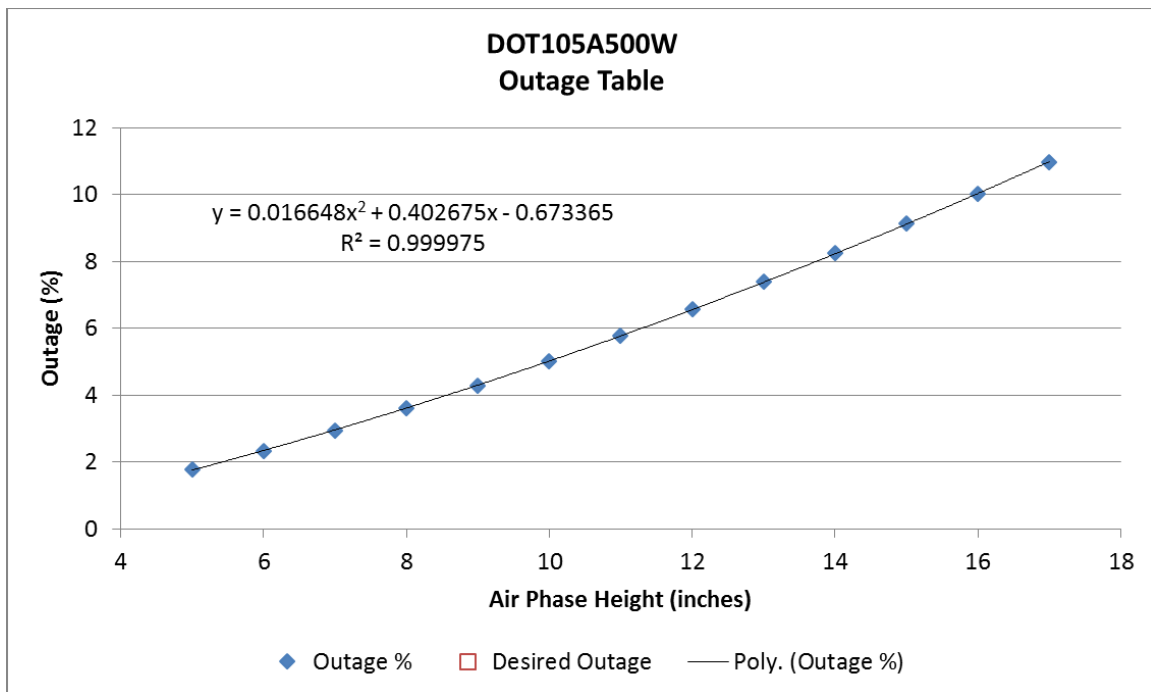
Figure D10. Outage Height versus Outage Volume for DOT-105 Tank Car Model

In addition to representing the surface of the interior of the tank, the membrane was also used to represent the mass of the water lading within the tank. This was done using a "nonstructural mass" feature in Abaqus. The total mass of the water was calculated based on the density of water and the volume enclosed by the membrane. This mass was then distributed through the

117

membrane representing the water phase of the lading, including the horizontal membrane dividing the water and air phases.

The properties of the membrane part are summarized in Table D7 for the pre-test and post-test models.

Table D7. Properties of Membrane Mesh

Parameter	Pre-test and Post-test Models
Type of Part	Deformable, Membrane
Material(s)	Membrane
Number of Elements	M3D4R: 9,540
Number of Elements	M3D3: 20
Part Weight	Membrane: 1,487.6 lbf
Part Weight	Additional Weight of Water: 65,162.5 lbf

D8 – Foam Insulation

A post-test FE model of the DOT-105 tank car included a deformable solid part representing the foam insulation between the tank and jacket. The material properties used to define the foam are described in Appendix F6.
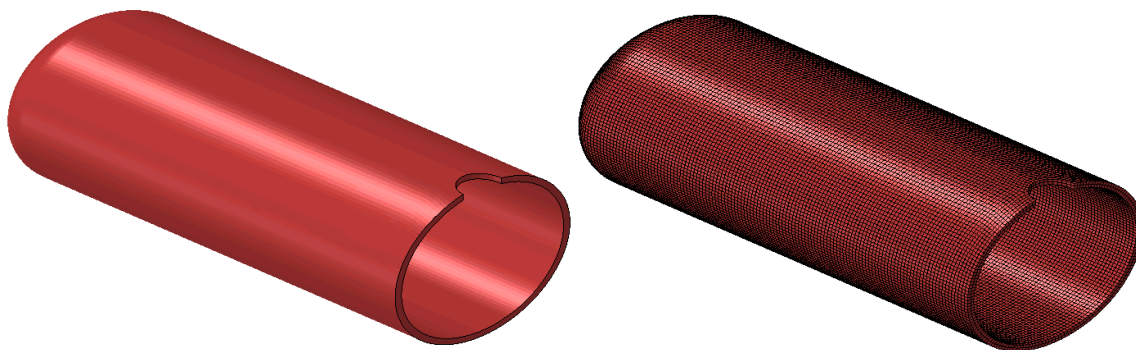
Figure D11. Foam Insulation Geometry (left) and Mesh (right)

The properties of the foam insulation part are summarized in Table D8 for the post-test model.

Table D8. Properties of Foam Insulation Mesh

Parameter	Post-test Model
Type of Part	Deformable, Solid
Material(s)	Insulation
Number of Elements	C3D8R: 44,498
Part Weight	419.6 lbf

Appendix E.
Modeling Techniques Common to Pre-test and Post-test Finite Element Models

This section describes the boundary conditions, initial conditions, constraints, and contact definitions within the FE model.

E1 – Symmetry Conditions

During the impact test, the test plan called for the impactor to strike the DOT-105 tank car at its longitudinal center. To improve computational efficiency, a half-symmetric model was used to simulate the test. A symmetry boundary condition was applied to the tank (solid and shell element portions), the jacket, and the internal membrane.

The symmetry conditions were not adjusted between the pre- and post-test models.

E2 – Rigid Impactor Boundary Conditions

The rigid impactor was constrained against all motion except for longitudinal displacement. The impactor was given an initial velocity corresponding to the simulated impact speed. The pre-test models were run at various speeds, and the post-test model at the measured test speed of 15.16 mph.

E3 – Rigid Wall Boundary Conditions

The rigid backing wall was restrained against motion in all degrees-of-freedom (DOF). This behavior was not adjusted between the pre- and post-test models.

E4 – Jacket-to-Tank Tie

The jacket and tank were attached to one another using a "tied constraint" acting over the region of the bolster in the physical tank car. Standoffs between the tank and jacket were not included in this model, so this tied constraint represented the only connection between the tank and jacket. A tied constraint was defined between the arc representing the bolster on both the tank and the jacket parts. A position tolerance of 4.5 inches was used to account for the gap between the tank and jacket, where the insulation (not included in the pre-test models) exists in the physical car.

The jacket-to-tank tie was not adjusted between the pre- and post-test models.

E5 – Tank-to-Skid Coupling

The tank was connected to the rigid skid through a kinematic coupling. This coupling applied to all 6 DOF. The coupling was between the arc of nodes on the tank representing the bolster and the rigid body reference point of the skid, as shown in Figure E1.
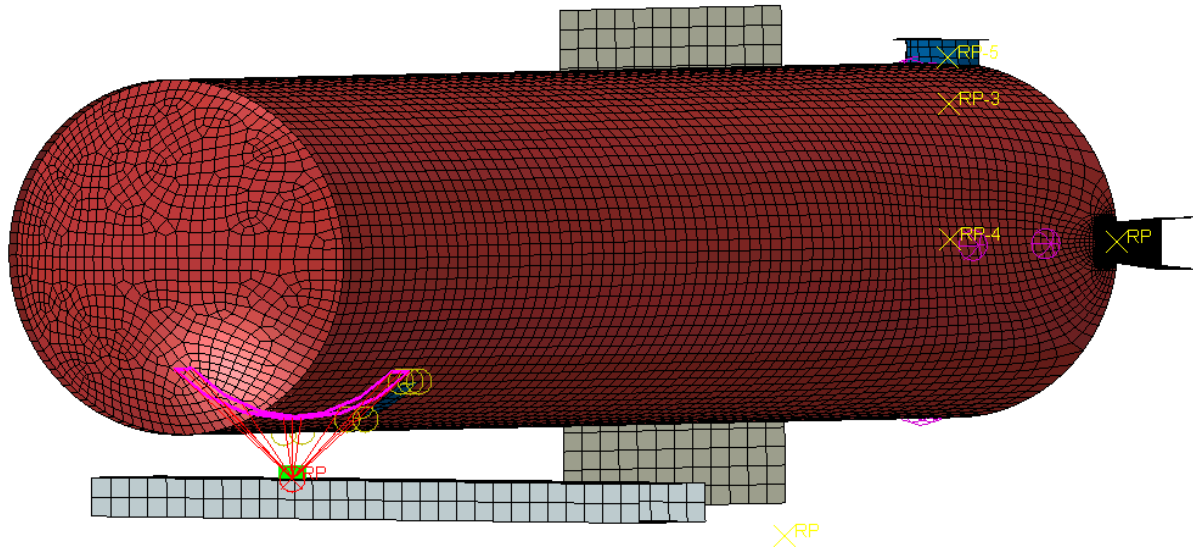
Figure E1. Tank-to-Skid Coupling

Additionally, boundary conditions were applied to the skid in the model. In both the pre- and post-test models the skid was allowed to translate in the direction of the impactor's initial travel, but was constrained against vertical motion and against rotation about the lateral (parallel to the tank's cylinder) axis.

The tank-to-skid coupling and skid boundary conditions were not adjusted between the pre-test and post-test models.

E6 – Shell-to-Solid Coupling

A shell-to-solid coupling was used to attach the patch of solid elements near the impact zone to the rest of the shell-meshed tank. This type of constraint is necessary to ensure a smooth transition from solid elements, which possess only translational displacement DOF, and shell elements, which possess translational and rotational DOF. As previously described in Section D.2.2, the meshes on the solid part and the shell part were controlled such that every element on the shell edges involved in the coupling spanned two solid elements. Since the shell part corresponded to the mid-plane thickness of the tank, the shell part was aligned with the mid-plane of the solid patch. The interface between the solid patch and the shell tank is shown in Figure E2. In this figure, different colors indicate different types of elements.
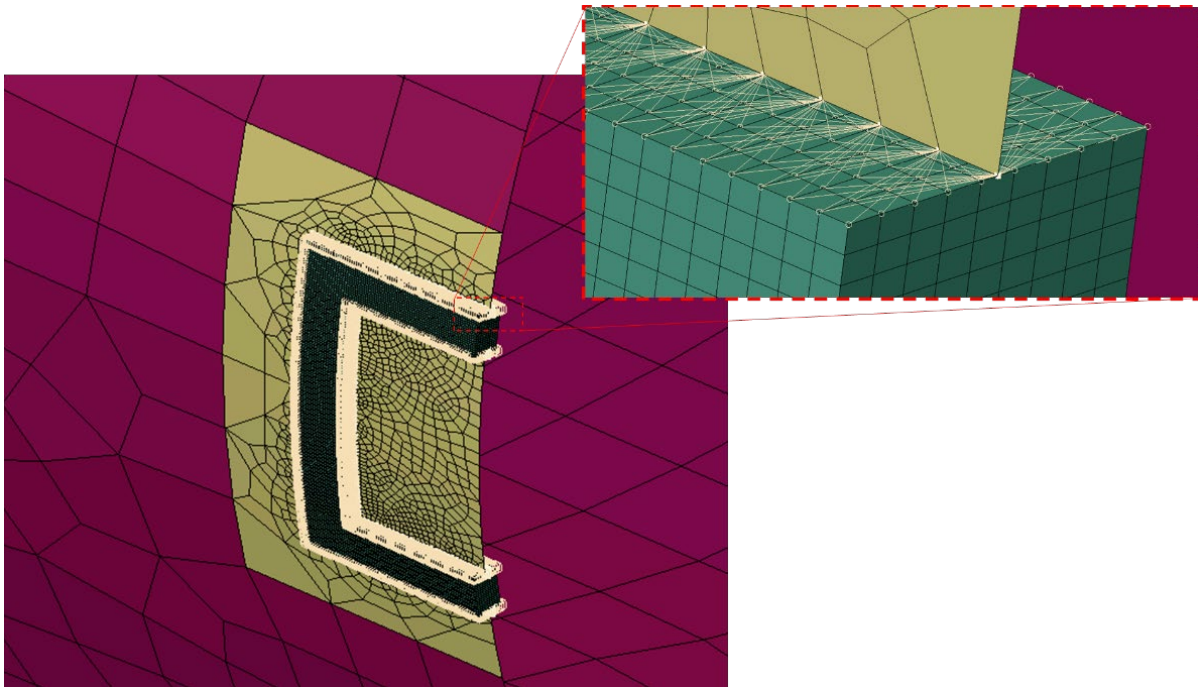
Figure E2. Shell-to-solid Coupling Region

The shell-to-solid coupling behavior was not adjusted between the pre- and post-test models.

E7 – Internal Pressures and Temperatures

The lading within the tank was given an initial pressure of 100 psi. As the surfaces describing the boundaries of the water and gas phases deformed, the pressure was free to change in response. The hydraulic cavity and pneumatic cavity definitions also require the definition of the ambient pressure outside of the cavity. A value of 12.3 psi [23], corresponding to atmospheric pressure at Pueblo, CO's, altitude of approximately 4,700 feet [24], was used for ambient pressure. Thus, the air within the tank was initially modeled at an absolute pressure of 112.3 psi.

The fluid cavity approach of modeling liquids and gases required an initial temperature to be defined for the ladings. Based on average historical climate data around the planned date of the DOT-105 tank car test, an initial temperature of 55 °F was chosen for the models [25]. This value was not changed in post-test modeling, as the measured temperature of the lading at the time of the test was found to be approximately 55 °F.

E8 – Springs

Soft springs (k=1x 10^{-6} lbf/inch) were placed within the model at locations corresponding to the string potentiometers installed within the tested tank (see Section 3.3). The use of springs allowed a direct comparison between the change-in-length of a string potentiometer during the test and the change-in-length of the corresponding spring in the FE model.

The spring behaviors were not adjusted between the pre- and post-test models.

E9 – Mass Scaling

Variable mass scaling was used in both the coupon models and the puncture-capable models. Because of the need for a refined mesh of solid elements in the impact zone, the puncture-

capable models feature a large number of very small elements. These two factors combine to create models with significant runtimes, even when executed on multiple central processing unit (CPU) workstations. Variable mass scaling was employed in the FE models to decrease the runtime without decreasing either the span or the resolution of the refined meshes. Variable mass scaling is a technique in which the user sets a target time increment for a set of elements within the model (up to and including all elements within the model) and the Abaqus solver increases the mass of each element to attempt to bring the minimum time step up to the user-defined minimum. "Variable" refers to the software's ability to increase the mass of each element by a different amount, based on the material and geometry of each element. While mass scaling is an efficient way of reducing runtime without re-meshing a model, care must be exercised when using this technique with highly dynamic simulations. If an overly aggressive mass scaling is applied, the amount of artificial mass added to the model in the refined mesh area can significantly affect both the overall dynamic response as well as the puncture behavior of the model.

The material coupon models did not use mass scaling. The pre-test puncture FE models used a variable mass scaling to achieve a target time increment of 3×10^{-7} seconds over the shell tank and shell jacket. The mass scaling factors were re-calculated at 20 intervals during the simulation.

The post-test puncture-capable models used a variable mass scaling to achieve a target time increment of 3×10^{-7} seconds over the entire model. The mass scaling factors were recalculated at 20 intervals during the simulation.

E10 – Contact

A general contact definition was used in this model. The global contact used frictionless contact, except for metal-on-metal contact. A coefficient of friction of 0.3 was defined between the impactor and jacket, between the jacket and tank, and between the rigid wall and jacket. Contact exclusions were defined between the jacket and itself, and between the shell tank and the solid tank patch.

Appendix F.
Material Behaviors in FE Models

## F1 – Introduction

This activity sought to methodically examine the stress-strain, damage initiation, and damage evolution/progression behaviors being defined for the external jacket and the tank itself in Volpe's Abaqus FE models. Additionally, the relationships between mesh size, element type, and material properties were examined. The jacket is modeled using American Society for Testing and Materials (ASTM) A1011 material and the tank is modeled using TC128 material.

This effort had an underlying assumption that the parameters input to the FEA to model damage initiation and progression were related to the element type and mesh size. Said another way, the damage initiation and progression parameters will vary based on the mesh in which these parameters are being applied.

This process compared the results of published stress-strain curves for A1011 and TC128 with the output of FE models, simulating a standard tensile test. For both materials, the initial model represented the tensile coupon with hexahedral (brick) elements. For the jacket, a second simulation was performed using shell elements, as it was anticipated that shell elements would be used to represent the much thinner jacket during tank car impact simulations. The overall process of simulating the tensile tests is shown in Figure F1.
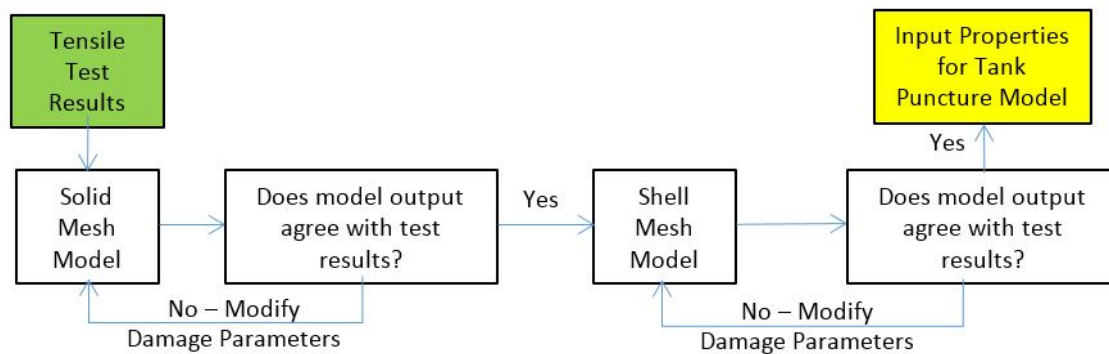
Figure F1. Overall Process for Estimating Material Input Properties

The published stress-strain curves for samples of A1011 and TC128 were obtained from the report "Detailed Puncture Analyses of Various Tank Car Designs" [7]. The plastic stress-strain curves were used as inputs to the FE models without being altered, and no further adjustments were made to the plastic stress-strain behaviors during this study.

This reference also provided the baseline ductile failure initiation envelope (i.e., Bao-Wierzbicki envelope) for TC128. No baseline ductile failure initiation envelope for A1011 was provided in this reference, so one had to be developed using available data. The ductile failure envelopes for each material were adjusted to provide the best agreement for a given element type and mesh size in the modeling of the tensile testing.

Additionally, no information was published in this report about the damage progression parameter. This parameter is used by the Abaqus FE software to determine how much additional deformation can occur to an element once it has exceeded the damage initiation envelope. This

parameter was adjusted for both materials as a part of this study to best fit the published stress-strain responses.

The overall process was intended to show that the damage initiation envelope and damage progression value must be chosen carefully, taking into account the intended mesh to be used in modeling. By modeling a dynamic impact test, it was hoped that the material properties derived for TC128 and A1011 using this methodology would provide reasonable agreement with the measured results of the test.

F2 – Simulation of Coupon Tests

The general approach in performing FE analyses of the coupon tests reported in "Detailed Puncture Analyses of Various Tank Car Designs: Final Report – Revision 1" was to obtain nominal stress-strain relationships from the FE models in as similar a manner to what was done in the tests as is practical [7]. Additionally, since the tensile simulations were being performed with the ultimate goal of providing input parameters for a puncture-capable model, certain tensile modeling variables were chosen with this goal in mind. For example, Abaqus/Explicit was chosen as the solver for the quasi-static coupon simulations, as Abaqus/Explicit would be the solver used in the dynamic tank car impact simulation.

"Detailed Puncture Analyses of Various Tank Car Designs: Final Report – Revision 1" provided the basic geometries of the coupons for the A1011 and TC128 samples [7]. Since the A1011 jacket is a thin sheet (11 gauge, or 0.1196-inch thick), a flat specimen (e.g., dogbone) was used. Since the jacket is thin, the FE model of the DOT-105 tank car was meshed using shell elements.

Since the TC128 tank shell was relatively thick plate (0.775-inch thick), a cylindrical specimen was used in its tensile tests. The FE model of the shell was meshed using hexahedral (brick) elements, with multiple elements through the thickness of the coupon.

For both geometries, a 2-inch gage length was used, as this was the value used in the tests. Within the FE models, a soft (1×10^{-6} lbf/inch) spring was included in the model with its ends attached to the coupon at the ends of the 2-inch gage. This spring was an analogue for an extensometer, and a simplified manner of requesting change-in-length calculations from within the model.

The geometry of the flat and cylindrical coupons from the FE models are shown in Figure F2. Note that this figure is color-coded to indicate different element types. In the A1011 model, the neck region (darker color) was meshed using fully integrated quadrilateral shell elements of type S4, while the lighter regions were meshed using reduced-integration quadrilateral shell elements of type S4R. In the TC128 model, the neck region was meshed using fully integrated incompatible mode C3D8I elements, while the regions outside of the neck were meshed using reduced integration C3D8R elements. Symmetry planes were used in both models to facilitate computational efficiency. In the flat sample of A1011, half-symmetry was used along the vertical-lateral plane. In the cylindrical sample, quarter symmetry was applied. Symmetry planes were used at the vertical-lateral and vertical-longitudinal planes.
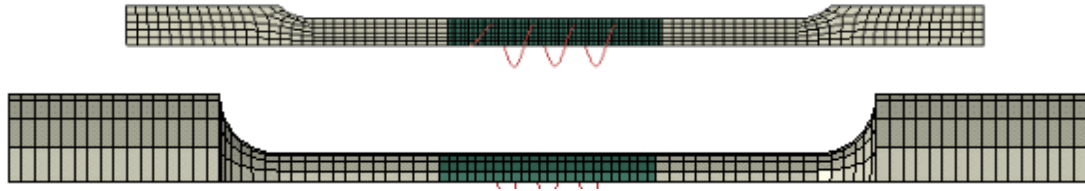
Figure F2. FE Models of A100 (top) and TC128 (bottom) Tensile Coupons

In both models, a boundary condition was applied to the bottom surface of the coupon to simulate the bottom grip during the test. A linear displacement boundary condition was applied to the top surface, simulating the top grip pulling the sample. The displacement was increased until the sample fractured.

The key quantities to be compared between the model and the test results are the nominal stress-strain behaviors [7]. Similar methods were used in the tests and the FEA to calculate these behaviors. The nominal stress was obtained by dividing the total applied force from the FE model by the original area of the sample in the gage region. The nominal strain was obtained by dividing the change-in-length of the spring extensometer by the original gage length, 2 inches.

Abaqus/Explicit requires metal plasticity to be defined in terms of plastic strain and true stress. The plastic behavior of each steel was input to the model according to Equation F1.

Equation F1. Stress-strain Relationships

$$\sigma_{true} = \sigma_{nom} \cdot (1 + \varepsilon_{nom})$$

$$\varepsilon_{ln}^{pl} = \ln(1 + \varepsilon_{nom}) - \frac{\sigma_{true}}{E}$$

|	
σ_{true}	True Stress
σ_{nom}	Nominal (engineering) stress
ε_{nom}	Nominal (engineering) strain
ε_{ln}^{pl}	Plastic strain

F3 – A1011

Tabular results for the stress-strain relationship for A1011 were not published in [7]. Rather, a series of stress-strain characteristics were plotted for the materials used in tank car construction. By overlaying a scatter plot with Figure 63, a piecewise stress-strain relationship for the plastic behavior of A1011 was approximated [7]. Based upon fitting a curve through the points presented in Figure 63, the input stress-strain response used in this effort is shown in Table F1 and Figure F3 [7].

**Table F1. True Stress/True Plastic Strain Inputs for A1011**

True Stress (psi)	Plastic Strain (in/in)
47,000	0
46,000	8.22E-04
46,200	1.20E-02

| True Stress (psi)	Plastic Strain (in/in)
53,000	3.00E-02
58,000	6.00E-02
62,000	1.10E-01
68,000	1.95E-01
125,000	1.15E+00
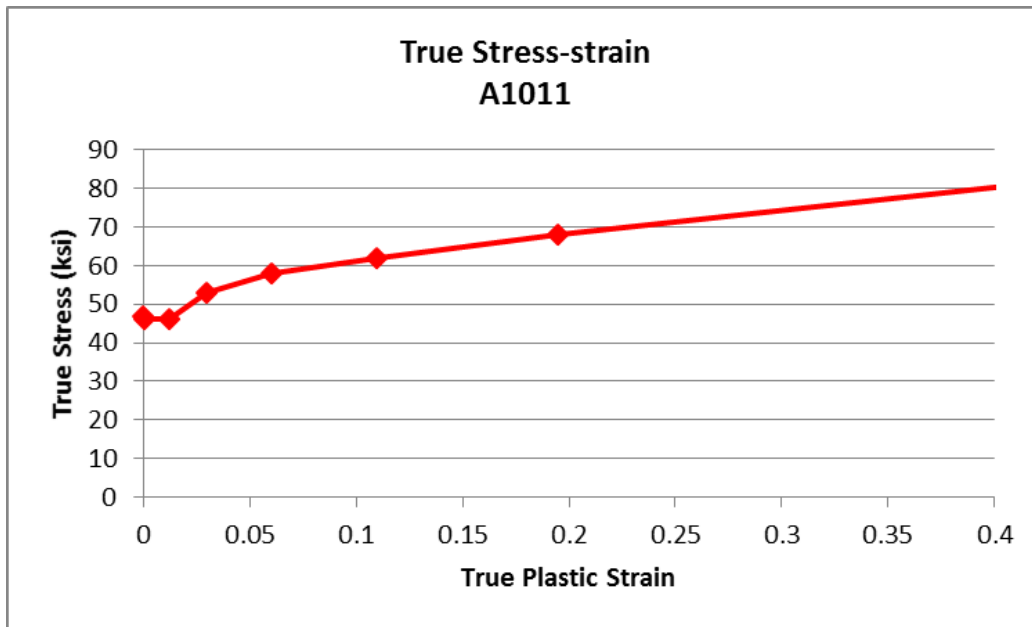
Figure F3. A1011 True Stress and Plastic Strain Behavior

Since no damage initiation envelope was published in "Detailed Puncture Analyses of Various Tank Car Designs: Final Report – Revision 1," an envelope had to be approximated in this current work [7]. At its simplest, damage initiation can occur when a certain PEEQ strain is reached. Choosing a constant strain-to-failure damage initiation criterion is analogous to choosing a triaxiality-based damage initiation criterion in which the strain-to-failure is the same for every value of triaxiality. This was the approach used in the first coupon model of A1011. This model used brick elements of type C3D8 and a mesh size of 0.04 inch in the neck region with a constant PEEQ strain to failure of 0.37. A damage progression of 0.02 inch was used once elements experienced PEEQ beyond the initiation value. The nominal stress-strain response of this model is shown in Figure F4.
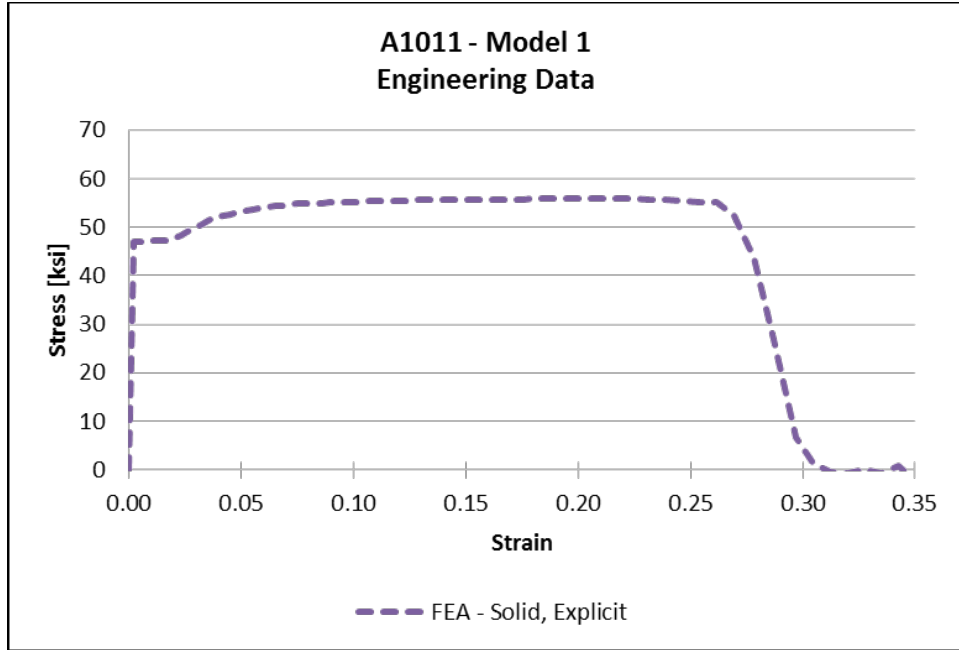
Figure F4. Engineering Stress-strain Results from A1011 Model 1

The results of A1011 Model 1, specifically the displacement at maximum force and reduction in sample thickness, were used to calculate a baseline B-W envelope using the "quick calibration" method developed by Lee and Wierzbicki [26]. The uniform strain-to-failure was then replaced with this B-W envelope to create A1011 Model 2. The tensile test was then re-simulated, using Model 2. The nominal stress-strain response from Model 2 is shown in Figure F5.
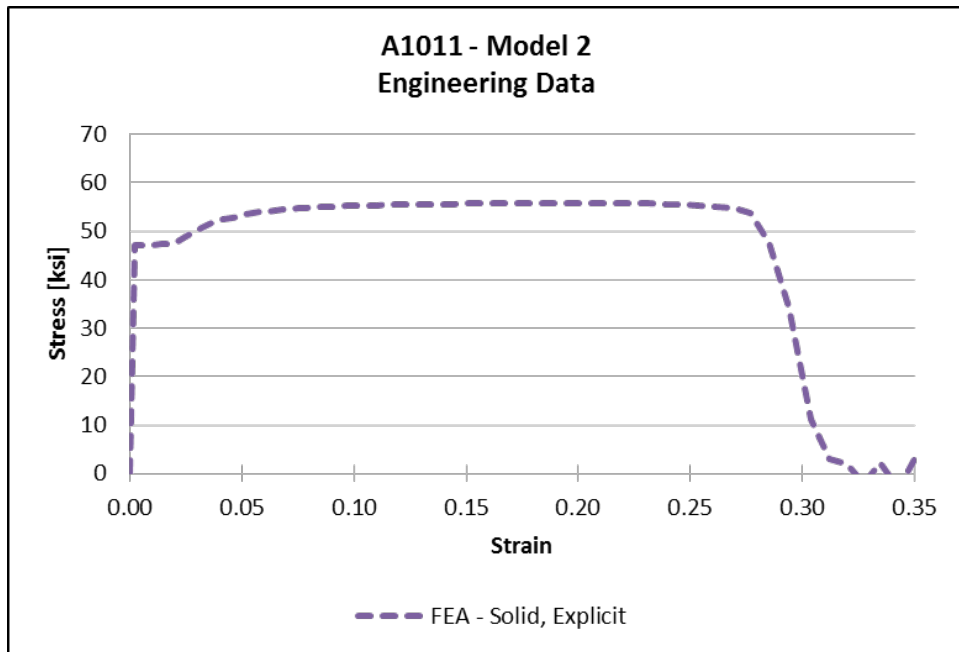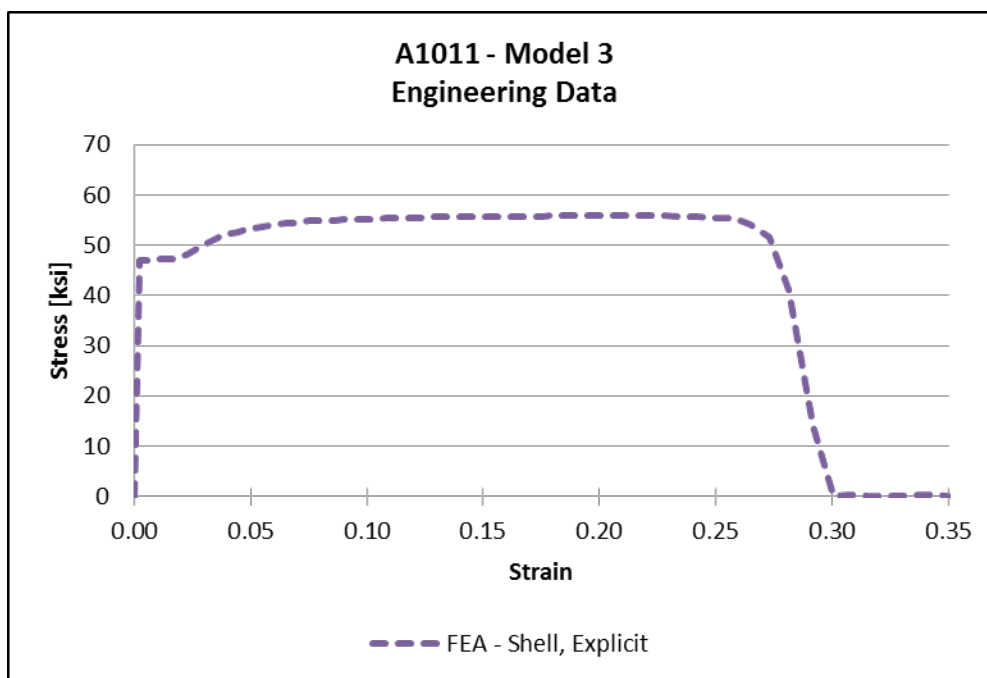

Figure F5. Engineering Stress-strain Results from A1011 Model 2

Finally, because the jacket of the tank car is typically represented using shell elements in FE models, the tensile simulation was re-performed using shell elements to represent the coupon.

127

Since shell elements do not produce a true three-dimensional stress state, owing to a stress of 0 in the through-the-thickness direction, shell elements do not capture triaxiality in the same way as solid elements. Using a B-W envelope and damage progression that produced reasonable agreement between a brick element model and test measurements may not produce similar agreement with applied to a shell element representation of the same test article.

One way of addressing the difference between solid elements and shell elements is to scale the baseline B-W envelope and adjust the damage progression value at the same time. Scaling the curve was accomplished by multiplying the value of PEEQ by a factor, while leaving the value of triaxiality alone. Through an iterative process, a scale factor of 0.72 was applied to the baseline B-W envelope, and a linear energy-based damage progression of 1,500 in-lbf/in^2 was found to give relatively good agreement in the shell element model, when compared to the test measurements from "Detailed Puncture Analyses of Various Tank Car Designs: Final Report – Revision 1" [7]. The nominal stress-strain behaviors from A1011 Model 3 is shown in Figure F6.


Figure F6. Engineering Stress-strain Results from A1011 Model 3

A summary of the three A1011 tensile coupon models is shown in Table F2.

Table F2. A1011 Tensile Coupon Models

A1011 Model Number	Mesh and Elements	Mesh Size in Neck	Damage Initiation	Damage Progression
1	Bricks – C3D8	0.04 inches	Constant PEEQ – 0.37	0.02 inches
2	Bricks – C3D8	0.04 inches	Baseline B-W Envelope	0.02 inches
3	Shells – S4	0.04 inches	0.72 x Baseline B-W Envelope	1,500 in-lbf/in^2 Linear Progression

The initial constant strain-to-failure envelope, baseline B-W envelope obtained using the quick-calibration method, and scaled B-W envelopes are all plotted in Figure F7.
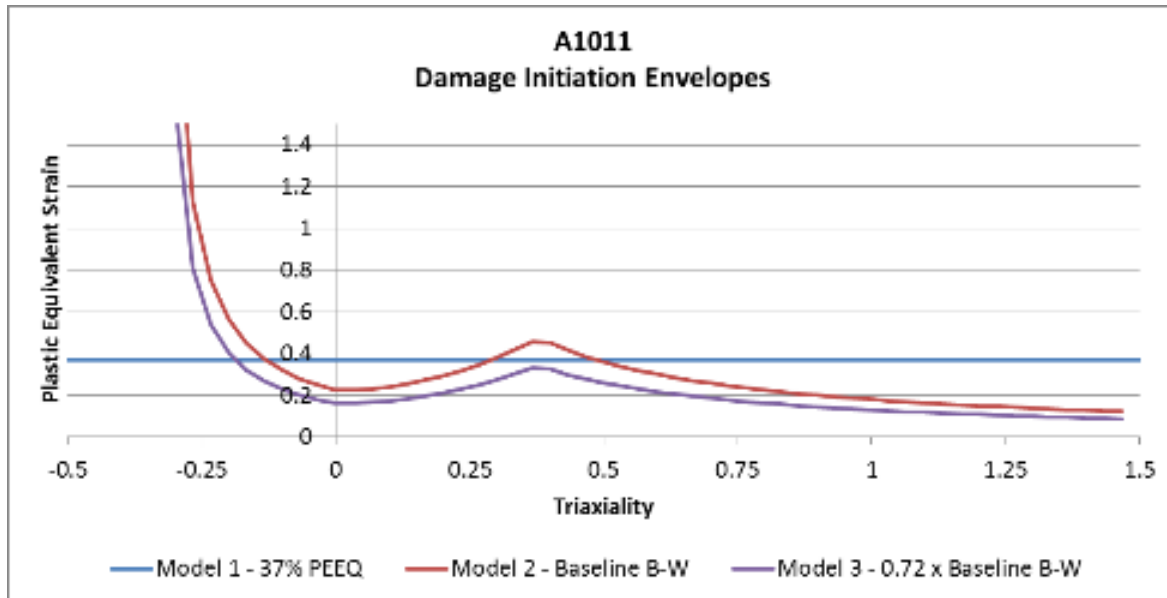
Figure F7. Damage Initiation Envelopes for A1011 Tensile Samples

With the results of Model 3 in reasonable agreement with the measurements from the test reported in "Detailed Puncture Analyses of Various Tank Car Designs: Final Report – Revision 1" [7], the particular combination of mesh size, element type, ductile failure initiation envelope, and damage progression value was carried forward for use in the DOT-105 tank car impact model.

F4 – TC128

Three characterizations of TC128 were developed over the course of this project. Prior to the test, two characterizations with different responses were developed, corresponding to Test 2 TC128 and New Normalized TC128 [7]. After the test, a third characterization was developed based on the measured properties of the TC128 from the tested DOT-105 tank car.

The TC128 coupon models are summarized in Table F3.

Table F3. TC128 Tensile Coupon Models

TC128 Model	Mesh and Elements	Mesh Size in Neck	Damage Initiation	Damage Progression
Test 2	Bricks – C3D8I	0.085 inches	B-W Envelope from [7]	700 in-lbf/in^2 Exponential Progression
New Normalized	Bricks – C3D8I	0.085 inches	Modified Quick Calibration B-W Envelope based on FEA	700 in-lbf/in^2 Exponential Progression
Actual Test Material	Bricks – C3D8I	0.085 inches	Quick Calibration B-W Envelope based on tensile testing	1,400 in-lbf/in^2 Linear Progression

Since the actual properties of the TC128 making up this car would not be known until coupons were cut from the material making up the car, the pre-test models required estimated TC128 properties to be used. The report "Detailed Puncture Analyses of Various Tank Car Designs: Final Report – Revision 1" contained plasticity and ductile damage modeling parameters for a TC128 material that was developed following a previous impact test referred to as Test 2 TC128 [7]. This reference also contained a stress-strain relationship for an additional sample of TC128, referred to as New Normalized TC128. These two materials exhibited very different responses, with Test 2 TC128 featuring a lower strength but a higher ductility compared to New Normalized TC128.

Since a variation in response was seen in just these two samples of TC128, additional information on the potential range of stress-strain responses of TC128 was sought to assist in developing a reasonable pre-test material model. As part of a previous research program, mechanical properties, including strength and elongation, were measured for material samples taken from dozens of tank cars retired from service [20]. From this reference, three samples were identified that came from DOT-105 tank cars built between 1979 and 1981, which correspond to the timeframe when the DOT-105 tank car planned for the impact test was constructed. The average yield strength, ultimate tensile strength (UTS), elongation, and reduction in area (RA) were calculated for each of these three tank cars. The average mechanical properties of the materials reported in "Detailed Puncture Analyses of Various Tank Car Designs: Final Report – Revision 1" and "Mechanical Properties of Tank Car Steels Retired from the Fleet" are summarized in Table F4 [7] [20].

130

Table F4. Mechanical Properties of TC128 from Previously Reported Sources

Source	Material ID	Average Yield ksi	Average UTS ksi	Average Elongation %	Average RA %
[20]	79a-SA	62.5	89.1	23.5	50.8
	79a-SB	65.4	90.2	22.5	47.2
	80a-SA	54.4	82.7	30.75	62
	81a-SA	74.1	100.3	22.5	46.6
	81a-SB	74.5	101.35	22	45.4
[7]	Test 2	58	80	32	-
	New Normalized	65	95	25	-

From this data, it is apparent that there is considerable variation in the mechanical properties of TC128 that can be expected, even from cars constructed in the same period of time to the same specification. However, the material data from the two sources also exhibited some similarities. TC128 Materials Test 2 and 80a-SA exhibit similar yield, UTS, and elongation behaviors, with each having an elongation that greatly exceeded the minimum requirement. Reduction in area (RA) data was not provided for the materials in "Detailed Puncture Analyses of Various Tank Car Designs: Final Report – Revision 1", so a comparison cannot be made for that behavior [7]. Further, New Normalized TC128 and sample 79a-SB exhibited similar behaviors to one another, with each having an elongation that did not greatly exceed the minimum required elongation.

Since the tank car materials for DOT-105 tank cars built between 1979 and 1981 exhibited a range of strength and elongation responses, no one material characteristic could be assumed to be representative of the material in the planned test car. Therefore, the pre-test modeling approach sought to simulate a range of material behaviors likely to be encountered. Due to the similarities between materials noted above, the pre-test modeling approach that was chosen approximated the responses of Test 2 TC128 and New Normalized TC128 to span a range of TC128 ductilities that were encountered in actual cars of the era. The Test 2 TC128 represents materials that greatly exceed the minimum ductility requirement, while the New Normalized TC128 exceeds the minimum ductility requirement by much less.

It was expected that the material in the subject DOT-105 tank car would have properties somewhere between these two responses, and thus, have a threshold puncture speed somewhere between the threshold speeds of the two pre-test material models. Since there was no way of testing the material of the test DOT-105 tank car without cutting a coupon from the car, it had to be assumed that the material making up the shell met the minimum requirements of TC128 at the time of construction, and thus, using a pre-test material model that only slightly exceeded the minimum ductility was a reasonable lower bound. Similarly, because the specification for TC128 does not place an upper limit on elongation, the Test 2 TC128 must be understood as being the upper limit of ductility *for which data are available*. It is possible for other samples of TC128 to meet the strength requirements of the specification while exceeding the minimum ductility by an even greater amount; however, no such samples had been identified in publicly available sources prior to the test.

Since the Test 2 TC128 material described in "Detailed Puncture Analyses of Various Tank Car Designs: Final Report – Revision 1" was developed for implementation in a software package other than the Abaqus/Explicit FE software used to model the DOT-105 tank car in this effort, this material model needed to first be translated into and verified in the Abaqus software [7]. Different software packages implement material characterization differently, so additional parameters were developed to allow the material to be modeled in Abaqus. Since the data provided in "Detailed Puncture Analyses of Various Tank Car Designs: Final Report – Revision 1" did not include the measured reduction in area from coupon tests, the average reduction in area from samples 79a and 81a from "Mechanical Properties of Tank Car Steels Retired from the Fleet" was used as part of the effort to implement the material modeling in the Abaqus software [7] [20].

A similar material development process was followed for the New Normalized TC128 material. In this effort, the reduction in area of sample 80a was used as a target value for comparison with the material simulation results. While "Detailed Puncture Analyses of Various Tank Car Designs: Final Report – Revision 1" included a ductile failure initiation envelope for the Test 2 TC128, it did not contain such an envelope for the New Normalized TC128 steel [7]. A corresponding damage initiation envelope was developed using the New Normalized TC128 properties and the "quick calibration" method described by Lee and Wierzbicki [26].

Pre-test Characteristic: Test 2 TC128

Tabular results for Test 2 TC128's true stress and true plastic strain behavior were published in "Detailed Puncture Analyses of Various Tank Car Designs: Final Report – Revision 1" as Table 2 [7]. These values were used to define the input plastic behavior for Test 2 TC128B in the Abaqus models. The tabular values and true stress-plastic strain behavior for Test 2 TC128 are shown in Figure F5.

Table F5. True Stress/True Plastic Strain Inputs for Test 2 TC128

True Stress (psi)	True Plastic Strain (in/in)
54,500	0
54,600	0.000822
54,800	0.013000
66,500	0.027600
79,500	0.054100
90,200	0.098700
96,000	0.149000
165,000	1.150000

Figure F8 shows Test 2 TC128 material true stress and plastic strain behavior.
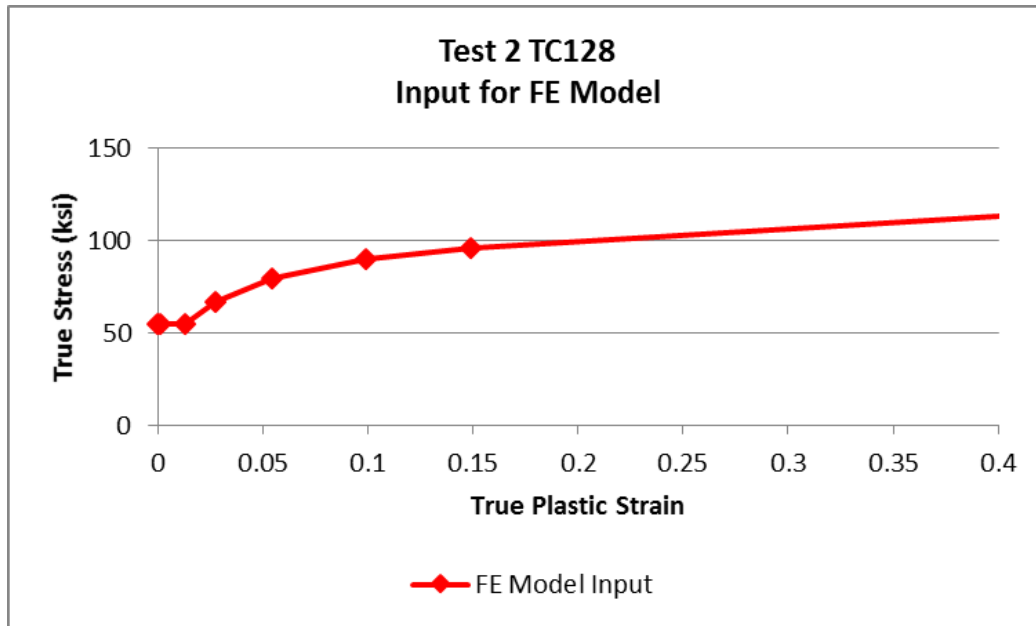
Figure F8. Test 2 TC128 True Stress and Plastic Strain Behavior

The puncture-capable modeling described in "Detailed Puncture Analyses of Various Tank Car Designs: Final Report – Revision 1" used a mesh of 0.04-inch solid elements [7]. A mesh of this size will lead to a considerable runtime for an FE model of a full-scale tank car impact test, owing to the need to mesh a sufficiently large patch of the tank with solid elements to accommodate contact with the impactor. Therefore, it is desirable to increase the element size without sacrificing the ability to capture the behavior of the tensile coupon. The tested TC128 coupon was cylindrical, which presents some difficulties in increasing the mesh size. For sufficiently small elements, the circular cross-section of the sample can be discretized using nearly rectangular elements. However, as the mesh size increases, the number of elements representing the cross-section decreases. This leads to trapezoidal-shaped elements around the circumference of the circle, with rectangular elements in the center.

A mesh size of approximately 0.085 inch was used in the TC128 coupon models. This size represents a significantly larger element than the 0.04-inch mesh, which would correspond to a significant decrease in simulation time in a full-scale tank car model using a mesh of this size. The coarser mesh is used C3D8I elements. These elements, referred to as "incompatible mode" elements, are formulated to provide a better stress response in bending than regular C3D8 elements.

A B-W failure initiation envelope was also published, and included discussion of the calculations necessary to create the envelope [7]. That envelope was reproduced in Abaqus as a baseline envelope for use in this study, and is shown in Figure F9. The original envelope is plotted in "Detailed Puncture Analyses of Various Tank Car Designs: Final Report – Revision 1" as Figure 65 [7].
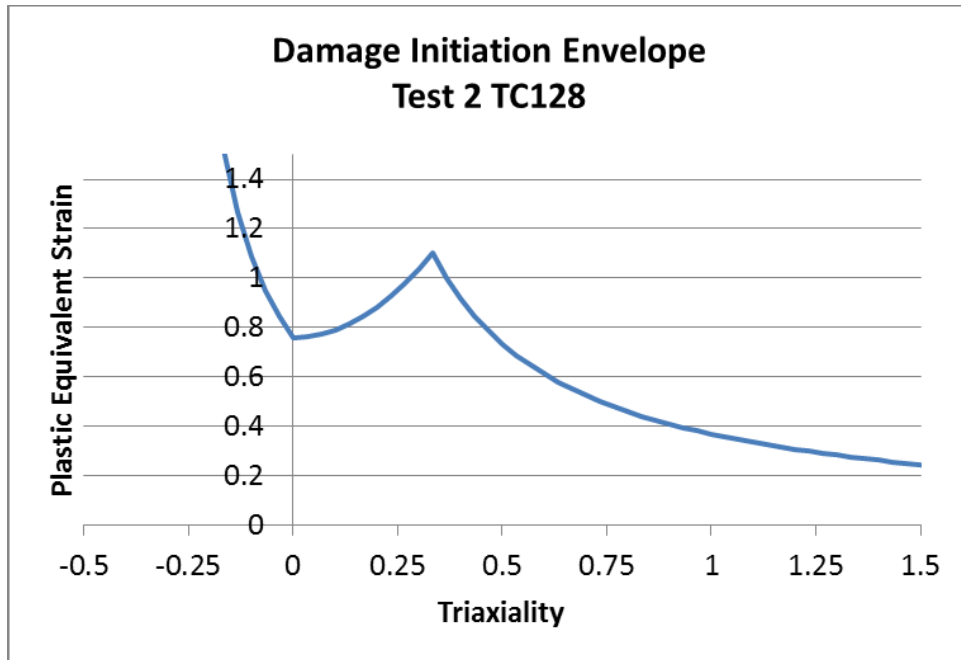
Figure F9. Test 2 TC128 B-W Envelope [7]

After running the FE simulation using a 0.085-inch C3DI mesh and the previously-published B-W envelope [7], the relevant FE results from this simulation were used to calculate the B-W envelope using the quick calibration method developed by Lee and Wierzbicki [26]. The envelope resulting from the quick calibration method is adjusted to have its cusp pass through a triaxiality of 1/3, consistent with the result reported in "Detailed Puncture Analyses of Various Tank Car Designs: Final Report – Revision 1" [7]. The resulting "modified quick calibration" damage initiation envelope is plotted alongside the envelope from "Detailed Puncture Analyses of Various Tank Car Designs: Final Report – Revision 1"in Figure F10 [7]. From this figure, it is apparent that the quick calibration method, when the cusp is forced through a triaxiality of 1/3, gives a result consistent with the envelope developed in "Detailed Puncture Analyses of Various Tank Car Designs: Final Report – Revision 1" for triaxialities greater than 1/3 [7].
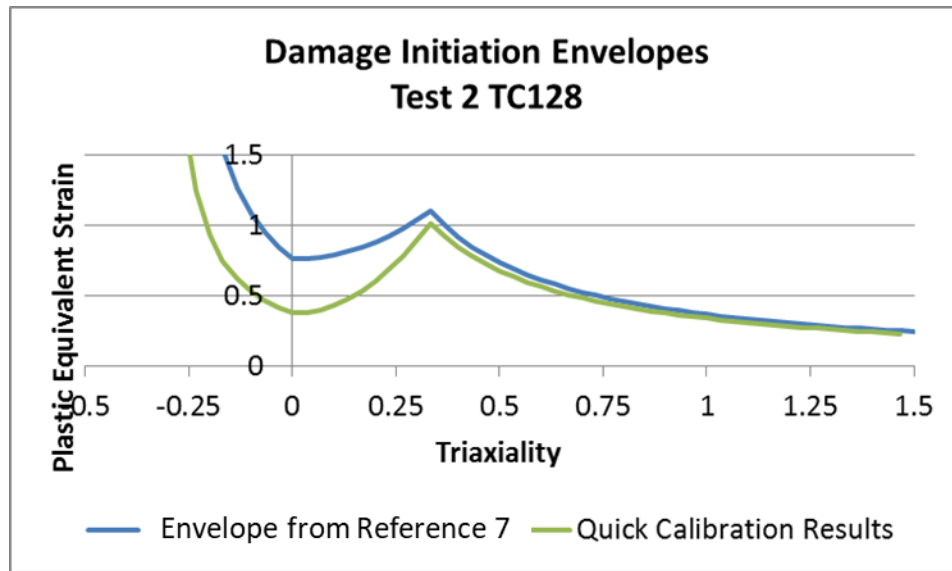
Figure F10. Comparison of Damage Initiation Envelopes obtained using Modified Quick Calibration Method [7]

The B-W envelope obtained from "Detailed Puncture Analyses of Various Tank Car Designs: Final Report – Revision 1" was not adjusted in this current modeling program [7]; however, it was necessary to develop the damage progression behavior within the model to achieve reasonable agreement between the tensile test and the analysis results. An energy-based exponential damage progression value of 700 in-lbf/in^2 was found to provide reasonable agreement for this mesh size. The FE results for Test 2 TC128's nominal stress-strain response is shown in Figure F11.
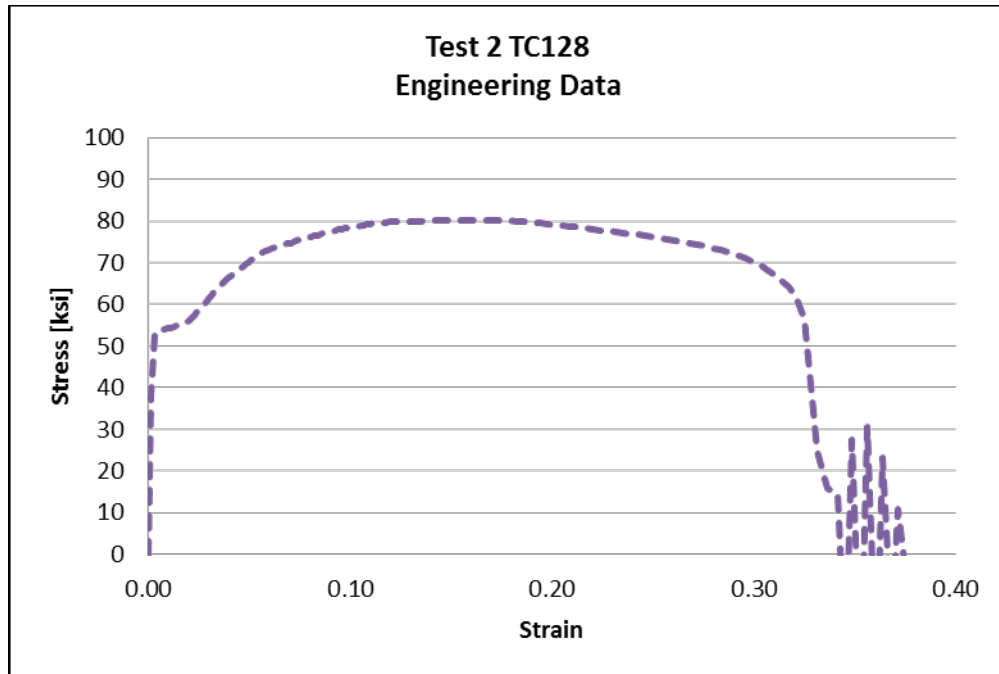
Figure F11. Engineering Stress-strain Results from Test 2 TC128 FE Simulation

Pre-test Characteristic: New Normalized TC128

A second pre-test TC128 characteristic was also developed in this modeling effort. Since the actual material behavior for the DOT-105 tank car being tested would not be known before the test, prudent test preparation called for simulating the "worst practical case" that was likely to be encountered during the test. In addition to the Test 2 TC128 behaviors, a stress-strain response for New Normalized TC128 was also examined [7]. The New Normalized TC128 exhibited a higher yield strength, higher UTS, and lower ductility than the Test 2 TC128. Due to its greatly decreased ductility, it was expected that a tank made of material similar to New Normalized TC128 would experience puncture at a lower speed than the same tank made of Test 2 TC128. Therefore, material behaviors were developed for New Normalized TC128 and included in pre-test models to study the behavior of a DOT-105 tank car made of less-ductile material that still met the requirements of specification TC128.

Figure 55 from "Detailed Puncture Analyses of Various Tank Car Designs: Final Report – Revision 1" provided nominal stress-strain behavior for New Normalized TC128 based on a series of tensile coupon tests [7]. However, there was no further development of material behaviors for the New Normalized TC128 [7]. Therefore, the true stress-true plastic strain behaviors, damage initiation envelope, and damage progression behaviors all needed to be developed to implement a puncture-capable model of the DOT-105 tank car made of New Normalized TC128 as a part of the test preparations.

Using Figure 55 from "Detailed Puncture Analyses of Various Tank Car Designs: Final Report – Revision 1," true stress – true plastic strain behaviors were approximated for New Normalized TC128 and implemented into a coupon model using the same mesh as that used to develop the Test 2 TC128 model previously described [7]. The true stress/true plastic strain input data for New Normalized TC128 are shown in Table F6 and plotted in Figure F12.

136
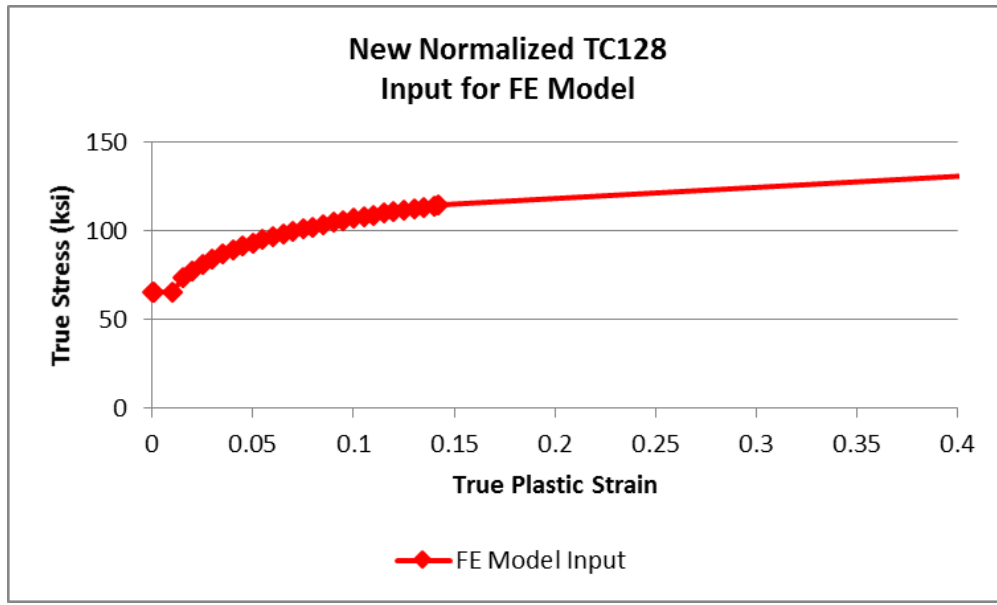
Figure F12. New Normalized TC128 True Stress and Plastic Strain Behavior

Table F6. True Stress/True Plastic Strain Inputs for New Normalized TC128

True Stress (psi)	True Plastic Strain (in/in)	True Stress (psi)	True Plastic Strain (in/in)
65400	0.00E+00	102307	8.00E-02
65520	8.22E-04	103545	8.50E-02
65760	1.00E-02	104726	9.00E-02
73395	1.50E-02	105855	9.50E-02
77706	2.00E-02	106938	1.00E-01
81224	2.50E-02	107978	1.05E-01
84216	3.00E-02	108979	1.10E-01
86831	3.50E-02	109945	1.15E-01
89162	4.00E-02	110877	1.20E-01
91270	4.50E-02	111779	1.25E-01
93198	5.00E-02	112652	1.30E-01
94977	5.50E-02	113499	1.35E-01
96631	6.00E-02	114320	1.40E-01
98178	6.50E-02	114643	1.42E-01
99632	7.00E-02	168862	1.00E+00
101005	7.50E-02		

Using an iterative process, the nominal stress-strain output from the FE model of the tensile coupon using the New Normalized TC128 behavior was matched to the nominal stress-strain responses plotted in "Detailed Puncture Analyses of Various Tank Car Designs: Final Report – Revision 1" [7]. A damage initiation envelope was developed using the modified quick calibration approach, where the cusp is forced to pass through 1/3. The envelope developed for New Normalized TC128 is plotted next to the envelope developed for Test 2 TC128 in Figure F13.
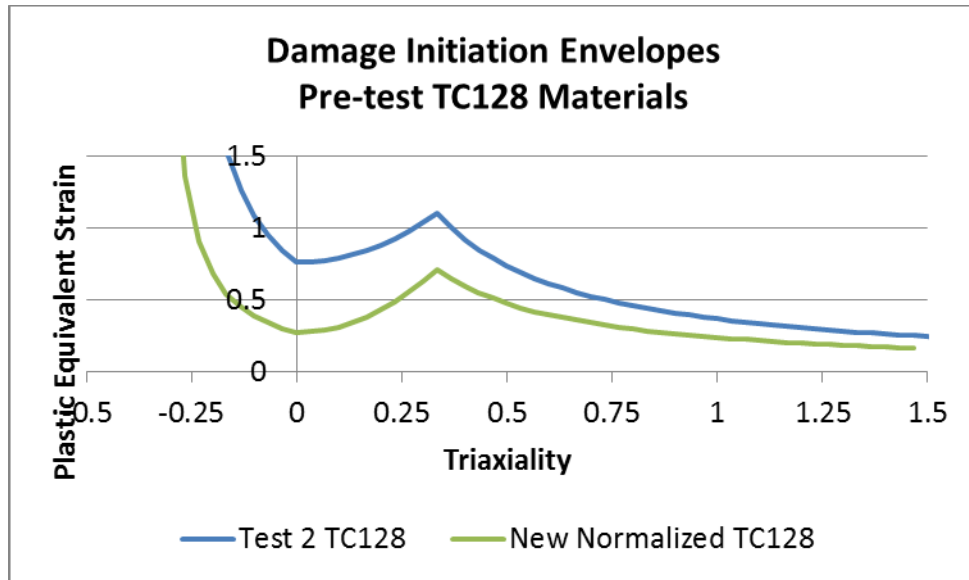
Figure F13. Damage Initiation Envelopes for Test 2 TC128 and New Normalized TC128

The damage progression value of an exponential progression of 700 inch-lbf/in^2 that was found to give good agreement for the Test 2 TC128 material was also found to give good agreement for the New Normalized TC128 material. The nominal stress-strain response for the New Normalized TC128 material used in pre-test modeling is shown in Figure F14.
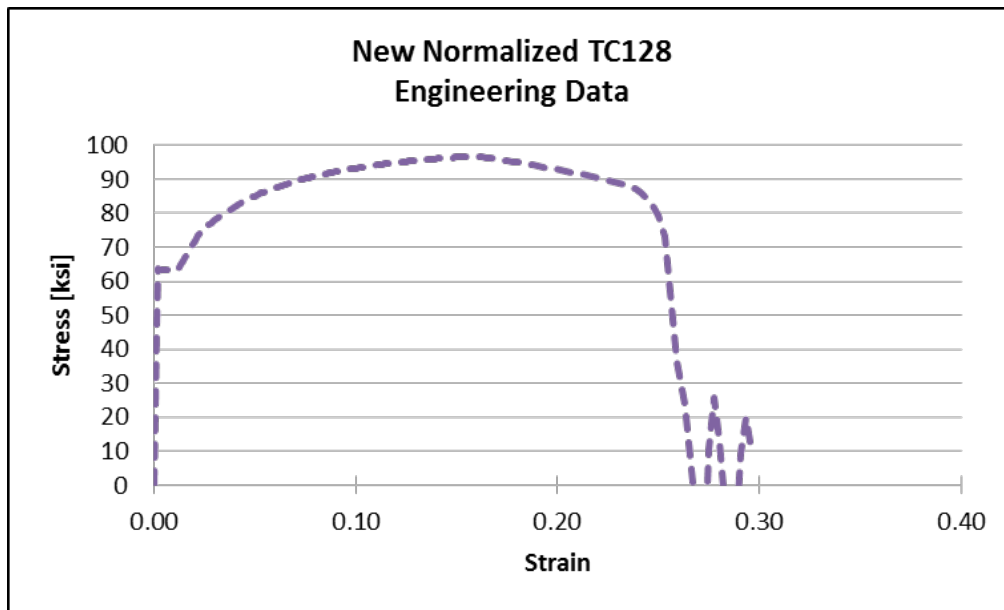

Figure F14. Engineering Stress-strain Results from New Normalized TC128

Post-test Characteristic: Actual TC128

Following the test, material coupons were excised from the tested DOT-105 tank car and sent off for tensile testing. The results of the tensile tests are included in Appendix B4. Additionally, the actual test data was provided to Volpe for use in developing an actual material response for the

material in the tested tank car. Figure F15 contains a plot of the six-nominal stress-strain responses from the tested tank car.
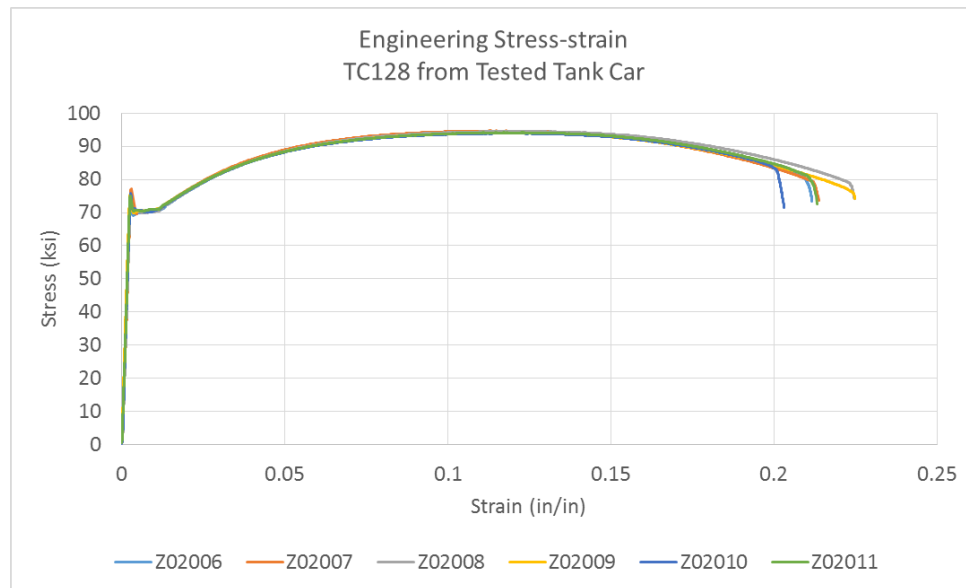
Figure F15. Measured Stress-strain Responses of Six Samples from Tested Car

The material characterization developed for the actual TC128 used in the test car was targeted to match one of the stress-strain responses in the middle of the range of responses observed from the tensile test results. Using an iterative process, the test measurements were used to develop a true stress-true plastic strain response that showed good agreement with the tensile test results. The resulting true stress-true plastic strain behavior is shown in Table F7 and plotted in Figure F16.
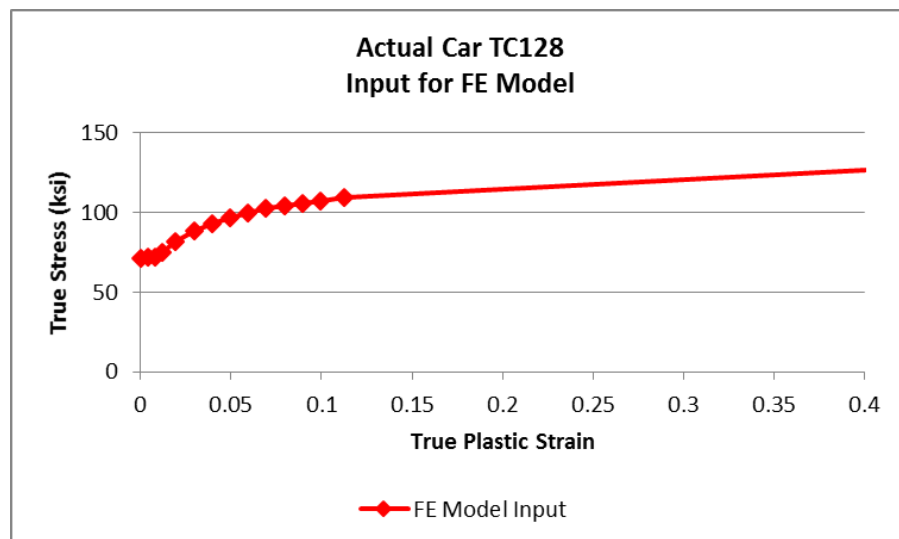
Figure F16. Actual TC128 from Test Car True Stress and Plastic Strain Behavior

Table F7. True Stress/True Plastic Strain Inputs for Actual TC128 from Test Car

True Stress (psi)	True Plastic Strain (in/in)
71500	0
71750	0.00435573
72000	0.00786665
75200	0.0118566
82067.4142	0.0195
88135.2508	0.0295
93021.6352	0.0395
96898.8040	0.0495
99938.9937	0.0595
102314.4410	0.0695
104197.3830	0.0795
105760.0550	0.0895
107174.6940	0.0995
109058.9390	0.112393746
162000	1

Using the tensile testing results as inputs, a damage initiation envelope was developed with the quick calibration approach. Using this approach, the cusp is not forced to occur at a triaxiality of 1/3, but is calculated based on the tensile test results. The envelope developed for Actual TC128 is plotted next to the envelopes developed for Test 2 TC128 and New Normalized TC128 in Figure F17. The values obtained from the quick-calibration method and used to define this envelope are provided in Table F8.
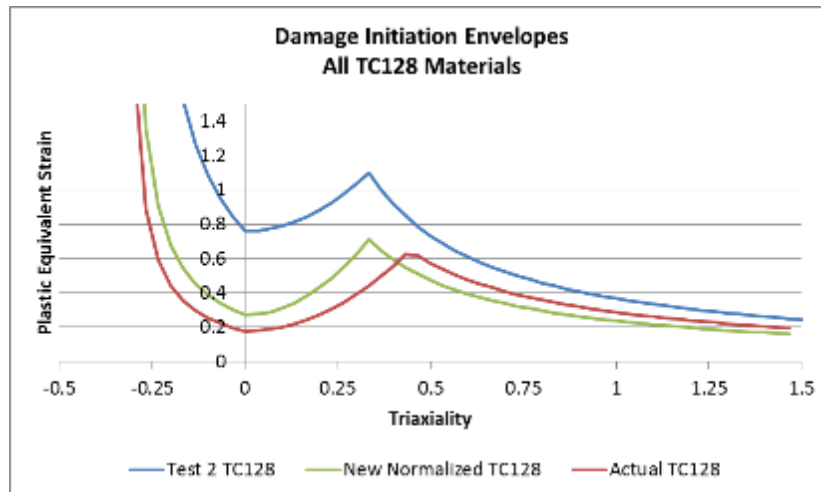
Figure F17. Damage Initiation Envelopes for Actual TC128, Test 2 TC128, and New Normalized TC128

Table F8. Damage Initiation Envelope for Actual TC128

Triaxiality	PEEQ	Triaxiality	PEEQ	Triaxiality	PEEQ
-0.300	1.776	0.467	0.615	1.234	0.233
-0.267	0.888	0.500	0.574	1.267	0.227
-0.233	0.592	0.533	0.538	1.300	0.221
-0.200	0.444	0.567	0.506	1.334	0.215
-0.167	0.355	0.600	0.478	1.367	0.210
-0.133	0.296	0.634	0.453	1.400	0.205
-0.100	0.254	0.667	0.430	1.434	0.200
-0.067	0.222	0.700	0.410	1.467	0.196
-0.033	0.197	0.734	0.391		
6.00E-05	0.178	0.767	0.374		
0.033	0.180	0.800	0.359		
0.067	0.188	0.834	0.344		
0.100	0.201	0.867	0.331		
0.133	0.220	0.900	0.319		
0.167	0.244	0.934	0.307		
0.200	0.273	0.967	0.297		
0.233	0.307	1.000	0.287		
0.267	0.347	1.034	0.278		
0.300	0.392	1.067	0.269		
0.333	0.442	1.100	0.261		
0.367	0.498	1.134	0.253		
0.400	0.559	1.167	0.246		
0.433	0.625	1.2	0.239		

The damage progression value was determined iteratively by comparing the results of the FE simulation of the coupon test to the actual test results. Best agreement was obtained using a linear damage progression of 1,400 in-lbf/in^2. The nominal stress-strain response for the Actual TC128 material used in post-test modeling is shown in Figure F18 alongside the measured stress-strain responses from the coupon tests.
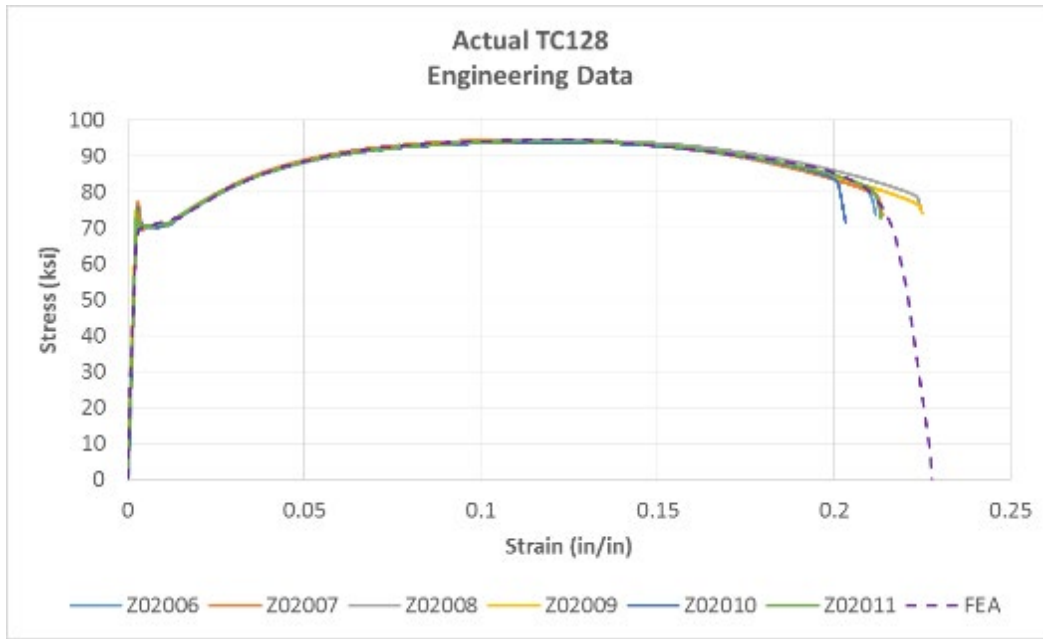
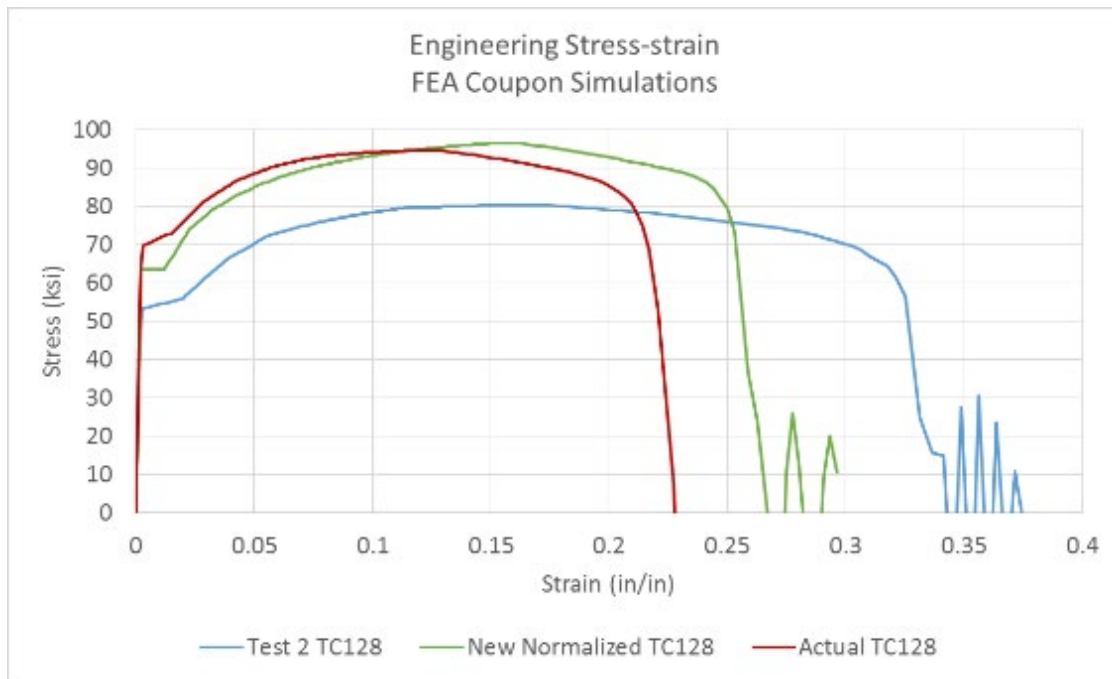**Figure F18. Engineering Stress-strain Results from Actual TC128**

A summary of the Test 6 material properties measured in the six coupons is compared with the results from the simulation of the tensile test in Table F9. The FE simulation demonstrates good agreement with the reduction in area, elongation, yield, and UTS measured from the tested coupons.

Table F9. Comparison of Actual TC128 Properties with FE Model Results

Tested Sample	UTS	Yield	Elongation	RA	Original Diameter	Final Diameter	Initial Gage Length	Final Gage Length
	ksi	ksi	%	%	inches	inches	inches	inches
R1-S1/ Z02006	94.4	69.5	21	48	0.5006	0.3599	2	2.42
R1-S2/ Z02007	94.7	69.7	22	49	0.5004	0.3589	2	2.43
R1-S3/ Z02008	94.5	70.6	22	49	0.5007	0.3578	2	2.44
R2-S1/ Z02009	94	70.2	22	52	0.5009	0.3487	2	2.44
R2-S2/ Z02010	93.9	70.8	21	41	0.501	0.3836	2	2.41
R2-S3/ Z02011	94.1	70.6	21	47	0.5012	0.3657	2	2.42
Average	94.3	70.2	21.5	48	0.5008	0.3624	2	2.4267
FEA	94.6	70.5	22.1	47	0.5	0.3656	2	2.44

A comparison of the nominal stress-strain FE simulations results for Test 2 TC128, New Normalized TC128, and Actual TC128 is shown in Figure F19. As can be seen in this figure, the

Actual TC128 exhibits a ductility below the two pre-test characterizations. The Actual TC128 has the highest yield strength of the three, and UTS that is comparable to that of New Normalized TC128.

Figure F19. Comparison of Engineering Stress-strain Responses of Test 2 TC128, New Normalized TC128, and Actual TC128

F5 – Membrane

As described in Appendix D7, an artificial surface was modeled within the tank to define the limits of the hydraulic and pneumatic cavities. Since this surface does not correspond to any physical structure within the tank, modeling techniques were chosen to minimize the increase in either mass or stiffness introduced into the model by the membrane. Additionally, the membrane material was modeled as having the same mass density of steel to avoid the minimum time increment becoming dominated by the artificial material in the membrane. The material properties of the membrane are summarized in Table F10.

Table F10. Material Properties Defined for Membrane Material

Density	0.00073499 lbf*s^2/inch
Modulus of Elasticity	30,000 psi

F6 – Foam Insulation (Post-test Models Only)

A simplified modeling approach was used to represent the foam insulation between the tank and the outer jacket. The basic technique for foam modeling was the same as found in the Abaqus Example Problem "Cask Drop with Foam Impact Limiter" [21]. This example problem modeled a foam material using elasticity, plasticity, and density. While more sophisticated foam materials are available within the Abaqus modeling software, this simplified approach was chosen for the post-test models including foam insulation, as the intent was not to perform an in-depth analysis of the foam behavior. Rather, the post-test insulation modeling was undertaken to attempt to

account for the force drop exhibited by the post-test model without material between tank and jacket.

From the certificate of construction for the DOT-105 tank car used in this test, the foam insulation was reported to have a density of 2 pounds/ft^3. The foam material described in the Abaqus example problem had a density of approximately 19 pounds/ft^3. Therefore, while the modeling techniques and general shape of the stress-strain curve from the example problem could be used in the foam insulation modeling, the mechanical properties from the example problem could not be directly duplicated due to this difference in foam densities.

The desired mechanical properties were the modulus of elasticity of the foam and the collapse stress (i.e., the stress at which plastic behavior initiates in the model). The stress-strain response from the Abaqus example problem could then be scaled based on the collapse stress for foam having a density of 2 pounds/ft^3. A reference was found that provided relationships between compression/tension moduli and collapse stress of foams as functions of density [22]. Values for modulus of elasticity and collapse stress were obtained using 2 pounds/ft^3 and this reference. The remainder of the stress-strain curve obtained from the Abaqus example problem were then scaled by the ratio of the calculated collapse stress to the collapse stress used in the example problem. The resulting mechanical properties used to model the foam insulation in the DOT-105 tank car post-test models are shown in Table F11.

Table F11. Mechanical Properties of Foam Insulation for Post-test models

Density	2 lbf/ft^3 (3 x 10^{-6} lbf*s^2/inch)
Modulus of Elasticity	941.5 psi
Collapse Stress	8.2 psi
Plastic Strain-to-failure	0.55

The plastic stress-strain response obtained by using density relationships to scale the plastic stress-strain behavior, shown in Figure F20 [22]. The values in this figure are given in Table F12.
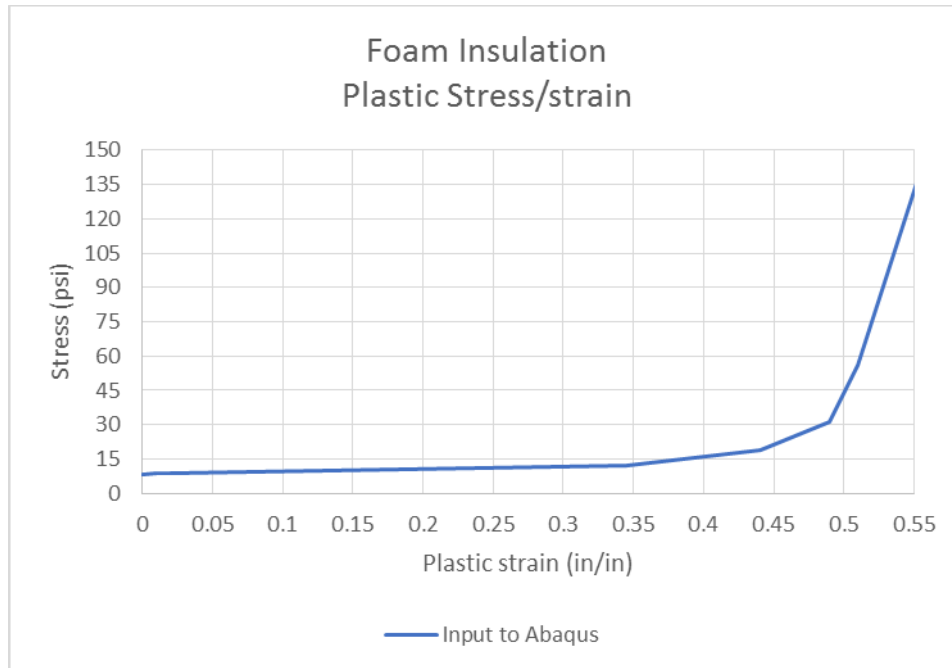
Figure F20. Plastic Stress-strain Response for Foam Insulation

Table F12. Plastic Stress-strain Input for Foam Insulation

Stress	Plastic Strain
psi	in/in
8.21	0
8.51	0.01
8.86	0.02
12.28	0.345
18.66	0.44
31.17	0.49
55.76	0.51
2884.70	2

Finally, based on the test observation that the foam had broken into pieces during the impact, a strain-to-failure was implemented in the foam material. From Figure F20, it is apparent that this strain corresponds to the region where the foam experiences a steep increase in stress for an incremental increase in strain. When the plastic strain reached a value of 0.55 in a given element, that element would begin to fail. The plastic strain to initiate failure was fixed at 0.55 regardless of the stress triaxiality of the element. A damage progression energy of 1.0 in-lbf/in^2 was used to ensure a conservative failure model (i.e., a model that was likely to fail sooner than the physical material).

Abbreviations and Acronyms

Abbreviations & Acronyms	Definition
B-W	Bao-Wierzbicki
CFC	Channel Frequency Class
DOF	Degree of Freedom
DOT	Department of Transportation
EOS	Equations-of-State
FE	Finite Element
FEA	Finite Element Analysis
FRA	Federal Railroad Administration
MW	Molecular Weight
PHMSA	Pipeline and Hazardous Materials Safety Administration
PEEQ	Plastic Equivalent
RA	Reduction in Area
SPH	Smoothed Particle Hydrodynamics
TC	Transport Canada
TIH	Toxic by Inhalation
TTC	Transportation Technology Center (the site)
TTCI	Transportation Technology Center, Inc. (the company)
UTS	Ultimate Tensile Strength
Volpe	Volpe National Transportation Systems Center